Ph.D. Thesis

Université de Limoges

University of Limoges

ED 653 - Sciences et Ingénierie (SI)

XLIM Research Institute, CNRS UMR 7252

A thesis submitted to University of Limoges
in partial fulfillment of the requirements of the degree of

Doctor of Philosophy

Science and Engineering for Information

Presented and defended by

Ceren YILDIRIM

On January 18, 2024

Using a Perovskite Oxide as Interfacial Layer for Halide Perovskite Optoelectronics

Thesis supervisor: **Sylvain VEDRAINE** and **Johann BOUCLÉ**

JURY:

President of jury
Mme Ulrike LÜDERS, CNRS Research Director, CRISMAT, University of Caen Normandie

Reporters
Mme Zhuoying CHEN, CNRS Researcher, LPEM, ESPCI, University of Sorbonne/University of PSL
M. Christophe TENAILLEAU, Associate Professor, CIRIMAT, University of Toulouse III-Paul Sabatier

Examiners
Mme Nadine WITKOWSKI, Professor, University of Sorbonne
M. Johann BOUCLÉ, Associate Professor, XLIM, Limoges of Limoges
M. Sylvain VEDRAINE, Associate Professor, XLIM, Limoges of Limoges
M. Pierre-Marie GEFFROY, CNRS Research Director, IRCER, Limoges of Limoges
M. Frédéric DUMAS-BOUCHIAT, Professor, IRCER, Limoges of Limoges

To my parents,
who have supported to me throughout my life…

I have not failed. I've just found 10,000 ways that won't work.
Thomas A. Edison

Acknowledgements

Rights

Table of Contents

List of Abbreviations

PSC: Perovskite solar cell

PeLED : Perovskite light-emitting diodes

STO: $SrTiO_3$

STFO: $SrTi_{0.7}Fe_{0.3}O_{3-\delta}$

PLD: Pulsed laser deposition

RTP: Rapid thermal processing

TA : Thermal annealing

HTL : Hole transport layer

ETL Electron transport layer

TCO: Transparent conductive oxide

ITO: Indium tin oxide

FTO: Fluorine tin oxide

LUMO: Lowest empty molecular orbital

HOMO: Highest occupied molecular orbital

EQE: External quantum efficiency

PLQY: Photoluminescence quantum yield

PCE: Power conversion efficiency

KPFM: Kelvin probe force microscopy

CPD: Contact potential difference

HOPG: Highly oriented pyrolytic graphite

SCLC: Space-charge limited current

I_0**:** Dark current

I_L**:** Photo-generated current

I_{sc}: Short-circuit current

J_{sc}: Current density

V_{oc}: Open circuit voltage

FF: Fill factor

R_s: Series resistance

R_{sh}: Shunt resistance

σ : Electrical conductivity

ρ : Electrical resistivity

μ : Mobility

List of Figures

List of Tables

Introduction

Halide perovskite is a semiconductor material that shows great potential due to its unique optoelectronic properties. It has a direct band gap, strong light absorption, high ion conductivity, strong carrier mobility, long carrier lifetime, and emission purity. These properties can be adjusted separately or combined, making it a popular choice for perovskite solar cells and light-emitting diodes, among other potential applications. This has generated significant research and industrial interest in the material.

Despite their high performance, perovskite optoelectronic devices still require significant improvements to become suitable for large-scale applications. For commercial use, these devices must meet several criteria, including high performance, long-term stability, low cost, and low toxicity. Further research is necessary to understand the optoelectronic properties of halide perovskite devices, as well as the impact of interlayers on their performance and stability. During operation, halide perovskite-based devices tend to suffer from rapid degradation due to their relatively poor photochemical stability. This is a primary concern for their long-term operation and commercial development. Therefore, current research is focusing on three key areas to address the instability issue in perovskite optoelectronic devices. These include developing new characterization methods for deeper investigation to gain information about instability mechanisms, enhancing the stability of perovskite and charge transport layers in devices, and material engineering for the fabrication of stable perovskites.

In order to prevent halide perovskite from experiencing issues with stability or degradation due to external factors, it is important that the charge transport layer (whether it is p-type or n-type) in the devices is both thermally and photochemically stable. Despite p-type interlayers being a general requirement for efficient devices, their use poses significant challenges. Although current p-type interlayers are effective in charge separation or injection and transfer processing, it is necessary to develop new interlayers and other interfacial engineering techniques to achieve better long-term stability of the devices. Researchers are currently working hard to develop innovative materials for p-type interlayers that offer high photochemical stability and highly tunable properties. However, there is still a need for materials that can provide superior properties.

The family of perovskite oxides has gained attention as interlayers in optoelectronic applications because of their stable properties under ambient conditions and high-quality structural properties. These materials are highly stable in environmental conditions, which makes them an interesting possibility for further investigation. The popularity of these materials is due to their ability to adjust their physical and chemical properties according to stoichiometry while maintaining stability against external factors under most conditions. Perovskite-type oxide structures are known to be stable when they are based on a broad majority of natural metallic elements such as iron and titanium. This allows for a wide range of properties to be demonstrated for many potential applications. Although only a few studies have been reported in the literature, they have been successful in integrating perovskite oxides into optoelectronic devices, achieving performance comparable to commercial materials.

The goal of this thesis is to explore the potential of perovskite oxide materials as p-type interlayers. Specifically, we will focus on using $SrTi_{0.7}Fe_{0.3}O_{3-\delta}$ (STFO) perovskite oxide thin films as charge transport layers for inverted halide perovskite devices, such as perovskite solar cells and light-emitting diodes. STFO is an excellent choice due to its versatility in terms of

synthesis and fabrication techniques. However, it is important to note that different techniques can affect the material's properties. For our purposes, we will be using pulsed laser deposition (PLD) as it is a highly effective and reproducible method for complex oxide heteroepitaxy. PLD offers precise stoichiometry transfer from the target to the substrate, fast growth rates, high crystalline film quality, and the ability to grow a wide range of complex materials. Overall, PLD is a versatile and reliable method for our study.

The manuscript consists of five chapters:

The first chapter of the thesis will provide a comprehensive overview of halide perovskites and their potential applications in solar cells and light-emitting diodes. It will start by discussing the various opportunities and dimensions of halide perovskites. The chapter will also present the evolution of perovskite solar cells and light-emitting diodes over time, highlighting the similarities and operational differences between these devices. Moreover, it will delve into the theoretical fundamentals of both devices, explaining their basic principles of operation. The chapter will also explore different device architectures and the functions of charge transport layers used in these devices. Additionally, it will present the current state-of-the-art of p-type interlayers (organic and inorganic) in this field, highlighting their advantages and drawbacks. Finally, the chapter will outline the scope and main objectives of the thesis.

In Chapter 2 of the thesis, we will be exploring the structural, optical, and electrical properties of STFO type oxide perovskite. We will also be examining different deposition techniques that come with their own advantages and drawbacks when it comes to STFO properties. We'll compare and evaluate these methods based on their suitability for material properties and selected substrate. Ultimately, we will provide information on the preferred deposition technique, which is PLD, and explain why it stands out in our study for fabricating STFO perovskite oxide. Lastly, we will present the working principle of PLD.

Chapter 3 of the thesis describes the process for depositing STFO thin films using PLD. The STFO films studied in this chapter are intended for use in halide perovskite optoelectronic devices. The process begins by identifying the ideal crystallization conditions for STFO at low temperature (~400°C) by PLD, which is compatible with the use of transparent conductive electrode substrates. Two different pressure conditions are compared to investigate the STFO characteristics in terms of optimal deposition condition in the PLD chamber: residual pressure (under vacuum) and oxygen partial pressure (reactive atmosphere). Although STFO successfully crystallizes under both conditions, some parasitic crystals form under residual pressure. Therefore, optimization based on the reactive atmosphere created by oxygen has been selected. In this step, three different oxygen partial pressures have been tested, and a comparative study has been presented to achieve high-quality crystallization of the STFO thin film. The optimal oxygen partial pressure meets specific criteria, including the achievement of thin films without pinholes, being dense, presenting a homogenous surface, and reduced impurity densities. The structural, optical, and electronic properties of the STFO thin films are then characterized to determine their suitability as an interlayer. Two different additional thermal treatments, rapid thermal processing (RTP) and conventional thermal annealing (TA), are applied to optimally crystallized STFO thin films, and their effects are discussed in detail in terms of structural, optical, and electrical aspects.

In Chapter 4 of this thesis, we will discuss the procedures for creating reference solar cells and PeLEDs based on halide perovskites. The first part of the chapter will cover the optimization processes necessary for improving the performance and reproducibility of inverted planar solar cells. This will include optimizing the hole transport materials, metal

electrodes, and electron transport materials. Additionally, we will discuss the limitations of these materials and their impact on device operation. This section will also provide details on the methodology for designing and fabricating these devices, including the deposition methods and synthesis process for the interlayers. The second part of the chapter will focus on fabricating and characterizing the performance of green perovskite LED (or PeLED) devices that meet reasonable benchmarks for being reference devices. We will provide details on the synthesis, fabrication, and design of PeLEDs.

In Chapter 5, we will discuss the integration of STFO perovskite oxide thin film into two halide perovskite optoelectronic devices, namely solar cells and PeLEDs. The first part of the chapter will focus on improving the poor wettability of the STFO surface towards halide perovskite deposition. We will use UV-ozone treatment to investigate the effects of short time (3 minutes) on the optical and structural properties of oxide perovskites. Our findings suggest that this treatment does not cause any qualitative changes in transmittance, crystal quality, and surface morphology properties. For the photovoltaic part, we will use $FA_{0.85}Cs_{0.15}Pb(I_{0.85}Br_{0.15})_3$ halide perovskite as an absorber layer. The STFO thin films' coating has been completed successfully, with full coverage, uniformity, and no pinholes. We will compare the structural and optical properties of as-grown and thermal-treated STFO thin films with those of PEDOT:PSS, which will help us discuss their potential for perovskite solar cells. In the second part of Chapter 5, we will delve into the emission properties of PeLED based on oxide perovskites as a hole injection layer. We will use $PEA_2MA_{n-1}Pb_nBr_{3n+1}$ halide quasi-2D perovskite as the emissive layer, according to our reference PeLED detailed in Chapter 4. We will investigate the optical and structural properties of these materials and compare them with PEDOT:PSS on the physical properties of the halide perovskite layer. Additionally, we will discuss electroluminescent properties based on STFO. Finally, we will summarize the potential of STFO thin films for PeLED only or also PV and discuss their future development.

In a brief summary, this Ph.D. thesis represents the first application of $SrTi_{0.7}Fe_{0.3}O_{3-\delta}$ type perovskite oxide in the field of halide perovskite optoelectronics, and it sheds light on their potential in this area. The fundamental knowledge gained from this research will significantly contribute to further development in this field, which involves multidisciplinary research encompassing various device structures, material optimization, different deposition techniques, and characterization of thin films.

Chapter I. Contextual Dimensions in Perovskite Optoelectronics

I.1. Brief History of Perovskites

In 1839, a group of German scientists found a black mineral in the Ural Mountains of Russia. They named it after Lev Aleksevich Perovski, a Russian politician and mineralogist[1]. This mineral, called perovskite, was identified to have a chemical composition of calcium titanium oxide ($CaTiO_3$)[2]. The analysis of crystal morphology led to the discovery of other minerals with the same crystal structure, including synthetic materials. Nowadays, perovskite is a group of materials and any crystal structure with the chemical formula ABX_3. A is a larger monovalent cation, B is a smaller divalent cation, and X is a monovalent anion[3]. Perovskites can be classified into different types, such as halide or oxide perovskites, depending on the composition and type of compound selected.

The main differences between halide perovskite and oxide perovskite are listed below:

a.   Composition: A wide range of materials can be used as perovskite compounds' A, B, and X elements.

Halide perovskites consist of an organic cation (such as methylammonium ($CH_3NH_3^+$), formamidium ($HC(NH_2)^{2+}$)) and a metal halide (such as lead halide (Pb^{2+}), tin halide (Sn^{2+}) or cesium halide (Cs^+))[4]. Here are some examples of them in below:

•   Methylammonium lead iodide ($CH_3NH_3PbI_3$): A = CH_3NH_3, B = Pb, X = I

•   Cesium lead bromide ($CsPbBr_3$): A = Cs, B = Pb, X = Br

On the other hand, oxide perovskites have includes both metal oxides (such as titanium oxides (TiO_2), iron oxide (FeO_2) or zirconium oxide (ZrO_2)) and alkaline earth metals (such as calcium (Ca), strontium (Sr))[5]. Oxide perovskites typically use oxygen for the X component and are monovalent halogens, while halide perovskites use just halogens. Here are some examples of them in below:

•   Calcium titanate ($CaTiO_3$): A = Ca, B = Ti, X = O

•   Strontium titanate ($SrTiO_3$): A = Sr, B = Ti, X = O

b.   Crystal Structure: In perovskites, certain sequences of phase transition may occur due to external conditions, such as temperature or pressure. These transitions can directly affect the molecular dynamics, revealing specific properties. Both types of perovskites share a crystal structure similar to Figure I.1, but the atomic arrangement within varies. Halide perovskites typically have a cubic crystal structure, whereas perovskite oxides can exhibit cubic, tetragonal, or orthorhombic structures due to the flexibility of perovskite structure based on molecular dynamics and the size of the ions involved in structure.
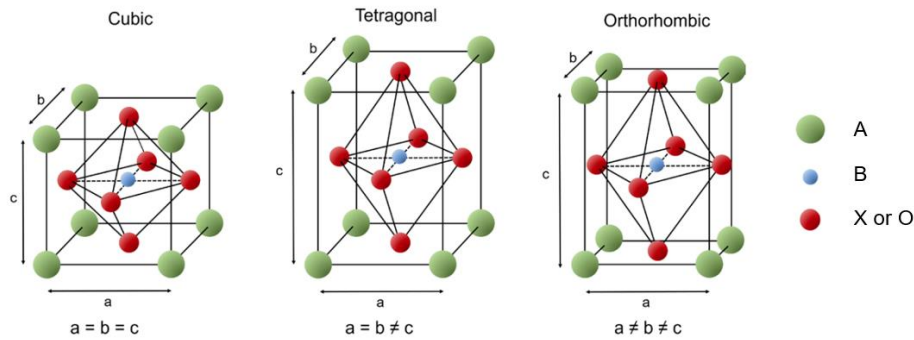
Figure I.1: Crystal structures of ABX_3 perovskite[6]

c.   Electronic and Optical Properties: Perovskite's optical properties are directly related to oxygen and halogen chemistry. Both perovskite types have tunable band gaps, but halides have a narrow band gap[7], while oxides have a broadband gap[8]. Halide perovskites show remarkable optical properties, including broad range of absorption coefficient and effective charge transport[9], while oxide perovskites exhibit fascinating optical properties such as light absorption in visible, ultraviolet, and sometimes infrared light based on the choice of materials and their bandgap[10].

d.   Stability: Halide perovskites are very sensitive to actual operational conditions, e.g., heat, oxygen, light, and humidity, so they degrade in time[11]. Oxide perovskites are the opposite and are known to be more stable. They also resist high temperatures and harsh external factors[12].

e.   Synthesis: There are several synthesis methods, such as sol-gel, dip-coating, evaporation, and doctor blade for halide perovskites. The sol-gel liquid-state synthesis method is the most widely used because it facilitates the transition to industry[13]. Oxide perovskites can be deposited using solid-state, liquid-state, and gas-state synthesis methods. However, the most preferred method is solid-state synthesis[14].

f.   Applications: Halide perovskites are generally preferred in optoelectronic applications like solar cells and LEDs, while oxide perovskites are used in various sensors, catalysis applications, water splitting, and memory devices[15].

I.2. Opportunities of Halide Perovskites

Perovskite materials can have dimensional properties which result in numerous specific features. The 3D perovskite known as ABX_3, can be transformed into 2D, 1D and 0D in terms of material and morphological levels[16], as illustrated in Figure I.2. This process involves reducing the A-cite cation dimensionally, leading to the creation of low-dimensional perovskites. The bulky organic cations like PEA^+ (phenylethylamine) and BA^+ (butylamine) meet the criteria for reducing process[17]. As a result, the low-dimensional perovskites can be expressed by the following general formulas: $A'_2A_{n-1}B_nX_{3n+1}$ and $A'A_{n-1}B_nX_{3n+1}$. The variable "n" represents the number of $[BX_6]^{4-}$ octahedra layers stacked between two organic spacers[18]. It varies from 1 to n=∞, indicating pure 2D (n=1), quasi-2D (1<n ≤10) and 3D (n=∞).
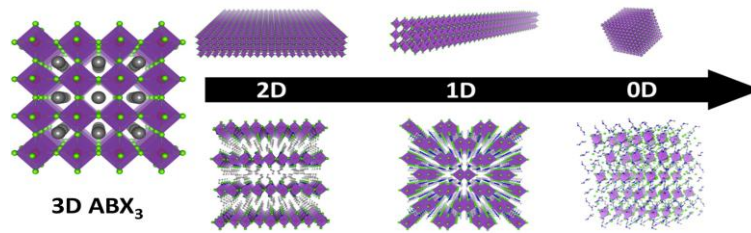
Figure I.2: 3D and low-dimensional hybrid perovskites[16]

Perovskites offer distinct opportunities, including tunable bandgap, improved stability, and solution processability from n=∞ to 1. While lower dimensional lead halides are mainly used for lighting, 3D lead halide perovskites are promising for solar cells. The compound's specific structure, characterized by short Pb-Pb distances due to edge-sharing PbX_6 octahedra and terminal X anions, allows for tuning the material properties of halide perovskites[19]. For instance, the 2D derivative perovskite is more moisture stable due to its bulky organic spacer, which also makes it more hydrophobic than 3D perovskites[20]. They can enhance phase and structural stability by improving interlayer contact[21] and stabilizing metastable phases[22]. It can also physically inhibit 3D perovskite ion migration, which is thought to be a major contributor to the hysteresis of photocurrent and device degradation under bias or thermal stress[23]. In contrast to these opportunities, they also come with challenges related to charge transport[24], anisotropic properties and complex synthesis[25][26]. Unlike 3D perovskite, 2D perovskite low mobility and carrier transport properties, leading to high irradiation-free recombination losses. The ideal perovskite structure is formed by combining the favorable properties of both of 2D and 3D. For that reason, perovskite structures with mixed 2D and 3D are being used as a double layer or quasi-2D structure that combines both properties, as illustrated in Figure I.3. Although both solar cells and LEDs prefer to use that scenario, it may reveal the potential for reduced light absorption in PSC. In LEDs, promising results have been achieved due to their ability to meet unique optical and electronic demands[27].
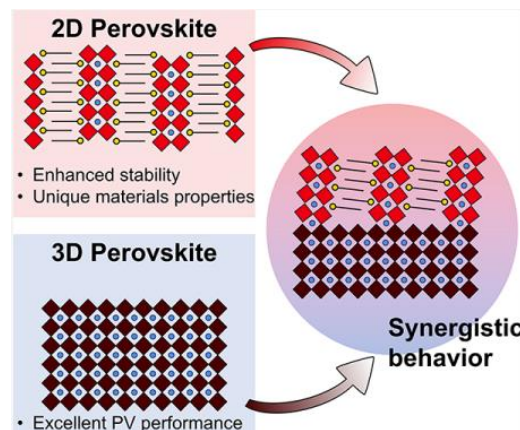
Figure I.3: The schematic of combination of favorable properties of 2D and 3D perovskites[28]

Radiative recombination is a crucial process that determines the efficiency of optoelectronic devices[29]. It involves the emission of a photon when an excited electron in the conduction band combines with a hole in valence band, following an optical and electrical excitation. One effective strategy to improve the radiative recombination efficiency in halide perovskites is to modify their electronic structure by reducing the dimensionality to quasi-2D structures[30]. The organic and inorganic layers can be thought of as altering wells and barriers, respectively. The band gap of the inorganic layers is lower than that of the organic layers by at least 3 eV[31]. As the number of organic sheets increases, the material band gap decreases

due to the quantum confinement effect. Additionally, the dielectric confinement enhances the interaction between electron-hole pairs, resulting in strong excitonic resonances. The optical transition energy of the quantum well decreases as the number of sheets increases. In experiments, the optical transition energy of the quantum well decreases with n, indicating a larger variation in confinement energies than exciton binding energy[32]. Figure I.4 shows how photo luminance of quasi-2D perovskites changes with stoichiometry (increasing n shifts the emission peak towards the red region).
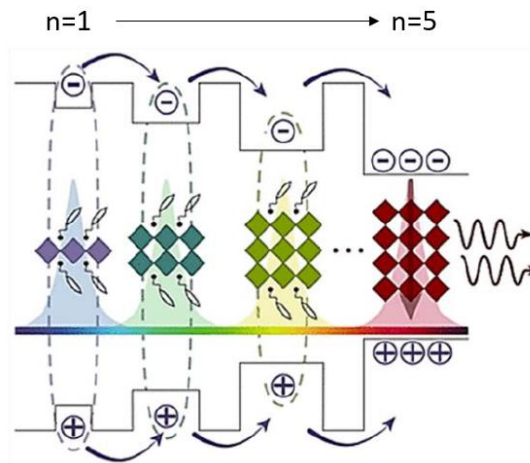
Figure I.4: Energy funneling effect in mixed phase low dimensional perovskites[33]

There are several opportunities to consider, including cost-effective, simple manufacturing processes and an abundant and wide range of material options to choose from. Thanks to them, there have been a wide range of processing techniques enabled to fabricate perovskite films. These techniques include one-step or two-step deposition methods based on solution processing, vacuum deposition, or vapor-assisted solution processing[34][35]. Various film properties of perovskite materials, such as grain size, surface coverage, morphology, and crystallography, are influenced by deposition and processing methods.

I.3. Halide Perovskite Optoelectronics

Organic-inorganic (hybrid) perovskites are gaining popularity in optoelectronic studies due to their numerous advantages[16]. They have led to their rapid progress due to their high charge-carrier mobility ($0.1\text{-}10$ $cm^2.V^{-1}s^{-1}$)[36], large charge-carrier diffusion length at open circuit (>500 nm)[37], high absorption coefficient (over 10^4 cm^{-1})[38].

In 2009, Kojima et al. reported a perovskite solar cell (PSC) with an efficiency of 3.8%[17]. The research that was conducted in this field had a significant impact and led to its rapid growth and success. In 2022, the University of Science and Technology of China (USTC) pioneered the development of a single-junction PSC. They increased the stabilization of the perovskite phase using certain methods, resulting in an efficiency of 26.1%[39]. Figure I.5 illustrates the significant progress made in developing PSCs over the years.
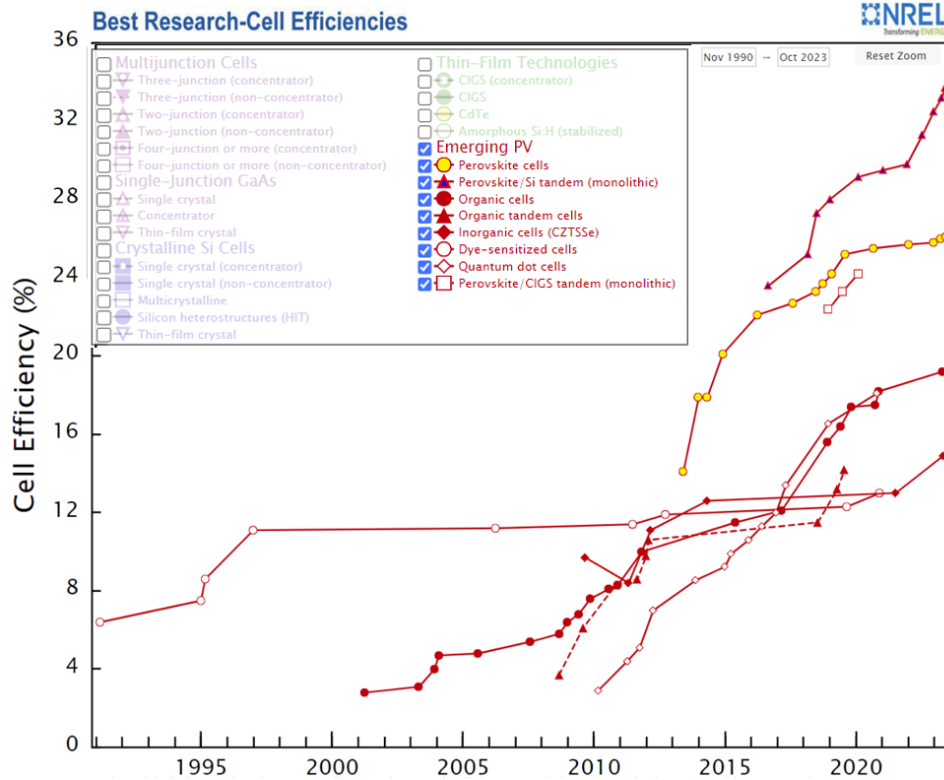
Figure I.5: The performance variation of perovskite solar cells[40]

The same can be said about enhancing performance in perovskite light-emitting diodes (LEDs or PeLEDs), as shown in Figure I.6.
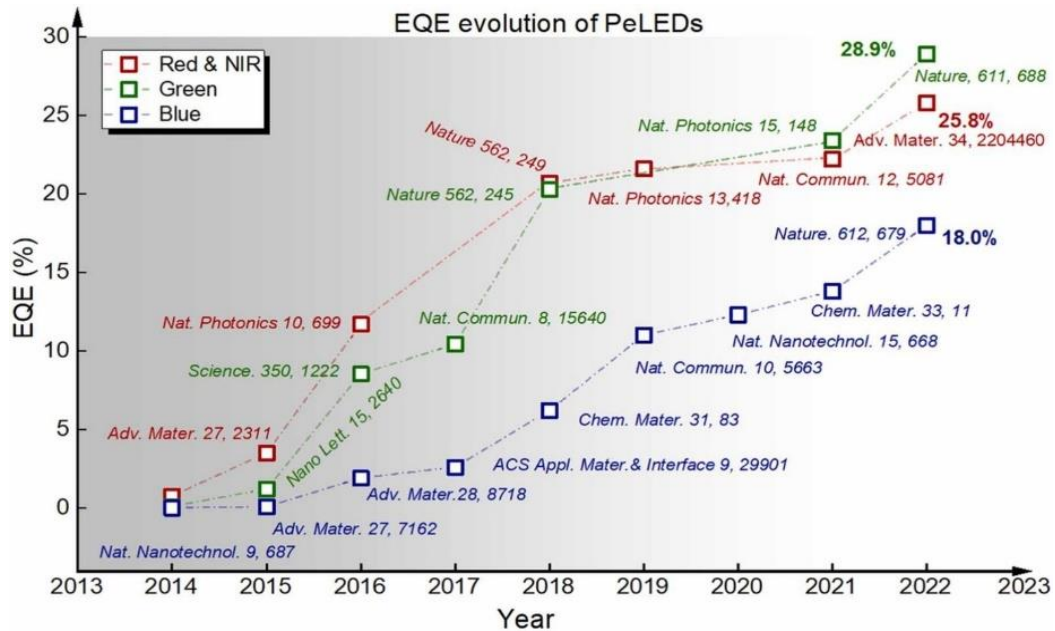
Figure I.6: Best perovskite LED performance depends on the emitted colors[41]

The use of metal halide perovskites for thin film LEDs was first studied in 1990s by Mitzi and his colleagues[42]. In 2014, a perovskite LED was demonstrated to have an external quantum efficiency (EQE) of less than 1%[43]. Through this research, it has been shown that perovskite can emit light and be adjusted to various colors. Its electroluminescence property has been proven effective. For perovskite LEDs to be successfully commercialized, it is crucial

to evaluate the performance of each color individually, even though they must ultimately work together. Creating high-performance green perovskite LEDs is more accessible than making blue and red ones due to their higher exciton energy[44] and narrower band gap[45], respectively. Bai et al. have achieved a milestone of over 30% EQE for green perovskite LEDs by 2023[46]. The researcher improved the balance of electron-hole recombination in the device by using a $Ni_{0.9}Mg_{0.1}O_x$ hole interlayer between the anode and hole transport layer. The highest performance for red perovskite LEDs is 25.8% of EQE, accomplished using quasi-2D perovskite[27]. High performance in blue perovskite LEDs is challenging due to non-radiative recombination losses[47], as evidenced by the highest EQE of 18% compared to green and red perovskite LEDs[48].

I.4. Operation and Performance of Solar Cells and LEDs

Halide perovskites are versatile materials that can be used as absorbers in solar cells and as emitter layers in LEDs despite their different operating principles. PSCs directly convert sunlight into electricity, while LEDs require an electric current to emit light. When PSCs absorb photons, increasing energy levels of electrons and electron-hole (charge) pairs are created. The charges get separated and converted into free electrons and holes with electric fields before being transported and collected at their opposite electrodes. The achievable short-circuit current (at zero voltage) and open-circuit voltage (at zero current) under a specific illumination, are conditioning the power conversion efficiency (PCE) of the device, and the PCE determines the performance of PSC for converting sunlight into electricity (mentioned below later). The operation is different in LEDs. A built-in voltage is applied to the device, causing electrons and holes to flow into the perovskite layer from the injecting electrodes. Confined in the perovskite emitter material, electrons and holes recombine by emitting light. For LED, the EQE corresponds to the percentage of photons emitted by injected charges carriers, at a specific wavelength. Together with other metrics such as luminance, the EQE is a measure of LED operating performance (mentioned below later).

Figure I.7 presents the working principles and differences of both PSC and PeLED. Efficient charge injection and extraction in perovskite optoelectronics relies on aligning the energy levels of the HTL or ETL with those of the perovskite layer. To enable the transfer of electrons, the charge injection/extraction layer typically has a low energy level called lowest empty molecular orbital (LUMO). This low LUMO aligns well with the conduction band of the perovskite layer, creating the small energy barrier that allows electrons to be injected easily. To ensure efficient hole transfer, the charge injection/extraction layer usually possesses a high energy level known as highest occupied molecular orbital (HOMO). It aligns well with valence band of the perovskite layer, resulting in a small energy barrier for hole transfer. As a result, these energy levels must have a low HOMO or high LUMO levels to prevent the opposing charge carrier from passing through.
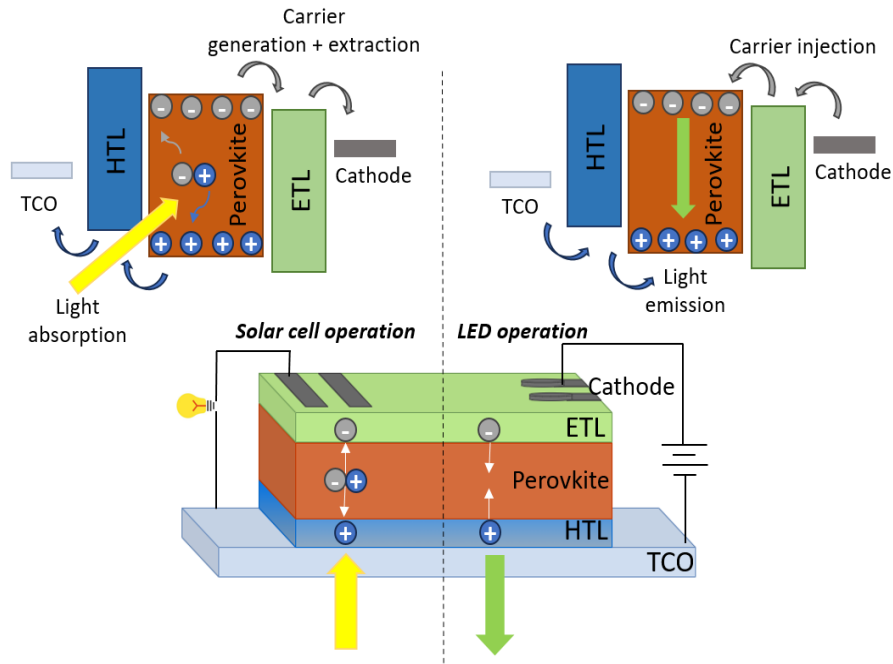
Figure I.7: Working principle of inverted PSC and perovskite LED with energy level diagrams

I.4.1. Fundamentals of Photovoltaic Cells

The process of generating electricity from solar cells involves different steps, depending on the technology considered. However, the general principle can be summarized in few typical steps. First, incoming photons are absorbed by the active layer material, generating electron-hole pairs (excitons). Under the influence of temperature or of an electric field, electron-hole pairs can dissociate, leading to free charge carriers which migrate to their respective electrodes. In open circuit conditions, these charges generate an open-circuit voltage associated with the splitting of quasi-Fermi levels for electrons and holes. Under varying load resistance, the device is characterized by its current-voltage curve from which its performance can be derived, for a specific illumination condition. The solar cell's current-voltage (I-V) curve is the superposition of the dark current (I_0) as a diode with the photo-generated current (I_L)[49]. The illumination (in Figure I.8) allows power extraction from the diode by switching the I-V curve to the fourth quadrant zone. The diode law, described in Equation I.1, is revised to include a photo-generated current under illuminated conditions[50].
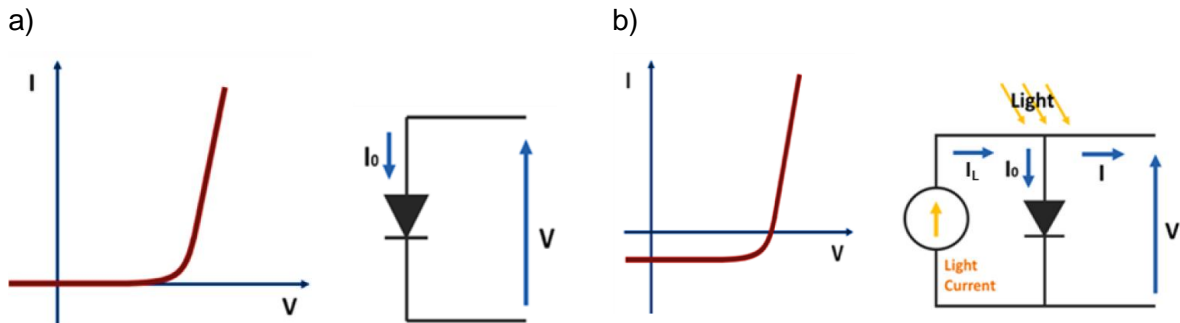
Figure I.8: Solar cell's I-V curves and equivalent circuits in case of a) dark and b) illuminated conditions

$$I = I_0 \left[exp\left(\frac{qV}{nkT}\right) - 1 \right] - I_L$$

<div align="right">Equation I.1</div>

where q is an elementary charge, n is the ideality factor (range of 1 to 2), k is the Boltzmann constant (1.38×10^{-23} m^2kg/s^2K), and T is the absolute temperature. According to the rule, I_L is taken as positive, and the curve is moved to the first zone. In this case, Equation I.1 is revised:

$$I = I_L - I_0 \left[exp\left(\frac{qV}{nkT}\right) - 1 \right]$$

<div align="right">Equation I.2</div>

The -1 shown in Equation I.2 is ignored under illuminated conditions. This is because the exponential term is dominant above 100 mV. I_L also dominates I_O at low voltages. The I-V curve is obtained by plotting the equation below.

$$I = I_L - I_0 \left[exp\left(\frac{qV}{nkT}\right) \right]$$

<div align="right">Equation I.3</div>

Some essential parameters of solar cell characterization for performance are discussed in the next step. The first is short-circuit current (I_{SC}), the current through the solar cell at zero voltage, as illustrated in Figure I.9[51].
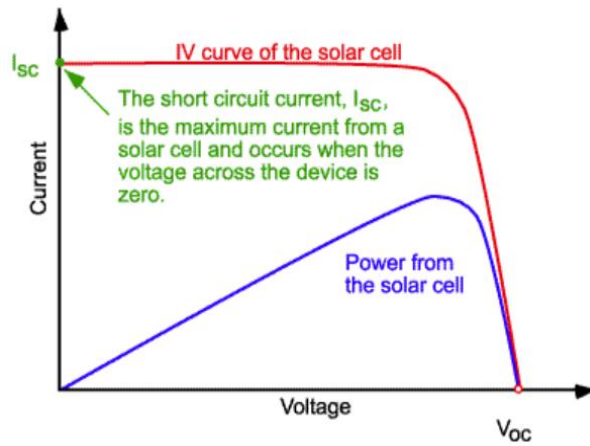
Figure I.9: Short-circuit current representing in I-V curve of the solar cell[51]

When the solar cell is in short-circuit mode, the maximum current that can be generated is called the short-circuit current. Current density (J_{sc} [mA/cm²]) is commonly used by dividing it by the active area to eliminate the current's dependence on the solar cell area.

The open circuit voltage (V_{oc}) is the maximum voltage obtained when no current flows, as seen in Figure I.10. When solar cells absorb light, the electric field separates electron-hole pairs which move towards opposite electrodes. This splitting of the half-Fermi levels of electrons and holes determines the V_{oc} and defines the free energy available after charge separation.
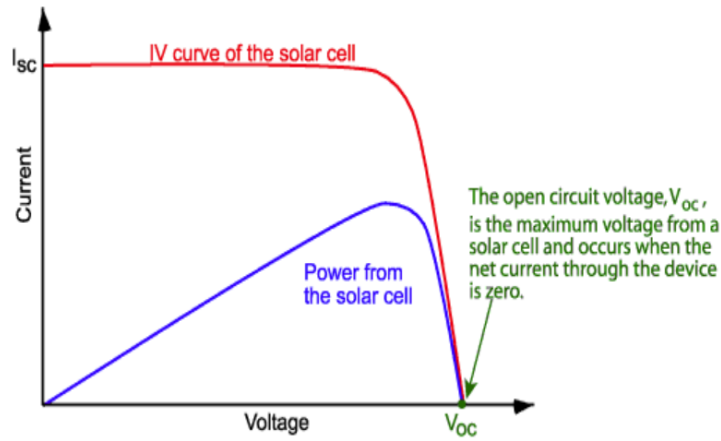
Figure I.10: Open circuit voltage representing in I-V curve of the solar cell[51]

By setting the net current to zero in solar cell Equation I.3, an equation for V_{oc} is found:

$$V_{OC} = \frac{nkT}{q} \ln\left(\frac{I_L}{I_0} + 1\right)$$

Equation I.4

where I_L is illuminated current and I_0 is dark current. The maximum V_{oc} value is a function of the material's band gap. Furthermore, the conditions under which the solar cell is operated (temperature, light, state of charge, etc.) are used to assess its performance[52].

The third parameter, the fill factor (FF), measures how effectively the solar cell converts sunlight into electricity. It is defined as the ratio between the maximum power (V_M, I_M) of the solar cell and its operating points, as shown in Equation I.5:

$$FF = \frac{V_M \cdot I_M}{V_{oc} \cdot I_{sc}}$$

Equation I.5

It provides a quantitative measure of I-V curve "squareness." Its value varies between 0 and 1, with 1 being the ideal, while for practical cells, its value is usually in the range of 0.6 to 0.85 for real-world efficient devices[53].

PCE is the ratio of a solar cell's maximum output (P_{max}) to the input from the sun (P_{sun}), commonly used for performance comparisons as seen in   Equation I.6:

$$PCE \; (\eta) = \frac{P_{max}}{P_{sun}} = \frac{V_M \cdot I_M}{P_{sun}} = \frac{FF \cdot V_{oc} \cdot I_{sc}}{P_{sun}}$$

Equation I.6

If the input power is changed to area units, I_{SC} can be modified by J_{SC} in   Equation I.6. In addition, standard test conditions defined by a norm (IEC 60904-3-Ed2) are used to characterize the performance of terrestrial PV devices, associated with a solar irradiance of type AM1.5G of P_{sun} = 100 W/cm² and at 25 °C.

Lastly, parasitic resistance can significantly affect the performance of the solar cell by reducing its fill factor, especially when the shunt and series resistance values are typical. These resistances can be calculated by analyzing the I-V graph. Figure I.11 illustrates the shunt (R_{sh})

and series resistances (R$_s$) in solar cell circuit and their characteristics in the I-V curve under illumination.

a)   b)
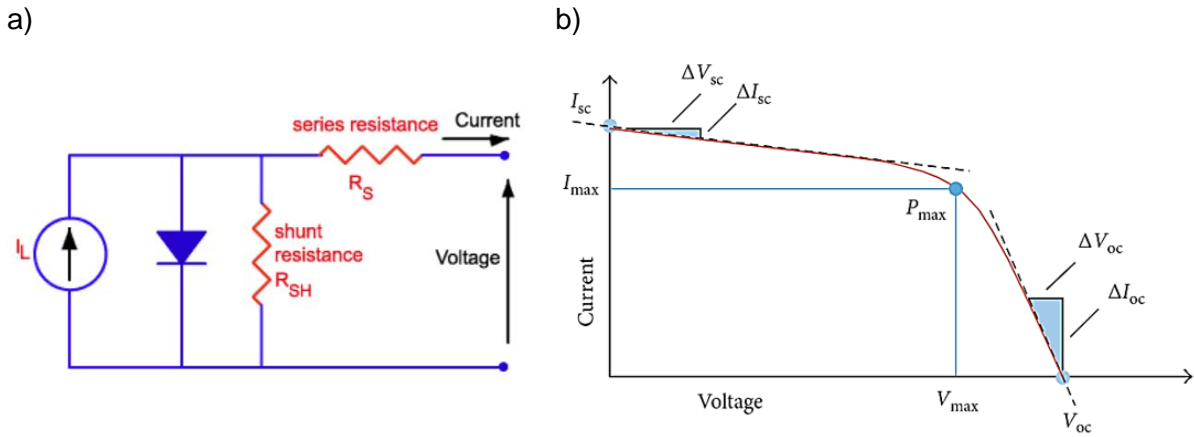
Figure I.11 : Solar cell a) equivalent circuit[51] and b) R$_{sh}$ and R$_s$ extraction from the I-V curve[54]

  The contact resistance of the two terminal electrodes is called R$_s$. The layers that form the solar cell are connected in series between these two terminal. Therefore, increasing the thickness of the absorbance layer can increase the R$_s$ and reduce the FF. The R$_{sh}$ represents the leakage current through the solar cell. Defects in the solar cell can cause leakage current, resulting in a lower FF and lower voltage across the p-n junction. The effect of R$_{sh}$ dominates when the light intensity is low. Lastly, R$_s$ and R$_{sh}$ can be extracted from the I-V curves basically by considering Figure I.11, b, as below:

$$R_s = -\frac{\Delta V_{oc}}{\Delta I_{oc}}$$

<div align="right">Equation I.7</div>

$$R_{sh} = -\frac{\Delta V_{sc}}{\Delta I_{sc}}$$

<div align="right">Equation I.8</div>

I.4.2. Fundamentals of LEDs

  Researchers are actively improving the efficiency, stability and performance of PeLEDs for various applications. To fully comprehend the operation of LEDs, it is essential to understand their modeling. In general, the equivalent circuit of LED contains components that depict its fundamental electrical characteristics. A typical LED can be represented in the equivalent circuit by an ideal diode, as shown in Figure I.12. This diode allows current to flow in one direction and blocks current in reverse direction when a forward voltage is applied. It has a small internal resistance, which is represented as a series resistance (R_s) in equivalent circuit. This resistance accounts for the losses due to the semiconductor material and contact resistances. Additionally, LEDs have a parasitic capacitance (C_P) caused by the device's structure. This capacitance can affect the LED's response to voltage changes and is usually small but can be significant at high frequencies.
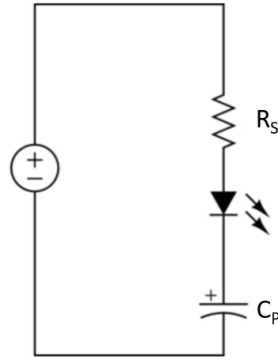
Figure I.12: The equivalent circuit of LED

The performance of perovskite LEDs is closely related to their charge carrier and recombination dynamics. Three main charge-carrier regimes include Shockley-Read-Hall (SRH), bimolecular, and Auger recombination. Figure I.13 demonstrates the implementation of recombination types. At low voltage, SHR occurs, while at intermediate voltage, it is bimolecular. At high voltage, there is Auger recombination. At low densities of carriers, the process of bimolecular radiative recombination competes with monomolecular losses that occur due to trap-assisted recombination. The mechanism that generates light emission from these materials is called a trap-limited electron-hole plasma bimolecular radiative recombination. If there are rough directions, weak interfacial energy, and mechanical mismatch, then there can be an even more significant increase in threshold current density, indicating the loss processes that arise from high densities of carriers, such as Auger recombination[55].
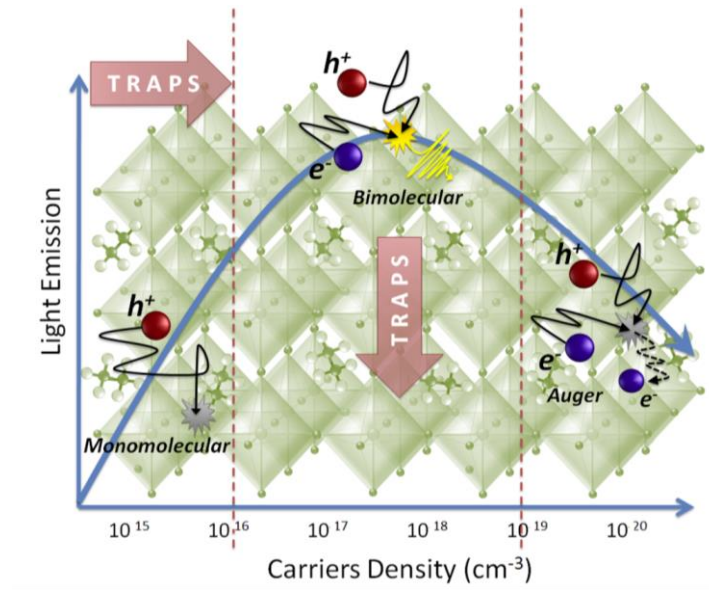
Figure I.13: Schematic representation of charge carrier regimes[55] SRH, bimolecular, and Auger recombination

The power efficiency of LEDs is the ratio of output optical power to input electrical power, as seen in Equation I.9. It is defined as a wall plug efficiency (WPE) in watts unit.

$$WPE = \frac{P_{out}}{P_{in}} = \frac{P_{out}}{I_{in}.V}$$

Equation I.9

where $I_{in}.V$ is the electrical power provided to LED.

Understanding characterization terms such as photoluminescence quantum yields (PLQY) and external quantum efficiency (EQE) is essential to enhance these properties. The EQE value is calculated as the ratio of emitted photons' flux to the number of electrons injected into the device per unit time, as shown in Equation I.10 with efficiency factors including the diode's EQE.

$$EQE = \frac{Photon\ emitted\ into\ free\ space}{Charges\ injected\ into\ emitter\ film} = \eta_{inj}.\eta_{rad}.\eta_{out} \qquad \text{Equation I.10}$$

where η_{inj} is the efficiency of injection. It is crucial to balance the injection of electrons and holes in perovskite devices to improve η_{inj}. Charge-blocking layers are often added to opposite electrodes to prevent leakage of one type of carrier, which negatively affects the IQE due to lower η_{inj}. Charge imbalance is also a very important limitation to achieve high injection yields. η_{rad} (also often referred as PLQY) refers to the efficiency of radiative recombination, which is the ratio of excitons that recombine radiatively to those recombining non-radiatively. η_{out} considers the efficiency of light extraction from LEDs by taking into account the escape of emitted photons from the LED structure.

EQE is determined by the internal quantum efficiency (IQE). It is the ratio of photons produced per unit of time to electrons injected into the device.

$$IQE = \frac{Photon\ generated\ in\ the\ emitter\ film\ per\ second}{Charges\ injected\ into\ emitter\ film\ per\ second} = \eta_{inj}.\eta_{rad} \qquad \text{Equation I.11}$$

The IQE is therefore directly affected by the PLQY, so to achieve a high EQE, it is necessary to have a high PLQY. It is an essential indicator for measuring luminescent materials and described as the ratio of emitted photons to absorbed photons, also expressed as the ratio of radiative to total recombination, as shown in Equation I.12:

$$PLQY = \frac{number\ of\ photon\ emitted}{number\ of\ photon\ absorbed} = \frac{\kappa_{rad}}{\kappa_{rad} + \kappa_{non,rad}} \qquad \text{Equation I.12}$$

The luminous intensity of LEDs is measure in Candela (cd), originating from the emitted intensity of a standard candle. Particularly, the candela measures the brightness of a light source in a specific direction. Today, it is defined as a monochromatic light source emitting 1/683 of a watt into a solid angle of 1 steradian.

The Lumen (lm) describes the total amount of visible light emitted by a light source, differing from the cd which describes the luminous intensity. These quantities are related through units of solid angle steradians (sr); $1\ cd = 1\ lm/sr$. If a light source emits 1 cd of luminous intensity in all directions, its luminous flux is 4π ($\approx$12.6) lm as a sphere makes up 4π sr of solid angle. The luminance of LEDs is measured in cd.m^{-2}, which is the luminous flux unit

projected solid angle per unit source area. For displays, reasonable LED luminance are in the range 100-1000 cd.m^{-2}, but this value can strongly depend on the required application.

I.5. Architectures of Perovskite Solar Cells

These optoelectronic devices carry out charge through or toward a perovskite layer using a metal electrode on one side and a transparent conductive oxide on the other. The two most commonly used transparent conductive oxides (TCOs) are fluorine-doped tin oxide (FTO) and ITO (indium oxide and tin oxide are combined together to form it) for perovskite applications due to their low resistivity (often <10 Ω/sq) and high transparency in the visible range (>90%)[56]. There are three different device architectures for perovskite optoelectronics, depending on the connections of these TCOs, as shown in Figure I.14.

a)   b)   c)
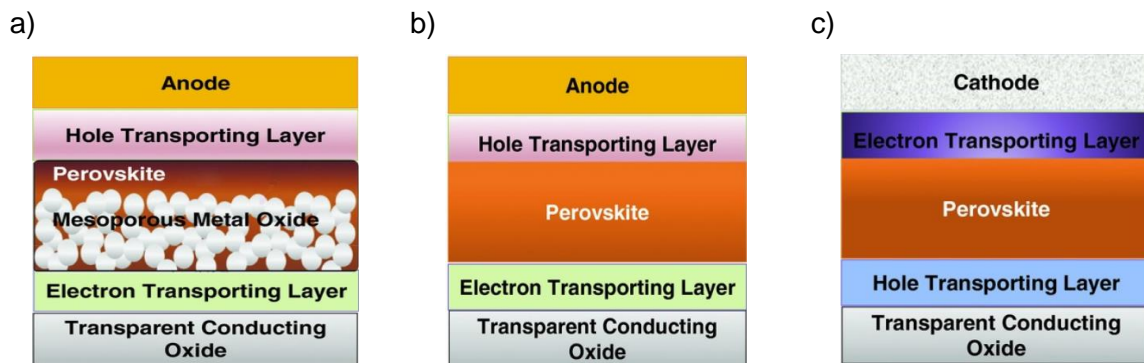
Figure I.14: Schematic of perovskite optoelectronics for different architectures[57] a) mesoporous, b) planar, and c) inverted planar structure

- Mesoporous structure: They are structures adapted from dye-sensitized solar cells (DSSCs)[29] and consist of a mesoporous metal oxide layer and an electron transport layer (ETL). This structure is commonly used in PSCs but not in LEDs. In this structure, the n-type ETL is typically deposited on the TCO instead of the p-type HTL, leading to n-i-p architectures.

- Planar structure: This structure is planarly connected to the TCO/ETL substrate via a dense layer of the perovskite.

- Inverted planar structure: In contrast to the planar structure, the perovskite layer is deposited on top of the hole transport layer (HTL), which is the first layer to encounter incident light after the TCO.

While the planar structure typically performs better, inverted planar structures are gaining popularity in research and development because of their numerous advantages. A benefit of utilizing this structure is that they can be easily incorporated into cutting-edge technologies like flexible and tandem solar cells[58]. Second, they exhibit lower hysteresis characteristics compared to other structures[59]. When measuring J-V characteristics by scanning the voltage at the terminals of device, hysteresis refers to the difference between the forward and reverse scan of the curves. This difference is due to the presence of mobile ions and their impact on the extraction and recombination of charge carriers, which most likely occur at the interfaces[60]. Third, the overall fabrication costs are lower due to the usage of low temperatures during production, which reduces energy consumption. Efficient and stable perovskite optoelectronic device performance depends on proper contact selection related to work function of other layers. Their mission should remove one charge carrier and block the

other to prevent losses due to recombination. Gold (Au) is typically the preferred contact material for planar structures due to its higher work function. However, inverted planar structures offer a lower work function, which enables the usage of less expensive metal electrodes like silver (Ag) and aluminum (Al). This results in a reduction in cost.

The functionality of inverted planar structures strongly depends on HTLs. They should exhibit p-type conductivity, required for hole transport and extraction (in PSC) or injection (for LED). In contrast to HTLs, ETLs mostly carry negative charges due to their excess electrons. They extract holes from the perovskite absorber layer to the HTL in PSCs and inject holes into the perovskite emitter layer from HTL for light emission in LEDs. HTLs and ETLs are also called p-type and n-type interlayers because of this characteristic. The following list highlights the essential functions that the HTL should perform:

- It extracts the holes from perovskite layer and transfer to the electrode in PSC or it extracts the holes from electrode and transfer to perovskite layers in LED.

- It behaves as a barrier of energy to stop electron transfer in the opposite direction.

- It enables charge transfer without accumulation between TCO and perovskite with optimum interface quality

- By isolating the perovskite layer from the TCO or metal electrode, it protects the active layer from moisture and reduces potential degradation of device.

- It ensures a good match in energy level of other layers and contributes the device performance.

Important criteria must be met for successful and efficient transfer to achieve high-charge transport performance. The valence band maximum (VBM) energy levels of the HTL and conduction band maximum (CBM) energy levels of the ETL must be aligned favorably to efficiently transfer one type of charge carrier while blocking the other[61]. When choosing an HTL, it's crucial to consider its energy level as it minimizes a barrier between the TCO or metal electrode and the perovskite layer. Figure I.15 displays the energy level of hole transport materials that are most commonly preferred in perovskite optoelectronic applications in the literature.
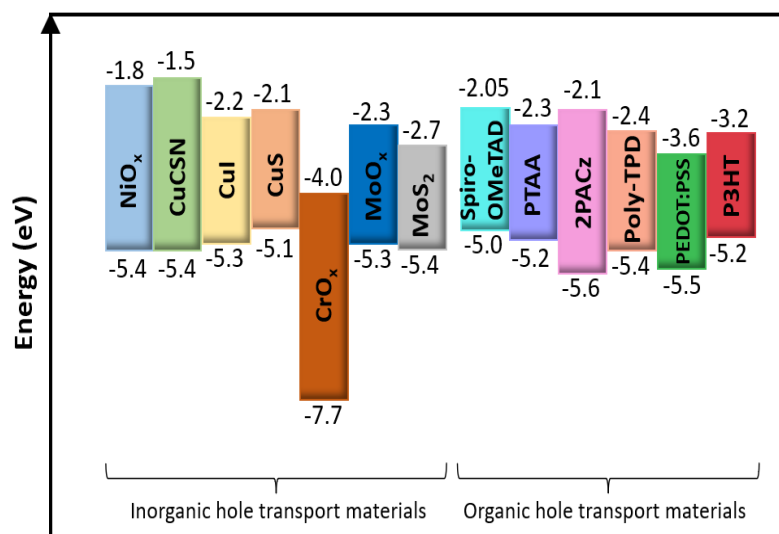
Figure I.15: VBM and CBM levels of certain hole transport materials for perovskite optoelectronics

One additional requirement for HTLs is to have high hole mobility efficiency values to prohibit carrier loss during extraction/injection and transportation[62]. The value of hole mobility can vary depending on the hole transport material. Faster transportation of holes typically leads to the fabrication of more efficient devices if they have a balance with ETL. This balance varies depending on several parameters such as thickness, charge density, and conductivity[63]. The thickness of HTL affects the distance holes travel to/from electrodes. If the HTL is too thick, it can result in longer hole transport paths and higher potential resistive losses. On the other hand, if the HTL is too thin, it may not be able to effectively transport holes through the device. This directly affects charge density. There are different techniques to improve hole mobility in materials, such as doping and morphology control.

HTL must have material properties such as solubility with a suitable solvent, as well as suitable properties, to prevent unfavorable reactions with different layers[64]. In addition, light absorption in the board-band (within 400 to 750 nm) of the solar spectrum is essential to minimize current losses[65]. Therefore, they must maintain maximum transparency. For optimal LED performance, the HTL should not interfere with its emission wavelength. As with PSC, it must remain transparent to the wavelength of the light emitted by LED. This transparency allows the light to pass through the HTL and exit the device efficiently for contributing to the overall brightness of device.

I would add a sentence that mention that the domain of interface layers has been strongly developed in the last decades for OPV and OLED. Perovskite devices have benefit from the know-how of researchers in these fields. In the next section, we review the most important families of hole transport materials and highlight their main features.

I.6. Hole Transport Layers

I.6.1. Organic Hole Transport Layers

While organic hole transport materials are preferred for their simple solution processing and low deposition temperature requirements, they have some important limitations. They often suffer from stability issues caused by ambient conditions (moisture, oxygen, light) and chemical or physical incompatibility with deposited surfaces. Researchers are working to find solutions to these issues through the investigation of doping and techniques to improve purity [66]. In addition, synthesizing them can be a laborious process that involves multiple steps, especially for spiro-OMeTAD (2,2',7,7'-Tetrakis[N, N-di(4-methoxyphenyl)amino]-9,9'-spirobifluorene), PTAA (poly(triaryl amine)) and PEDOT:PSS (poly(3,4-ethylenedioxythiophene)), which increase the manufacturing costs. The commercialization of perovskite optoelectronic devices is negatively impacted by these factors.

• PEDOT:PSS

PEDOT:PSS remains a best-seller for hole injection/extraction into/from the perovskite active layer for inverted planar structure PSC and LEDs. This material is highly favorable due to its high optical transparency in the visible range (~89%)[67], simple film growth, and ability to enhance conductivity with additional treatments. According to the literature, typical reported values for hole mobility and conductivity are 0.045 $cm^2V^{-1}s^{-1}$ and 440 S/cm, respectively[67][68], but they are highly tunable by its doping state. Its VBM and CBM lies around -5.5 eV and -3.6 eV versus vacuum, respectively.

Certain significant drawbacks of PEDOT:PSS has a direct impact on PSC or LED's performance and stability. First, the chemical structure of the PSS (polystyrene sulfonate)

chain (as shown in Figure I.16) makes it acidic, which can cause issues with TCO and the perovskite layer. Second, it is a conjugated polymer that can dissolve in water and has hydrophilic characteristics. This characteristic can lead to the fast degradation of perovskite-based optoelectronic devices. Third, the work function value of this material is relatively low when compared to common halide perovskite active layers. This can cause an energy mismatch between the layers, resulting in a decrease in available free energy after charge separation (in the case of PSC)[69]. Forth, PEDOT:PSS is surrounded by insulator PSS chains that slow down the transfer of holes. In comparison to conventional ETLs such as C_{60} and PCBM ([6,6]-phenyl-C_{61}-butyric acid methyl ester), its conductivity is lower. When charge transfer is not balanced between the layers, it can cause charge build-up, which limit the number of photogenerated carriers (again for PSC), negatively affecting the performance of devices[70]. Such space charge limitations are also crucial for LED.
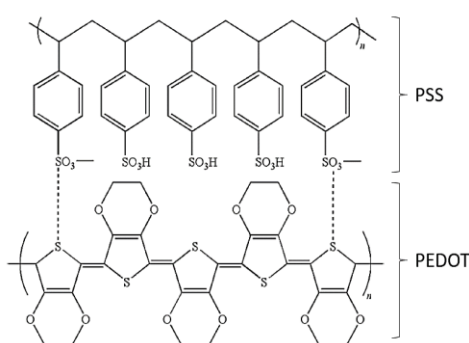
Figure I.16: Chemical structure of PEDOT:PSS

In 2013, Ten-Chin Wen group was the pioneer in utilizing PEDOT:PSS in an inverted planar structure[71]. In this study, 3.9% PCE was achieved by using $CH_3NH_3PbI_3$ type of perovskite as a donor and PCBM as an ETL. After a few months of the initial work, the device's performance was enhanced and subsequently declared to be at 7.8% for the identical structure [72]. Since these beginnings, the application of optimizations in studies using PEDOT:PSS-based PSCs has led to increasingly improved results, as shown in Figure I.17[73]–[81]. Upon examination of these studies, the focus is primarily on improving the surface morphology and tuning the work function with the electrical properties of PEDOT:PSS. Zhao et al. improved the film morphology and prevented short circuits by adding GeO_2 to PEDOT:PSS solution[74]. In one study, smoother and higher energy surfaces were obtained by depositing sodium benzenesulfonate[80], while another study deposited alcohol-soluble PTPAFSONa and PTPADCF$_3$SONa on PEDOT:PSS[75]. Doping NaCl[76] and CsI[78] to PEDOT:PSS not only enhanced its electrical properties but also made the energy levels more favorable and suppressed recombination. In particular, the CsI modification has reduced the work function of PEDOT:PSS and led to negligible hysteresis, improving the possibilities of this type of device. Khan et al. enhanced the conductivity of the film by immersing it in ethylene glycol and methanol after the film deposition process, respectively. This resulted in a PEDOT-rich film with lower PSS content, resulting in an efficiency increase from 13.23% to 18.18%[79]. Yifang et al. developed three polymer analogs- polyaniline, polyaniline-phenoxazine, and polyaniline-phenothiazine- as passivation layers for PEDOT:PSS[82]. Different energy levels, interface modifications, and perovskite growth control were carried out to achieve high open circuit voltage (V_{oc}) of 1.13 V and 21.06% PCE using polyaniline-phenoxazine.
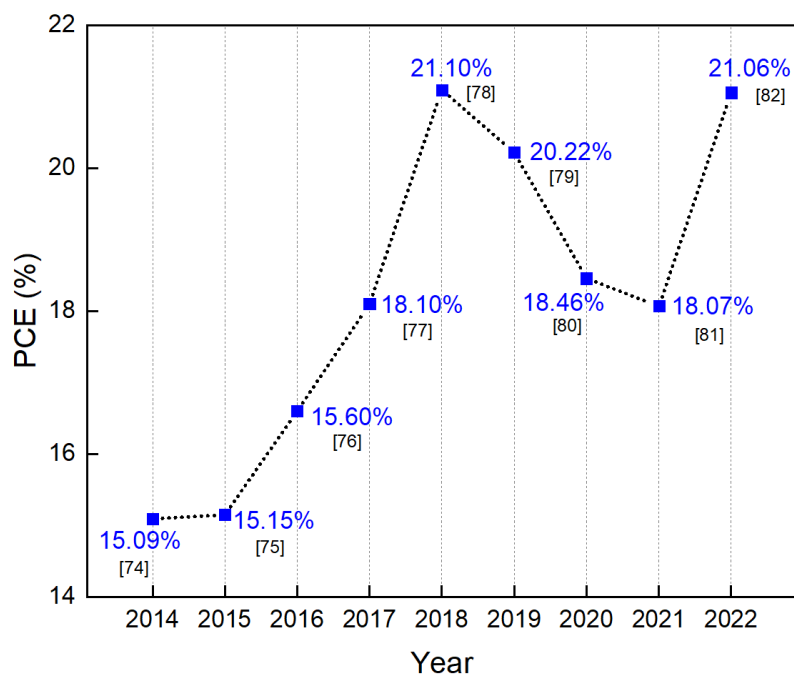
Figure I.17: The best PCE of PEDOT:PSS-based PSCs in over years

As mentioned earlier, PEDOT:PSS has several benefits that make it a favorable option for optoelectronic devices, especially perovskite LEDs. In 2014, Friend et al. fabricated the first PEDOT:PSS-based perovskite LED with 0.1% EQE and 364 cd.m^{-2} luminance performance [40]. They designed the first green-colored perovskite LED simultaneously. In 2015, Tae-Woo Lee's group created a self-organized conducting polymer by using PEDOT:PSS. They discovered that the first large surface (2x2 cm^2) perovskite LED had a performance of 42.9 cd.A^{-1}[83]. In this study and future ones, there are methods to enhance device performance by controlling the conductivity, surface passivation, and defects between PEDOT:PSS and perovskite layers[84][85]. As the regulation of PEDOT:PSS properties became more complex, researchers started using buffer layers like PMAA (polymethyl methacrylate) and PVK (poly(9-vinylcarbazole)) in between the layers[86][87]. In recent years, significant improvements have led to a rapid increase in performance values. Finally, a device utilizing PEDOT:PSS as its HTL and quasi-2D perovskite as its emitter demonstrated a brightness of 18683 cd.m^{-2} and 15.5% EQE in 2022[88]. Improving the surface quality and doping process for PEDOT:PSS resulted in better performance for both solar cells and LEDs, as evidenced by the studies conducted. It is common to use it with an additional layer, as explained in the following sections.

•   Spiro-OMeTAD

Spiro-OMeTAD is an organic hole transport material that consists of a small molecule forming a molecular glass (in Figure I.18) and is commonly used in planar structures. The key benefit of this material is its excellent solubility in solvent and the fact that it does not require annealing after deposition due to its amorphous nature and 3D structure. It is mainly used in PSCs rather than for LEDs. This is due to its ability to serve as a good electron blocker, which prevents charge recombination and ultimately limits emission efficiency.
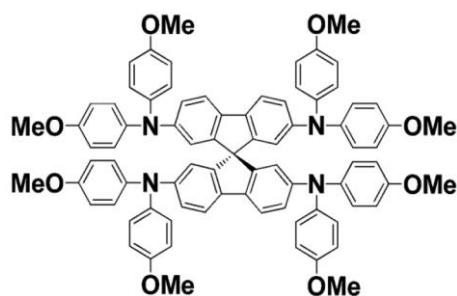
Figure I.18: Chemical structure of Spiro-OMeTAD

Its CBM and VBM values for this are -2.05 and -5.0 eV, respectively[89]. The electrical properties of dopant-free spiro-OMeTAD are often improved using LiTFSI (bis(trifluoromethane) sulfonamide lithium salt) and 4-tBP (4-tert-butylpyridine) due to its low hole mobility and conductivity. Doping is a process that boosts the hole conductivity (through increased charge carrier density) from 2.5×10^{-7} to 2×10^{-5} S/cm, and it's frequently utilized in efficient PSCs[90][91]. After doping, the operational stability of the device decreases at high temperatures, and several degradation problems show up such as thermal decomposition of spiro-OMeTAD and morphological changes like pin-holes and/or cracks.

Spiro-OMeTAD was initially researched for its application as a heterojunction with titanium oxide in DSSCs. Thanks to the efforts of the Grätzel and Snaith groups, it was first published in 2012 regarding the hybrid perovskite absorber[29][92]. Since it was first introduced, extensive studies have been conducted which have shown that its performance has surpassed 25% in planar PSCs[93][94]. Although it can lead to high performance PSC, the search for alternative hole transport materials is ongoing due to the drawbacks and high costs associated with it.

• PTAA

PTAA (Poly(triaryl amine) or Poly[bis(4-phenyl)(2,4,6-trimenthylphenyl)amine]) is a well-performing hole transport polymer material (Figure I.19), known for its ability to be processed at low temperatures and its chemical neutrality, making it ideal for inverted planar structures. This material is noteworthy for its higher resistance to high temperatures compared to other types. The hydrophobicity and air stability of the material have a positive impact on the stability of perovskite-based devices. After annealing, this material produces a smooth thin film surface that enhances the interface quality with the perovskite layer and minimizes recombination, despite its high wettability. The deposition of perovskite in solution is difficult due to non-wetting, thus requiring surface treatment. However, the commonly used UV-ozone method damages the organic PTAA functional group[95]. In addition, a significant disadvantage is the high cost (1000 euros per gram) and high series resistance for undoped PTAA. Its VBM and CBM values are -5.2 eV and -2.3 eV, respectively. Its hole mobility is around 4×10^{-4} cm^{2}V^{-1}s^{-1}[96].
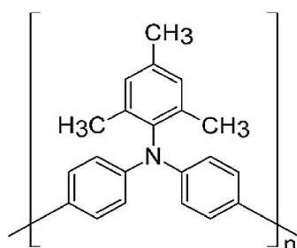
Figure I.19: Chemical structure of PTAA

Originally, it was used in polymer LEDs to inject holes, as stated in the literature[97]. In 2013, the first work was conducted on planar PSC, which resulted in a 12% PCE[98]. Since then, the usage area of this material has evolved from planar and inverted planar PSCs to include tandem, flexible, and even large-area solar cells. In 2015, the use of doped-PTAA with F4-TCNQ (2,3,5,6-Tetrafluoro7,7,8,8-Tetracyanoquinodimethane) in an inverted planar structure led to reducing device resistance and a groundbreaking achievement of 17.5% PCE for the first time[99]. Starting in 2020, we saw significant and rapid progress after initially promising results. In 2020, Gutierrez-Partida's group focused on improving the crystallization of double-cation perovskite and reached a 22.5% PCE by using PTAA[100]. In the same year, Alsalloum et al. boosted the PCE to 22.8% by utilizing a mixed-cation single crystal absorber layer[101]. In this study, the researchers emphasize the significance of PTAA's hydrophobicity in enhancing the diffusion of perovskite solvents, which results in the growth of crystalline films with better quality. Chen et al. made a further advancement by achieving a 23.6% PCE through blade-coating technique for both PTAA and perovskite layers, which they later applied to the mini-module[102]. Despite the high performance, when using more than 10% DMSO (dimethyl sulfoxide) in the solution of perovskite ($MA_{0.6}FA_{0.4}PbI_3$), PTAA creates voids on the perovskite surface (in Figure I.20) and peels off from ITO with time. The holes created by the light around vacancies cannot be rapidly transferred by HTL. This results in charge accumulation that speeds up perovskite degradation. Just recently, Li et al. achieved 25% PCE with superior perovskite film quality through surface passivation treatment[103].
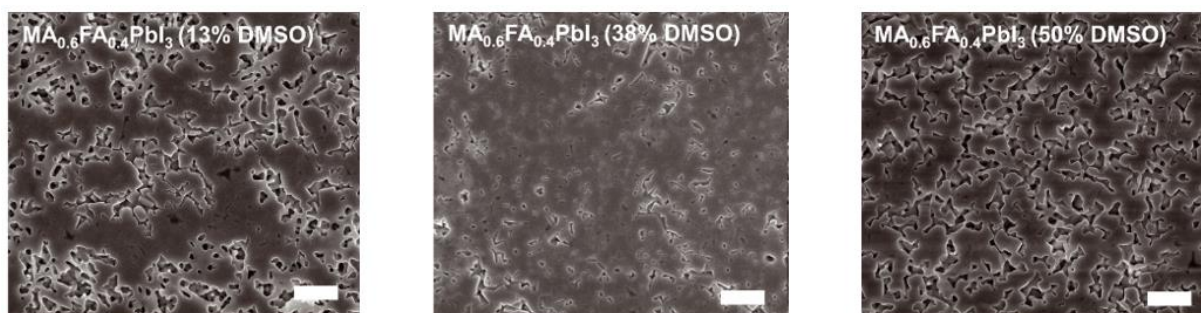
Figure I.20: Top-view SEM images of perovskite on PTAA with varying concentrations of DMSO[102]

• Poly-TPD

Poly-TPD (poly(N,N′-bis(4-butylphenyl)-N,N′-bis(phenyl)benzidine)) is an organic material made up of polymers (shown in Figure I.21), which is frequently utilized as a hole transport material in perovskite LEDs and inverted planar structure PSCs. Like PTAA, it is desirable for hydrophobic material properties and low annealing temperature. The material has a hole mobility of approximately 1×10^{-4} cm^{2}V^{-1}s^{-1}[104]. Its VBM and CBM values are -5.4 and -2.4 eV, respectively.
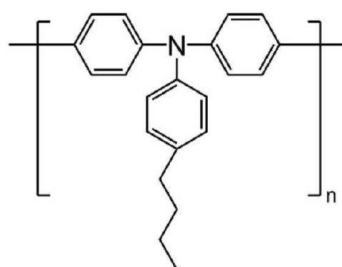
Figure I.21: Chemical structure of poly-TPD

In 2013, poly-TPD was introduced as an additional HTL by depositing it between PEDOT:PSS and the perovskite layer to organize energy band alignment[105]. However, the approach did not yield the expected results. Next, the team made an effort to enhance the performance by up to 15% by eliminating PEDOT:PSS to reach better energy alignment and co-evaporating perovskite with it[106]. By using this technique, the surface quality of the perovskite film is improved. Tsang et al. reached more than 18% PCE in inverted planar PSC by utilizing UV-ozone treatment to adjust the surface wettability of poly-TPD. Therefore, the energy levels of the HTL were aligned and the stability of the device was improved[107]. In 2021, Qu's team made a significant advancement by resolving the wettability problem of poly-TPD with the help of a solvent additive method as seen in Figure I.22. They improved the connection between HTL and the perovskite layer by combining chlorobenzene and water, which increased their contact surface. Despite efforts, the issue has not been entirely eradicated. They obtained a remarkable result in the study of poly-TPD-based PSCs, resulting in a high PCE of 22.1%[108].
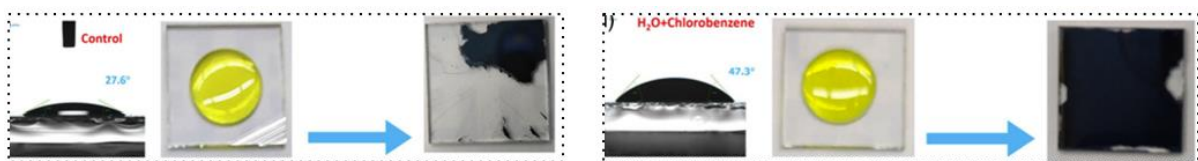
Figure I.22: The surface wettability treatment of poly-TPD[108]

In perovskite LEDs, Poly-TPD serves as an extra HTL placed on top of PEDOT:PSS for passivation, similar to its use in PSCs. Several studies have been conducted on using this material for passivation in different structures[109], as given in previous studies. Its role, as detailed in 2022 research[110], is to uphold the equilibrium of charge carriers. A different research found in 2023 that a highly luminous LED, boasting 23.8% EQE and releasing light in the near-infrared region, was fabricated using this material as HTL[111].

• SAM-Based HTLs

SAMs (self-assembled monolayers) are small molecule hole transport materials that are highly ordered and well-packed with a thickness at the molecular level. Compared to other organic HTLs, SAMs are both cost-effective and scalable due to their minimal molecular material requirements for synthesis. Simultaneously, these are simple to deposit, highly adaptable, and stable, making them convenient for various applications, such as planar inverted PSCs, LEDs, and tandem solar cells. The stability of them can be a problem in planar inverted PSCs due to their exposure to incident light[112]. One of the main drawbacks to thin film growth is that it tends to be a slow process for liquid phase deposition[113].

The diversity of SAMs increases when their permanent dipoles and multifunctional groups undergo changes[114]. SAM molecules consist of three fundamental groups. The first group is known as the anchoring or head group, which enables the molecules to attach to atoms on the surface and significantly influences the material's electronic states. The spaces group comes after the anchoring group, provides the molecular arrangement, and forms the packing geometry. The functional group, which is the third group, is in charge of arranging the properties of the surface and interface[115].

In 2018, Getautis et al. conducted research on SAM-based carbazole derivate HTL using a new molecule named V1036 (Figure I.23a) in the inverted planar PSC. It was discovered that a small amount of current loss is caused by parasitic absorption in V1036. By combining it with butyl phosphonic acid (C4), they enhanced its contact angle and ionization

potential, resulting in a PCE 17.8%[116]. Then, the same team synthesized two more molecules: MeO-2PACz ([2-(3,6-dimethoxy-9Hcarbazol-9yl)ethyl] phosphonic acid) and 2PACz ([2-(9H-carbazol-9-yl)ethyl] phosphonic acid)[117] (Figure I.23b and c). After thorough analysis, it has been determined that the newly developed SAMs offer superior energy alignment than V1036. Additionally, they improved the charge transfer and reduced defects by utilizing passivation effects via a phosphonic group in the synthesis steps. The HTL/perovskite interface showed no signs of non-radiative recombination, resulting in the V_{oc} above 1.19 V. Azmi and their team achieved a 24% PCE in 2022 by implementing surface passivation with 2D/3D perovskite heterojunction to ensure thermal and photostability[118]. The heterojunction maintained 95% performance after 500 hours of stability testing, while the control device's performance dropped to less than 90% after 100 hours. In 2022, Jen and co-workers synthesized a co-SAM named DC-PA ((2,7-dimethoxy-9H-carbazol-9-yl) methyl) phosphonic acid containing alkyl ammonium by adjusting the energy level[119]. This improved the stability of the device and resulted in a higher 23.59% PCE. In another study, 2PACz was used as a HTL in planar inverted PSC. The perovskite roughness was treated with a small molecule called 3-(aminomethyl) pyridine. It behaved like a 2D layer and resulted in PCE efficiencies exceeding 25%[120]. As a result, SAM-based HTLs mostly achieve high V_{oc} and PCE, but stability and surface enhancement must be considered.

a)   b)   c)
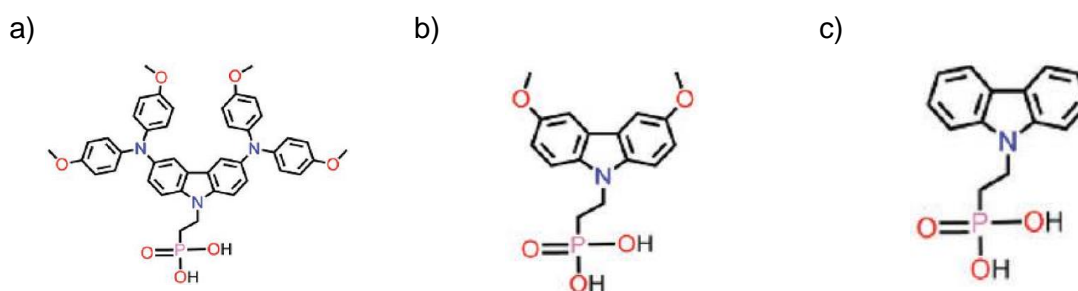
Figure I.23 : Chemical structure of a) V1036, b) MeO-2PACz, c) 2PACz

SAM-based HTLs have demonstrated positive outcomes in perovskite LEDs, such as surface passivation for metal ions by using in perovskite precursor[121], enhancing perovskite crystallization[122], and regulating the contact resistance between interlayers[123]. In 2023, a comparison was made between PEDOT:PSS for green perovskite LEDs in high humidity (60%) environments using MeO-2PACz and 2PACz[124]. The 2PACz, using quasi-2D type perovskite, demonstrated the highest performance in ambient conditions, achieving 4.87% EQE and 7143 cd.m^{-2} luminance. This outcome represents a significant advancement in ensuring the operational stability of perovskite optoelectronics in ambient conditions.

I.6.2. Inorganic Hole Transport Layers

Inorganic HTLs are becoming increasingly popular due to their numerous advantages compared to organic HTLs. They have four noteworthy attributes: exceptional stability, high conductivity, low-cost fabrication process, and abundant reserve of materials[62]. In addition, various manufacturing methods, such as vacuum evaporation, spray pyrolysis, and spin coating, can be utilized to fabricate inorganic HTLs. When it comes to oxide-based inorganics, methods such as pulsed laser deposition (PLD), RF sputtering, and atomic layer deposition (ALD) are effective in producing films that are dense and of high quality[125]. As a commonly known fact, inorganic materials are typically less expensive than organic materials. Moreover,

the utilization of manufacturing techniques on a large industrial level simplifies the process of depositing these materials on a large scale and promotes commercialization.

Up to date, devices that use inorganic HTLs have not shown the same level of performance as those that use organic HTLs. Achieving uniform and pin-hole-free surfaces using inorganic hole transport materials can be challenging. When it comes to making electronic devices using flexible and plastic substrates, inorganic interlayers are required to ensure good charge carrier properties. However, achieving the desired level of crystallinity in these interlayers requires annealing, which can be a challenge when working with low temperature (<150 °C) compatible substrates[126]. As a result, their fabrication requires more complex procedures. If the film surface has some defects, it can directly impact connection between interlayers. After all, the efficiency of charge injection or extraction may be reduced[127].

- NiO$_x$ (Nickel Oxide)

NiO$_x$ is a p-type of oxide semiconductor that is commonly used in planar inverted structures. It is known for its optical transparency and wide bandgap material (3.4-4 eV)[128]. Its VBM and CBM values are -5.4 and -1.8 eV respectively. It includes different species like Ni$_2$O$_3$ and NiOOH. Because of these, NiO$_x$ is non-stoichiometric and has an excess of oxygen due to vacancies in the Ni sites, resulting in its display of p-type properties. The intrinsic NiO$_x$ demonstrates a low hole mobility of approximately 10^{-4} S.cm^{-1}. As a result of the low hole transfer, holes tend to accumulate in the interface of the perovskite layer. This can increase the likelihood of hole-electron recombination in that area, which may ultimately result in loss of performance[129].

There are multiple methods for depositing NiO$_x$, though spin coating and spray pyrolysis necessitate high-temperature annealing (around 500 °C) post-deposition of thin films[130][131]. Besides, these methods have drawbacks for NiO$_x$, such as creating inhomogeneous coverage, morphological defects, and nonuniform thickness[130]. It can be difficult to optimize the ideal thickness. However, physical methods like PLD, RF sputtering, ALD, and e-beam evaporation that are mentioned above are better suited for obtaining high transparency and uniform film surfaces at lower temperatures (around 200 °C)[132][133].

In 2014, the first inorganic HTL, NiO$_x$, was tested in a planar inverted structure PSC[130]. In this study, mesoscopic NiO$_x$ was added to NiO$_x$ HTL to increase the time of the charge separation state and achieve a 9.51% PCE. The same team utilized RF sputtering of NiO$_x$ to deposit the identical device structure at low temperatures in a follow-up study[134]. Argon and oxygen gases were used during the deposition process to enhance conductivity. The team was able to increase the efficiency to 11.6%, proving that physical vapor deposition methods are more efficient for this material. In 2015, Seok et al. used pulsed laser deposition (PLD) to create NiO$_x$ nanostructures with varying oxygen partial pressures[132]. The crystal structure of the film was then controlled through adjustment of the deposition pressure using that method. In addition, it assists in managing the conductivity of the thin film. After reaching the ideal HTL properties for the device, a PCE of 17.3% was achieved. Molecule doping of intrinsic-NiO$_x$ with Cu[135], Cs[128], and F6TCNNQ (2,2′-(perfluoronaphthalene-2,6-diylidene)dimalononitrile)[137] can improve conductivity with efficiency values exceeding 19%, according to studies. Especially F6TCNNQ, a strong electron acceptor, raised the VBM and Fermi level of NiO$_x$, increasing its ability to accept holes. In 2019, He et al. improved NiO$_x$/perovskite interface and surface passivation with alkali halides NaCl and KCl, resulting in a 21% PCE[138]. Sargent et al. achieved 23.9% efficiency in planar inverted PSC in 2022 using a 2D perovskite layer to

improve device stability and performance[139]. While NiO$_x$-based PSCs demonstrate impressive performance, they often have a lower V$_{oc}$ than organic HTLs. In order to address this problem, McGehee and the team found that depositing perovskite directly onto NiO$_x$ prompts a redox chemical reaction between the precursor and the surface[140], as illustrated in Figure I.24. The Ni metal cation creates a barrier of PbI$_2$ that stops its access to the amine and iodine group from the precursor. Essentially, the NiO$_x$ surface causes the perovskite precursor to dissolve, which is a major disadvantage.
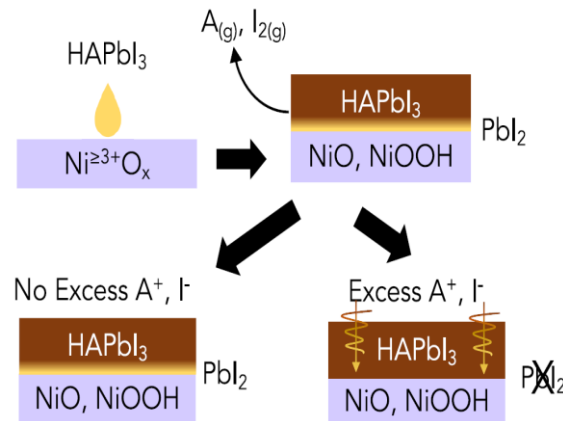
Figure I.24: The redox reaction between the NiO$_x$ and perovskite precursor[140]

NiO$_x$ is a frequently used material for hole injection in blue light perovskite LEDs[141]–[143]. However, directly placing the emissive layer on top of NiO$_x$ can result in fluorescence quenching in the perovskite. Therefore, surface treatment is often necessary like in PSCs, and interlayers like PVK[144], TFB (poly(9,9-dioctylfluorene-alt-N-(4-sec-butylphenyl)-diphenylamine))[141], and PSSNa (poly(sodium-4-styrene sulfonate))[143] are commonly used to optimize the performance of NiO$_x$. Unfortunately, studies indicate that while the EQE of the devices has improved, there has not been a significant increase in luminance.

- Cu-Based HTLs

CuSCN and CuI are popular Cu-based HTLs used in perovskite optoelectronic applications. Although both HTLs are used in both planar and planar inverted structures, CuSCN is generally favored for planar structures, while CuI is preferred for planar inverted structures.

CuSCN or copper(I) thiocyanate is an economical copper-based HTL that has a wide band gap (~3.9 eV) and high transparency in the visible solar spectrum. Its VBM and CBM values are -5.4 and -1.5 eV, respectively. Its remarkable thermal and chemical stability has made it a subject of interest. The hole mobility range of the material is 10^{-2} to 10^{-1} cm^{2}V^{-1}s^{-1} [145]. The higher concentration of thiocyanate ions compared to copper results in the formation of copper vacancies, leading to p-type characteristic dominating.

In a planar inverted structure PSC, CuSCN was synthesized and incorporated by Ye et al.[146]. Electro-deposition was the technique utilized to deposit CuSCN in this research. An efficiency of 16.6% was achieved with a structure that had high conductivity and low roughness. In 2016, Jung et al. successfully produced the material at a low temperature (70 °C) and utilized it in a mesoscopic structure, surpassing the 20% efficiency as same as spiro-OMeTAD[147]. The research has confirmed that CuSCN is capable of withstanding high temperatures better than spiro-OMeTAD. In 2017, the team of Anthopoulos used an NH$_3$ (aq) solvent to dissolve CuSCN instead of the classic solvent DMS (dimethyl sulfide), and the

conductivity increased five times more[148]. They improved the operational stability of the planar inverted PSC by using PEDOT:PSS as double HTLs, resulting in a device efficiency increase from 10.7% to 17.6%. In 2022, the same team managed to enhance the conductivity of CuSCN through the introduction of chloride gas via a dry etching system[149]. They deposited it on PEDOT:PSS as the previous study, resulting in a PCE of over 20% with better stability.

Although CuSCN is stable at room temperature, research has found that SCN⁻ ions tend to diffuse towards the perovskite at the perovskite/HTL interface when the temperature changes during the device fabrication process[150]. The presence of SCN vacancies in CuSCN resulted in a shift in the band alignment, as seen in Figure I.25a. This led to a mismatch with the perovskite, resulting in a decline in performance. In a different study, it was found that the degradation of perovskite occurs even in a nitrogen atmosphere when the films are heated due to the presence of CuSCN coating[151]. The color of the film changed to yellow in only four days, as seen in Figure I.25b).

a)

b)
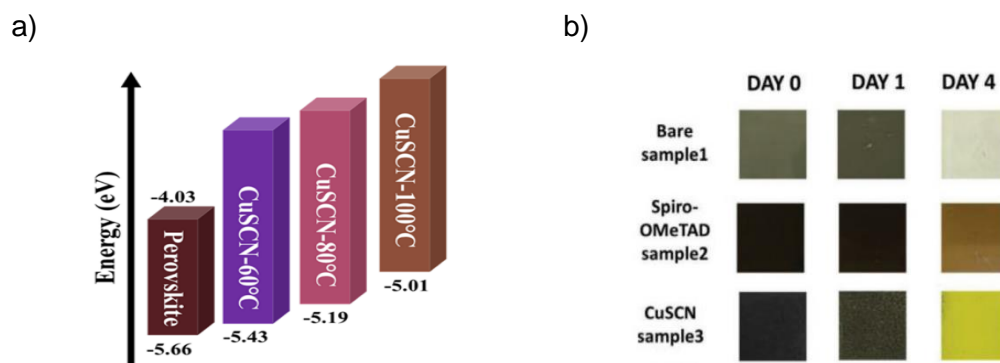
Figure I.25: a) The temperature affects the energy diagram[117] and b) degradation of CuSCN[151]

CuI, also known as copper iodide, is an affordable HTL that can be made using abundant elements. This material exhibits outstanding optical transparency and has high mobility for holes within the range of 0.5 to 2 $cm^2V^{-1}s^{-1}$[152]. Its band gap is narrower than CuSCN, with VCM and CBM values of -5.3 and -2.2 eV, respectively.

In 2014, CuI was tested in a mesoporous PSC and compared to spiro-OMeTAD for its higher hole mobility[153]. However, the device's performance was surprisingly low, achieving only 6% PCE with a low V_{oc}. Further investigation revealed that low V_{oc} is related to high potential recombination of CuI. In 2015, Chen et al. experimented with a planar inverted PSC and were able to achieve a more successful outcome by using a solution process with a PCE of 13.28%[154]. Typically, Cu-based HTLs have a low V_{oc} performance due to a lack of charge concentration at the interfaces and a high series resistance. Following initial research, it has been determined that improvements such as doping and modifying the interface or surface are necessary to address this issue. In 2018, CuSCN was added into CuI in planar inverted PSC to achieve higher hole mobility (0.23 S.m⁻¹) and improve film quality, resulting in an 18.76% PCE[155]. In the presence of iodine, Cu can undergo easy oxidation, resulting in the formation of CuI. Coating CuI on Cu nanowires hybrid structure effectively improves the conductivity of HTL[156], reaching a PCE of over 18%. Moreover, it was noticed that once the temperature surpassed 120 °C, the degradation of CuI occurred[157]. The diffusion of iodine ions within the material resulted in a change in electrical conductivity. It is obvious that further improvements are necessary for Cu-based HTLs. The utilization of CuI as an interlayer in LEDs is rare, but it has been studied as a hybrid material in perovskite emissive layer with long term air

stability[158]. Like CuI, limited transparency of CuSCN in visible light region restricts its use as HTL in LEDs.

Cu-based oxide (CuO_x and Cu_2O) and sulfide (CuS) species are prevalent in nature. When Cu_2O is heated in air at 250°C, it reacts with oxygen and transforms into CuO. Similarly, if CuI film is subjected to temperatures above 300°C in air, it transforms into CuO film[159]. In addition, both groups have a very low solubility in solvents[160]. These characteristics make them less appealing.

- Transition Metal Oxides-based HTLs

There are various metal oxide HTLs, with MoO_x, VO_x, and CrO_x being the most prevalent, except for NiO_x (mentioned above).

MoO_x, especially MoO_3, has been identified as having the highest potential as a metal oxide HTL after NiO_x. It is cost-effective, non-toxic, and has a broad bandgap, including deep electronic states[161]. In 2015, Beom and colleagues utilized MoO_3 and NPB (N, N'-Di(1-naphthyl)-N, N'-diphenyl-(1,1'-biphenyl)-4,4'-diamine) to create a planar inverted PSC with a double HTL using a vacuum process[162]. Their efforts resulted in a 13.7% PCE and a high V_{oc} of 1.12V. For the planar inverted structure, the MoO_3/PEDOT:PSS bilayer was utilized again[163]. The purpose of using MoO_3 was to act as a barrier between PEDOT:PSS and ITO, which resulted in an observed PCE of 14.87%. Studies have shown that the interface between perovskite and MoO_x creates a high potential barrier for hole transfer (1.36 eV), unlike electron transfer (0.14 eV). The cause of this was a chemical reaction occurring between the two interfaces. The iodine ion in perovskite transferred electrons to MoO_x, causing a gradual decrease in the concentration of iodine due to evaporation[164].

VO_x is another transition metal oxide with a large bandgap that is also cost-effective. First, the solution process was tested on planar PSC using V_2O_5[165]. The precursor had transformed at a high temperature of 500°C. In order to address the challenges posed by high temperatures in some scenarios[166][167], deposition techniques that enable crystal formation at lower temperatures have gained popularity. By utilizing the ALD method in combination with UV-ozone treatment, it became achievable to attain crystal formation at low temperatures[168], leading to a PCE of 11.53%. Another study achieved an efficiency value of 14.53% PCE using a low-temperature solution process. However, the problem of poor crystallization with pin-holes and roughness (R= 74 nm) still needs to be addressed[169], as illustrated in Figure I.26. Then, it can enhance the performance of other HTLs when used as a buffer layer[170][171].

a)   b)
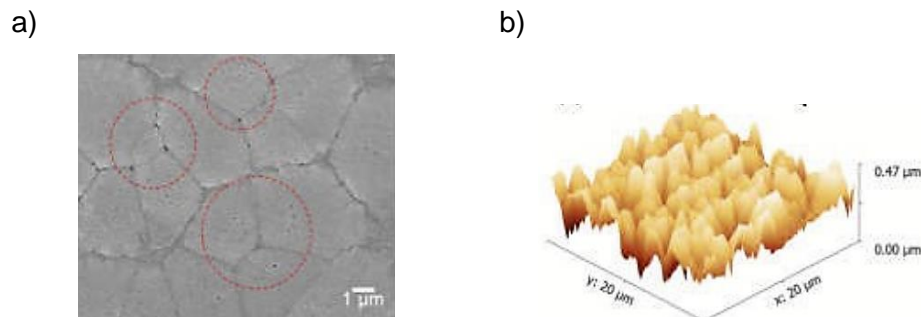
Figure I.26: The morphology of VO_x[169] with a) pin-holes and b) high roughness

CrO_x, also known as chromium multi-oxide, is a metal oxide that exhibits oxidation states of Cr^{3+}, Cr^{4+}, and Cr^{6+} at 200 °C. It possesses a p-type characteristic, with primary defects being Cr vacancies[172]. Cr_2O_3 has a highly stable grade that can endure harsh conditions, including oxidation[173]. A study was conducted by Ping-Li et al. in 2016 on planar inverted PSC, which involved the use of RF-sputtering and Cu doping of CrO_x[174]. By comparing devices using CrO_x and $Cu:CrO_x$, there was an increase in PCE from 9.27% to 10.99%. In addition, the use of Cu helps to protect the perovskite interface from the damaging effects of oxidizing and halogenating substances. In the next study of the team, they enhanced the performance of both CrO_x and $Cu:CrO_x$ devices, resulting in a PCE of 14.76% and 17.66%, respectively[175]. Their HTLs/perovskite interface study discovered that chromium diffuses into it, which changes the surface contact and p-type characteristics. But using Cu inhibits the chromium diffusion.

Transition metal oxides have been extensively studied and gained popularity a decade ago. Despite their numerous benefits, certain areas require attention for all types: i) requires high temperatures for good crystallization, ii) needs surface passivation, iii) ion migration happens between the interfaces, and iv) suffers from low V_{oc}[176].

•   Carbon-based HTLs

Carbon-based or carbonaceous materials types are graphene oxide (GO), reduced graphene oxide (rGO), and carbon nanotubes (CNTs) such as single-walled (SWCNT) and multi-walled (MWCNT). These materials are utilized as ETL, HTL, electrodes, or doping material in the perovskite active layer or charge transport layers. They are well-known for their low cost, excellent hydrophobicity, and long-term stability properties.

The GO and rGO are widely used carbon-based materials and are made up of a typical 2D single graphene nanosheet. Generally, GO is acquired via the process of oxidizing graphite and then exfoliating it. After the oxidation procedure is done, the GO surface develops three distinct functional groups, namely epoxide (-O-), hydroxyl (-OH), and carboxyl (-COOH), as in Figure I.27. rGO is a GO with a reduced number of functional groups[177]. These materials are commonly used as electrodes or doping materials for both HTLs and perovskites.
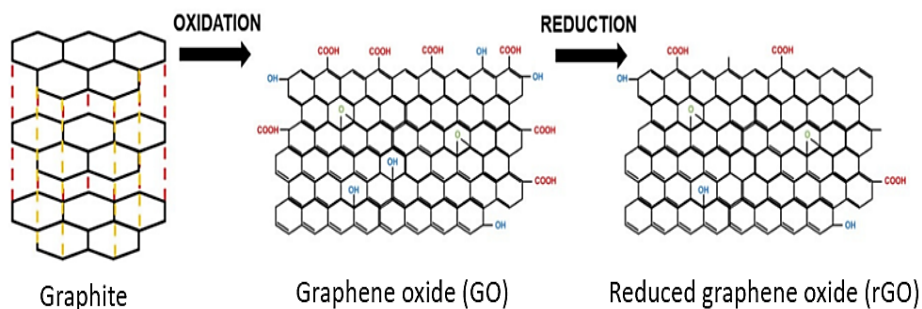
Figure I.27: Oxidation and reduction process of graphene[178]

Carbon-based nanomaterials that are smaller than 10 nm in size at a 1D cylindric structure are referred to as CNTs. SWCNTs are made up of a single layer of graphene wall, while MWCNTs consist of two or more cylindrical graphene walls[179]. These are favored because of their great mobility, long lifetime as carriers, and stability[180].

In 2017, Jokar and co-workers conducted a study on using GO and rGO as HTLs in planar inverted PSC[181]. Their research showed that rGO had a higher PCE of 16.4% compared to GO's 13.8%. The reason for this was attributed to rGO having a more uniform

surface and lower charge recombination in the perovskite interface. When utilizing GO and rGO as HTLs, planar inverted PSCs do not exhibit enhanced performance. Nonetheless, they are frequently employed as interlayers between perovskite and other HTLs to enhance stability [182], additive in perovskite precursor[183] or HTLs[184]. Efforts to utilize SWCNTs and MWCNTs solely as HTL in mesoporous and planar structures have not been successful. Instead, they are more effective when used as interlayers, similar to other types, and have shown encouraging outcomes, especially for mesoporous structures[185]–[187]. While carbon-based materials have shown promise in stabilizing perovskite PSC over a long period, their progress has been hindered by manufacturing constraints that cause surface layer imperfections.

I.7. Overview of The Thesis

As a conclusion of this chapter, the perovskite has been defined with a particular regard on the differences between halide and oxide perovskite. The performance evolution of perovskite-based optoelectronics, including their basic working principles and commonly used p-type interlayers in terms of technical properties and performances, and the fundamental parameters for optoelectronic devices has been introduced, and the promising and weak points of perovskite explained.

Long-term stability became the main concern due to the inherently soft ionic crystal structures of perovskites, despite the rapid performance improvement that paved the way for commercialization of perovskite optoelectronic devices. Current research is addressing obstacles to commercializing perovskite optoelectronics, such as poor stability, hysteresis and environmental concern in terms of toxicity. The main obstacle to practical implementation is instability because of heat[188], moister[189], oxygen[173], and light[190]. Recent research is focused on three main areas to tackle the stability problem in perovskite optoelectronic devices. Firstly, developing characterization methods to gain a deeper understanding of instability issues. Secondly, implementing strategies to improve stability and mitigate interface issues in perovskite and interlayers. And thirdly, utilizing materials engineering strategies to synthesize and fabricate stable perovskites.

The commonly utilized p-type interlayer presents noteworthy obstacles in literature. Intense research efforts have been put into the development of innovative p-type interlayer materials but there is still a need for materials presenting highly tunable properties as well as a high photo-chemical stability. In this context, the family of perovskite oxides have been recently explored to act as interlayers for optoelectronic applications, considering their stable physical properties under ambient conditions. While only few examples have been reported in the literature[191]. In this study, a p-type interlayer of $CaTi_{0.8}Fe_{0.2}O_{3-\delta}$ was successfully integrated into PeLED, achieving brightness comparable to commercial material.

In this thesis, the family of perovskite oxides have been explored as p-type interlayers for optoelectronic applications, considering their stable physical properties under ambient conditions. This thesis comprises three main steps: First of all, selecting a perovskite oxide type based on specific criteria. Second, optimizing the deposition method parameters of the material using PLD. Finally, integrating the developed perovskite oxide into PSC and LED. In the end, we will summarize the key points and future outlook of the thesis.

Chapter II. Selection of Perovskite Oxide Type and Deposition Technique

This chapter contains two main sections: material selection and comparison of deposition techniques for fabricating thin films.

Oxide perovskites are known for their multifunctional behavior, meaning they can exhibit multiple useful properties simultaneously. This makes them an attractive option for integrated devices with functionalities. Recently, this family has been explored in few works as an interlayer for halide perovskite optoelectronic applications due to their stable physical properties even under ambient conditions. Despite intensive research efforts to develop innovative p-type interfacial layer materials, there is still need for materials that offer high photochemical stability, as well as properties that can be easily tunable. $SrTiO_3$ is the most widely preferred oxide perovskite type but it has low conductivity. In this work, $SrTi_{0.7}Fe_{0.3}O_{3-\delta}$ has been chosen because it is a model that represents acceptor-doped wide bandgap oxide perovskites.

The advantage of this material is its versatility in terms of synthesis and fabrication techniques. However, different techniques can affect the material properties. It is necessary to investigate the desired material properties and their relation with fabrication methods from a technical standpoint. After providing an overview of all the connections, we will present detailed information on the preferred deposition techniques.

II.1. Properties of $SrTi_{0.7}Fe_{0.3}O_{3-\delta}$

Perovskite oxides such as $CaTiO_3$, $LaNiO_3$, $SrTiO_3$, $LaAlO_3$, and $BaTiO_3$ are widely used in various applications due to their good chemical stability and high-quality surface[192]. $SrTi_{1-x}Fe_xO_{3-\delta}$ (STFO) is another type of oxide perovskite and also an electroceramic material with versatile properties. STFO covers the entire composition range between strontium titanate ($SrTiO_3$) and strontium ferrite ($SrFeO_3$). In $SrTi_{1-x}Fe_xO_{3-\delta}$ formulation, x, and δ correspond to the concentration of the Fe doping and the oxygen sub-stoichiometry for the STO material, respectively. Under typical circumstances, intrinsic $SrTiO_3$ (STO) has low conductivity. The introduction of Fe as doping alters the substitution arrangement between Ti and Fe, as shown in Figure II.1. It increases the concentration of oxygen vacancies, resulting in increased conductivity[193]. After doping with Fe, which is an acceptor, STO can show semiconductor properties or even a metallic conductor.
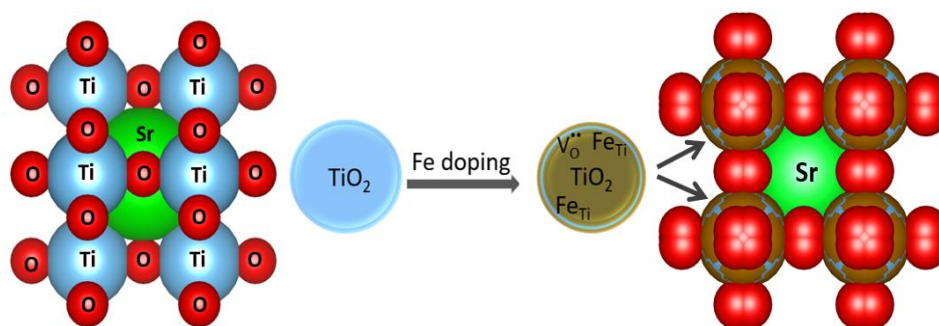
Figure II.1: Fe doping mechanism of $SrTiO_3$ to obtain $SrTi_{1-x}Fe_xO_{3-\delta}$

The type of material - n-type or p-type - is determined by the ratio of anions and cations in the compound, which is controlled by the substitution of elements A and X in the perovskite structure. The formalism of point defects in the solid state chemistry is usually described using the Kröger-Vink notation[194].

Iron, as a mixed-valence cation, typically substitutes Ti cations in the perovskite lattice by the Fe^{3+} and Fe^{4+} valence states. When Fe is doped in STO structure to create p-type material, oxidation occurs due to the presence of electronic holes in the structure. The material can be oxidized by oxygen absorbing from the surrounding gas at high temperature (up to 500°C), leading to the conversion of Fe^{2+} ions to Fe^{3+} ions and Ti^{3+} to Ti^{4+} as well[195][196]. In contrast, Fe-doping to STO can introduce a reduction reaction with increasing electron concentrations. When the material is exposed to reduction, ion formation in oxidation occurs in the opposite direction[193]. Replacing Ti^{4+} with Fe^{3+} (Fe'_{Ti}) leads to the creation of oxygen vacancies ($V_{\ddot{O}}$) and the development of holes which can be seen as Fe^{4+} (Fe^x_{Ti}). Ideal stoichiometry for ABO_3 compositions allows only for tetravalent cations such as Ti^{4+}. The A-site can accommodate Sr^{2+}, while the B-site can accommodate Fe^{3+}. The desired results is the formation of oxygen vacancies with one oxygen vacancy per two trivalent cations[197]. Moreover, the sites where anions are supposed to be are currently filled by both O^x_O oxygen and $O^{''}_i$ oxygen interstitials. The following are the stages of defects equilibrium in Fe-doped STO under the intrinsic regime[198], as seen in Table II.I.

Table II.I: The equilibrium of main point defects in Fe-doped $SrTiO_3$ under the intrinsic regime, based on the Kröger-Vink formalism

Oxygen incorporation:	$\frac{1}{2} O_2 + V_{\ddot{O}} \rightleftharpoons O^x_O + 2\dot{h}$	Equation II.1
Iron reduction:	$Fe^x_{Ti} \rightleftharpoons Fe'_{Ti} + \dot{h}$	Equation II.2
Electron-hole pairs generation:	$0 \rightleftharpoons e' + \dot{h}$	Equation II.3
Fe mass balance:	$[Fe_{total}] = [Fe^x_{Ti}] + [Fe'_{Ti}]$	Equation II.4
Charge neutrality:	$n_0 + 6[O^{''}_i] = p_0 + 2[V_{\ddot{O}}]_0$	Equation II.5

In Equation II.2, Fe'_{Ti} and Fe^x_{Ti} represent cations of Fe in 3+ and 4+ oxidation states, respectively. Due to the low excitation of the weak bandgap and the absence of free charge carriers in STO, Equation II.5 can be rewritten as a non stoichiometric condition with respect to reference state of oxygen access.

$$\delta = \frac{[O^{''}_i] - [V_{\ddot{O}}]}{[Sr(Ti,Fe)O_3]}$$

Equation II.6

The concentration of oxygen vacancies in the material is determined by the amount of Fe added. Then, the oxygen activity (or oxygen partial pressure) in the surrounding atmosphere affect the redox balance between the Fe^{3+} and Fe^{4+} in the material. In other words, the average oxidation state of Fe depends on the concentration of Fe, oxygen partial pressure (pO_2), and temperature[199]. The oxidation state of the Fe atoms serves as a unique identifier for the various defect structures and provides valuable insight into the electronic structure of STFO. In the dilute regime, where Fe centers are isolated[200], there is no interaction between Fe dopant atoms in STO when its concentration is less than 1 mol%. Fe-rich compositions (x>0.1) maintain high conductivities and stabilize the perovskite phase. Increasing the Fe concentration in STO above 3-6 mol% results in the gradual formation and broadening of a Fe impurity band within STO's electronic bandgap. Increasing the Fe content results in a decrease

in band gap and an increase in conductivity, as well as an increase in oxygen vacancy concentration[201]. This ability to control the transport and electronic properties of STFO makes it an attractive conductor for various applications.

STFO is a mixed ionic electronic conductor due to the two different oxidation states of the Fe^{4+} and Fe^{3+} under substitution of Ti in perovskite structure, which creates oxygen vacancies. This leads to a predominant conductivity at intermediate partial pressures of oxygen[202]. At low pressures, it shows n-type electronic conductivity. At moderate oxygen pressures, it exhibits ionic conductivity. At high oxygen pressures, it shows p-type electronic conductivity in the cuvette shape. The impact of Fe concentration on both electron and hole conductivities is inconclusive, as shown in Figure II.2. Fe, like Ti, Sr, and O, should be considered one of the main components shaping the energy band structure of STFO, and its electrical conductivity should also be studied.
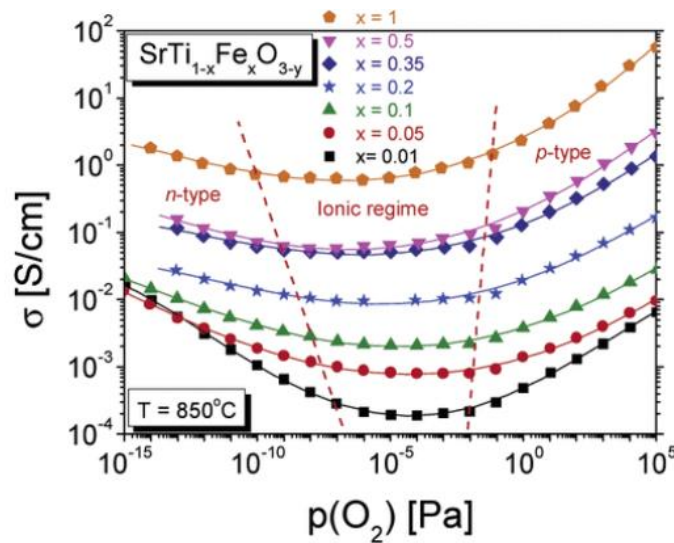
Figure II.2 : Variation of the electrical conductivity with different oxygen partial pressures for STFO compositions[202]

STO is a wide bandgap semiconductor. Its bandgap energy is approximately 3.2 eV at 0 K. This energy decreases as the concentration of Fe increases while the oxygen vacancy concentration increases. When Fe is introduced into the lattice, the band gap decreases from 3.2 eV to 2 eV in STFO. The valence band of undoped STO consists mainly of O 2p-orbital states, while the conduction band consists of Ti 3d-orbital states. The introduction of 3 mol% Fe creates an energy level within the band gap, as shown in Figure II.3. The band gap can be adjusted by varying the Fe content and the oxygen partial pressure.
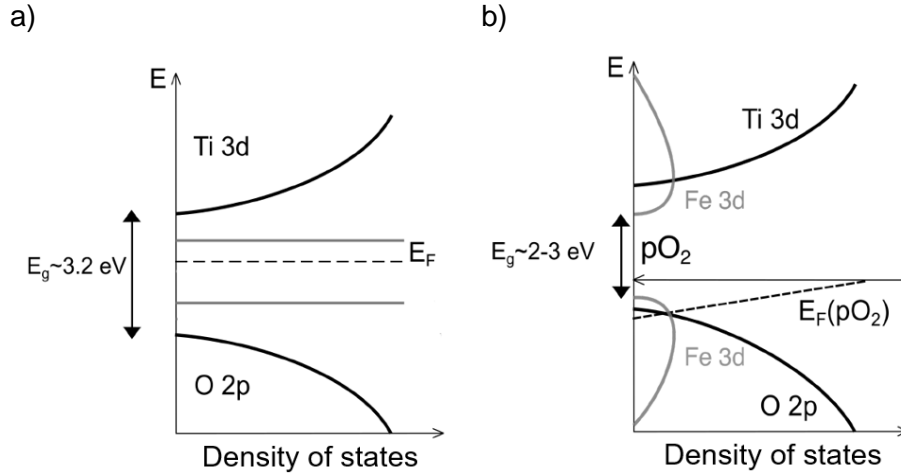
Figure II.3 : The schematic of changing bandgap of STO a) pre-doping and b) post-doping of Fe[203]

Fe-doping in the TiO_2 lattice creates an impurity energy level between the conduction and valence bands, resulting in the absorption of visible light when 3d electrons are excited. Figure II.4 shows the absorbance spectra of undoped STO and Fe-doped STO, where the addition of Fe cations in the STO lattice results in absorption from the UV to 650 nm. Morin et al. show that Fe^{3+} and Fe^{2+} doping creates isolated energy levels within the forbidden band of STO, with the observed absorption tail at 650 nm partially due to electron excitation from two isolated energy levels into the conduction band of STO[204][205]. It has been observed that the optical absorption increases as the concentration of Fe increases. When the system is oxidized, higher Fe concentrations result in greater availability of electrons in the valence band, allowing for deeper energy-level states[196].
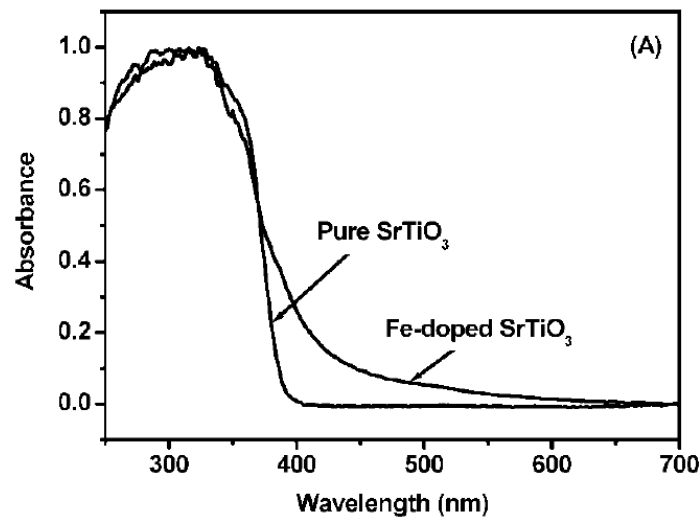
Figure II.4: The absorbance spectra of undoped and Fe-doped STO[204]

The Goldschmidt tolerance factor (t) can provide insight into the stability and characteristics of the perovskite, including its material properties and geometric structure and the distortion type from ideal cubic perovskite structure[206].

$$t = \frac{r_A + r_O}{\sqrt{2}(r_B + r_O)}$$

Equation II.7

In Equation II.7, r_A, r_B, and r_O represent the radius of cations A, B, and the anion oxygen, respectively. The tolerance factor of an ideal cubic structure in perovskite materials should be between 0.9 and 1. A tolerance factor less than 0.9 or greater than 1 indicates a non-cubic structure[207]. Due to their high degree of structural flexibility, perovskite materials can take on various symmetries including orthorhombic, hexagonal, tetragonal, or brownmillerite-type structures. This allows them to accommodate metallic elements on their A and B sites.

The tolerance factor of STO in its cubic cell form is (1.001). The cubic structure of STO is preserved by the addition of iron, with no long-range ordering between Fe and Ti at the B-sites. In the case of $SrFeO_3$, the presence of ordered oxygen vacancies results in a complex phase diagram. The phase formed by $SrFeO_{3-\delta}$ varies with the oxygen content ($0<\delta<0.5$). The cubic phase of $SrFeO_{3-\delta}$ is present from 0 to 0.03. When δ is 0.125, the material exhibits the tetragonal phase; when it is 0.25, it adopts the orthorhombic phase[203].

Figure II.5 shows that the STFO crystal structure remains stable at temperatures above 400°C. All $SrTi_{1-x}Fe_xO_{3-\delta}$ forms between 0 to 0.3 exhibit cubic perovskite structure[203]. The progressive substitution of Fe^{4+} by Fe^{3+} in the lattice causes the symmetry to decrease from cubic to tetragonal, then to orthorhombic, and finally to the brownmillerite phase. This is stabilized by the formation of oxygen vacancies[208]. Besides, the brownmillerite phase also exhibits an increasing oxygen excess with decreasing temperature and has stoichiometry-free characteristics[209].
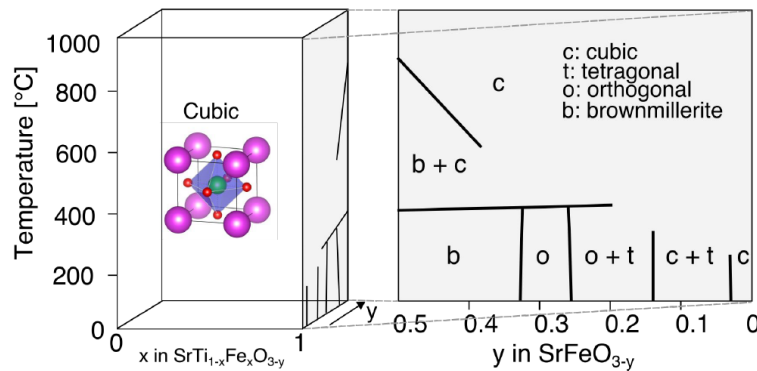
Figure II.5 : $SrTi_{1-x}Fe_xO_{3-\delta}$'s phase diagram with variations in temperature and composition[203]

In brief summary, STFO is a mixed ionic electronic perovskite oxide that has been widely studied due to its stable cubic phases in both oxidizing and reducing conditions and across a wide temperature range. Their popularity results from the ability to adjust their physical and chemical properties according to stoichiometry and maintain stability against external factors under most conditions.

Various techniques can be used to deposit perovskite oxides, such as sol-gel[209], hydrothermal[210], chemical vapor deposition (CVD)[211], and ALD[212]. The deposition method must maintain a specific crystallographic orientation between the film and the substrate, preserving the perovskite lattice structure and allowing for accurate manipulation of film thickness and crystal orientation based on atomic arrangements[213][214]. Moreover, strain relaxation typically creates dislocations and structural defects in the oxides. The critical thickness is a few tens of nanometers at a 1% strain magnitude and smaller at larger strains. For wide bandgap conductors may experience increased resistance due to structural defects[214]. The only way to fulfill these requirements is through epitaxial growth techniques for complex crystal structures to achieve the ideal stoichiometry and properties of the material. Epitaxial growth produces uniform layers with specific crystal orientations on a seed layer while

maintaining control over composition and growth[213]. Further information regarding its main features will be provided in a subsequent section. Four techniques- molecular beam epitaxy (MBE), PLD, sputtering, and CVD- grow films by epitaxial but differ in their physical mechanisms, resulting in varying film properties.

II.2. Cataloging and Comparative Analysis of Deposition Processes

The selection of thin film deposition methods must be carefully considered based on the desired film properties required to create functional coating or component. There are two main methods of deposition: chemical deposition and physical deposition methods. Physical deposition methods transfer materials physically, like evaporation, laser ablation, etc., while chemical deposition generally involves the reaction of precursor molecules to form a solid film on the substrate.

There are two main chemical methods of thin film deposition: solution-based and chemical vapor deposition (CVD). A precursor solution with desired elements is applied to the substrate in solution-based deposition methods. The precursor molecules react to dissociate on the substrate surface to form a solid thin film. Methods like spin-coating, sol-gel, dip-coating, inkjet printing, and spray pyrolysis are categorized as solution-based deposition. Using plasma or thermal chemical reactions, CVD creates high-quality thin films on a substrate. The types of CVD are commonly used to produce top-quality coatings and polymers that are high-performing and dense. A broad range of CVD processes is available for this purpose, such as low-pressure and atmospheric CVD, horizontal and vertical CVD, hot-wall and cold-wall CVD, metal-organic CVD, hot filament/wire CVD, plasma, photo-assisted, laser-assisted CVD, chemical beam epitaxy and ALD[215][216].

PVD is a thin film deposition process in which solid material is evaporated in a high vacuum and then depositing it onto a substrate using mechanical and thermodynamic processes. The surface of source material is vaporized into gaseous atoms and molecules or partially ionized into ions under vacuum conditions. In PVD, energetic particles or thermal energy are used as the energy source, while CVD uses plasma, light, or heat from chemical reactions as the energy source. The main differences between PVD, CVD, and solution-based chemical depositions and their respective properties are illustrated in Table II.II.

Table II.II: The general properties of PVD, CVD, and solution-based depositions

Property	PVD	CVD	Solution-based
Reaction	Vapor + Ionization of atoms	Surface + vapor reaction	Precursor molecules reactions
Coating thickness	Thinner (0.1-2 μm)	Thicker (1-10 μm)	Thinner (<1 μm)
Coating adhesion	Excellent	Good	Mean
Impurity	Very low (<1%)	A few (<3%)	Several (>3%)
Deposition temperature	Low (<500 °C)	High (>1000 °C)	Low (<500 °C)
Growth rate	Fast (100 nm-1 μm/min)	Middle (10-100 nm/min)	Fast (100 nm-1 μm/min)
Growth mechanism	Continuous	Continuous	Layer-by-layer/Nucleation
Crystallization quality	Good	Good	More challenging than PVD and CVD

The sub-methods of PVD can be categorized as follows: evaporation (thermal and electron-beam), sputtering (DC and RF), molecular beam epitaxy, and pulsed laser deposition.

The choice of evaporation method should take into account material properties such as phase transition and potential contamination. Thermal evaporation, while low-cost and straightforward, may not be optimal for all highly reactive materials with low vapor pressure, such as nickel and platinum. Electron-beam (e-beam) evaporation offers precise control over deposition and can evaporate materials with high melting points but requires advanced equipment. The films, produced by evaporation, exhibit high roughness and poor crystallization, which may require post-deposition treatments. In addition, these methods have limitations in achieving high thicknesses, typically in the range of a few nanometers to micrometers.

The sputtering technique uses plasma excitation to deposit material from a gas energized with DC or RF power in a high vacuum. This method can achieve high crystallization and reproduction with lower roughness. During deposition, plasma particle kinetic energy, emission, and heat may damage sensitive substrate layers on ITO (SnO_2:In) and FTO (SnO_2:F) [217].

Molecular beam epitaxy (MBE) is a process where the crystallites of material grow on a heated substrate under an ultra-high vacuum by interacting with absorbed species from atomic or molecular beams. It can deposit incredibly thin layers with exceptional accuracy. This method can produce high-quality films with low roughness. Controlling growth is critical for high-quality films for this method. Higher temperatures make the material more orderly, but interfaces become smoother due to atom diffusion. Lower temperatures result in more abrupt interfaces but also more point defects in layer[218].

Pulsed laser deposition (PLD) uses an excimer laser with a narrow frequency bandwidth to vaporize the target (source material). It is possible to achieve identical stoichiometry in both target and deposited thin film using this method. This particular feature of PLD holds significant importance for our study. The process is more complex than other methods, involving evaporation, ablation, and plasma formation[219] (The next section will provide an explanation of these terms.) PLD films typically have high crystallinity and varying roughness but appear relatively smooth, thanks to the influence of energetic feather species during deposition.

In general, Table II.III shows a summary of the characteristics of deposition methods discusses above.

Table II.III: Comparison of PVD's deposition methods

Deposition Methods	Benefits	Drawbacks
Thermal Evaporation	Simple process, cost-effective	Limited material range, contamination risk, high roughness, poor crystalization
E-beam Evaporation	Precise control over deposition, high growth rate, wide material range, epitaxy	Evaporation source contamination, equipment complexity and cost, energy consumption
Sputtering	High transparancy, high crystalization, high reproducibility, epitaxy	Complex process control, damage to layers underneath, expensive
Molecular Beam Epitaxy	High purity, wide material range, high crystalization, low roughness, epitaxy	Low deposition rate, energy consumption, point defects creation in lower temperatures
Pulsed Laser Deposition	Precise stoichiometry, high crystalization, high reproducibility, epitaxy	Large-scale limitation

Table II.III illustrates that PLD shares some similarities with MBE and sputter depositions. One of its benefits is the rapid growth rate and the superior crystalline growth of the thin films. Additionally, it has advantages in achieving results close to the stoichiometric transfer of target compounds, making it a viable option for damage-free deposition. Experimental evidence suggests that the most successful way to achieve undamaged deposition through PLD is by thermalizing the energy of incoming species via the background gas at high deposition pressures, rather than through sputtering[220].

When it comes to deposition rate and stoichiometry, PLD is competitive with other thin film deposition methods, as shown in Figure II.6, especially when considering doped-free STO. It is possible for the thin film deposited on a substrate to not match the target stoichiometry, which may cause issues. This often occurs when heavy materials or those containing highly volatile elements[221] are used, especially if the laser power used for PLD is either too low or too high[222]. To address the issue, optimizing the laser power density and selecting suitable deposition materials are crucial. One way to solve this problem is by introducing gas into the chamber during PLD processing. This can effectively address the issue.
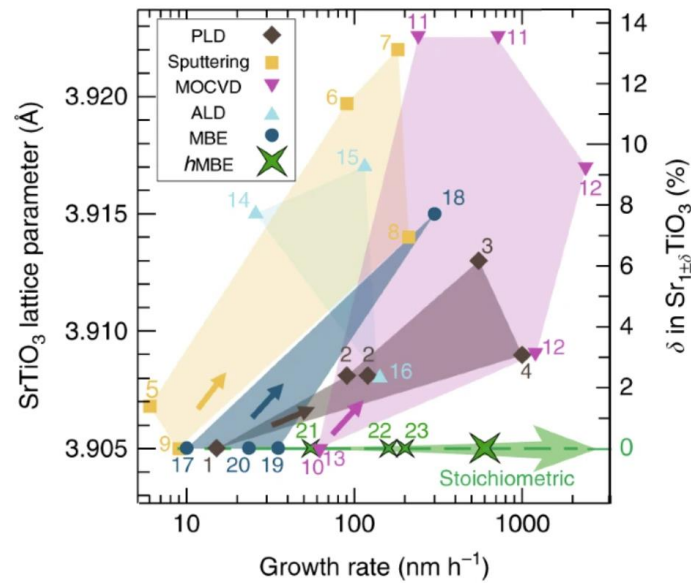
Figure II.6: Growth rate and stoichiometry control of STO for different deposition methods (the numbers serve as references utilized in the research)[223]

Below is a brief summary of the features mentioned above that make PLD stand out for our work:

• High-quality thin films with complex stoichiometry or multilayer structures can be produced from the target with a similar composition[224].

• Some process parameters decoupled from the laser-target interaction such as background pressure, gas type, and temperature[225].

• The number of particles reaching the substrate can be adjusted by controlling the number of pulses and laser fluence[226].

II.3. Pulsed Laser Deposition (PLD)

PLD is a process used to deposit a wide range of materials, even the most refractory, including oxides, semiconductors, and insulators. The principle of Pulsed Laser Deposition (PLD) is straightforward. A laser is focused onto a target material composed of the elements to be deposited, which is set in rotation. If the laser is sufficiently powerful, it enables the ablation of the target, generating a plasma plume within an ultra-high vacuum or controlled pressure environment. This plasma plume expands in a direction perpendicular to the target surface and subsequently condenses onto a substrate positioned opposite the target. Given its flexibility, PLD serves as an ideal tool for scientific research dedicated to the study and development of thin film materials, with thickness ranging from nanometers to micrometers. Before deposition with PLD, a suitable target for thin film must be synthesized via multiple solid-state synthesis steps. The fabrication stage is critical for achieving desired thin film properties. The process of solid-state synthesis can be explained in the following steps and also shown in Figure II.7:
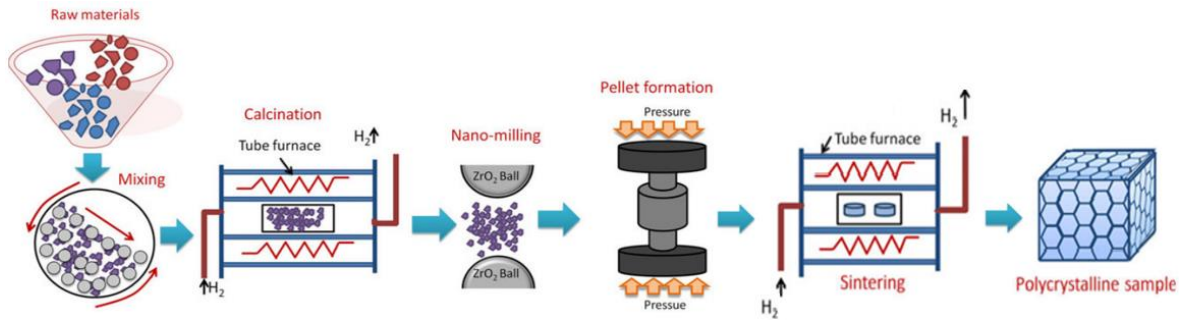
Figure II.7: The process of solid-state target synthesis[227]

1) Mixing: The highly pure raw materials are calculated stoichiometrically to determine their powder states. They are then homogeneously mixed under solvent using zirconia balls.

2) Calcination: In general, the process involves heating the powder or precursor compound to a high temperature without reaching the point of melting or decomposition. The main objective is to eliminate any volatile components and induce chemical reactions that modify the material into the desired phase or structure.

3) Nano-milling: Achieving a greater homogeneity of the mixture and reducing the particle size can increase the chemical reactivity of the material. In the case of oxide perovskites, it is important to allow for partial diffusion of both A and B cations. To ensure the targeted stoichiometry is achieved, it is recommended to perform X-ray diffraction (XRD) before pelletization.

4) Pellet formation: To create a dense pellet or target from milled powder, a press is used to apply enough pressure to minimize porosity. During this process, it is crucial to ensure that the powders are compacted sufficiently. A poorly compacted target may break when the laser is delivered to its surface, so it's important to pay close attention to this step.

5) Sintering: This process involves keeping the target at a temperature between its melting and decomposition points, which allows for particle rearrangement and solid-state diffusion.

6) Cooling: The target undergoes a series of slow cooling steps after sintering.

Strontium nitrate ($Sr(NO_3)_2$), titanium dioxide (TiO_2), and iron(III) nitrate nonahydrate ($Fe(NO_3)_3.9H_2O$) were used as raw materials for STFO. These are the identity of materials used in target: $Sr(NO_3)_2$ (98%, Alfa Aesar), TiO_2 (99.9%, Alfa Aesar) and $Fe(NO_3)_3.9H_2O$ (98+%(metal basis), Alfa Aesar). They were present in concentrations of 18.71%, 42.02%, and 39.27%, respectively. After combining all ingredients with distilled water and citric acid, the subsequent steps were carried out according to the previous instructions. The mixture underwent calcination by heating it to 1000°C for 8 hours. Once the stoichiometry conformity was confirmed through XRD (see Appendix), the material was subjected to nano-milling at 1000 rpm. Pelletization was used to create 4.5 mm-thick and 28 mm in diameter targets at 60°C and 100 MPa. Once the target has been created and placed in the PLD system, the deposition process can commence.

The PLD system comprises a pulsed excimer laser operating at a wavelength of 248 nm and an Ultra High Vacuum (UHV) chamber. This specific wavelength imparts high photon energy (approximately 5 eV), enabling the disintegration of atomic bonds within the target

material, facilitating a uniform and congruent deposition process. Within the chamber, the laser is meticulously focused on either metal or ceramic source materials. The targets within the chamber exhibit both rotational and translational movement.

As material is ablated from the target surface, the energetic photons undergo a conversion into electronic impulses, yielding thermal, chemical, and mechanical energy[215]. Material vaporization occurs perpendicular to the target surface, generating a material flow, leading to the formation of a plasma plume on the substrate, as depicted in Figure II.8. The plasma plume's expansion induces interactions among electrons, ions, and laser radiation, resulting in ionization, heating, and the creation of a high-density plasma. This phenomenon also promotes the fusion of target materials. As various species within the plasma cloud interact with the substrate, they adhere to its surface, ultimately forming a thin film. To mitigate subsurface boiling and minimize particle formation on the film surface, it is imperative that the majority of the energy is absorbed within a shallow layer near the target surface.

In our specific setup, we employ a KrF laser with a 248 nm wavelength and a pulse duration of approximately 25 nanoseconds. Additionally, the laser fluence, which measures energy per unit area, is set at 3 joules per square centimeter for our system.

a)   b)
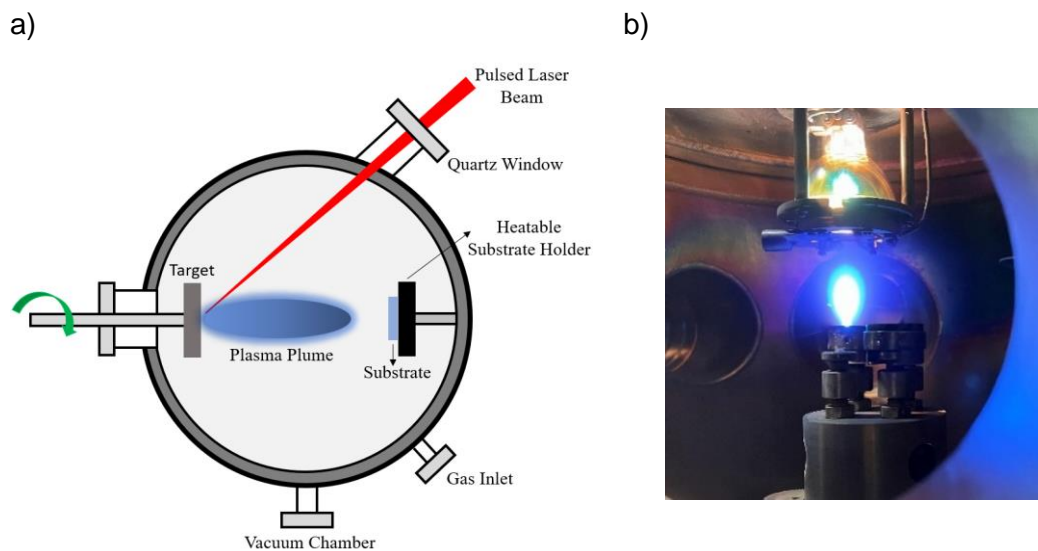
Figure II.8: a) Schematic of PLD process and b) an example of a plasma plume view from our system

The vacuum pressure in the PLD chamber usually falls between 10^{-5} to 10^{-8} mbar. To create a vacuum in the chamber, it is necessary to use at least two different pumps. The preliminary pump can reduce the pressure from atmospheric to $\sim 10^{-2}$ mbar. A turbo-molecular vacuum pump is also used to achieve the pressure range until $\sim 10^{-8}$ mbar. These pumps ensure that there is no significant loss of vacuum after a sample has been delivered into the chamber. During the deposition process, direct injection of specific gas ensures the maintenance of a reactive pressure. Similarly, the cooling process that follows the deposition is also carried out under constant pressure with the assistance of the gas flow. Proper control of oxygen content and a wide pressure range are crucial for oxide materials using PLD.

As we have previously mentioned, PLD uses thin film growth via epitaxy, which has two main types:

  i)   homoepitaxy, in the deposited material, has the same composition as the substrate, and

ii)   heteroepitaxy, which refers to the situation where the thin film and substrate are made of different materials, but the substrate has a structure that can guide the growth of the thin film[228].

The process of epitaxy is strongly associated with the formation of a crystalline interface. When thin films are deposited on substrates with different lattice parameters, it creates a mismatch that induces strains in the film. These strains can be either compressive or tensile. Depending on the type of strain, the crystal structure, bond properties and even electronic properties of the thin film may be altered. Using PLD, strain tunability in oxide deposition triggers phase transitions via heteroepitaxial growth, due to a strong association with lattice symmetries. This enables the expansion and availability of different material properties.

II.4. Conclusion

STFO is a type of cubic oxide perovskite. It is an electroceramic material that possesses versatile properties. Due to its ability to control transport and electronic properties based on stoichiometry, STFO is an attractive conductor for numerous applications. However, it requires high crystallization temperature. It is not possible to deposit on glass/FTO substrate at high temperatures because of deformation.

PLD is a commonly preferred method of deposition because of its ability to produce high-quality crystal structures without causing damage to the substrate. Additionally, this technique allows for a direct transfer of the desired stoichiometry to the thin film. The concentration of oxygen vacancies in oxide perovskite films is significantly influenced by the deposition conditions, particularly the partial pressure of oxygen, as we mentioned previously. The main drawbacks of PLD are the large deposition area. Surfaces larger than 200 mm in diameter cannot be evenly coated, resulting in non-homogenous coating. However, this disadvantage does not apply to us as the size of glass/FTO substrate for STFO deposition is standardized at 12x12 mm^2. As a results, it aims to manage good crystallization of STFO in PLD system with oxygen partial pressure in the back gas atmosphere with the glass/FTO substrate temperature.

Chapter III. Investigation of Perovskite Oxide Thin Films

The aim of this chapter is to provide a detailed explanation of the process used to fabricate STFO thin films through PLD. The characteristics of STFO thin films investigated here will provide insight before their integration in halide perovskite optoelectronic devices.

The first part of the chapter will focus on determining the ideal crystallization (i.e. pinhole free, dense, uniform and large crystals, etc.) conditions for STFO oxide perovskite. This will involve assessing different partial pressure conditions and using the optimal conditions as a reference for the fabrication of thin films through PLD. Following this, optical and electrical properties of the thin films will be evaluated to assess the effectiveness of the oxygen partial pressure condition.

In the second part of this chapter, two different additional thermal treatment methods which are rapid thermal processing and conventional thermal treatment will be applied to the optimally crystallized as-grown STFO thin films, and their effects will be discussed from structural, optical, and electrical points of view.

III.1. Different Partial Pressure Conditions

In optoelectronic devices, the charge transport layers (specifically, hole transport layer or HTL here) should possess certain essential properties such as high conductivity, high transparency, high stability and suitable work function for energy-band alignment in device structure. The quality of the thin film is directly related to these properties and is determined by the grain growth mechanism. Therefore, this section aims to investigate the impact of different oxygen partial pressure on STFO thin film to investigate the requirements for being HTL.

Among the most important parameters in the PLD system, the reactive atmosphere and substrate temperature are often the key point to develop adapted thin films for micro-components. In addition to laser properties (wavelength, beam profile etc.) and target material, the ablation atmosphere also affects the PLD process. The atmosphere of the chamber is created using gas inlets available in the system. The gases (such as oxygen and argon) used may vary depending on the requirements. Introducing gas into the chamber helps regulate reactive atmosphere thus enabling partial pressure-dependent deposition.

In order to achieve optimum crystallization, perovskite oxides must be either deposited at high temperatures (>700 °C) or undergo post-annealing at high temperatures (600-800 °C). This heat requirement is necessary to eliminate excess oxygen or oxidize the unoxidized metal, depending on the oxygen partial pressure used during deposition[229]. Working with high temperatures poses a challenge in our case as the preferred substrate, glass/FTO, can lose its original form and even melt well below 700°C. First, we determined the maximum experimental temperature at which the FTO can maintain its properties in order to identify an upper-temperature limit for perovskite oxide deposition. Our system consumes 60W to heat the FTO and operates at an average temperature of 400°C (see Appendix 1.2). Growth conditions for STFO crystallization were determined by maintaining a constant temperature and optimizing oxygen partial pressure.

The deposition process in PLD is controlled by high-pressure conditions that optimize crystal structure growth, prevent fouling, and influence material transfer[230]. The pressure range in our system is restricted to values between 10^{-1} and 10^{-8} mbar. An oxidizing

atmosphere with an O_2 (dioxygen) pressure (by entering a very pure oxygen gas (99.99%) inside the PLD chamber) above 10^{-2} mbar is necessary to achieve the appropriate stoichiometry of the oxide layers[231]. In order to investigate the effect of oxygen, STFO thin films were grown under two different conditions without additional oxygen back atmosphere at 3×10^{-7} mbar which is residual pressure and reactive atmosphere with oxygen pressure at 3×10^{-2} mbar.

XRD (2θ-θ scan) was utilized to investigate effect of two different conditions on crystal structure (see Appendix 2). Figure III.1 presents the crystallization of STFO thin films under high and low-pressure conditions, with significant variations. Only the characteristic diffraction peaks of the FTO and STFO were observed when grown in an reactive atmosphere at high pressure. However, unknown peaks were observed alongside the expected peaks at 30.6°, 43.9°, and 44.8° in the low pressure under vacuum. It is promising to see the characteristic peak of STFO (110) even under vacuum, as this result demonstrates that better crystalline quality can be achieved with oxygen. In summary, STFO diffraction peaks occur without any parasitic peaks in 3×10^{-2} mbar, such pressure is favored for these conditions. It would be useful to analyze the characteristics of STFO by investigating the crystallization under different reactive atmospheres with oxygen.
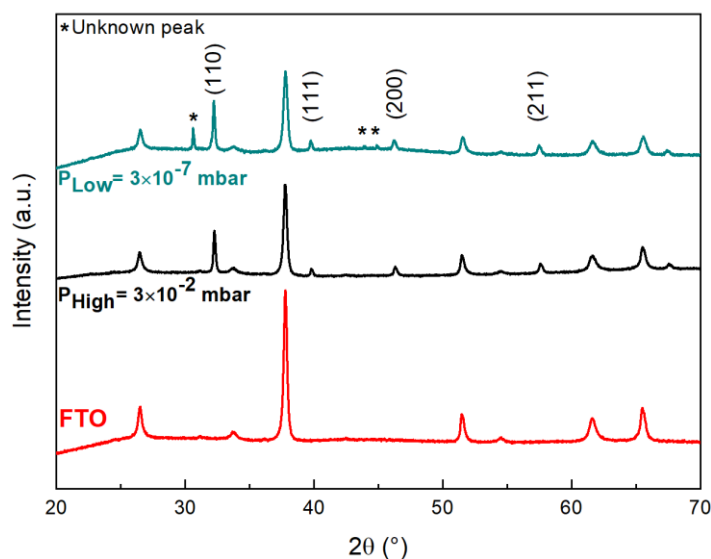
Figure III.1 : XRD pattern of STFO thin films growth at low and high pressures

Maintaining the pressure below 10^{-2} mbar is critical as higher pressures can negatively impact the shape of the plasma plume, potentially leading to narrower plumes that can adversely affect the thin film growth process. Once we confirmed crystallization at the appropriate stoichiometry under high oxygen pressure (3×10^{-2} mbar), we further investigated three different pressures approaching the deposition system limit to determine the optimal conditions for scale-up. Deposition pressures of 3×10^{-2}, 6×10^{-2}, and 9×10^{-2} mbar were determined. Thin film layers with thicknesses of 195 nm, 107 nm, and 95 nm were successfully crystallized, even though the deposition duration (20 minutes) was the same. The different oxygen partial pressures resulted in varying plasma plume dynamics, which caused differences in the thicknesses of the layers. In the next section, we will focus on evaluating the structural effects of varying oxygen partial pressures, while in the following part of this chapter, we will better control the effect to compare layers of similar thicknesses.

III.1.1. Structural Properties of Different Partial Pressures

The crystal structure of three different conditions based on oxygen partial pressure was analyzed using XRD. Three peak characteristics of the STFO phases (ICDD 04-022-5932) are present at 32.3°, 39.8°, and 46.3°, as shown in Figure III.2. The crystal phases correspond to (110), (111), and (200) Miller planes, respectively. Additionally, the peaks at 57.6° and 67.6° correspond to the (211) and (220) planes, respectively.
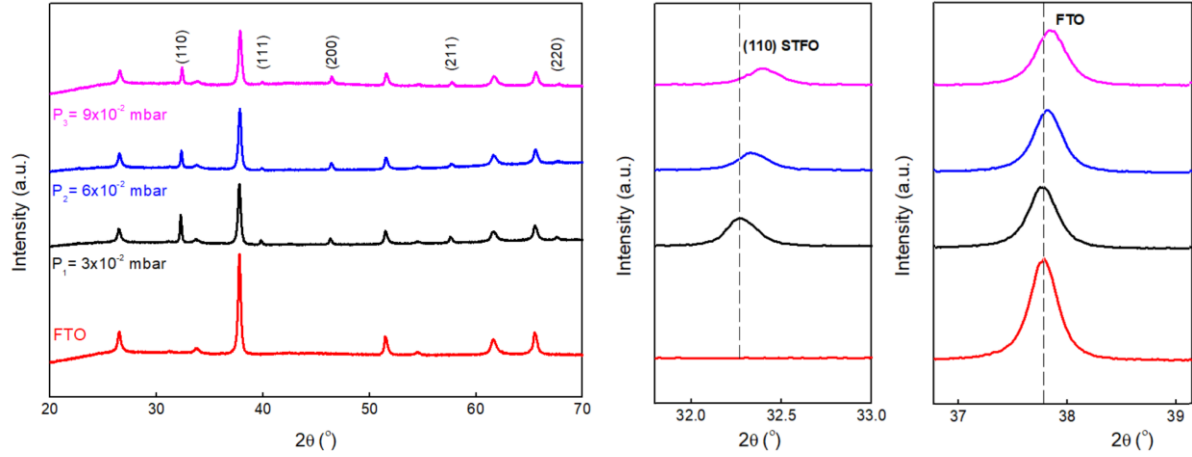
Figure III.2 : XRD patterns of STFO for different oxygen partial pressures

Upon close examination of the XRD pattern on the right side of Figure III.2, it can be inferred that the shift in both STFO and FTO peaks indicates varying degrees of lattice expansion and crystal size, depending on the oxygen partial pressure. The lattice constants for 3×10^{-2}, 6×10^{-2} and 9×10^{-2} mbar are 2.771, 2.767, and 2.761 Å, respectively for STFO (110) plane. The shift in the peak position occurs due to the continuously changing lattice constants as a function of composition for STFO. Lattice strain can cause diffraction peaks to widen, with the degree of broadening proportional to the magnitude of the stress[232]. Overheating in the pre-heating stage for PLD due to structural changes or incorrect positioning of the FTO on the measurement holder can cause peak shift in the FTO.

The XRD pattern indicated successful crystallization, but it is still challenging to determine the effect of pressure on the crystal structure. It is possible to use the following Scherrer equation to quantify differences in crystal quality related to D, the average size of ordered crystalline domains (or crystallites)[233]:

$$D = \frac{K\lambda}{\beta \cos\theta}$$

Equation III.1

Here, K is the shape factor and it is typically considered as 0.89 for perovskite oxides[234]. λ is the wavelength of the X-ray (Cu, K_α is 1.5406 nm in our case), β is half maximum values representing the peak expansion, i.e. the full-width half maximum (FWHM) in radians, and θ is the Bragg angle. It is possible to obtain D which is considered a parameter of crystal quality. This calculation is based on the peak intensity of the highest peak of the thin film in general. For the STFO (110) orientation, the D values for 3×10^{-2}, 6×10^{-2}, and 9×10^{-2} mbar are 332 nm, 241 nm, and 104 nm, respectively. Based on these results, 3×10^{-2} mbar showed better crystal quality. The FWHM values are 0.18, 0.18, and 0.20 radians, respectively in the same order. It was impossible to compare these values with previous studies as using

FTO as the substrate for STFO is relatively new. The FWHM values obtained from two different partial pressures are identical for 3×10^{-2} and 6×10^{-2} mbar, and differ from 9×10^{-2} mbar. A smaller value of D results in a narrower β, leading to a sharper and more intense diffraction peak. This indicates different crystal sizes due to more uniform and less disordered crystals[235]. Broadening of the diffraction peaks occurs due to the shortening of the crystal size. As the ordered areas of crystals become smaller, the FWHM increases. These patterns suggest that 9×10^{-2} mbar exhibits lower crystal quality than others. XRD reveals the atomic and crystallographic structure, which can differ from the external structure. Consequently, it is not feasible to draw a definite structural conclusion based solely on the XRD pattern, and additional analyses are necessary to explore the structural properties in detail.

In order to obtain particular informative details on the influence of oxygen partial pressure on STFO crystallization, we preferred to examine the microstructure, as shown in Figure III.3 (see Appendix 2 for measurement details).
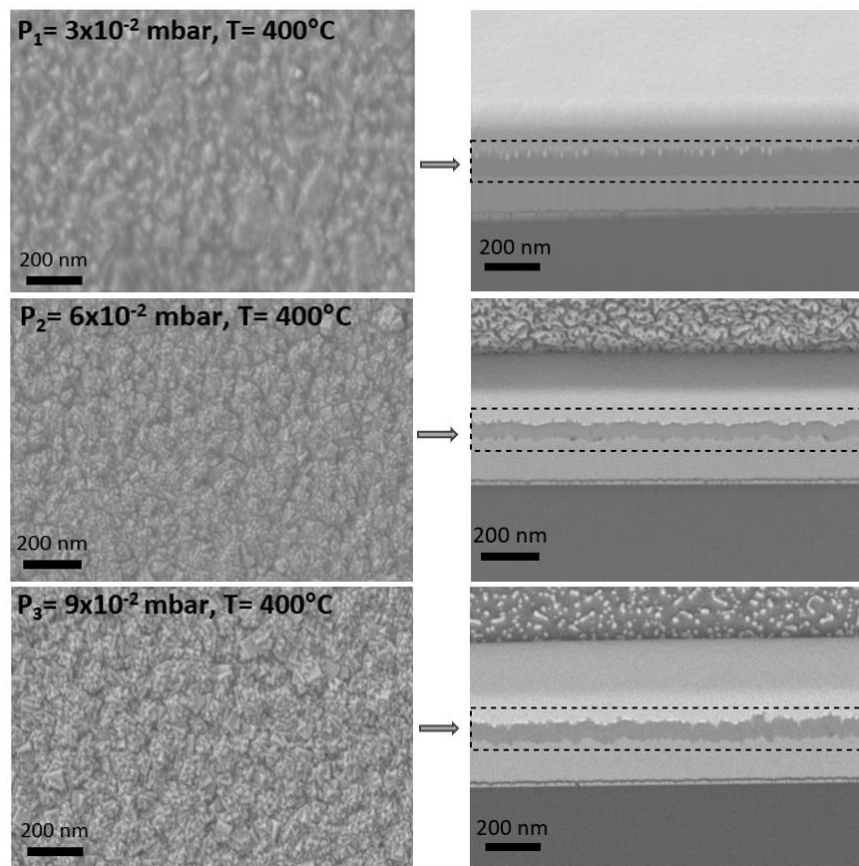
Figure III.3: The variation of perovskite oxides microstructure with oxygen partial pressure

The higher oxygen partial pressure (from 3×10^{-2} to 9×10^{-2} mbar) tends to lead to better changes in the microstructure and provide smoother and more homogeneous surfaces with bigger grain sizes. It is evident that STFO grain morphology positively changes with partial oxygen partial pressure. The cubic shape of the particles became more defined at $P_3=9\times10^{-2}$ mbar, indicating a bigger crystal size and more defined peak shapes.

The interfaces of STFO layers with their adjacent layers (either the bottom substrate or top layer) are crucial as they significantly impact device performance. Cross-sectional SEM analysis reveals pin-hole-free and dense STFO thin films with quite similar views for 6×10^{-2} and 9×10^{-2} mbar. Unlike others, there is observable ionization in the interface $P_1=3\times10^{-2}$ mbar.

During SEM imaging, if a material is exposed to high-energy electron beams, it may cause the electrons to penetrate the material. Therefore, the electron beam and the sample may interact and cause ionization. This phenomenon is more prevalent in materials with low electrical conductivity, as this results in low free ion concentration[236]. In addition, the presence of interfaces, grain boundaries, and defects in the thin film structure can affect local electron properties, making certain regions more susceptible to ionization.

The FWHM and lattice constant values differ with varying oxygen partial pressures. However, SEM images reveal differences in crystal size more clearly. Moving forward, only $P_3=9\times10^{-2}$ mbar will be analyzed among three deposition conditions, and we will discuss its suitability as the interlayer in terms of surface morphology and elemental composition.

In Figure III.4, the surface morphology of the films was studied using Atomic Force Microscope (AFM) (see Appendix 2), from which topographic images and roughness analysis were performed. The surface roughness (RMS) Ra of $P_3=9\times10^{-2}$ mbar condition was measured to be 9.6 nm for 100 nm thick-STFO thin film. This relatively small value is suitable for optoelectronic applications, as it allows the deposition of high-quality and uniform thin films on the top, without large surface irregularities and defects.
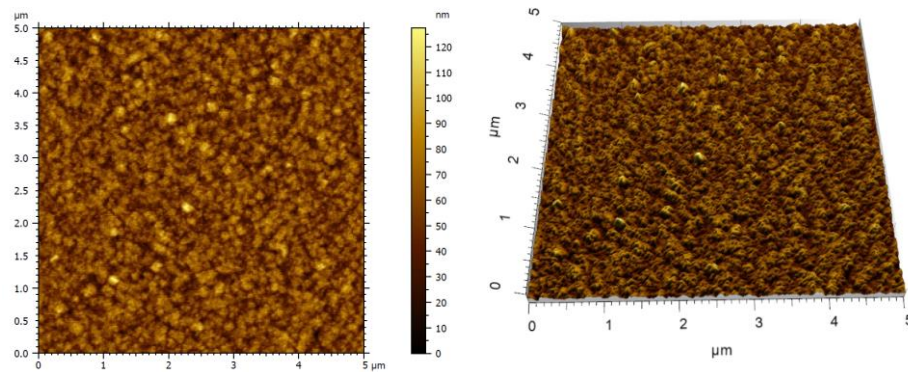
Figure III.4: AFM images of STFO at 9×10^{-2} mbar pressure

A first level elemental analysis was performed using Energy Dispersive X-ray Spectroscopy (EDS or EDX), coupled to our SEM. The EDS was used to analyze the elemental composition of sample processed at $P_3=9\times10^{-2}$ mbar oxygen partial pressure. It was found that our thin film contains only Sn, O, Sr, Ti, and Fe from FTO and STFO with no impurities besides their chemical composition, as shown in Figure III.5. It is interesting to note that the presence of fluorine in FTO has not been detected. Fluorine with a low atomic number (Z=9) emits X-rays with lower energy, making detection difficult when competing with higher atomic numbers that produce stronger signals despite 30 kV probe operation[237]. It is possible that the peaks of fluorine and oxygen overlap due to their close K_α values of 0.525 and 0.677, respectively[238]. Carbon elements were detected due to the conductive carbon layer during sample preparation for analysis.
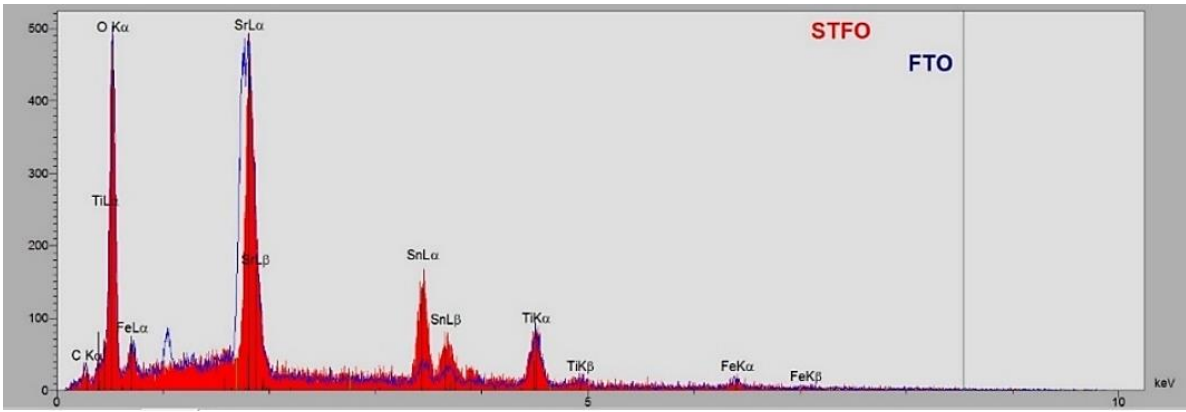
Figure III.5: EDS elemental analysis of STFO on FTO substrate

After conducting experiments, it was discovered that the best conditions for STFO crystallization are at low temperatures while using undamaged FTO. An optimal oxygen pressure of 9×10^{-2} mbar was determined to be the most suitable due to its bigger grain of microstructure, smooth, and homogeneous thin film surface. Additionally, the chemical composition of the crystal was free of impurities. In the following steps, STFO thin film fabricated at 9×10^{-2} mbar and 400 °C will be investigated in terms of its optical and electrical properties.

III.1.2. Optical Properties of STFO Thin Film

It is important to increase the photocurrent of solar cells by maximizing the transparency of the interfacial layer. This allows more light to reach the active layer of the cell. STFO thin films need to have high transparency (>75%) in the visible range to be used as an interfacial layer. Therefore, it is crucial for the films to possess appropriate optical properties.

The use of different substrates provided valuable insights into the thin film's growth and optical properties. Figure III.6 displays the absorbance spectrum of a 100 nm STFO thin film deposited on glass, glass/FTO, and C-sapphire substrates for each of them at 9×10^{-2} mbar and 400 °C (see Appendix 2).
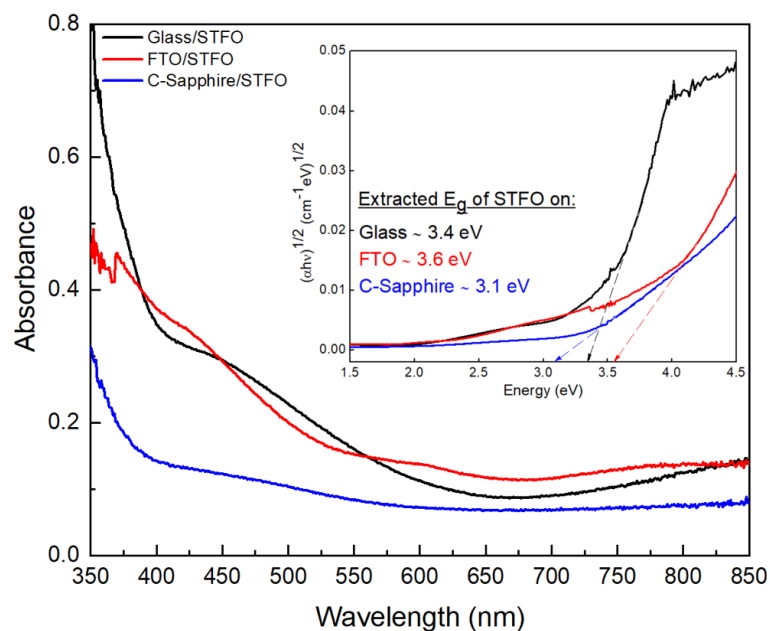
Figure III.6: Absorbance of STFO as a function of substrates and Tauc's plot in the inset

Glass is an amorphous substrate. FTO is a thin layer deposited on glass and has a polycrystalline structure. Sapphire belongs to the highly crystalline structure with hexagonal crystal system as structure of alumina. We observe different absorbance profiles for the different materials, which indicates different properties, such as reflective index, crystal structure, roughness, etc. A band gap estimation using Tauc's plot (see the inset of Figure III.6) shows an estimate of 3.1 eV, 3.6 eV, and 3.4 eV for glass, FTO and c-sapphire substrates, respectively. The Tauc's plot method offers a distinct outcome for STFO deposited on c-sapphire, as evidenced by a sharp graphical curve. However, the glass and FTO have some default for extraction by using Tauc's plot. This is primarily due to the varying crystallization of STFO on different substrates. STFO always demonstrates indirect and wide band gap semiconductor properties. If these materials are used as an interfacial layer where radiative band-to-band transitions are not required, the indirect band gap is not a limiting factor. However, the gap must have a very high value to prevent the charge carrier from being blocked in interlayers[191].

Glass and FTO substrates absorb light before 370 nm, and the STFO band gap is the background, which makes it challenging to use Tauc's plot method. Additionally, Urbach tails cause an exponential increase in localized states between 400-550 nm in glass and FTO. These tails typically appear in poorly crystalline, disordered, and amorphous materials, and they are usually associated with the effects of structural disorder[239]. This indicates that the interaction between the charges and the lattice has a significant impact on the optical properties of the defects present in the thin film. The sharper tails observed on glass compared to sapphire indicate more traps, which suggests the presence of significant populations of localized tail states and deep band gap states in the electronic structure, possibly linked to layer being below the oxygen stoichiometry. Consequently, the substrate types showed expected results related to their common characteristic and STFO on FTO has a suitable band gap for being interfacial layer in optoelectronic applications. But ensuring proper alignment of energy-band levels is critical to know electronic functionality of interfacial layer.

III.1.3. Electronic Properties of STFO Thin Film

The work function of charge transport material, such as STFO, is a significant property that aids in energy band alignment with other layers during device integration. One effective technique to approach this solution is Kelvin Probe Force Microscopy (KPFM). Even though it cannot determine VBM and CBM, it is crucial to determine if the WF is sufficiently high. In terms of its specific working principle, detailed steps of the analysis are presented as follow.

The position of the Fermi level within the bandgap of a semiconductor is impacted by several factors associated with the composition of the materials, its intrinsic electronic properties, and by the presence of impurities. The WF of a semiconductor is the difference between the Fermi level and vacuum level, which means that the Fermi level position can be determined from the WF. The estimation of the WF was performed by KPFM by using the contact potential difference (CPD) principle between the AFM cantilever tip and the surface of the semiconductor. The semiconductor's WF can be determined by calibrating the AFM cantilever tip based on a reference surface with a known WF. The reference of highly oriented pyrolytic graphite (HOPG) and gold (Au) was utilized with a work function of 4.4 eV[240] and 5.1 eV for AFM tip calibration under ambient conditions, respectively. The CPD is defined in Equation III.1[241]:

$$CPD = \frac{\emptyset_{sample} - \emptyset_{tip}}{|e|}$$

where $\emptyset_{sample}$ and $\emptyset_{tip}$ are the WF of sample and tip, respectively. The value of the elementary charge is denoted by the e. The first step is to determine the AFM tip's WF with Au as 4.70±0.03 eV. In the second step, we need to calculate the WF of the HOPG reference using the function of the AFM tip and verify the calibration by comparing the results with reference[191][240]. Last and third steps, using the WF value of the tip, we determined that the WF of STFO is 4.90±0.05 eV. All the steps as presented as schematically in Figure III.7.
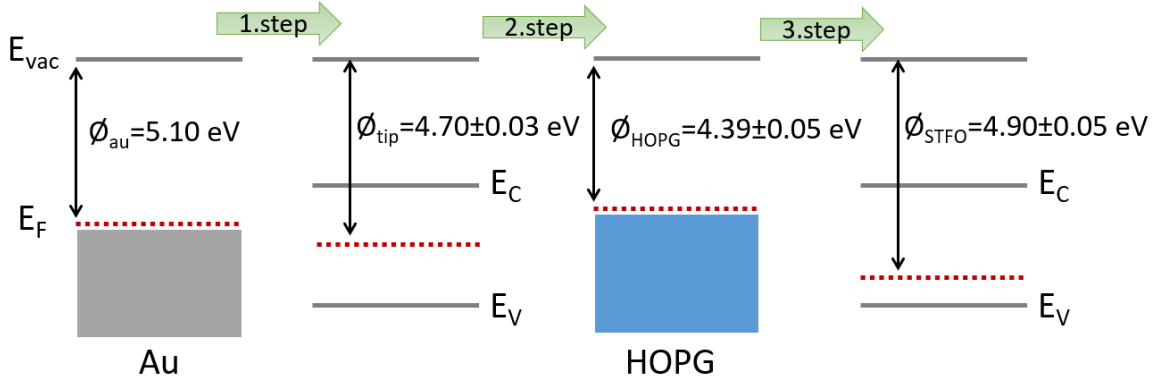
Figure III.7: The steps of CPD principle by using AFM tip for WF of STFO

Efficient transport of holes from the halide perovskite to HTL is possible due to their well energy band alignment, while electron movement is blocked. The WF of STFO is close to that of PEDOT:PSS (WF= 5 eV)[242], which can be low. As this value is much smaller than the maximum valence band of most halide perovskites, it can cause significant energy offset and loss of performance. However, the WF of the STFO is not only criterion for efficient charge transport, other thin film properties and improvement are crucial as well.

III.2. Investigating The Impact of Additional Thermal Treatments

Additional thermal treatments can directly affect the crystal structure and grain size of particles, leading to modifications in the electrical, mechanical, and optical properties of the thin film. Depending on the material type and annealing conditions, such as duration, temperature, and atmosphere, they can have both positive and negative effects towards a specific application. Positive effects may include increase crystallinity, defect removal and reduced porosity, while negative effects may include increased internal stress due to change in stoichiometries and elemental diffusion/segregation. In terms of perovskite oxides, these processes typically restore oxygen vacancies and alter the ion oxidation state, resulting in the modification of electrical properties.

Two different additional thermal treatments were applied to STFO in our case. The first is that conventional thermal annealing (TA) is a widely used method involving high-precision temperature control. Gradual resistance heating is used to reach the desired annealing temperature and prevent thermal shock for uniform heating. The temperature protection during the annealing is maintained within a narrow range based on the set temperature. Both gradual and natural cooling options are available for the cooling process. Different types of gas can be used in the furnace for heating or cooling processes. In the TA treatment (see Appendix 2) used, we annealed the samples at 500 °C for 4 hours with a temperature ramp of 5 °C/min.

The second technique for the annealing was rapid thermal processing (RTP). This method uses a tungsten IR-lamp to rapidly heat and cool, achieving high temperatures with a fast ramp rate of 50°C/s (at the maximum). In principle, the technique allows the rapid heating of a silicon wafer to a temperature extending 1000 °C and held briefly before cooling. Temperature control in the system can be regulated through the use of thermocouples. One effective strategy for temperature control involves using in situ pyrometry, which allows for real-time control. In our RTP treatment, we annealed the samples at 550°C for 100 seconds (see Appendix 2), which is the highest temperature recommended for FTO, as presented in Figure III.8. There is a significant difference between conventional TA and RTP. In TA, the annealing time is given in hours, including long pre-heating, while in RTP, it is measured in seconds. As a result, the diffusion process in each method is distinct from one another. The process of including oxygen into the STFO takes time, leading to differing effects between the two processes.

a)

b)
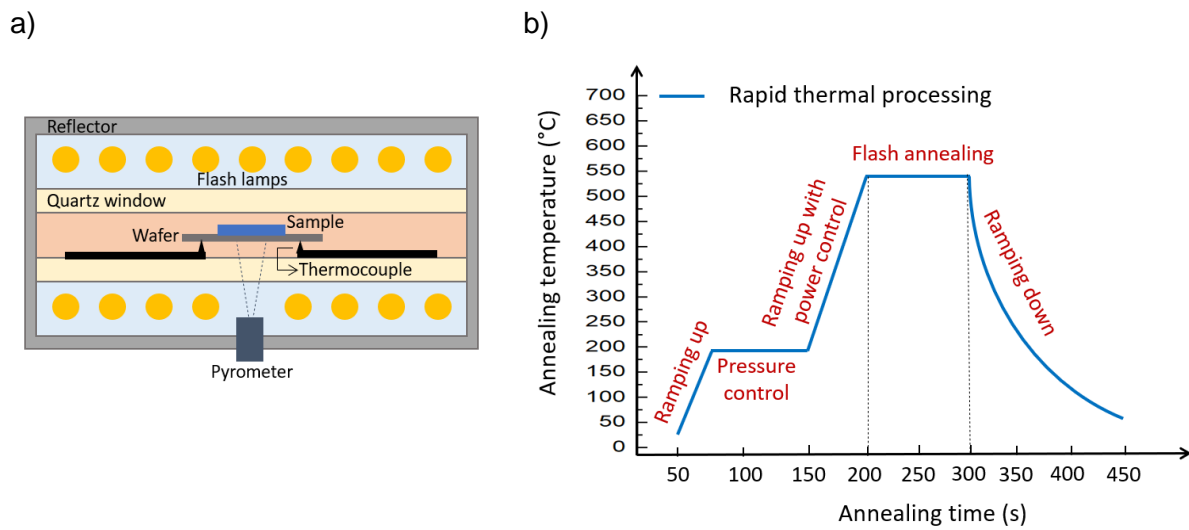
Figure III.8: a) Basic schematic of RTP and b) annealing steps

III.2.1. Impact of Additional Thermal Annealing on Structural Properties

Thermal annealing is a common process for the modification of the structural properties of thin films. Firstly, the effect of RTP and TA on STFO thin films crystallization analyzed by XRD, as depicted in Figure III.9.
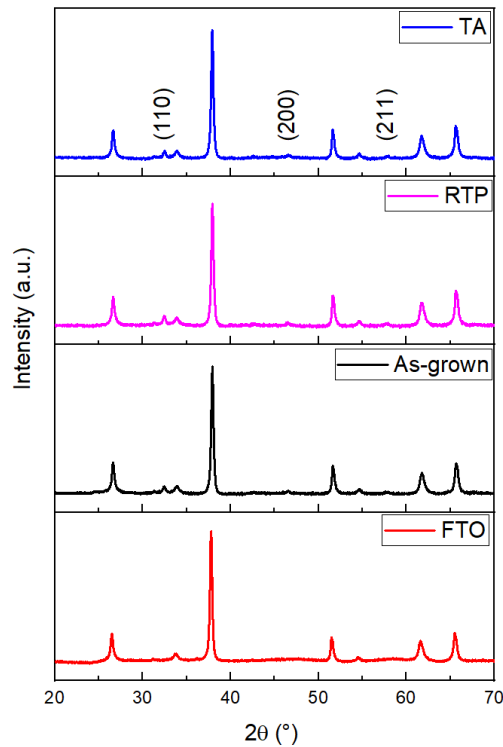
Figure III.9: XRD patterns of STFO depending on the additional thermal treatments

If the thin film has a preferred orientation that differs from that of the substrate, or if the thin film is randomly oriented (which is not the case in our situation), it may not generate diffraction peaks that align with those of the substrate. It is also noticeable that the three peaks of the oxide perovskite are visible here for (110), (200) and (211) orientation. Upon analysis, we were unable to observe the previously identified (111) and (220) planes. In addition, the identified peaks are quite small and it was not possible to calculate the FWHM as the peak of the diffraction exact points and inconsistency of fitting. This can be attributed to the diverse elements present in the crystal lattice of oxide perovskites, as well as their arrangement and varying symmetries. These factors can lead to a multitude of diffraction peaks in the XRD pattern, rendering them difficult to visualize[243].

Secondly, the impact of additional thermal treatment on the morphology of STFO thin films deposited on FTO has been investigated, as illustrates in Figure III.10. There is no significant difference in morphology between as-grown and RTP-treated films. While the grain size for TA is not significantly different, some grains exhibit cubic enlargement. In the previous section (III. 1. 1), we obtained different crystal sizes for as-grown STFO using the Scherrer formula. This is normal because the Scherrer formula focuses only one crystal (110 orientation for us), while AFM includes crystals on the entire surface. The XRD-based Scherrer formula assumes that the crystallites are well-formed and have a specific crystal structure. If the crystal structure is not known exactly or the material is not well crystalized, this can not affect the results. On the other hand, if particles have irregular shapes, AFM and SEM can capture the true morphology more effectively, providing a more accurate representation of their size.
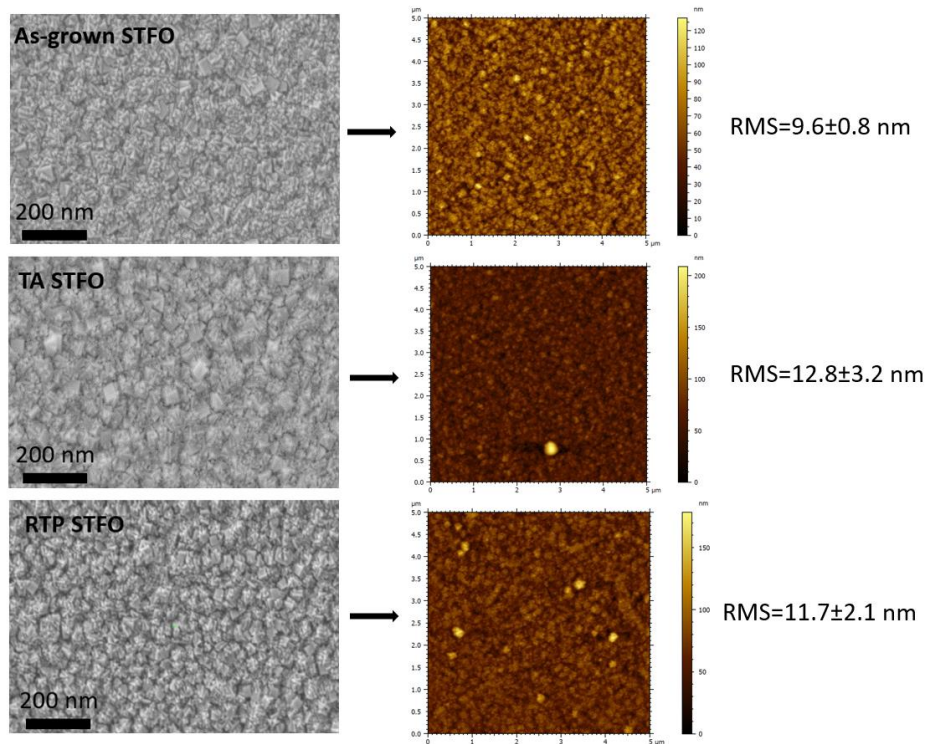
Figure III.10: SEM and AFM images in terms of the effect of additional thermal treatment on the STFO

The as-grown STFO thin film displays a highly uniform surface without much variation in the size of grains. With TA treatment, the increase in grain size was more consistent, but the growth in RTP has the largest variation. To elaborate further, RMS of TA and RTP 11.7±2.1 nm and 12.8±3.2 nm was observed, respectively. With thermal treatments, the RMS value slightly increased in as-grown STFO (9.6±0.8 nm). The difference in treatment time between TA and RTP is probably the main reason for the observed results. The RTP is very brief, which may cause uneven growth of all grains. It has been observed that the growth process of oxide perovskite particles varies depending on the specific elements used in their formulation. As a result, some grains may expand more than others, leading to a wider range of sizes. The morphology of the thin film, including surface roughness, grain size, overall structure changes, plays a crucial role in determining the characteristics of the film interacting with light.

III.2.2. Impact of Additional Thermal Annealing on Optical Properties

To ensure optimal performance of perovskite solar cells, it is crucial for the interlayer to shield the active layer from harmful UV light while still allowing visible light to penetrate. This necessitates the interlayer to have high transparency for visible light, allowing for maximum light absorption in the active layer. The optical correlation between 100 nm-thick STFO thin films deposited on FTO (during 20 minutes deposition by PLD) and annealing treatment is shown in Figure III.11. This fixed thickness value is chosen for optical characterization only, and the optimum value for the device application will be determined after.
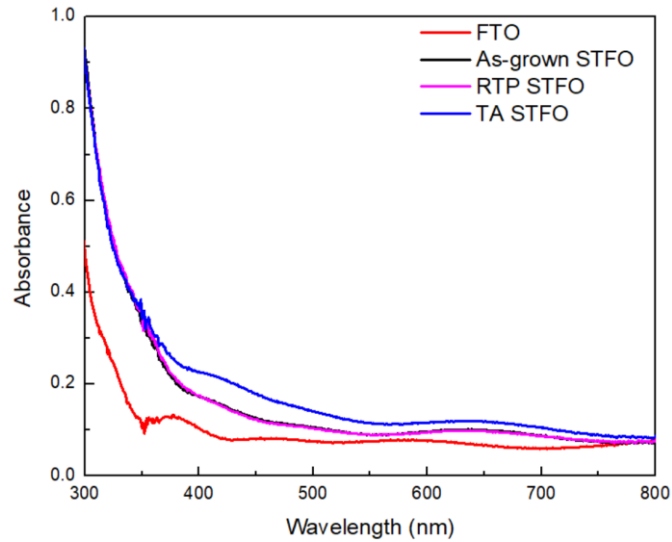
Figure III.11: Absorbance of STFO in relation to the annealing types

It is evident that all films have high transparency in the visible region, ranging between 70-80%. Specific oscillations across the spectrum are observed due to internal optical interference, indicating high-quality films. We observed a small decrease in transparency (~4%) of STFO after TA treatment compared to its as-grown and RTP counterparts. This trend has always existed and also the sample colors get darker after TA. Our prior report indicated an increase in grain size cubic expansions with TA treatment. Hence, the increase in surface roughness (from 9.6±0.8 nm to 11.7±2.1 nm) can scatter light in multiple directions, leading to reduced transparency. Scattering is typically associated with the hyperbolic absorption profile observed in TA[244]. After thermal treatments, the thin-film absorption or reflection coefficient may change due to the variation of stoichiometry under oxygen atmosphere, and it can be another reason for that case.

Noticeably, the sharpness of the Urbach tail increases within the wavelength range of 400-550 nm for TA. This is due to the presence of localized states within the bandgap, which may be caused by oxygen vacancies in the oxide perovskites. The localized states linked with the Urbach tail have the capability to capture charge carriers, which can impact the electrical properties and lifetime of the material. It is clear that the TA and RTP have different optical traps. Therefore, it is expected that the concentration of oxygen vacancies in the material is more important after RTP instead of the TA. This difference of oxygen vacancy concentration leads likely to the electrical properties of the material, in particular to a decrease in conductivity.

III.2.3. Impact of Additional Thermal Annealing on Electrical Properties

Space charge limited current (SCLC) is a widely used method to analyze charge transport. To accurately characterize the electrical properties such as conductivity and mobility here, it is crucial to understand how the applied electric fields affect the moving ions. The current in a solid is determined by both the intrinsic properties of the material and the carrier concentration gradients, which strongly depend on the trap density of states. The current density (J)-voltage (V) characteristics can help in studying the properties of electron and hole transport, injection and production of charge carriers. This analysis uses current injection as a probe to study the defect states in the bandgap of semiconductors and the mobility of the charge carriers[245]. It is commonly observed in insulators, wide bandgap semiconductors, and

weakly conducting polymers[246]. As the injection bias increases, the materials that exhibit SCLC can operate in several different modes, as shown in Figure III.12.
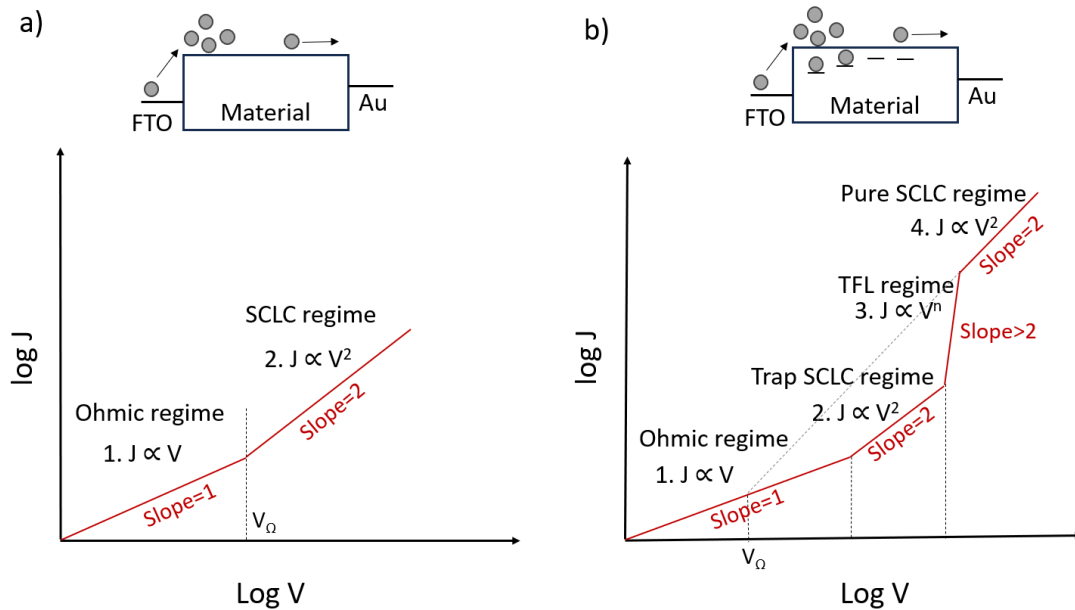
Figure III.12: Schematic statement of principle a) pure SCLC regime and b) trap-filled limited regime

There are two types of SCLC regimes. The first one (Figure III.12a) is a pure SCLC regime called trap-free, when the number of injected carriers is higher than the thermally generated carriers and impurities. At low voltages, the region displays ohmic behavior characterized by a linear relationship between voltage and current. Upon voltage increase, the transition from ohmic to second-order regime forms the voltage region, wherein charge injections still exceed traps. Trap density and mobility can not be extracted from this region with classical model[247].

The second type (Figure III.12b) is the trap-filled limited (TFL) regime, which is characterized by the presence of trap states. In this regime, it is possible to define multiple regions. It can be observed four different region:

1) Ohmic regime ($J \propto V$): The nature of the first region in the pure SCLC regime is identical to that of SCLC itself.

2) Trap SCLC regime ($J \propto V^2$): Unlike the pure SCLC, the traps are barreled and the size of the SCLC is greatly reduced due to the compression of the transport carriers in this quadratic region[248].

3) TFL regime ($J \propto V^n$, $n>2$): SCLC assumes that trap states are exponentially distributed at high voltages. After filling of the trap states due to increasing quasi-fermi level, there is a transition to the fourth region.

4) Pure SCLC regime ($J \propto V^2$): In this area, the majority of the charge injection occurs due to the saturation of traps with charge carriers leading to the estimation of intrinsic mobility of the material[249].

To determine the electrical conductivity (or resistivity) properties of the thin films by using SCLC model, the two-probe method was employed. This involves applying a voltage (V) across the film using two probes (one connected to the FTO electrode, one connected to a metallic electrode deposited on top of the layer) analyzing the resulting current (I) flow, as

represented in Figure III.13. The I-V characteristics of the material were obtained using a Keithley 2400 source meter with the device placed on a Linkam© HFS600E stage probes at room temperature in ambient air.
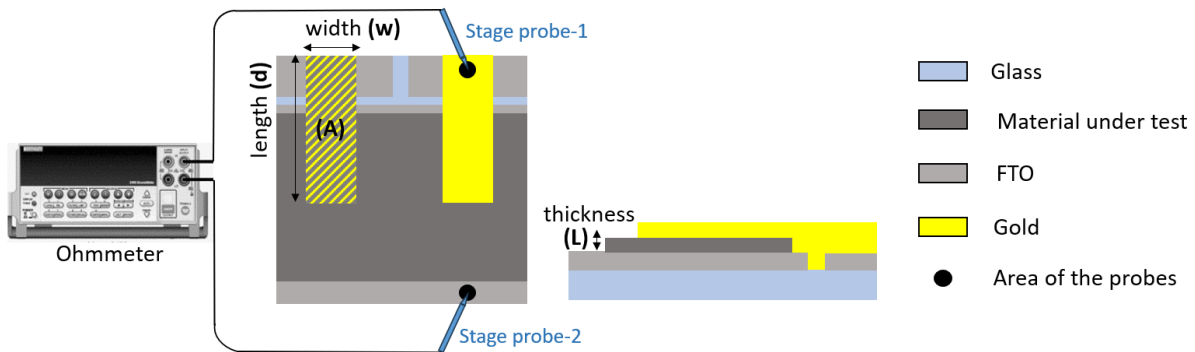
Figure III.13: The processing of two-probe method measurement with the sandwich structure configuration

The material is typically rectangular in shape and intended to create a sandwich structure with two parallel layers which are FTO and gold as the electrodes. A thin film that is to be measured is typically placed between two electrodes vertically in this structure (Figure III.13), where both schematic top and cross-sectional views of the sandwich structure, with probe areas indicating measurement locations for vertical transport. The electrodes in this structure comprise glass/FTO and gold. Although another metal can replace gold, it is preferred in our structure due to its stability and ease of deposition using vacuum thermal evaporation. The conductivity or resistivity of the sandwiched thin film is measured by applying a known voltage across its upper (gold) and lower electrodes (FTO) and measuring the resulting current. The sandwich structure provides a controlled and well-defined approach for experimental analysis. The distance between the electrodes and the size of the sample can be regulated, the contact resistance is minimized, and the geometry of this structure contributes to creating a more uniform electric field across the material.

Low conductivity or high resistivity thin films are typically measured using the four-point probe method. There are fundamental differences between four-point probe measurements and the two-point probe method, which make the former more accurate. Here are some of them. First of all, there is typically some electrical resistance between the contact probes and the material being measured or within the measuring equipment itself. The presence of these extra resistances results in an artificially higher resistance value for the material. Secondly, a potential problem for semiconductors is the modulation of sample resistance with applied current. A common issue is inaccurate sample resistance estimates due to the electrical properties of contact between metal electrodes and semiconductor samples[250]. Measuring thin films was not possible with the four-point probe method because of the resistance measurement capacity, so the two-point probe measurement was preferred. The two probes technics will allow us to measure specifically the transversal resistance (related to the volume), in contrast to four-probe which measure generally the lateral resistance (generally related to the grain boundary resistance). In the case of solar cell, our oxide will act as interfacial layer and transversal resistance will be crucial. We adjusted resistance values using an impedance system (see Appendix 2) to validate our two-probe system, so no impedance analysis will be presented in next parts.

The two-point probe resistivity of the material can be described in this case by:

$$\rho = R\frac{A}{L} = R\frac{w.d}{L} \qquad \text{Equation III.2}$$

where ρ is the resistivity in Ω.cm unit, and R is the resistance. L is the thickness, and A is the cross-sectional area, which can be calculated from the width (w) and length (d). The calculation of conductivity (σ) based on resistivity can be determined using Equation III.3:

$$\sigma = \frac{1}{\rho} \qquad \text{Equation III.3}$$

The purpose of this method is to fit a model to experimental J-V curves. The fitting is done by interpreting data obtained from single-carrier devices where only one type of charge carrier, either holes or electrons, dominates the current flow. Accordingly, the verifications of the working principle of the model based on Ohmic conduction[251], as shown in following equations:

$$J = \sigma.E \qquad \text{Equation III.4}$$

$$\frac{I}{A} = \sigma.\frac{V}{L} \qquad \text{Equation III.5}$$

$$V = I.\left(\frac{L}{\sigma.A}\right) \qquad \text{Equation III.6}$$

$$V \equiv I.R \qquad \text{Equation III.7}$$

Equation III.5, the electric field E is constant throughout the active area of the sandwich structure. After rewriting all variables in rounds, the rate of change of J and V is determined. In the following part, we will provide information on the material properties of FTO, and STFOs (as-grown, RTP, and TA), including resistance, resistivity, and conductivity. Also, we will interpret them using the SCLC method and derive mobility from it.

The FTO was the focus of the first investigation due to its widespread recognition. Measurements were taken at 0.05 V intervals using a continuous forward bias voltage ranging from 0 to 6V for all samples (symmetric ramps were first applied on the devices to identify the most suitable sweep direction in forward bias by minimizing the contact resistance and injection barriers). In this case, it can be difficult to determine which layer is being analyzed. The charge transfer and SCLC behavior can be significantly influenced by the interface material, which may become clearer after STFO analysis. It exhibits Ohmic or linear conduction with a compliance slope of about 1 due to microscopic behavior of electrons in metal during the forward scan at low bias, as depicted in Figure III.14. It can be said that in the case of $J \propto V$, the FTO follows Ohm's Law first principle related to Drude's model. It is a basic model used to explain conduction. It uses classical mechanics and considers the solid as a fixed array of ions that are not bound to electrons. The electrons do not interact with each other but are scattered by the ions[252].
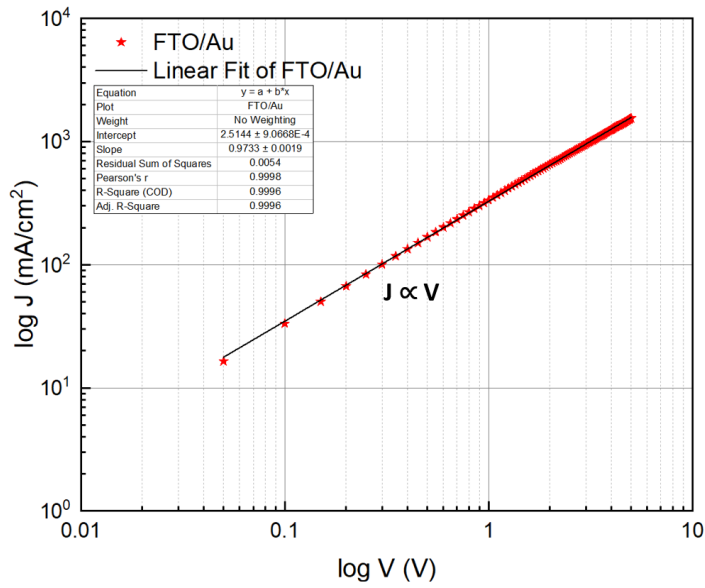
Figure III.14: Log-log scale J-V characteristics of FTO

The calculated resistance value of FTO is 21±1.00 Ω which will be called contact resistance as well. It is important to consider the resistance from the FTO when determining the actual electrical properties of the material being tested in the sandwich structure. Essentially, in order to determine the resistance of the material being tested, the contact resistance should be subtracted. The calculated resistivity and conductivity values are $2.25 \pm 1.10 \times 10^{-5}$ Ω.cm and $4.44 \pm 1.10 \times 10^{4}$ Ω.cm^{-1}, respectively and nearly identical with the literature[253]. The consistency of FTO allows to investigate the electrical properties of STFO thin films.

The J-V characteristics of STFO are depicted in Figure III.15, which represents the as-grown sample with a 100 nm-thick thin film. The resistance was measured to be 340±20 Ω. The literature's resistance value of STFO in our preferred specific stoichiometry ($SrTi_{0.7}Fe_{0.3}O_{3-\delta}$) is not clearly established. However, it has been reported that the resistance is reduced by several tens of kilohms through the Fe-doping process for STFO[254].
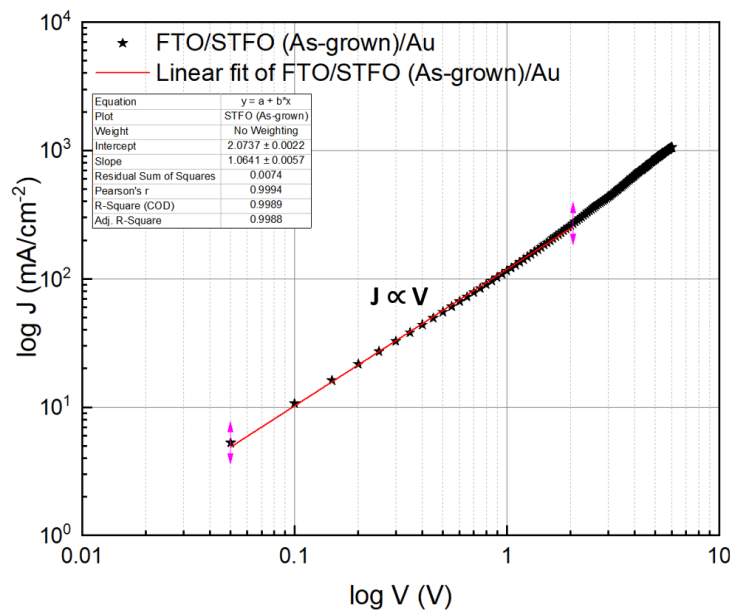
Figure III.15: Log-log scale J-V characteristics of STFO (as-grown)

The calculated values for resistivity and conductivity of as-grown STFO are $4.95\pm0.04\times10^6$ $\Omega.cm$ and $2.02\pm7.50\times10^{-7}$ $(\Omega.cm)^{-1}$, respectively. The calculated conductivity value agrees well with the literature. It has been reported that the conductivity of $SrTi_{1-x}Fe_xO_{3-\delta}$ for stoichiometries $x\leq5$ is around 10^{-7} $S.cm^{-1}$, while it increases for Fe>0.5[193]. It is mentioned that the Fe concentration be increased by at least 30% to ensure sufficient charge transfer as the interlayer. The slope value in the 2V to 6V range is not evaluated since it does not belong to either linear or SCLC regime. It is likely that an SCLC regime would be observed at higher voltage, but the drastic Joule effect prevented reaching such a regime for our case.

Figure III.16 shows that applying RTP on STFO results in different electrical properties compared to the as-grown STFO sample mentioned earlier. Here, we used the 100 nm STFO (RTP) sample, which is of equal thickness to as-grown.
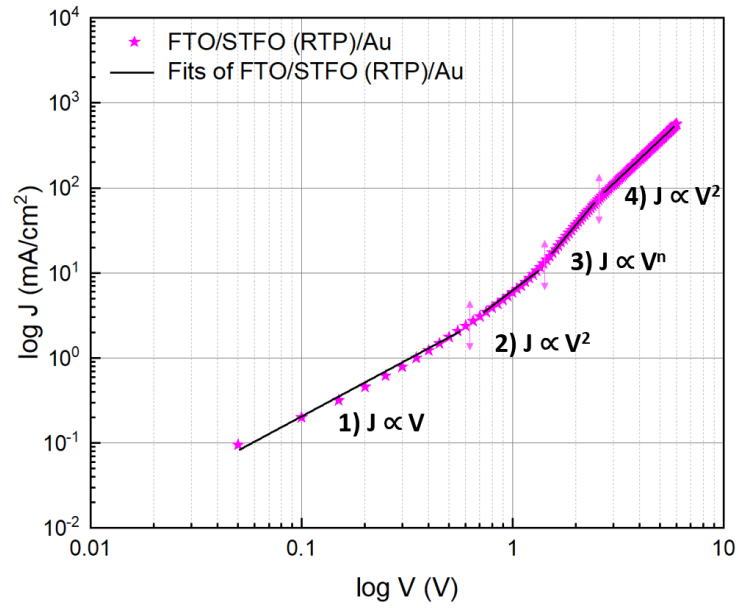
Figure III.16: Log-log scale J-V characteristics of STFO (RTP)

For the STFO (RTP) sample, four charge transport regions are visible, in relation with the presence of traps for this case. These four regimes are fitted (m is slope here) to their corresponding seminal laws, from which we extracted the related parameters as follow:

    i)   Ohmic regime ($J \propto V$), m=1.35,

    ii)   Trap SCLC regime ($J \propto V^2$), m=2.02,

    iii)   TFL regime ($J \propto V^n$, n>2), m=3, and

    iv)   Pure SCLC regime ($J \propto V^2$), m=2.10

In the ohmic regime, the resistance of STFO (RTP) sample is estimated at specified to be 3.5 ± 1.50 kΩ, which is considerably higher than the resistance of STFO (as-grown). In this region, the values of resistivity and conductivity are calculated to be $4.20\pm0.07\times10^7$ $\Omega.cm$ and $2.38\pm3.00\times10^{-8}$ $(\Omega.cm)^{-1}$, respectively. Additional thermal treatments can result in less resistive behavior by improved crystallinity, reduced defect densities in the structure and smoothing of the grain boundaries. These structural rearrangements usually enable charges to move more easily. However, we observe the opposite trend when RTP is applied on STFO films. It seems that after RTP, the status of defects changes. These defects could be related to alterations in the microstructure or oxygen vacancies. In RTP recipe, the system operates in a range of

atmospheric pressure to 5 mbar without inert gases. The STFO thin film is annealed when the pressure is 5 mbar and then brought back to atmospheric pressure. While annealing, the thin film is exposed to a lower pressure with a lower oxygen concentration at 550°C. This can cause changes in resistance by reducing the number of oxygen vacancies[255]. Previous studies have shown that microstructural changes occur slightly after RTP, which may be a reason for high resistance. Firstly, the increase in surface roughness of STFO after RTP can affect the contact resistance between materials leading to a change in its electrical resistance. Secondly, it is reasonable to hypothesize that the very short annealing time (100 seconds) was chosen to protect the substrate of FTO, but this rapid temperature rise may cause structural microcracks[256]. Therefore, to make more conclusive statements, atomic resolution imaging analyses with TEM (transmission electron microscopy) would be helpful.

When the charge carrier concentration is increasing with applied bias, the current characteristics switch from the Ohmic regime to the TFL regime. During this transition, the second region represents the shallow traps SCLC where charge carrier transport is limited by charge trapping with a low activation energy. Next, the space-charge effect occurs when the injected free carrier concentration exceeds the back-load carrier concentration in the TFL regime. This approach assumes that there are more traps than free charges[257]. The region's J-V characteristic exhibits a rapid increase in current density with applied voltage, including the injection barrier. When dealing with the region classified as the SCLC regime, the current density tends to conform to the Mott-Gurney law[258], as Equation III.8:

$$J = \frac{9}{8}\varepsilon_0\varepsilon_r\mu\frac{V^2}{d^3}$$

Equation III.8

where ε_0 is the permittivity of free space (8.854×10^{-12} F/m), ε is the dielectric constant of the material, μ is the charge-carrier mobility, V is the applied voltage, and d is the thickness in trap-states solid. Under standard conditions, the dielectric constant of STFO is 300[259]. When there are traps in the system, the flow of current follows the ohmic regime at low voltages. However, as the charge carriers become trapped, their mobility is limited and the system switches to the trap SCLC regime with quadratic gradient. When charges are injected, the quasi-fermi level of the charge carriers increases and the traps start to fill up until the TFL regime. In this case, it is evident that the space charge effect impacts the trap-filled confined TFL regime[257]. Once all the traps are filled, a pure SCLC regime is started. Even though there might still be traps present, they no longer impact the transport because the quasi-fermi level is too high and they are already filled with electrons[260]. If we examine the two fits from first region ($J \propto V$) to fourth region ($J \propto V^2$), their intercept voltage is 0.45 V and the calculated mobility is about 2.45×10^{-6} cm^{2}V^{-1}s^{-1}. When the mobility is limited, load carriers encounter greater resistance while moving through the material, resulting in increased resistance which is what we observe in this case.

Figure III.17 shows that applying TA to STFO produces similar electrical properties to STFO (RTP) but is different from those of as-grown STFO. In this case, it is preferred to have equal thickness and to use 100 nm-thick STFO (TA) sample for the measurement.
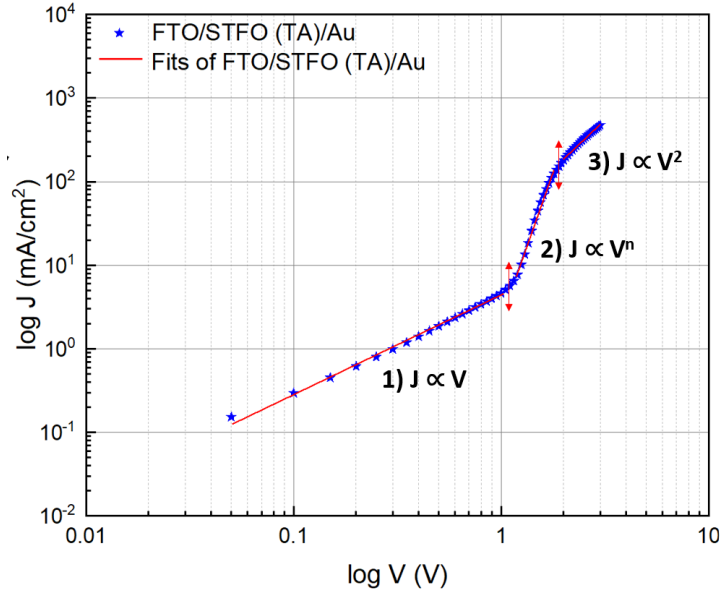
Figure III.17: Log-log scale J-V characteristics of STFO (TA)

For this sample, the presence of traps is observed, leading to three distinctive regions of current limitations:

i)   Ohmic regime (J ∝ V), m=1.21,

ii)   TFL regime (J ∝ Vn, n>2), m=7, and

iii) Pure SCLC regime (J ∝ V^2), m=2.25.

The resistance of STFO (TA) for Ohmic regime is determined to be 420±30 Ω, which is slightly higher than the as-grown STFO. However, the resistance increases lower when TA is applied, as than in the RTP application. The result remains consistent even if the measurements are repeated multiple times with different samples having same properties. The reasons behind this after annealing, as explained for RTP, are also applicable for TA. The increase in resistance in TA is comparatively small when compared to RTP, and it is more likely related to the previously determined increase in roughness, which leads to an increase in contact resistance between metal and STFO. However, in both annealing processes, which differ from each other in terms of process and duration, the resistance increase is more likely to be due to material-oriented reasons. This is because the annealing processes create oxygen vacancies, which lead to increase in defect concentration in the materials.

In Ohmic regime, the resistivity and conductivity have been calculated 2.24±0.15x10^5 Ω.cm and 4.47±0.23x10^{-6} (Ω.cm)$^{-1}$, respectively. TA has been found to slightly increase in the conductivity of STFO. The μ_{TA} value of 3.82x10^{-5} cm^{2}V^{-1}s^{-1} can be calculated for SCLC regime (V=0.2) by using Equation III.8. The second region has a steep incline with a slope of 7, which is associated with the filling of traps as the injection level increases (hence quasi-Fermi levels)[261]. The STFO (RTP) exhibits the shallow trap region, which is not present in STFO (TA) possibly due to different trap energy levels. Additionally, the high slope of STFO (TA) as it transitions to the TFL regime is a further evidence of distinct trap energy levels[262].

Table III.I summarizes electrical properties and SCLC behavior by material types. It is noted that the resistivity, conductivity and resistance values of STFO (RTP) and STFO (TA) have been calculated based on Ohmic regime. The electrical properties of materials vary naturally due to differences in the density of charge carriers and their mobility within the

material. There are significant differences in resistance among materials due to their intrinsic properties. Based on the comparison of STFO types, it has been observed that TA STFO exhibits higher conductivity than the others. Additionally, both RTP and TA exhibit similar behavior, which is primarily due to the observed increase in resistance from additional thermal annealing. As-grown STFO and TA STFO have suitable electrical properties for device application, while RTP STFO falls short of expectations as HTL due to its high resistivity.

Table III.I: Electrical properties of as-grown, RTP, and TA STFO

Electrical Properties	STFO (As-grown)	STFO (RTP)	STFO (TA)
Resistance (Ω)	340±20	$3.5±1.5 \times 10^3$	420±30
Resistivity (Ωcm)	$4.95±0.04 \times 10^6$	$4.20±0.07 \times 10^7$	$2.24±0.15 \times 10^5$
Conductivity (Ωcm)$^{-1}$	$2.02±7.50 \times 10^{-7}$	$2.38±3.00 \times 10^{-8}$	$4.47±0.23 \times 10^{-6}$
Mobility (cm^{2}V^{-1}s^{-1})	----	$\approx 2.45 \times 10^{-6}$	$\approx 3.82 \times 10^{-5}$
Principle of SCLC	Trap-free	Trap-Limited SCLC	Trap-Limited SCLC

III.3. Conclusion

In this chapter, we investigated the optimum conditions required for crystallization of the STFO thin film. The maximum temperature for damage-free FTO substrate correspond to 400°C and three different oxygen partial pressures (3×10^{-2}, 6×10^{-2}, and 9×10^{-2} mbar) have been tested, while keeping the heating temperature constant. The XRD pattern obtained at a pressure of $P_3 = 9 \times 10^{-2}$ mbar showed crystallization with polycrystalline thin film properties, characterized by narrower peaks. This feature was confirmed by SEM analysis, and we observed that higher oxygen partial pressure resulted in better changes in the microstructure and smoother, more homogenous surfaces with smaller grain sizes. Moreover, the crystal's chemical composition was free of impurities. The parameters of 9×10^{-2} mbar and 400°C were determined to be the most suitable for developing STFO thin films.

STFO thin film deposited on glass, glass/FTO, and sapphire always exhibit indirect and wide band gap semiconducting properties with energy band gap of 3.1 eV, 3.6 eV and 3.4 eV, respectively. However, if these materials are used as an interfacial layer where radiative band-to-band transitions are not required, the indirect bandgap does not need to be a limiting factor. The WF value obtained through the KPFM technique is 4.90±0.05 eV.

Two additional thermal treatments which are RTP and TA were applied to improve the structural, optical, and electrical properties of the thin film. It was challenging to differentiate the minor alterations observed in the microstructure with SEM and crystal structure with XRD analyses. The roughness of the thin film moderately increased after the thermal treatments. While some grains showed cubic expansion with TA, there were no apparent changes noted in the structural properties. Increased surface roughness with TA caused light to scatter in multiple directions, leading to decreased transparency of the thin film (confirmed with several same trends). However, it is important to note that the transparency of the as-grown, RTP and TA STFO thin films varies between 70-80% which is highly suitable for being the interfacial layer.

In analyzing the effect of additional thermal treatments on the electrical properties of STFO, it was found that as-grown STFO had trap-free, whereas STFO that underwent RTP

and TA exhibited trap-limited SCLC behavior. However, in the case of as-grown STFO, it was difficult to reach SCLC regime at higher voltage due to the severe joule effect. Interestingly, thin film resistance was observed to increase with RTP and TA, and this increase was particularly significant with RTP. The process of flash annealing raised concerns about the formation of microcracks, but it was found that the same situation occurred in TA as well, indicating that changes in oxygen vacancy concentrations were the likely cause. The vacuum system used during the RTP process can increase the number of oxygen vacancies to 5 mbar. Before drawing a definitive conclusion, deeper analysis is necessary. For instance, the identification of microcracks can be achieved through TEM, while the analysis of oxygen vacancies can be performed using Electron Paramagnetic Resonance (EPR). It was determined that thin films of STFO exhibited conductive properties, with conductivity increasing during TA, which is a promising result. During RTP, the conductivity decreased, indicating that RTP is not a suitable method for STFO type oxide perovskite.

When conducting SCLC analysis, it may be necessary to adopt multiple attitudes. Simulation programs such as SIMsalabim and Scaps should support these tests to ensure consistency and reliable results. In addition to investigating single-carrier devices like our case, the adjunct of the perovskite layers could provide right approach for predictable integration of new materials in optoelectronic devices.

Chapter IV. Fabrication of Perovskite Optoelectronic Devices

The purpose of this chapter is to provide comprehensive explanation of experimental processes involved in the fabrication of inverted halide perovskite solar cells and light emitting diodes.

After the reference devices have been developed, the p-type interlayer will be added to the device by depositing perovskite oxide through PLD. For the perovskite oxide to crystallize optimally, high temperatures (>400°C) are required. However, it is not feasible to deposit perovskite oxide using PLD at such temperatures in planar halide perovskite optoelectronic devices without causing damage or degradation to other interlayers. Therefore, inverted planar structures are preferred as a reference device architecture. Figure IV.1 displays the reference device structure of an inverted planar halide perovskite solar cell and LED. Despite their different operating principles, they share the same device structure with different materials.
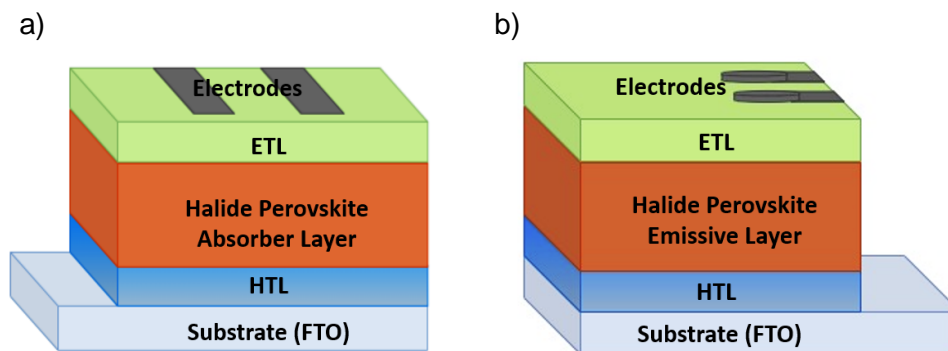
Figure IV.1 : Inverted planar halide perovskite a) solar cell and b) LED device structure

Transparent conductive oxides, such as FTO and ITO, are widely preferred in perovskite optoelectronics as the substrate. The most suitable substrate for our case is FTO in solar cell and LED. It is preferred over ITO due to its superior performance under our working conditions. The chemical composition of ITO causes it to melt faster than FTO at high temperatures in PLD system. ITO is a combination of indium oxide and tin oxide, with a typical composition ratio of 90% and 10%, respectively. The melting point of ITO is mainly affected by indium oxide. In contrast, FTO is also composed of tin oxide, but it has added fluorine, which makes it more stable at high temperatures and thus suitable for our working conditions.

In the first half of this chapter, we will explain how to develop the perovskite absorber layer for a reference halide perovskite solar cell from scratch. Then, we will discuss the selection of suitable materials and several optimization procedures for the device's interlayers. Lastly, we will outline the methodology for designing and fabricating the corresponding multilayer devices.

In the second part of this chapter, we will explore the properties of reference halide perovskite light-emitting diodes that were developed in our lab, as well as the materials employed in the interlayers. Unlike with solar cells, we will not discuss any optimization by applying an already existing and developed recipe. Additionally, we will provide a detailed description of the methodology used for designing and fabricating these multilayer devices.

IV.1. Reference Halide Perovskite Solar Cells

IV.1.1. Experimental Background of Halide Perovskite Solar Cells

The biggest challenge facing the commercialization of halide perovskite-based PCSs are their instability. In addition to charge transport layers, increasing the thermal stability of halide perovskite thin films is also crucial. One way to achieve this is through careful design of perovskite composition. Studies have shown that FAPI-based PSCs retain 85% of their initial PCE even after being thermally stressed at 85 °C for 400 hours[263]. The metastability of black cubic α-FAPbI$_3$ at room temperature has been found to be a crucial challenge in the first years of its development. It has been established that the incorporation of organic methylammonium (MA$^+$) or inorganic cesium (Cs$^+$) into the A-site or substitution of bromine (Br$^-$) or chlorine (Cl-) into the X site can result in more stable and efficient photocurrent generation. There have been numerous reports in the perovskite research community that the incorporation of Cs$^+$ and Br$^-$ can effectively suppress the unwanted yellow phase of unconverted PbI$_2$, thereby stabilizing the black colored α-FAPbI$_3$ phase[264][265]. Adding a small amount of Cs$^+$ to the pure FAPbI$_3$ structure makes it more stable than unsubstituted FAPbI$_3$. The perovskite structure allows for precise control over the bandgap by selecting different cations. Since each cation has a unique electronic configuration, its interaction with the other side's ions can alter the energy levels of electronic bands in the material. Introducing Br$^-$ to the halide site is a well-known method for producing higher band gap perovskites (ranging from 1.5 eV to 1.7 eV). This alteration to the material's structure and morphology directly affects its electrical and optical properties[266]. FA$_{0.85}$Cs$_{0.15}$Pb(I$_{0.85}$Br$_{0.15}$)$_3$ was chosen due to the fundamental reasons that favored the perovskite-type. We preferred to use the formamidinium lead iodide-based perovskite absorber layer with mixed cations and mixed halide (FA$_{0.85}$Cs$_{0.15}$Pb(I$_{0.85}$Br$_{0.15}$)$_3$) in for our reference devices, as it was extensively used in our past studies[267]–[269].

Figure IV.2 presents the absorption spectrum of a typical 500 nm-thick FA$_{0.85}$Cs$_{0.15}$Pb(I$_{0.85}$Br$_{0.15}$)$_3$ (more easily named CsFAPbIBr) halide perovskite thin film on FTO, which exhibits the typical absorption spectrum of FAPI. The second absorption edge is observed at 780 nm. Moreover, the Tauc's plot indicates a band gap of 1.60 eV, demonstrating consistency with the observed absorption spectrum.
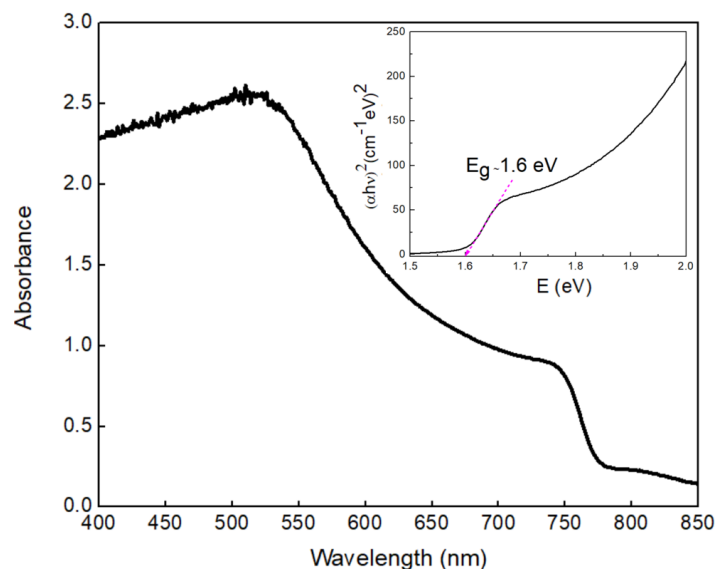
Figure IV.2 : Absorbance spectra of FA$_{0.85}$Cs$_{0.15}$Pb(I$_{0.85}$Br$_{0.15}$)$_3$ perovskite (or CsFAPbIBr) and its Tauc's plot in inset

A cross-section SEM image of the halide perovskite displays no pinholes and exhibits well-defined crystallization, as shown in Figure IV.3. Larger grains generally lead to more efficient solar cells due to reduced trap-densities, hence reduced charge recombination. One positive aspect is that the grain boundaries are not clearly noticeable at this observation scale, although some grain boundaries are already visible. The presence of grain boundaries can create trap states in the perovskite material's band gap, which impede charge carrier movement, leading to decreased performance.
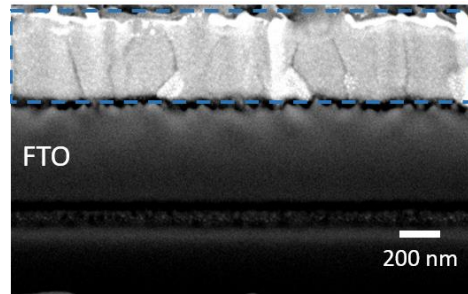
Figure IV.3 : Cross-section SEM image of $FA_{0.85}Cs_{0.15}Pb(I_{0.85}Br_{0.15})_3$ perovskite on FTO

Our team has previously achieved reproducible and is well-performing devices using spiro-OMeTAD-based planar structures as an HTL[267]. This device structure is FTO/SnO$_2$/ CsFAPbIBr/Spiro-OMeTAD/Au. First of all, a set of devices was repeated to check that active layer in the planar structure still performs the same with high current density and decent efficiencies. The performance of the champion cell from this set of device is shown in Figure IV.4. Although no device optimization was applied, the obtained high current density is comparable to devices with the same structure in literature[270][271], indicating that our active layer still well-performing.

	Forward	Reverse
V_{oc} (V)	0.97	0.91
J_{sc} (mA.cm^{-2})	24.82	23.52
FF	0.58	0.51
η (%)	14.17	11.41
R_s (Ω)	24.47	30.3
R_{sh} (Ω)	5336.96	2378.15
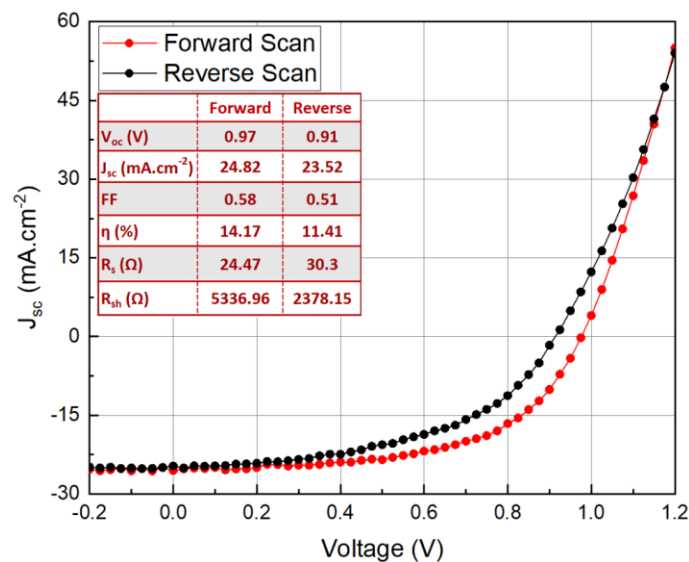
Figure IV.4 : J-V characteristics of a planar device structure with spiro-OMeTAD as HTL

To transition from planar to inverted planar structure, the same materials were utilized with reverse order deposition. However, when coating halide perovskite on spiro-OMeTAD during the transition from planar structure to inverted planar structure, this leads to unfavorable results. In this case, spiro-OMeTAD encountered the issue of redissolution in polar solvents, such as DMF and DMSO, due to their different molecular polarities and solvent selectivity[272]. CuSCN is often used to replace spiro-OMeTAD due to its favorable band positions in the same

structure[273]. This is why we chose CuSCN as a starting point to solve redissolution issue and fabricate FTO/SnO$_2$/CsFAPbIBr/CuSCN/Au device structure. The performance of the champion device after replacing spiro-OMeTAD with CuSCN is presented in Figure IV.5. Although preliminary and without optimization of device, these findings demonstrate that CuSCN has potential for higher performance. Its fill factor (FF) is comparable to the literature[274], indicating that it can be further improved.
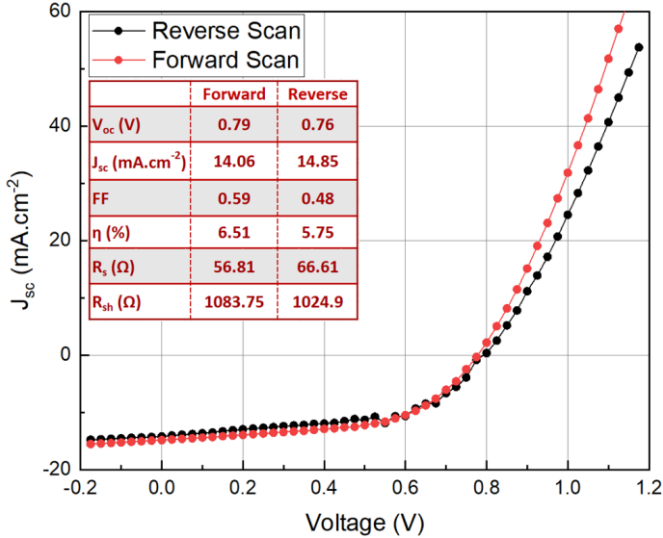
Figure IV.5 : J-V characteristics of a planar device structure with CuSCN as HTL

The PV performance of 8 devices fabricated in the same batch with spiro-OMeTAD and CuSCN in planar structure are shown in Figure IV.6.
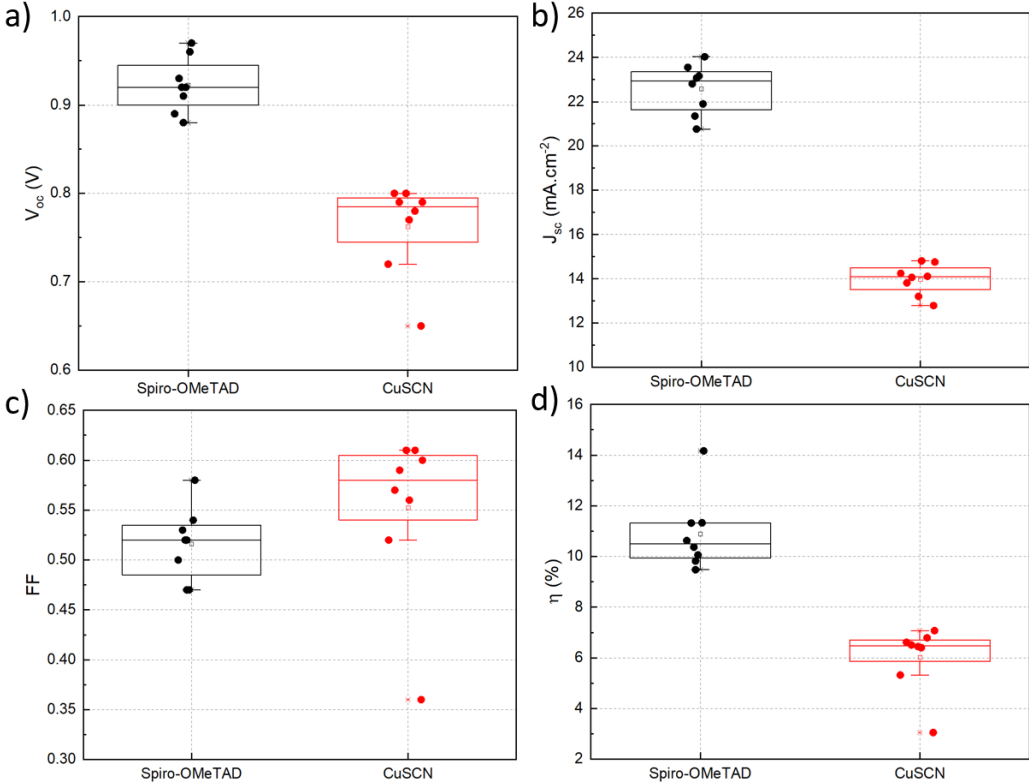
Figure IV.6 : Statistical properties of PV performance parameters (a) V$_{oc}$, b) J$_{sc}$, c) FF, and d) η) based on 8 cells with spiro-OMeTAD and CuSCN as HTL in planar structure

We have successfully fabricated devices with reproducible performances for both materials. The typical J_{sc} range for spiro-OMeTAD is 21-24 mA.cm^{-2}, while for CuSCN it is 13-15 mA.cm^{-2}. This indicates that spiro-OMeTAD performs better than CuSCN. However, when CuSCN comes into contact with Au, it can cause the device to decompose, leading to lower performance. To prevent direct contact between CuSCN and Au, interfacial layers such as carbon are often added between them for planar structure[275]. While spiro-OMeTAD has been extensively studied, CuSCN shows promising results but requires some optimization to reach its full potential. Once we achieve reproducibility with CuSCN, we can shift our main focus to transitioning to the inverted planar structure without having to optimize for the planar structure. Since the performance of the halide perovskite type has been proven in these studies, optimization work only focuses on the HTL, ETL, and electrodes for inverted planar structure.

IV.1.1.1. Optimization of Hole Transport Layer

Shifting from direct to inverted device architectures brought many challenges in our studies because this is the first time inverted structure has been studied in our laboratory. The first issue was the low wettability of the CuSCN surface. Halide perovskite films of smaller grain and less crystalized often result from polarity mismatch the halide perovskite precursor solution and the underlying contact materials, as shown in Figure IV.7. We applied a DMF solvent coating on the surface to solve this issue and then annealed the sample at 100°C for 10 minutes. Coating the surface with a solvent such as DMF can enhance its wettability by reducing the contact angle[276] (not shown here) of the precursor solution, which ensures that it spreads uniformly. After cooling, the surface coverage of halide perovskite was more homogenous and well-covered except for the sides of FTO. Following that, additional issues emerged. The degradation of the halide perovskite structure becomes evident on the surface as soon as the FTO/CuSCN/halide perovskite structure is left in the glove box for a day.

Figure IV.7 : The wettability of CuSCN and fast degradation problem of halide perovskites

Inhomogeneous material repartitioning of CuSCN was observed in the majority of a set of samples after solvent evaporation. However, it was integrated into the device as HTL in order to observe in-device characteristics. The device structure preferred in Zhao et al.'s study[274] is as follows: FTO/CuSCN/FA$_{0.85}$Cs$_{0.15}$Pb(I$_{0.85}$Br$_{0.15}$)$_3$/PC$_{61}$BM/Al. PC$_{61}$BM as the ETL material and aluminum as the preferred electrode material were used. The corresponding devices have been characterized both in the dark and under calibrated solar simulator (100 mW.cm^{-2}, AM1.5G) inside the glove box with nitrogen filled atmosphere. The devices did not shown any illumination performance, as shown in Figure IV.8. Moreover, low current density (~10^2 mA.cm^{-2}) was obtained in the dark conditions (inset Figure IV.8).
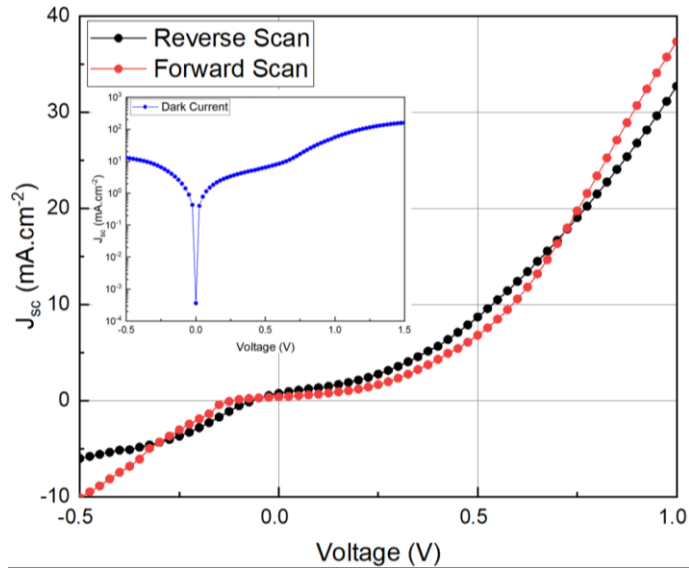
Figure IV.8 : J-V characteristic of CuSCN-based device as HTL; inset: dark current in semi-log scale

The reason behind this performance can be instability of the perovskite absorber and CuSCN heterojunction, even in dry nitrogen atmosphere, and the development of an interfacial degradation mechanism. The issue is that most solvents with high solubility for CuSCN tend to disrupt the perovskite layer[277]. The interaction between two materials (shown in Figure IV.7) is responsible for this mechanism, which leads to the non-performance of the device. The fact that CuSCN material easily leads to halide perovskite degradation has been reported as a common problem in the literature[151], as we mentioned on it at Chapter 1. To improve the performance and stability of perovskite layers, it is important to add an extra layer between the perovskite layer and CuSCN[278]. It was determined that CuSCN was not a suitable candidate for HTL due to various issues. Therefore, other alternatives will be investigated.

As a next step, the structure developed by Yaoguang et al.[279] is taken as a reference. The device architecture (in Figure IV.9a) based on the use of PEDOT:PSS as the HTL and PC$_{61}$BM as the ETL were was selected. The energy levels of the selected materials (Figure IV.9b) are typical values obtained from literature[280].
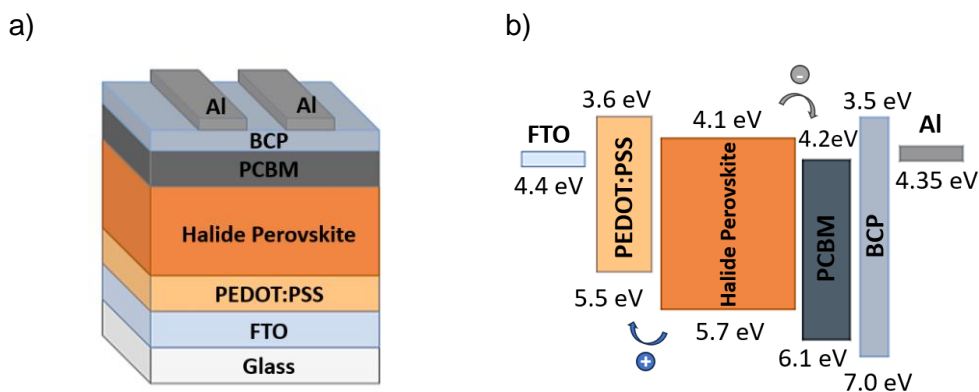
Figure IV.9 :PSC's a) device architecture and b) energy-band diagram

The suitable electrode for this purpose is aluminum (Al), due to its relatively low work function (WF$_{Al}$=4.35 eV) function required for efficient electron extraction. Aluminum is separated from the PC$_{61}$BM ETL by an extremely thin BCP (bathocuproine) interlayer. This interlayer's purpose is to create a barrier to enhance electron extraction and to block exciton

thanks to having a deep-lying HOMO and LUMO, which are 7.0 eV and 3.5 eV, respectively[281]. It is crucial that the thickness of the BCP interlayer does not exceed 5 nm, as it may act as an insulator otherwise[282].

The PCE obtained for this structure was <1%, much lower than reported in literature[283][284]. The J-V measurements especially showed low FF (0.2), J_{sc} (~5 mA.cm^{-2}) and quite high R_s (~10^3 Ω) but low hysteresis. These issues are mainly caused by a high level of recombination, which may result from crystal defects or harmful impurities. This can be due to the active layer properties, defects in the interfaces, inadequacy of charge transport layers, and the blocking effect of some inappropriate energy landscapes that may occur[285]. The main focus of this section is to address HTL's concerns, such as the inadequacy of the charge transport layer with high recombination.

Low J_{sc} often results from PEDOT:PSS-based devices due to mismatched energy band alignments with halide perovskites. Additionally, its highly doped nature leads to high interfacial recombination[286], which may be associated with poor HTL properties. We first attempted to use 2PACz as an alternative hole transport material for PEDOT:PSS, which is a self-assembled monolayer commonly used to create high J_{sc} devices. In this part, we examine the properties of HTL materials deposited using two different methods - dip-coating and spin-coating, particularly for 2PACz. According to the literature, both methods produce similar characteristics in the thin film and are expected to achieve the same level of device performance[117]. Considering the ultra-thin characteristics of SAM on top of substrates, one efficient way to evidence that efficient surface modification was achieved is the use of contact angle measurement, which emphasizes the wettability (hydrophilic or hydrophobic nature) of the surface before and after deposition of the monolayer.

A comparison of surface wettability of deposition methods for 2PACz and PEDOT:PSS on FTO substrate was conducted by using contact angle measurement (see Appendix 2) of a water droplet, as illustrated in Figure IV.10.
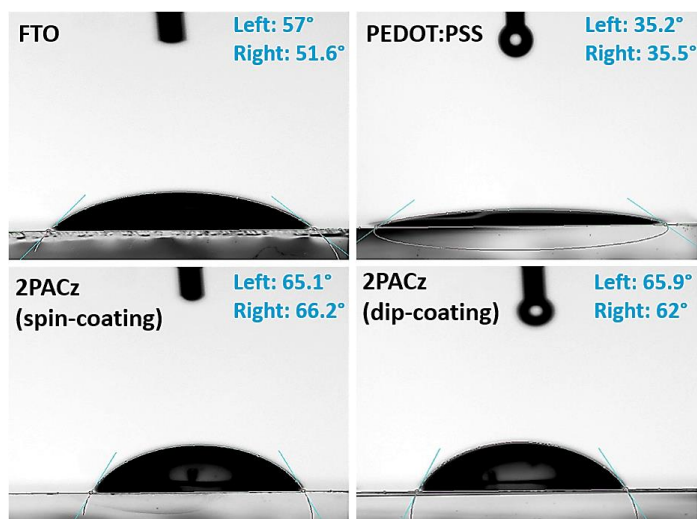
Figure IV.10 : Contact angles of FTO, PEDOT:PSS, and 2PACz (spin-coating and dip-coating)

The contact angle between a liquid and a surface is governed by the interaction energies involved, and therefore depends on both the liquid properties and the surface properties[287]. We evidence similar behaviors for 2PACz deposited on top of FTO by spin-coating or dip-coating from Figure IV.10. The very clear change of contact angle with 2PACz compared to FTO indicates that a relevant surface modification is achieved by the SAM

deposition. Moreover, the wetting properties of water on 2PACz are significantly distinct than those on PEDOT:PSS. A higher contact angle means that the material has a lower surface energy. Materials with low surface energy tend to repel liquids, while materials with high surface energy promote wetting. In comparison to 2PACz, PEDOT:PSS displays hydrophilic properties with a higher surface energy than 2PACz. Hydrophily reduces the lifespan of halide perovskite under certain external factors, such as humidity[288].

We then compared the optical properties difference between FTO/PEDOT:PSS and 2-PACz-treated FTO substrate by optical absorption measurements, as shown in Figure IV.11. When a photon of a certain wavelength interacts with an material, it can excite electrons to higher energy levels or excite them into conduction bands. The energy required for these transitions corresponds to specific wavelengths of light[289]. Additionally, the interaction of a material with light can be impacted by its microstructure or surface morphology. Surface roughness and microstructural defects can scatter and absorb light, leading to transmission and reflection properties changes.
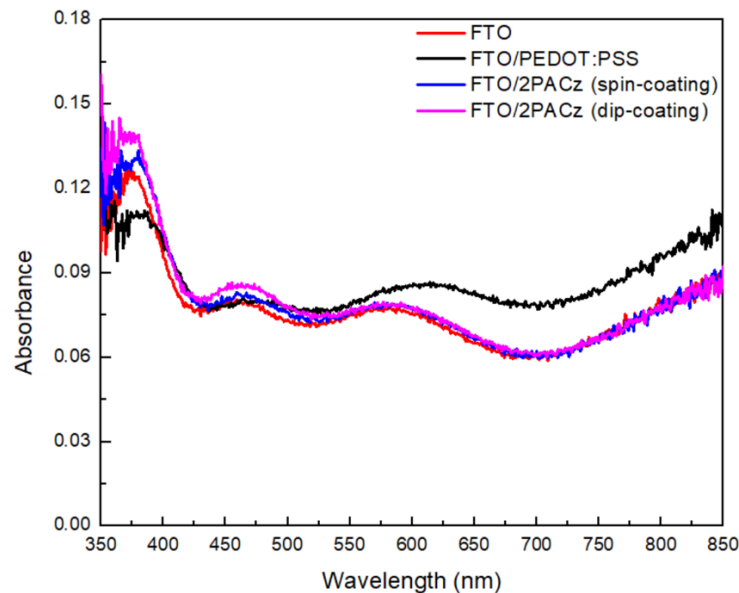
Figure IV.11: Absorbance spectra of PEDOT:PSS and 2PACz (spin-coating and dip-coating)

The results of absorbance measurements (in Figure IV.11) carried out before and after SAM functionalization indicate that there was a slightly higher absorbance in the presence of 2PACz as compared to bare FTO. While this is a clue to the existence/association/self-assembly of SAM formation, it is not enough. Other spectroscopic techniques (e.g. FT-IR) may be more relevant. The FTO/2PACz demonstrated higher absorbance than FTO/PEDOT:PSS within the UV region (350-400 nm range). Furthermore, dip-coated 2PACz exhibits higher absorbance, possibly due to the higher density of the molecules resulting from the concentration of the solution. This is expected to be advantageous in protecting the overall perovskite from UV-light. The PEDOT:PSS thin film reduces the amount of light that passes through in the 550-850 nm wavelength range by absorbing it slightly, unlike FTO. The Urbach tails exhibit a sharper exponential increase in 2PACz types, indicating weaker or disorder crystallinity.

The dip-coating may be more practical for large-area applications, while spin-coating provides precise control over film properties for small-scale like research-oriented studies. While dip-coating and spin-coating require different concentrations (0.01 mmol/L and 1

mmol/L, respectively), dip-coating requires more solution to fill the processing vessel during the deposition. Using spin-coating is a more cost-effective method than dip-coating. Moreover, dip-coating takes more time to deposit 2PACz as the growth of the grafting film can be slow with SAM-based materials. Therefore, for future studies, the decision was made to use 2PACz deposited by the spin-coater.

The XRD patterns of PEDOT:PSS and 2PACz indicate that they have distinct crystal structures, as shown in Figure IV.12. The FTO substrate displays only three diffraction peaks, at 26.5°, 34.1° and 37.7°.
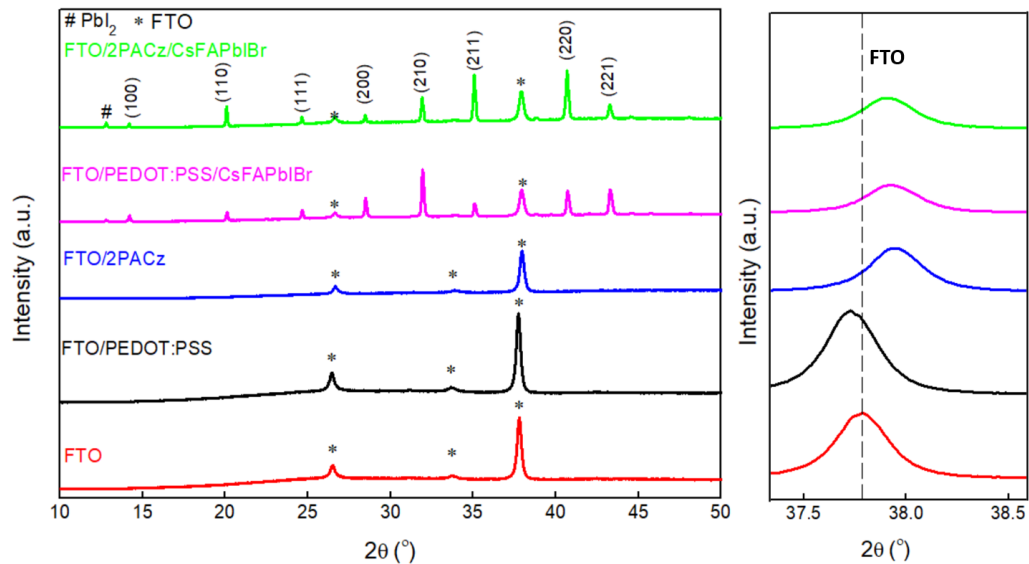
Figure IV.12 : XRD patterns of PEDOT:PSS and 2PACz on their own and with halide perovskite indexed

The diffraction peaks of FTO substrates and FTO/PEDOT:PSS substrates are almost identical due to the amorphous nature of PEDOT:PSS layer. The difference in structure could lead to mismatches when grown on the FTO (on the right side of Figure IV.12). The orientation of the substrate and the grown material can be influenced by the symmetry and lattice constants. This often results in the material adopting a different crystallographic orientation compared to the substrate. Growth on a substrate can subject the material to stress and strain, leading to modification in cell parameters. It is interesting to note that there is a peak shift in the FTO/2PACz structure, even though 2PACz is a monolayer. This finding is not common but present in the literature for ITO substrate[290]. But there has been no statement regarding this matter.

The choice of the PEDOT:PSS and 2PACz can significantly impact the interactions between the halide perovskite (CsFAPbIBr here), which in turn can affect the orientation of halide perovskite crystals deposited on top. The kinetics of the growth process can favor different crystal orientations with different HTLs. Additionally, the surface morphology and roughness of the HTL can affect the nucleation and growth of halide perovskite crystals, leading to further variation in crystal orientation. The small peak at $2\theta = 12.8°$ indicates trace amounts of PbI_2 in both samples. The characteristics features of the CsFAPbIBr layer are observed (in Figure IV.12), indicating mainly the presence of the α-FAPI phase. The halide perovskite peak around 14° can be observed in both perovskite films deposited on different HTLs at the same 2θ position. This peak is an indication of the favorable black phase of the formamidinium-based perovskite and is attributed to the (100) planes[291]. This contribution is

narrower and stronger when the halide perovskite is deposited on PEDOT:PSS, compared to 2PACz which demonstrates that crystallization on PEDOT:PSS is more favorable than on 2-PACz in our case.

Devices were finally processed using either PEDOT:PSS or 2PACz HTL, using the FTO/HTL/CsFAPbIBr/PC$_{61}$BM/BCP/Al structure. However, we were unable to obtain functioning devices of either type. There could be several underlying reasons that may have caused the main issues in this situation and we will try to eliminate them one by one. First of all, during the development of 2PACz, it has been identified that certain surface treatment are necessary because of the poor wettability. After coating the 2PACz solution on the FTO (Figure IV.13a), the deposited 2PACz surface must be washed with IPA (isopropyl alcohol) (Figure IV.13b) using a spin-coater before annealing.
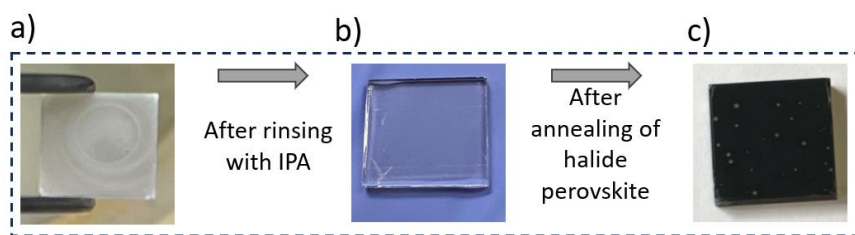
Figure IV.13 : The deposition process of a) deposited 2PACz, b) after rinsing, and c) issue for halide perovskite

Specifically, the process of depositing 2PACz using a spin-coater, followed by thermal annealing, etching for preparation of halide perovskite deposition, is quite challenging. The etching process should be applied before and after annealing to avoid potential short circuits. This is in contrast to standard HTLs like PEDOT:PSS, where etching is done just before annealing. It is important to handle 2PACz with care as it may easily bring shortcuts in the device. Another issue is related to the fact that small white dots can appear on the halide perovskite surface after thermal annealing (in Figure IV.13), but their origin is still unclear. The deposition process for 2PACz requires further development as the short-circuit limitation was not fully addressed and the control of the halide perovskite deposition surface quality is inconsistent. In fact, we did not have the opportunity to conduct a full optimization procedure during this PhD using this novel material. For the next steps, we will continue to work with PEDOT:PSS as the HTL, which is widely used in our laboratory for perovskite LED and OPV and easy to handle. Our next goal is to focus on the enhancement of metal electrode and ETL optimization.

IV.1.1.2. Optimization of Metal Electrode

The aluminum electrode is another factor contributing to the issue related to non-working devices from the beginning due to two main reasons. Firstly, the deposition rate control during thermal evaporation of Al is highly variable and very high in some points, which can lead to the diffusion of Al into the ETL and then into the perovskite layer[292]. The tungsten crucible can even break down due to the variability and difficulty in controlling the Al deposition rate. Secondly, halide ions on the surface of the perovskite layer are more active in redox reactions and may even corrode the contact electrodes. This degradation process starts with interfacial instability, which is evident from the high series resistance of the devices. Because mobile halide ions can easily migrate through the ETL (PC$_{61}$BM for us) to the metal electrode and get a form of insulating metal halide compound (such as Al-iodine), which contains the inner surface of the metal electrodes[293]. This situation results in ineffective charge collection

or recombination, causing a low J_{sc} due to blocking effects at low charge collection. Depending on the non-functioning device or very low performance with either PEDOT:PSS or 2PACz HTLs, we will replace the metal electrode because of the problem that we mentioned (high R_s and low J_{sc}).

At this stage, the electrode was replaced with Ag while keeping the device structure (FTO/PEDOT:PSS/CsFAPbIBr/PC$_{61}$BM/BCP/Metal electrode) unchanged. Al has a slight challenge with its higher work function (WF$_{Al}$= 4.35 eV), whereas Ag has a lower work function (WF$_{Ag}$= 4.26 eV). This can be beneficial for extracting and collecting electrons for ETL. Ag is an outstanding electrical conductor and is often preferred due to its high conductivity (σ_{Ag}=0.63x10^6 Ω.cm), which allows efficient charge collection and transport in solar cells. Although also a good conductor, Al has lower electrical conductivity than Ag (σ_{Al}=0.37x10^6 Ω.cm), which can result in slightly higher resistance losses in the device. Figure IV.14 shows the J-V characteristics of devices under solar simulation, both in forward and reverse scan directions. Table IV.I shows the performance parameters of this measurement.
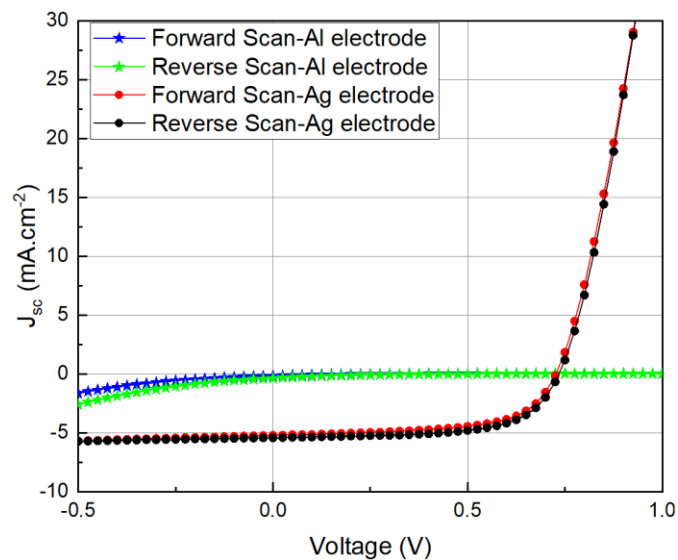
Figure IV.14 : J-V characteristics of device with Al and Ag electrodes

Table IV.I : PV performance parameters of device with a) Al and b) Ag electrodes

a)

	Forward	Reverse
V_{oc} (V)	0.44	0.55
J_{sc} (mA.cm^{-2})	0.15	0.39
FF	0.12	0.11
η (%)	0.01	0.02
R_s (Ω)	67x10^3	49x10^3
R_{sh} (Ω)	6252.01	2841.12

b)

	Forward	Reverse
V_{oc} (V)	0.71	0.72
J_{sc} (mA.cm^{-2})	5.21	5.41
FF	0.63	0.65
η (%)	2.33	2.53
R_s (Ω)	18.29	16.03
R_{sh} (Ω)	2918.21	3121.67

We have observed significant advancements in the development of devices based on Ag. The high series resistance in the Al-based device clearly reveals the blockage in the device. As a first observation, low hysteresis can be noticeable for both, as expected from inverted planar structures. The low PCE of approximately 2.5% may be attributed to low J_{sc}, despite the improvement in FF after the electrode change. Also, expected V_{oc} of inverted architectures can be expected above 0.9 V under normal conditions, but our structure reaches only 0.72 V. A well-crystallized absorber layer and its interface with other interlayers is important to achieve a higher V_{oc} corresponding to the natural bandgap of the FAPI-based perovskites[294]. If the interlayer is problematic, one of the indications is having a lower V_{oc} than normal. As a result, the Ag electrode is more favorable for its higher R_{sh}, lower R_s and therefore higher V_{oc} in the device. After optimizing the HTL and electrode, the next step is to optimize the ETL.

IV.1.1.3. Optimization of Electron Transport Layer

Exploring alternatives for ETLs in PSCs beyond TiO_2, SnO_2, ZnO, graphene, graphene oxide and P3HT polymers can be preferred. However, not all of these types are suitable for inverted planar structures. For instance, TiO_2, graphene, or graphene oxides are compatible with planar structures, but ETLs like nanoparticles of SnO_2 and ZnO can cause degradation when deposited on halide perovskite, because their solvent can dissolve on the halide perovskite as in Figure IV.15. It is advisable to consider other options as well.
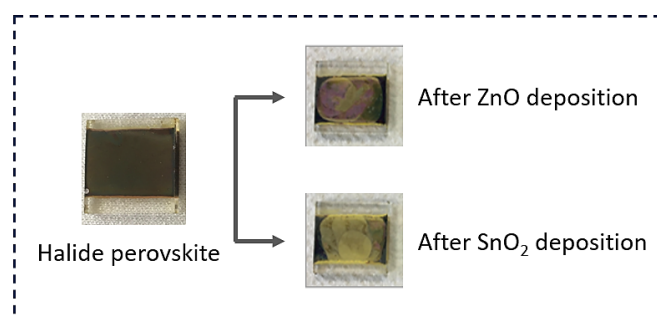
Figure IV.15 : The halide perovskite degradation after deposition of ZnO and SnO_2 on top

$PC_{61}BM$ (Phenyl-C_{61}-butyric acid methyl ester) is a widely used acceptor material in organic photovoltaics[295] and electron transport material in PSCs[296]. It has a good solubility in organic solvents such as chlorobenzene or toluene which are unable to dissolve perovskites. Hence, it is a popular choice for use in PSCs. This material was initially tested with PEDOT:PSS, which is commonly used in traditional recipes[297] for our research. However, we will now analyze it from a problem solving perspective.

PCBM-types (i.e. $PC_{61}BM$ and $PC_{71}BM$) present several challenges, such as limited absorption, high price, inherent tendency to agglomerate, and relatively stable structure and properties. Using pure fullerenes results in agglomeration and poor film morphology due to their strong crystallization tendency. Given this possibility of the material, a direct contact between the HTL (PEDOT:PSS) and the ETL ($PC_{61}BM$) can take into account for low J_{sc}. The device structure was cross-sectioned to check for parasitic circuits, crystallization quality, and layer thickness against optimal conditions, as shown in Figure IV.16.
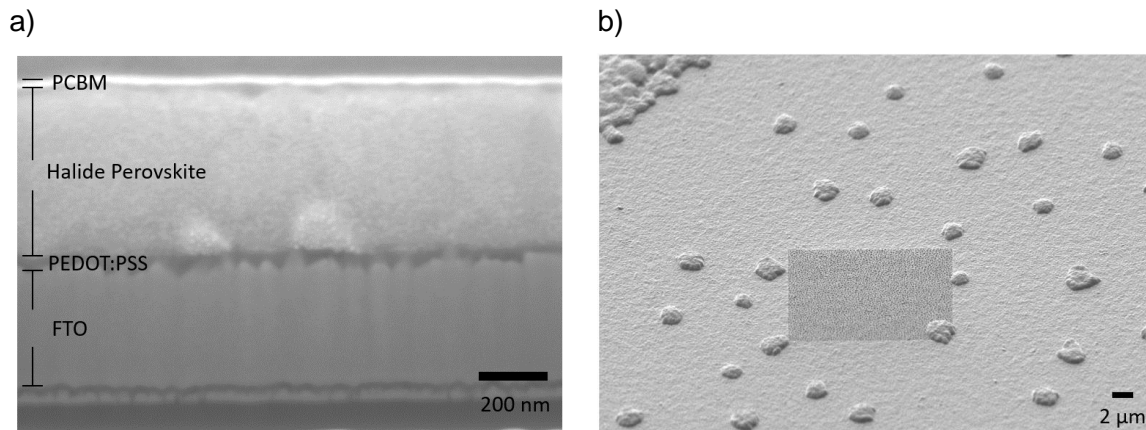
Figure IV.16 : The image of a) device with layers without top electrode and b) $PC_{61}BM$ surface

Achieving the optimum thickness of the active layer and other interlayers is a crucial step in maximizing solar cell performance. The thickness of these layers should not be too thin or too thick as it directly impacts light absorption, interfacial recombination, and short circuit conditions. The thicknesses of the layers in the solar cell were estimated from cross-sectional SEM images as follows: 51±6 nm for PEDOT:PSS, 500±20 nm for halide perovskite, and 55±5nm for $PC_{61}BM$. These values are consistent with the intended thicknesses in the literature[298]. It is evident that the $PC_{61}BM$ solution is densely agglomerated on the surface of the halide perovskite layer (in Figure IV.16b). During the early stage of $PC_{61}BM$ deposition by spin-coating, the solvent starts to evaporate. If this evaporation is too fast, the concentration of solvent decreases, leading to a fast aggregation of $PC_{61}BM$ molecules. PCBM-types can form aggregates or agglomerations that can affect device performance, depending on their size and distribution. Low aggregation can positively impact charge transport due to full surface coverage, while high aggregation can reduce device performance[299]. If the size is large, halide perovskites can come into direct contact with metal electrodes. This increases non-radiative recombination and accelerates the metal-perovskite electron transfer reaction as we mentioned previously[300]. It is crucial that this issue is tackled in a more effective manner.

Researchers optimized spin-coater speed for $PC_{61}BM$ surface coating, aiming to improve adhesion and minimize aggregation. Lower speeds have been found to be more effective in allowing solvents to spread and evaporate evenly, leading to better adhesion. Previously, the deposition method involved a speed of 3000 rpm, but it has since been reduced to 1500 rpm while keeping the same acceleration on time (500 rpm/s and 40 seconds) for our case. Although these conditions increased the J_{sc} from 5.5 mA.cm^{-2} to 6.5 mA.cm^{-2} and V_{oc} from 0.72 V to 0.74 V, they only made a slight impact on performance, ranging from 2.53% to 2.92% PCE. In this case, there is a significant increase in both FF (0.55 to 0.62) and R_{sh} (2 to 5 kΩ). It can be inferred that the improvement in the surface coating of the $PC_{61}BM$ has resulted in a reduction of contact between ETL and perovskite. This reduction has led to a decrease in recombination. However, it is important to note that the spin-coater deposition parameters are not the main cause of the aggregation due to less dispersion of performance parameters. There are additional factors that are contributing to the aggregation.

In order to address both aggregation and low current density issues, a comparison was made between a PV device incorporating $PC_{61}BM$ or $PC_{71}BM$. A main difference between these two molecules is the ellipsoidal shape of $PC_{71}BM$ compared to the more spherical $PC_{61}BM$ molecule[301]. C_{70} in $PC_{71}BM$ has also a lower symmetry and longer-lasting

conjugation, allowing for energetic transitions prohibited in C_{60}. This leads to a wider photo-absorption profile of the corresponding derivatives in the visible region of the solar spectrum. As a result, using $PC_{71}BM$ instead of $PC_{61}BM$ is expected to increase photon harvesting and potentially lead to higher photocurrent in devices where PCBM can contribute to current generation (such as in OPV for instance).

PC$_{71}$BM was prepared at the same concentration as $PC_{61}BM$ and deposited under the same parameters by the spin-coater. The thickness of the samples was 61±5 nm for $PC_{61}BM$ and 63±7 nm for $PC_{71}BM$. Figure IV.17a demonstrates that $PC_{71}BM$ exhibits broader photo-absorbance than $PC_{61}BM$, consistent with the literature for types deposited on the glass substrate. $PC_{71}BM$ has stronger absorbance at 300-315 nm than $PC_{61}BM$ due to differences in HOMO and LUMO transitions[302]. The aggregation present in $PC_{61}BM$ is also observed in $PC_{71}BM$ (in Figure IV.17b), but with larger size in some areas. It will be enlightening to see how this will affect the performance parameters of the device.

a)   b)
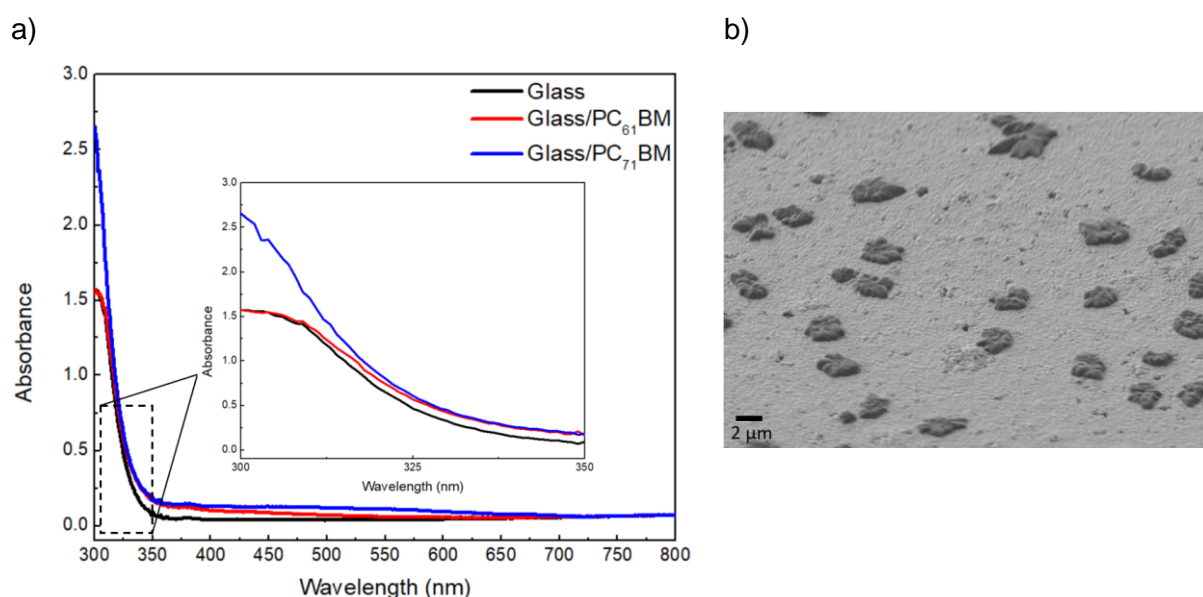
Figure IV.17 : a) Absorbance spectra of $PC_{61}BM$ and $PC_{71}BM$, and b) $PC_{71}BM$ morphology on top of CsFAPbIBr perovskite

When a solar cell is in operation, its overall current is made up of both dark current and photocurrent. The light illuminates the cell and generates electrical power, thus contributing to the photocurrent. But, when there is no light, carriers can still be generated through saturation current with the contribution of non-radiative recombination of trapped charges. In the device, $PC_{71}BM$ exhibits a higher current density ($>10^2$ mA.cm^{-2}) than $PC_{61}BM$ in dark conditions, as shown in the inset of Figure IV.18. However, under illumination, the performance difference between the two materials is not significantly distinct. In conclusion, there were no significant improvement made using $PC_{71}BM$ instead of $PC_{61}BM$. One main issue seems to be related to the morphology and homogeneity of the fullerene layer. Regarding it, improving the deposition process is by creating a more uniform surface and this can be a solution.
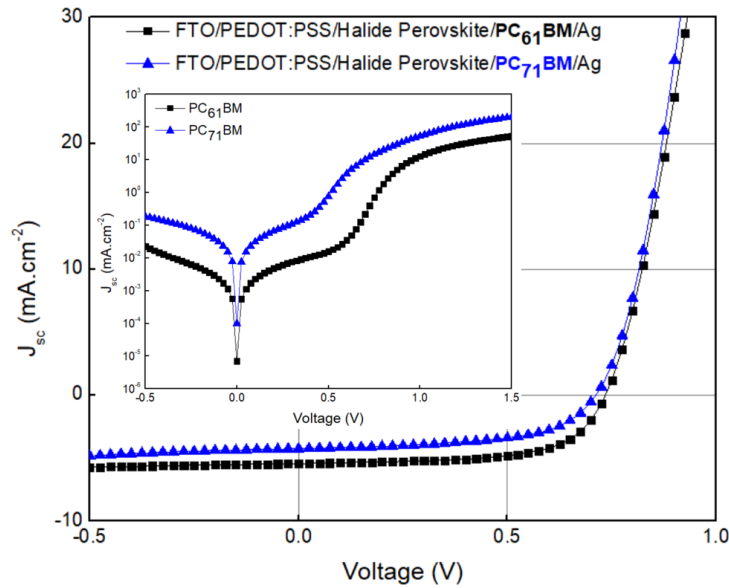
Figure IV.18: J-V characteristic of devices with $PC_{61}BM$ and PC71BM as the ETL, Inset: dark current in semi-log scale

In order to try to address this homogeneity issue of $PC_{61}BM$ layer, we decided to shift from solution processing to thermal evaporation. This technique is commonly used in organic solar cells to achieve a more uniform morphology in the $PC_{61}BM$ material. Thin film thicknesses of $PC_{61}BM$ were similar (~60 nm) for both spin-coating and thermal evaporation methods. These results (in Figure IV.19) indicate that the $PC_{61}BM$ is more effectively coated on the surface and facilitates charge extraction transport, as evidenced by the increased J_{sc} value. As a result, the PCE has improved from 2.92% in the previous device to 4.5% with increasing J_{sc} (6.5 to 10.5 $mA.cm^{-2}$). The increase in R_{sh} from 5 to 6 kΩ indicates a decrease in leakage due to a more uniform surface coating achieved through thermal evaporation. However, the increase in V_{oc} is limited due to the restriction of R_{sh}. In other words, the V_{oc} is limited by non-radiative recombination processes that occur within the absorber layer, at interfaces, and within the charge transport layer. It can explain why V_{oc} does not increase with higher PCE and J_{sc}. In this case, using evaporated $PC_{61}BM$ can improve device performance but requires an alternative ETL due to its high cost and material usage compared to spin-coating.

	Forward	Reverse
V_{oc} (V)	0.61	0.64
J_{sc} ($mA.cm^{-2}$)	10.28	10.55
FF	0.66	0.67
η (%)	4.20	4.51
R_s (Ω)	64.34	59.75
R_{sh} (Ω)	6754.69	7334.50
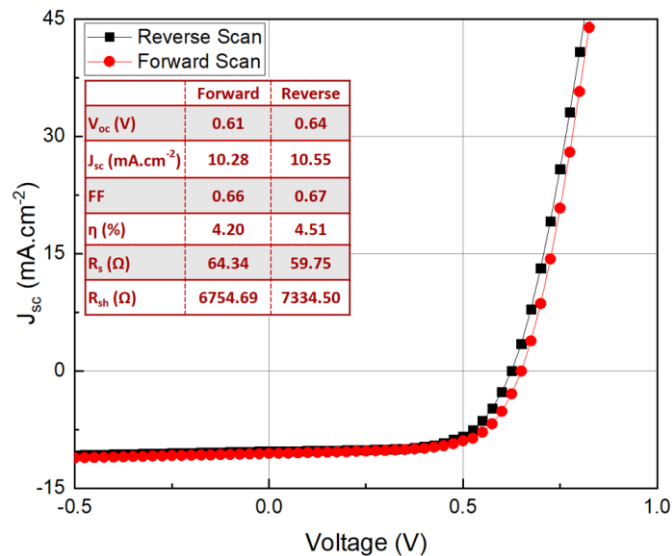
Figure IV.19 : J-V characteristic of the device with evapoted-$P_{61}BM$ as the ETL

The addition of a BCP buffer layer between ETL and metal electrode can be one of the reasons for low J_{sc}, depending on its thickness. If the BCP layer is either too thin or too thick, it can cause charge accumulation or blocking at the interfaces, which can ultimately lead to a decrease in device performance. Therefore, it is recommended that the ideal thickness of the BCP layer should be in the range of 3 to 5 nm[282] for optimal shunt resistance. To assess the effect of BCP in the device, we compared 3 nm BCP between $PC_{61}BM$ and Ag with and without BCP, as shown in Figure IV.20. The two types of devices display comparable current density ($\sim 10^2$ mA.cm^{-2}) and no severe blocking effect was observed in the BCP-based device. When it comes to the device with BCP, it is apparent that it functions more properly when placed in the interface. On the other hand, the device without BCP experiences fluctuations due to charge accumulation or recombination. Therefore, it is recommended to continue using BCP as it helps to regulate contact between halide perovskite and electrode and prevent such distortions in our case. In summary, BCP did not impose significant limitations and other factors should be investigated to identify the root cause of the issue.
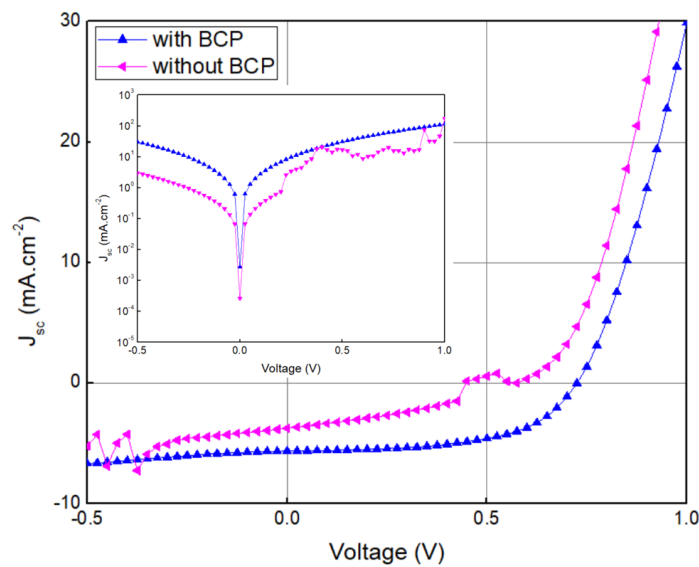
Figure IV.20: J-V characteristics of the device varying with 3 nm BCP and without BCP layer, Inset: dark current in semi-log scale

Pristine C_{60} fullerene is an excellent electron transport material for state-of-the-art inverted perovskite solar cells, making it the optimal choice for our optimization of ETL. The most commonly used acceptors in organic electronics are based on fullerenes, such as C_{60} or C_{70}. Unlike $PC_{61}BM$, C_{60} does not have any additional functional groups and is insoluble in most solvents. Therefore their usage in the sol-gel method is impractical. The thermal evaporation method is preferred for C_{60} deposition in nitrogen-filled glove box. Upon reviewing two types of HTLs (2PACz and PEDOT:PSS) previously tested with $PC_{61}BM$, this part investigates their characteristics with the C_{60}, which is preferred for optimization.

Previous studies have not been able to fully understand the actual function of 2PACz in $PC_{61}BM$ and Al electrode device structure due to issues with other materials. Only the impact of C_{60} in the device will be analyzed. Note that 2PACz is not favorable for HTL in our case because of not fully optimized, the focus is on ETL investigation and its characteristics. Figure IV.21 illustrates the energy-band diagram of the device, using typical values from literature for the materials and device performance and J-V characteristics C_{60}-based device.
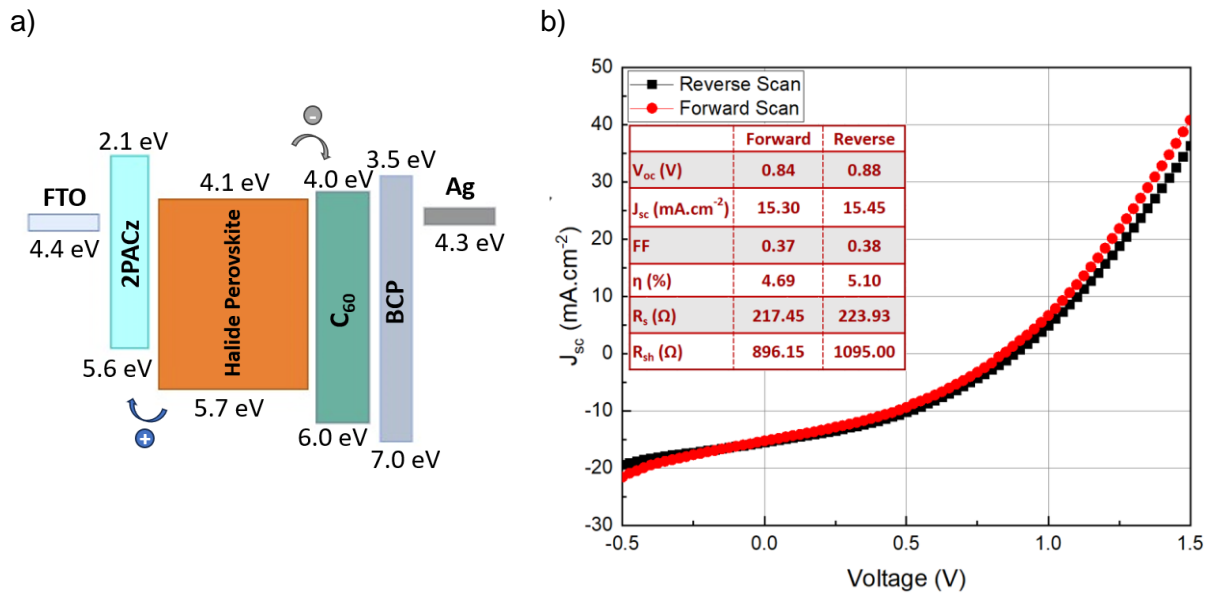
Figure IV.21 : a) The energy-band diagram and b) J-V characteristics of device with C_{60} ETL and 2PACz HTL

Shifting from $PC_{61}BM$ to C_{60} based on 2PACz clearly induces a larger short-circuit current density over 15 mA/cm². Despite a reasonable value, it remains well below the expected current obtained for similar active layers and inverted architecture (23 mA/cm² such as in[117]). There is also a positive improvement in V_{oc} (from 0.6 with $PC_{61}BM$ to over 0.8V with the C_{60}). It remains however still below the typical values observed in the literature (above 1V). V_{oc} can undergo changes due to various factors. However, the most significant factors are changes in bulk properties and radiation-free recombination rates at one or both interfaces. The latter can occur due to a higher selectivity caused by more homogenous surface covering of C_{60} with thermal evaporation and a lower number of defect states at one or both interfaces in relation to the charge-selective contacts of interest[117]. Notably, FF values significantly decrease compared to $PC_{61}BM$ based device with PEDOT:PSS (see in Figure IV.19). It is challenging to make direct conclusion about ETL in this particular case due to different ETL and metal electrode. Although J-V measurements under illumination indicate that series resistance (~223 Ω for our case) limits FF, the shape of the J-V curve suggests that low FF is not due solely to ohmic series resistance. In addition to the current-dependent component, there must also be a component that is dependent on voltage. The series resistance that causes internal voltage drops due to transport limitations within the absorber is often voltage-dependent and is likely a significant contributor to the low FF for this cell[303]. In order to increase the efficiency of solar cells, it is crucial to reduce the series resistance, but also to increase the shunt resistance as it is also clearly non ideal in our case. This may be due to inadequate coating of 2PACz on the FTO surface, causing direct contact between FTO and the absorber layer. Although decent results have been obtained in terms of C_{60} surface coverage, the real characteristic of it cannot be clearly established with 2PACz. Our laboratory has extensively studied PEDOT:PSS previously, which will provide better characterization of C_{60}.

The device architecture (in Figure IV.22) incorporates PEDOT:PSS as HTL and C_{60} as ETL, while previously used layer. Chien-Hung et al.'s work is used as a reference for the next step[77].
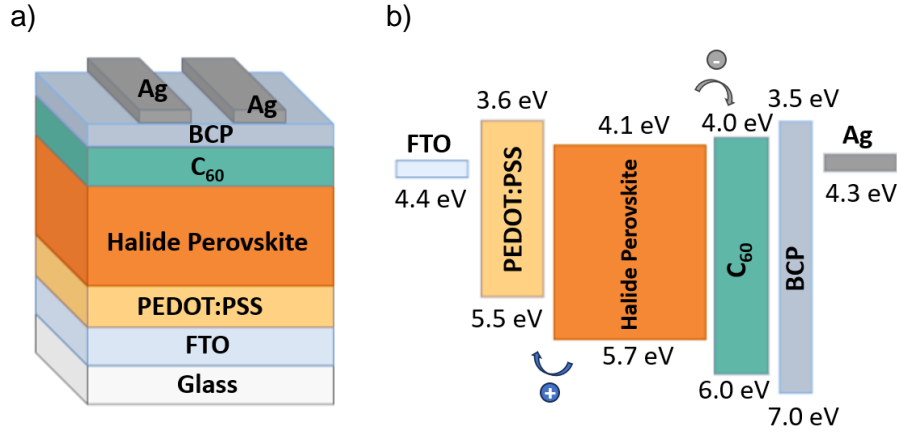
Figure IV.22 : PSC's a) device architecture with C_{60} as the ETL and b) energy-band diagram

We achieved performance improvements with low hysteresis in these devices using PEDOT:PSS and C_{60}, as illustrated in Figure IV.23.
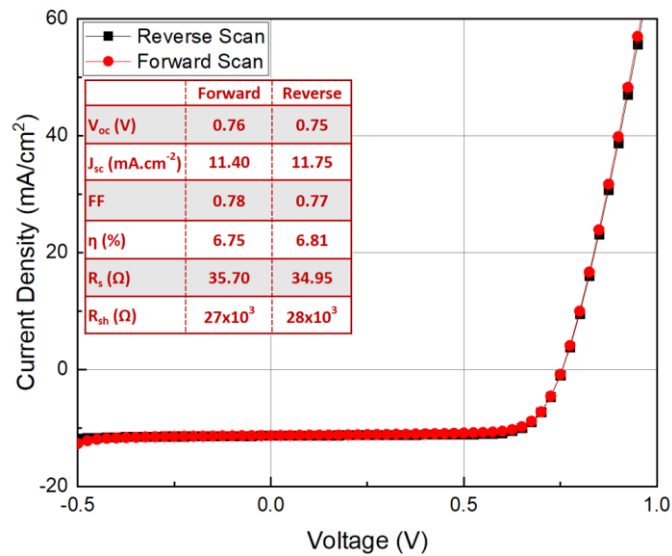
Figure IV.23: J-V characteristics of device with C_{60} as the ETL

Based on the results obtained, it appears that the PSC's FF has increased compared to previous devices with $PC_{61}BM$. This can be attributed to the decrease in series resistance (from ~ 60 Ω to 35.70 Ω) and the increase in shunt resistance (from ~6.8 kΩ to 27 kΩ). Although the J_{sc} obtained is quite low from the beginning of the study, the PSC parameters from the C_{60} devices are comparable to those of $PC_{61}BM$ and slightly higher. The improvement of the device attributed to the fact that the surface of C_{60} is more uniform compared to $PC_{61}BM$. In addition to achieving a more uniform surface, it is also important to fabricate reproducible devices with final structure which is FTO/PEDOT:PSS/CsFAPbIBr/C_{60}/BCP/Ag.

The PV performance statistics of 8 devices fabricated in two different batches with FTO/PEDOT:PSS/CsFAPbIBr/C_{60}/BCP/Ag structure are shown in Figure IV.24. Despite high reproducibility of devices with decent dispersion, current density is still low for all (average 11.2 mA.cm^{-2}). It can be observed that dispersion in J_{sc} for both lower and higher efficiency (5.6 to 6.8%) is relatively small. The J_{sc} is directly linked to the limitation of the low R_{sh} and high R_s. The blocking effect in device may be caused by the poor structural property of the thin films

and also low energy level of PEDOT:PSS. Therefore, optimization of HTL is still essential for those who will use this structure in future.
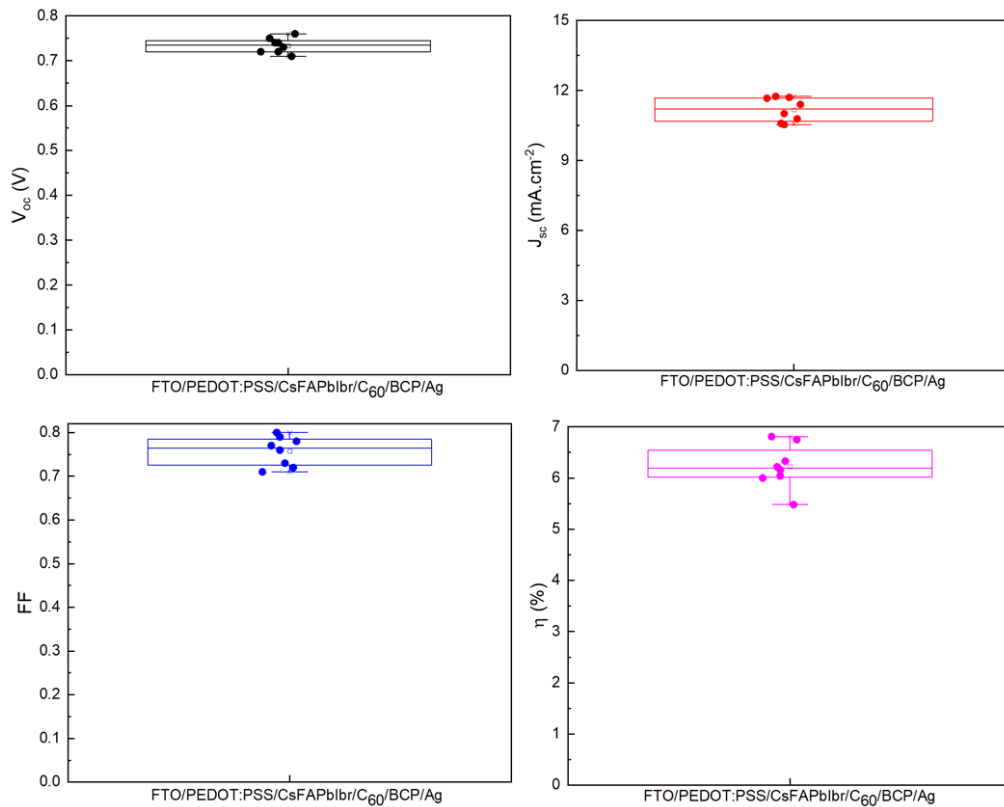
Figure IV.24 : Statistical properties of PV performance parameters in a set of 8 PSC devices

In conclusion, the inverted planar PSCs were created from scratch and optimized in three main stages. Firstly, the optimization of the hole transport layer was carried out, during which three different materials, namely CuSCN, PEDOT:PSS and 2PACz, were studied. Secondly, the metal electrode was optimized, and both Al and Ag were investigated. Finally, the optimization of the electron transport layer was performed on three different materials: $PC_{61}BM$, $PC_{71}BM$, and C_{60}.

The first structure that was worked on is FTO/CuSCN/CsFAPbIBr/PC_{61}BM/Al. This CuSCN-based structure had a very low current density with non-functioning device. The main reason for this problem was found to be the high solubility of CuSCN in many solvents, which disrupted the perovskite layer and led to degradation mechanism. Secondly, the characteristics of PEDOT:PSS was investigated using the same structure. The solar cell performed at a low efficiency of less than 1%, as well as its low J_{sc} and high R_s values were spectacular. This is primarily due to the materials used in the device and the resistive contacts. The low WF of PEDOT:PSS results in an energy-band mismatch with perovskite, which leads to low V_{oc}. Therefore, as an alternative, a binary comparison was performed with the third option, 2PACz. The black α-phase of the halide perovskite has a distinct characteristic which is evident from the narrower and stronger diffraction peak on PEDOT:PSS as compared to 2PACz. This indicates better crystallization for active layer. Further optimization is required for 2PACz due to poor wettability and short-circuit creation at high potential. Therefore, PEDOT:PSS has been identified as the preferred HTL.

During the optimization of electrode, it was analyzed that the use of an Al electrode has negative impact on the device due to difficulties of deposition and creating interface instability. When Ag electrode replaced to Al, a significant decrease in R_s (10^3 to 19 Ω) was observed. The reason behind it is that the migration of halide ions from ETL to electrode can cause blockage and increase R_s due to the formation of a metal halide compound at the interface. Ag was ultimately chosen as preferred electrode.

During the optimization of ETL, it was discovered that $PC_{61}BM$ did not cover the entire surface of the active layer due to aggregation. This led to direct contact between the perovskite and electrode in some areas, causing non-radiative recombination and reducing the charge transfer capability. The problem persisted even after using $PC_{71}BM$ under same conditions, due to lack of surface homogeneity and coating improvement. However, when $PC_{61}BM$ was deposited with thermal evaporator instead of spin-coater, the device performance improved from 2.92% to 4.5%. It was also observed that leakage current decreased, which was directly attributed to the more homogenous surface coating. Work on the C_{60} was initiated due to the high cost of coating $PC_{61}BM$ with thermal evaporator, despite the improved performance. C_{60} leads to higher FF (0.70), higher R_{sh} ($\sim 10^3$ Ω), and lower R_s (35 Ω). However, the issue of low J_{sc} persists. The latest device structure, $FTO/PEDOT:PSS/CsFAPbIBr/C_{60}/BCP/Ag$, demonstrates reproducibility and low dispersion.

After considering the inverted planar PSC cluster, the initial PCE value was less than 1% and we were able to reach up to 6.8%. My thesis work has made significant progress towards developing an inverted PV device, which now exists in our laboratory. Although there is still scope for improvement, we have established a basic reference for this device. It is unclear whether integrating oxide perovskites would allow for consistent performance analysis with developed inverted planar PSCs due to the limitation of low J_{sc}. In addition, our laboratory has also developed light-emitting diodes that are based on hybrid perovskites. These diodes possess the ideal structural foundation for our oxides. Therefore, we conducted our research simultaneously on these devices.

IV.1.2. Synthesis and Design of Halide Perovskite Solar Cells

- Substrate Preparation

A 12x12 mm^2 FTO-coated glass substrate with 2 mm thickness was used (FTO thickness in the order or 300 to 500 nm depending on the 15 Ω/sq surface resistivity and >75% optical transmission between 500 to 1000 nm trade-off). For any cell fabrication process, the initial step is substrate preparation.

The first step is FTO etching or patterning, followed by the cleaning phase. The surface of the FTO is covered with 3M tape to create the specific design depicted in Figure IV.25. Afterward, the wet etching is applied to the FTO surface. During this process, the areas where the FTO is to be etched are exposed to concentrated hydrochloric acid solution (37%) for a short duration (less than 1 minute), in the presence of zinc powder which helps activating the reaction (catalysis).
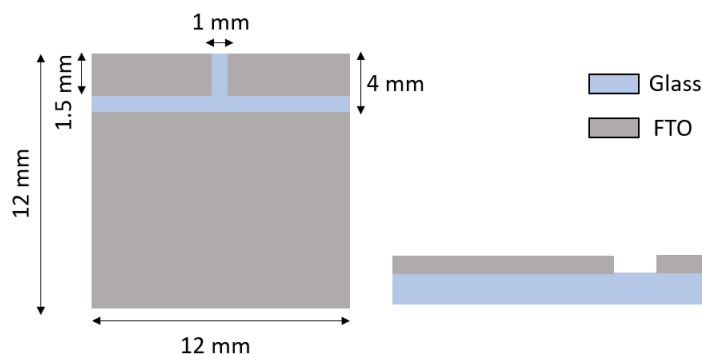
Figure IV.25 : The design of FTO for the wet etching process of PSC

After etching, FTOs undergo a 15-minute ultrasonic bath in acetone, isopropanol, and ethanol, respectively. This is followed by drying with nitrogen flow and UV-ozone treatment for 20 minutes. This treatment is crucial for effectively removing organic pollutants using intense ultraviolet light without damaging surfaces, particularly in non-acidic and dry environments. It modifies the surface energy properties of the substrate, which in turns improve its wettability during the next deposition steps.

- Hole Transport Materials

We tested three different hole transport materials: (a) CuSCN (Copper(I) thiocyanate), (b) PEDOT:PSS, and (c) SAM-based 2PACz ([2-(9H-Carbazol-9-yl)ethyl]phosphonic acid). Deposition of all material types is done by using the spin-coating technique (for more details[304]). The process of dip-coating is also used to apply for 2PACz (for more details[305]).

(a)   To prepare the precursor solution of CuSCN, a 35 mg/mL solution is prepared with diethylsulfide as solvent. The solution should be stirred on a hot plate for 30 minutes at room temperature and filtered with a 0.45 μm filter before use. Then, 35 μl solution should be deposited on the substrate using a micropipette, before spin coating at a speed of 5000 rpm for 30 seconds with an acceleration of 2000 rpm/s. Finally, the thin films should be annealed at 100 °C for 10 minutes in order to remove any residual solvent.

(b)   To prepare PEDOT:PSS, the commercial mother solution (Al 4083, Ossila) is placed in an ultrasonic bath for 30 minutes at room temperature, followed by magnetic stirring on the hot plate at 50 °C for 15 minutes. Then, the solution is filtered using a 0.45 μm filter. When spin coating in ambient conditions using 55 μl of solution, the deposition parameters should be set to 3000 rpm for 50 seconds with an acceleration of 2500 rpm/s. After deposition, the samples are annealed at 100 °C for 40 minutes on a hot plate. The expected thickness should be 50±5 nm.

(c)   Two ways of deposition are possible for 2PACz :

If a spin-coating method is preferred, a 1 mmol/L solution of 2PACz (C3663, TCI Chemicals) should be prepared with isopropanol as the solvent. The ultrasonic bath is applied to the solution for 15 minutes and stirred on the hot plate at room temperature for an hour. Prior to its use, it is important to filter the solution using a 0.22 μm filter. Afterward, the 120 μl solutions can be deposited by a spin-coater for 30 seconds at a speed of 3000 rpm with 2000 rpm/s acceleration inside the glove box. Then, the samples were annealed at 100 °C for 10 minutes.

If a dip-coating method is preferred, the samples can be dipped in 0.1 mmol/L solution of 2PACz for 2 hours at room temperature.

After each deposition of HTL, regardless of the material used, the deposited layer undergoes surface etching with a cotton swab wetted with a specific solvent according to the device's design, as shown in Figure IV.26. The choice of solvent for etching varies by deposited material: CuSCN - hydrogen peroxide, PEDOT:PSS - methanol, 2PACz - isopropanol.
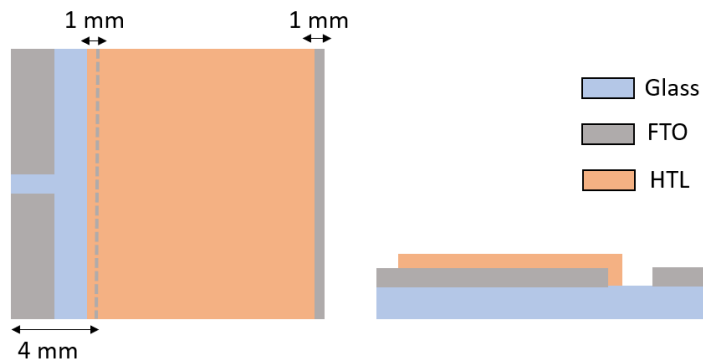
Figure IV.26 : The design of HTL for the etching process on the FTO substrate

- Halide Perovskite as an Absorber Layer

We selected the formamidinium lead iodide-based perovskite absorber layer with mixed cations and mixed halide ($FA_{0.85}Cs_{0.15}Pb(I_{0.85}Br_{0.15})_3$) for our reference devices, as it was extensively used in our past studies[267]–[269]. The preparation of perovskite solution is carried out inside a glove box. The solution is mixed with 146.3 mg of formamidium iodide (FAI), 392 mg of lead iodide (PbI_2), 39 mg of cesium iodide (CsI), and 55.4 mg of lead bromide ($PbBr_2$). Along with this, 600 μl N,N-dimethylformamide (DMF) ,and 87 μl dimethyl sulfoxide (DMSO) are added as solvents, and they are stirred at least 2 hours at 65 °C on the hot plate. Prior to deposit, the solution undergoes filtration with a 0.45 μm filter. The filtered 30 μl solution is deposited by a spin coater with 4000 rpm speed for 30 seconds with 2000 rpm/s acceleration. Approximately 10 seconds after the spinning start, the sample surface is washed by an anti-solvent treatment, by dispensing 500 μl of diethyl ether on the top and at the center of the sample during the rotation, to optimize the crystallization of the perovskite layer. Once the spinning process is completed, the samples are subjected to annealing in the glovebox at 100 °C for 5 minutes, followed by another 15 minutes at 150 °C.

The process of etching the halide perovskite on HTL involves using DMF with a cotton swab wet with DMF, as shown in Figure IV.27. This step is crucial because DMF can diffuse by capillary action into the rest of the layer. It requires careful DMF usage control to avoid any perovskite layer degradation.
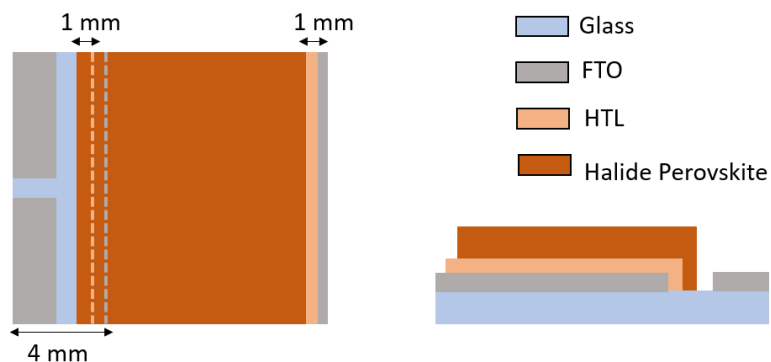
Figure IV.27 : The design of the halide perovskite layer for the etching process on the HTL

- Electron Transport Materials

We worked on three different electron transport materials, which are (a) [6,6]-Phenyl-C_{61}-butyric acid methyl ester ($PC_{61}BM$) and (b) (6,6)-Phenyl-C_{71}-butyric acid methyl ester ($PC_{71}BM$) deposited from solution, and (c) [60]Fullerene (C_{60}), deposited through thermal evaporation under vacuum as described below.

(a)-(b)   To prepare a 20 mg/mL solution of PCBMs, chlorobenzene is used as a solvent, and a 3% volume of 1.8-diiodooctane is used as a supplier to achieve more even homogeneity of PCBMs on the surface. The solution should be stirred at 50 °C overnight. Before deposition, the filtration is applied with a 0.22 μm filter. The recommended deposition method is spin-coating inside a nitrogen-filled glove box using a 20 μl solution. The ideal conditions are 1500 rpm for 40 seconds with 500 rpm/s acceleration (explained in the experimental background part). After deposition, the samples are annealed at 50 °C for 10 minutes.

(c)   Thermal evaporation is the preferred method for the deposition (for more details[306]) of C_{60}, with the interlayer bathocuproine (BCP) is used to balance the work function between the electron transport layer and the electrode.

When the halide perovskite is used as a sublayer for $PC_{61}BM$ deposition, chlorobenzene is utilized for etching by using a cotton swab. However, this process is not required for C_{60} as it is deposited through thermal evaporation, and a the metal mask is used to ensure its dimensional design in the device. The same procedure is followed for BCP since its deposition design is similar to that of C_{60}. Figure IV.28 illustrates the designs for these materials.
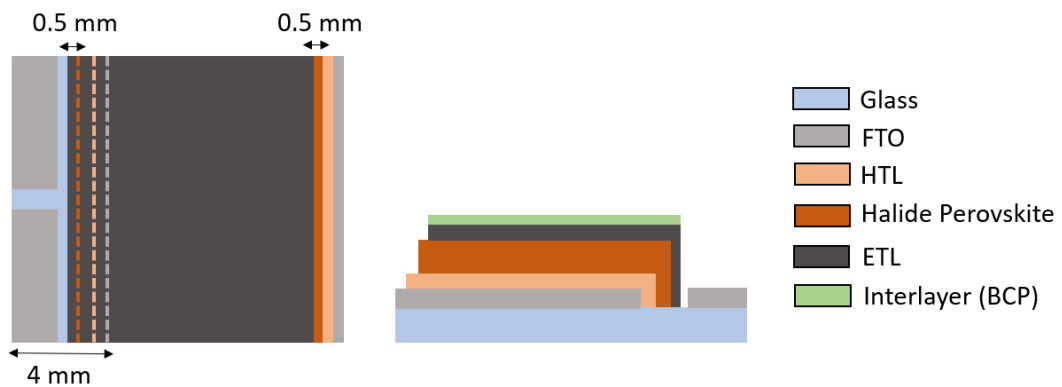
Figure IV.28 : The design of ETL and interlayer on the halide perovskite layer

- Electrodes

Both aluminum and silver electrodes were tested and deposited using the thermal evaporation technique due to their suitable work function with other layers. The electrodes are arranged in a metal mask to form a two-pixel cell, and their design is shown in Figure IV.29. This is also the final representation of the device design.

Figure IV.29 : The design of metal electrodes on the ETL

IV.2. Reference Perovskite Light-Emitting Diodes

This part of the chapter is based on a recipe developed by PhD student Quang-Huy Do during his studies from 2020 to 2023 at XLIM, covering the methodology of the reference LED and the precursor preparation.

IV.2.1. Experimental Background of Perovskite Light-Emitting Diodes

The family of quasi-2D perovskites can be described by the formula $L_2(ABX_3)_{n-1}BX_4$. In this formula, L represents a large organic spacer cation (PEA or n-BA), A is a small monovalent cation (MA^+ or FA^+), B refers to a divalent metal cation, and X refers to halogen anions[307]. The value of "n" in the formula represents the number of layers and determines the composition of the perovskite. The emission properties of quasi-2D perovskites depend heavily on their composition.

Quasi-2D perovskites are materials with a unique grain distribution that ranges in dimensionality from 2D to 3D. They have optical properties that are different from conventional 3D and 2D materials. These materials have a higher exciton binding energy around several hundreds of meV due to quantum and dielectric confinement enhancing the coulombic attraction of electron-hole pairs, which is leading to more excitonic semiconductors than their 3D counter parts. Radiative recombination can produce better results than the less desirable trap-assisted radiative recombination process by increasing the concentration of carriers. By precisely tailoring the n-value phase distribution, an efficient and fast energy funnel process can be achieved, making high-luminous LEDs practically feasible. Moreover, arranging the energy funnel terminal correctly, which is the smallest bandgap phase, can enable stable emission over the complete visible spectrum, even in the short-wavelength regimes. As a result, the particular energy funnel process's multitude of possibilities has made quasi-2D perovskites particularly appealing for various light emission applications[33].

The reference PeLEDs, based on a bromide quasi-2D perovskite, are designed to emit light between 500 nm and 550 nm in the green region. $PEA_2MA_{n-1}Pb_nBr_{3n+1}$ is one of the most promising compounds for quasi-2D types due to its high performance. Several studies in the literature suggest that it is a leading candidate for this type of compound[308][309]. We used PEA and MA in a 1:2 ratio with the $(PEA)_2(MA)PbBr_4$ formula. Figure IV.30 presents the UV-vis absorption, electroluminescence (EL) and XRD spectra of a quasi-2D perovskite film of $(PEA)_2(MA)PbBr_4$.
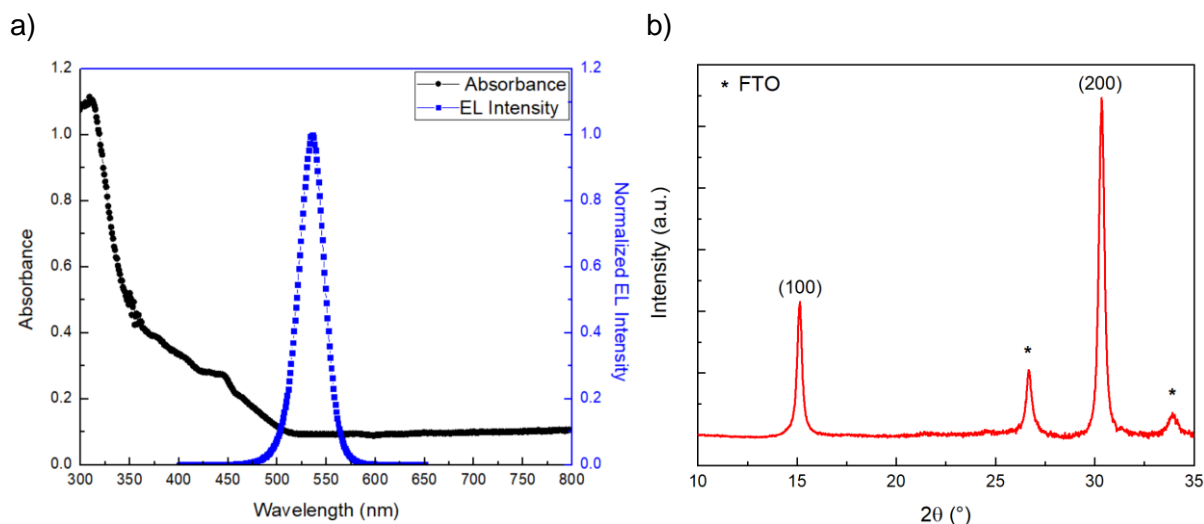
Figure IV.30 : (PEA)$_2$(MA)PbBr$_4$ type quasi-2D perovskite a) absorbance spectra and EL spectra and b) XRD pattern on FTO

The absorbance spectrum displays a single peak at 435 nm, indicating the n=2 phase, which represents the low phase (n<5) in the mixed-size halide perovskite. Moreover, based on the EL intensity, we can confirm that the peak observed at 525 nm (~2.36 eV) represents the expected green light region. A narrow luminance peak is often a sign of high-quality crystals without any defects. Figure IV.30b displays the XRD pattern of (PEA)$_2$(MA)PbBr$_4$ polycrystalline film on FTO substrate. The (100) and (200) planes are represented by a single peak around 30.2° in 2-Theta, while a peak 14.8° denotes high crystallinity along this direction[310]. The perovskite exhibits high crystallinity and stability, as evidenced by the absence of broad peaks, stronger and narrower peaks, and lack of degradation.

The PeLED device structure of the FTO/PEDOT:PSS (50 nm)/quasi-2D bromide perovskite (120 nm)/TPBi (40 nm)/Ca (30 nm)/Ag (30 nm) is depicted in Figure IV.31a. It is crucial to ensure that the band alignment allows an effective charge injection and charge carriers into the emitter layer, while facilitating radiative recombination towards intense light emission. The energy levels and band offsets are specific to the materials that are used in the device and are carefully designed (in Figure IV.31b) to optimize the device's overall performance, color purity, and luminance.
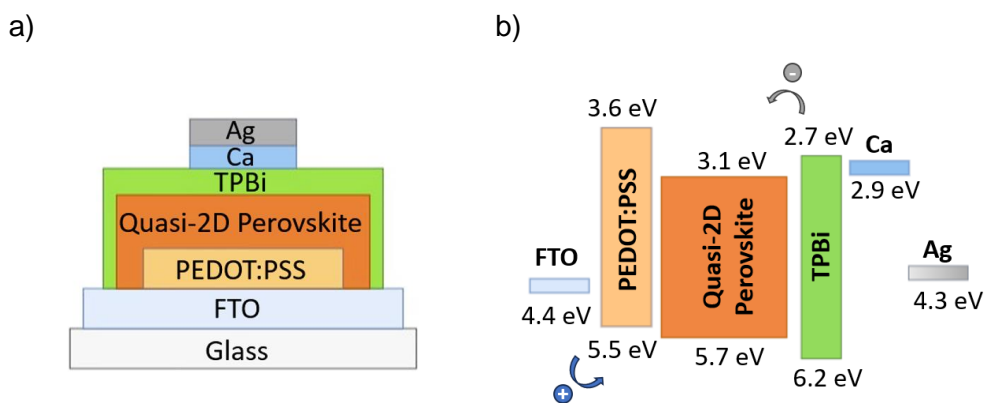
Figure IV.31: The reference PeLED's a) architecture and b) energy-band alignment

A high carrier mobility is recommended for HTL and ETL to efficiently inject into the emissive layer and reduce the operating voltage. Like the PSCs, the PEDOT:PSS is preferred as the HTL in this case. TPBi (1,3,5-Tris(N-phenylbenzimidazol-2-yl)benzene) possesses exceptional electron transport properties due to its decent mobility (6.5×10^{-5} $cm^2V^{-1}s^{-1}$)[311], which is crucial for the efficiency of the transportation of electrons to the emitter layer. It is also known for its chemical stability, which plays a significant role in ensuring the long-term performance and reliability of PeLEDs. The TPBi LUMO level misalignment with the Ag metal electrode creates an energy barrier and voltage drop at the ETL/Ag interface. This results in local heating and accelerates electrochemical reactions. Calcium (Ca) should be used as an interlayer to balance the energy barrier between these two layers[312]. In addition, Ca is a cost-effective option due to its abundance. Figure IV.32 depicts the J-L-V plots of four reference quasi-2D bromide-based perovskite PeLEDs.
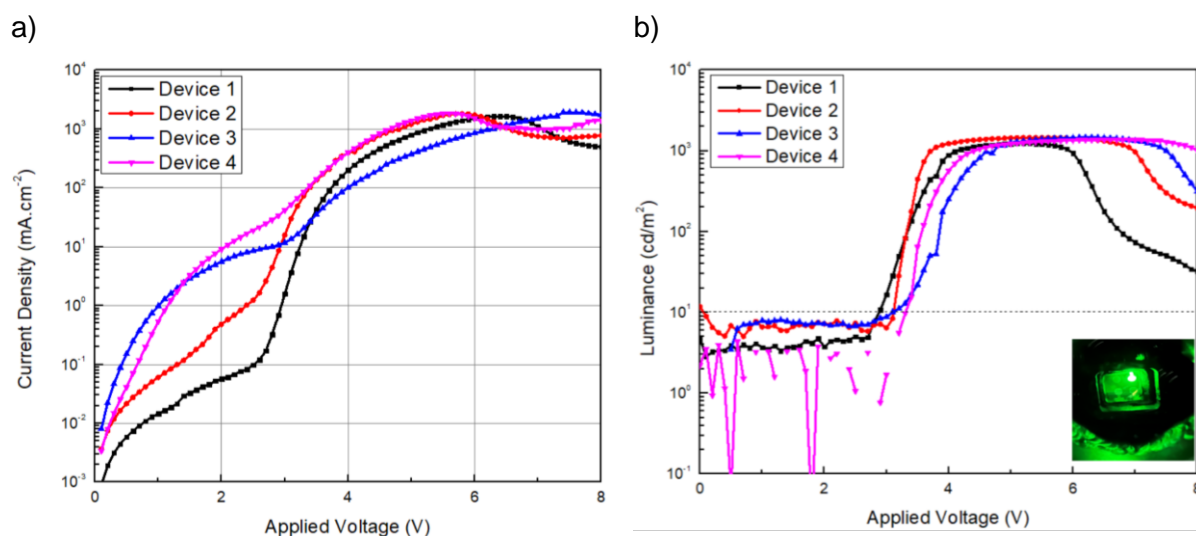
Figure IV.32 : Quasi-2D bromide perovskite reference PeLEDs a) J-V and b) L-V curves characteristics, Inset: an image of functioning device

These devices demonstrate a high current density ($\sim 10^3$ $mA.cm^{-2}$) at low driving voltages (V_{ON}= 3 V), and an overall high leakage current (>10^{-2} $mA.cm^{-2}$). The dash lines indicate the 1 cd/m^2 threshold for turning on (in Figure IV.32b). The image inset displays a uniform surface on the device with the highest brightness without any blinking issues. Generally, the brightness values of these devices are similar to each others, ranging from 1225 to 1460 cd/m^2 (typical luminance targets for display applications). The performance of these device architecture is lower than that reported in the literature for PeLEDs using similar emitter materials[313]. The reason behind it can be the high leakage current causes non-radiative recombination losses, leading to reduced radiative path emissivity of devices. From the four device luminance variation, it is clear that they are reproducible with low dispersion. However, the EQE is very low (<0.07%). The unbalanced organic spacers in perovskite layer decrease EQE of PeLEDs due to increased trap densities and less homogenous layer[314].

In addition to performance parameters, operational stability is crucial for PeLEDs. It is determined by its ability to maintain brightness, which tends to decrease over time. The most obvious implication of degradation in L-V characteristics is seen after 6V, as shown in Figure IV.32b. Over time, changes in device characteristics resulting in performance losses may occur due to the mixed electronic-ionic properties of PeLEDs. They often degrade due to a combination of factors such as exciton quenching, unbalanced charge carriers, ion migration

and Joule heating under intense electrical excitation[315]. These reasons may cause electrical short circuits, which can lead to rapid degradation. Gradual degradation, similar to what our devices experience, can occur due to increased internal stress and recombination-enhanced point defect responses. The observed high leakage current, low EQE and performance degradation in devices may result from non-radiative recombination losses. This is related to the intrinsic properties of the emitter material, while the charge injection unbalance is due to the device architecture, including the choice of transport and injection materials[313]. All of this should be considered for next term optimizations of operational durability and device performance.

In summary, we have successfully fabricated high brightness, low turn-on voltage, and homogeneous emission reference PeLEDs. Moreover, reproducible and proper devices performance was observed. They can emit bright light over 1000 cd/m^2 with acceptable device lifetime compared state-of-art by using low-dimensional perovskites. While there are certain features that could be improved, such as low EQE and high leakage current, it is possible to improve them by implementing optimizations in future.

IV.2.2. Synthesis and Design of Perovskite Light-Emitting Diodes

- Substrate Preparation

To reach the targeted device structure (Figure IV.33, a), the initial step involves FTO etching, which is then followed by a thorough cleaning process. The FTO surface is first covered with 3M tape to design the structure displayed in Figure IV.33,b. Subsequently, a wet etching process is employed on FTO, similar to that used for photovoltaic devices. During this process, the specific areas of the FTO that need to be etched are briefly exposed (for less than a minute) to the chemical reaction of concentrated hydrochloric acid (37%) and zinc power.
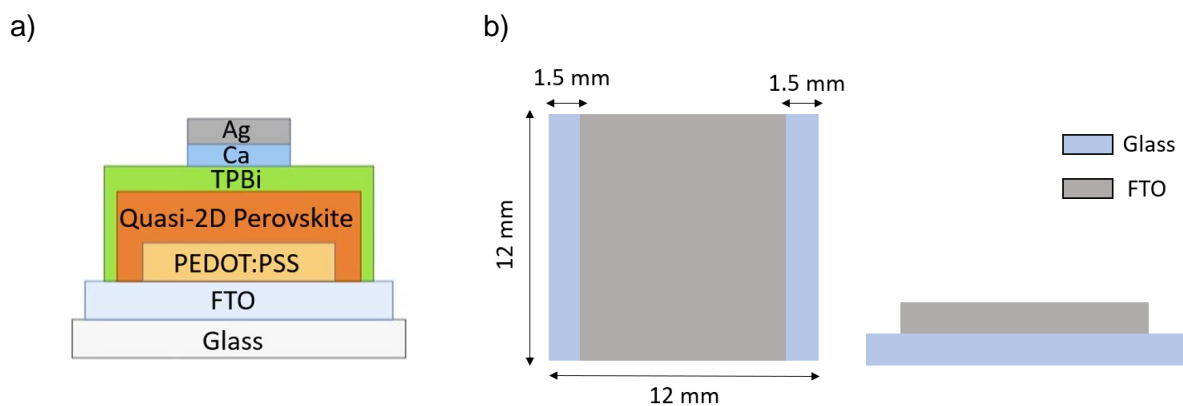
Figure IV.33 : a) Final device structure and b) the design of FTO for the wet etching process of device

The FTOs are cleaned using the same protocol as PSC after etching and are dried with nitrogen flow before use. The UV-ozone treatment should be applied for 20 minutes before the hole transport layer deposition process.

- Hole Transport Layer

In PeLED, PEDOT:PSS (same as solar cell, Al 4083-Ossila) is still used for the hole injection. The material preparation and deposition process with the spin-coater is exactly the same as what is described for PSC. However, there are changes in the etching process due to the different designs of the device. Instead of etching PEDOT:PSS as a single layer before

annealing, it will be etched together with the halide perovskite. This last part differs from the solar cell as all layers are not etched separately.

- Halide Perovskite as an Emissive Layer

$(PEA)_2(MA)PbBr_4$ type quasi-2D perovskite is used for the emissive layer, according to recent developments made in the group in the frame of dedicated projects (Huy Do Quang thesis). The solution preparation is carried out inside the glovebox. Initially, 26 mg of phenethylammonium bromide (PEABr), 34 mg of methylammonium bromide (MABr), and 115 mg of diethylammonium bromide ($PbBr_2$) are mixed with 1000 μl of DMF. The solution is stirred overnight at 50 °C. It is filtered before use with a 0.22 μl filter. Spin-coater is the preferred deposition method for the solution, which is deposited at 7000 rpm for 40 seconds with an acceleration rate of 7000 rpm/s. For deposition, 25 μl of solution is used, and the samples are annealed at 90 °C for 15 minutes on the hot plate. After completing the deposition of the emissive later, deionized water is used to etch with a cotton swab, as shown in Figure IV.34. At this stage, PEDOT:PSS is etched simultaneously with the emissive layer.
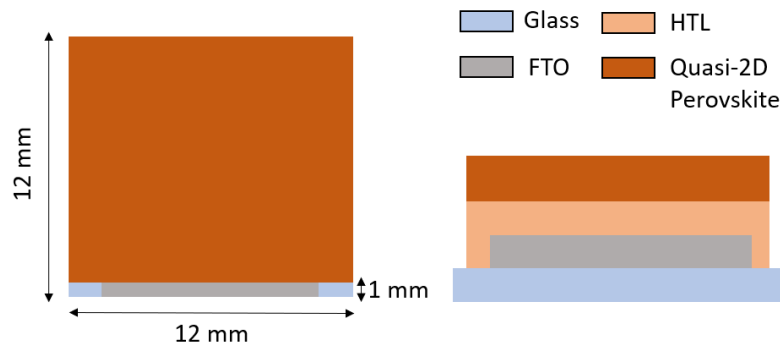
Figure IV.34 : The design and etching for quasi-2D perovskite and HTL

We emphasize that the atmosphere and temperature in the glovebox are crucial factors influencing the reproducibility of the devices, and we demonstrated that regular regeneration/purification of the glovebox, while storing the chemical precursors in a separated glovebox, was necessary to achieve a suitable level of reproducibility of device performance.

- Electron Transport Layers and Metallic Electrode

TPBi (2,2',2''-(1,3,5-Benzinetriyl)-tris(1-phenyl-1-H-benzimidazole)) is a preferred electron injection material in green PeLEDs due to its appropriate work function and ability to yield efficient devices[316]. A better choice for the metallic top electrode in this structure would be Ca/Ag instead of LiF/Aluminum due to the deposition difficulties. The reason for this is that Ca has a work function of 2.9 eV, which matches well with the TPBi and Ag, making it the preferred material for the electron injection layer. Furthermore, using Ca can help to reduce manufacturing costs as it is one of the most abundant metals[317]. Thermal evaporation method is used to deposit TPBi, Ca, and Ag with thicknesses of 30 nm, 40 nm, and 100 nm, respectively. A uniform metal mask with identical dimensions is used for each device. Four independent perovskite LEDs with an active area of 4.53 mm² are defined on each substrate, as shown in Figure IV.35.
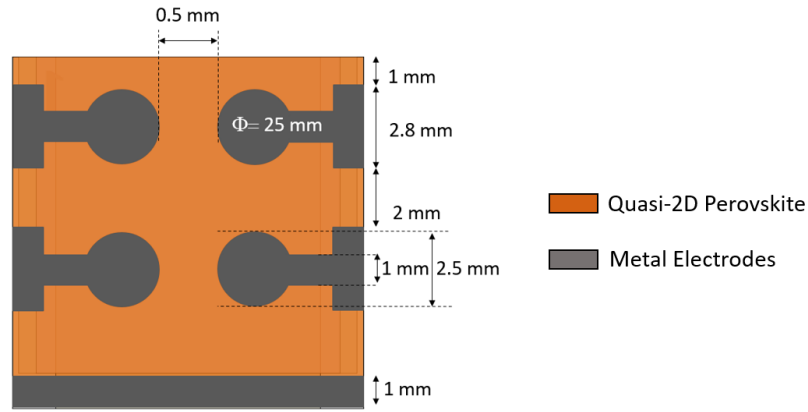
Figure IV.35 : The final design of the PeLED

IV.3. Conclusion

In this chapter, we covered the fabrication, synthesis, and characterization of the reproducible inverted planar PSCs and green PeLEDs.

We have successfully developed reproducible inverted planar perovskite solar cells for the first time in our laboratory. Despite trying various tests and methods to improve the device performance, we were only able to achieve a reasonable level of efficiency. Further research is required to better understand the limitations of these devices and to improve their performance. It would be beneficial to assess the integration of our optimized STFO thin films as hole transport layer in optoelectronic devices based on halide perovskite active layer as an alternative to HTLs like PEDOT:PSS.

We have successfully used a well-established recipe for quasi-2D perovskite, which was developed in our laboratory and is widely used in the literature, to create green PeLEDs. The study showed that our devices are both reproducible and efficient, and that this approach provides a promising way to explore the potential of STFO thin films.

Chapter V. Integration of Perovskite Oxide Thin Film in Optoelectronic Devices

The purpose of this chapter is to provide a detailed description of the processes involved in integrating $SrTi_{0.7}Fe_{0.3}O_{3-\delta}$ (STFO) perovskite oxide into two type of perovskite optoelectronic devices. As described in the previous chapters, the STFO thin films have been deposited by the PLD technique before specific annealing steps were applied (RTP or TA).

In the first part of this chapter, the photovoltaic properties of halide perovskite thin films deposited on oxide perovskites will be investigated in terms of their optical and structural characteristics. Even if the performance of the reference halide PSCs is limited, we will integrate the STFO oxide perovskite into device and try to gain insight into its characteristics.

In the second part of this chapter, we will focus on exploring the optical and structural characteristics of thin films while integrating oxide perovskite into halide perovskite LED (PeLED). We will replace the convention HTL of reference PeLED by the oxide perovskite and evaluate its performance. Lastly, we will give preliminary data on the stability of devices based on reference HTL or oxide perovskite.

V.1. Oxide Perovskites as HTL in Halide Perovskite Solar Cells

This section discusses the characteristics of STFO/halide perovskite and PEDOT:PSS/halide perovskite rather than just thin films. Therefore, the halide perovskite coating must first be successfully applied to the oxide perovskite surface.

V.1.1. Rheological Properties

The wettability properties of the STFO and PEDOT:PSS surfaces are characterized using contact angle measurements with water drop. Very different contact angles are measured for PEDOT:PSS and STFO in Figure V.1, indicating different wettability behaviors of both materials, in line with their chemical nature. The PEDOT:PSS sample used here is post-annealed at 100°C, which is a typical deposition methods (as mentioned in Chapter 4). However, STFO is an as-grown sample without post-annealing. PEDOT:PSS, processed from an aqueous commercial solution, exhibits a more hydrophilic property in comparison to STFO, as indicated by the widening of the contact line and the reduction in the contact angle. This characteristic differs depending on the liquid used to wet the surface.

a)   b)
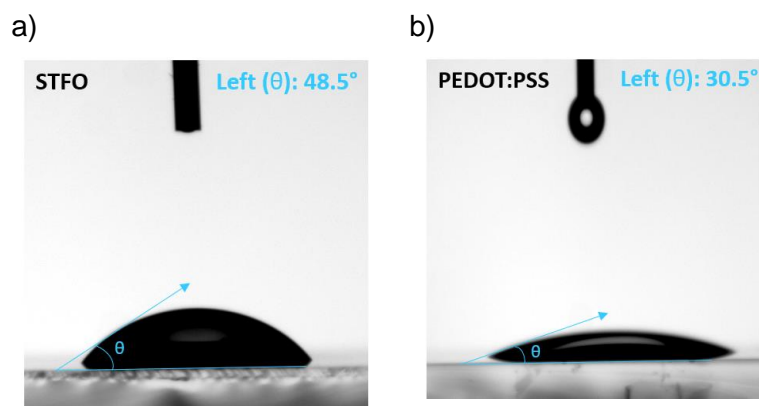
Figure V.1: Contact-angle images with water droplets on a) STFO and b) PEDOT:PSS on glass/FTO substrate

During the contact-angle experiment using DMF as the halide perovskite solvent, no images were obtained due to the rapid wetting of both surfaces. The reason for the different wetting properties of water and DMF on the same surface is due to their varying surface tensions (37.10 mN/m and 72.80 mN/m[318], respectively). For a liquid to effectively wet a surface, its surface tension must be lower than the surface energy of the surface material. For instance, PEDOT:PSS has a surface tension of 73 mN/m[319], which is higher than water, therefore making the surface easily wettable. In the case of STFO, its surface tension is expected to be greater than that of water, but lower than DMF, indicating that it is an ideal surface for DMF deposition.

The deposition of halide perovskite on PEDOT:PSS is well-established as it is used in a broad range of devices in the literature since the last years. However, STFO was not explored in this area before, and optimization may be necessary to achieve homogeneous halide perovskite deposition suitable for optoelectronic applications. The initial attempts to apply the halide perovskite deposition by spin-coating onto STFO thin films, using conventional deposition parameters, were unsuccessful due to the difficulty to spread the perovskite precursor solution uniformly over the surface (Figure V.2a). When precursor is added to the DMF solution, it changes the final surface tension of the solution based on its concentration. Striation defects in thin films created by the spin-coating technique occur due to improper capillary forces generated during the physical processes involved in spinning. As the solvent slowly evaporates during the spinning process, it causes slight changes in the coating's composition, leading to instability in the surface tension. This instability causes lateral movement of the liquid until it reaches a point where it solidifies and freezes within the thickness variations[320]. Various methods can be used as a solution of these cases.
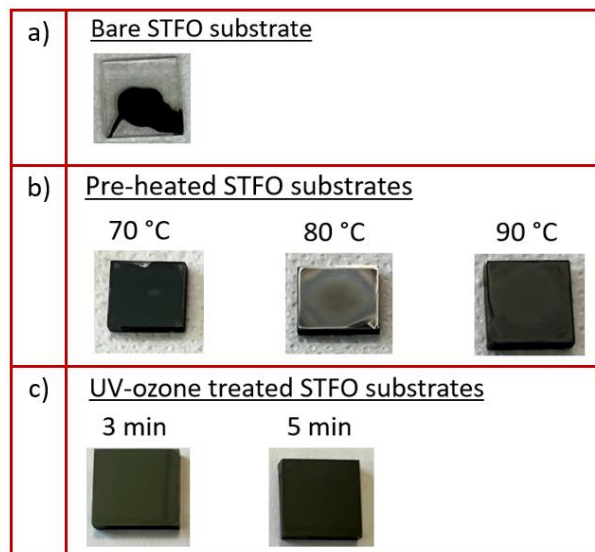
Figure V.2: Halide perovskite deposition on a) bare, b) pre-heated, and c) UV-ozone treated FTO/STFO substrates

As a first option to address the issue, we heated the STFO thin films on a hot plate before applying the halide perovskite coating. The reference annealing temperature range for CsFAPbIBr halide perovskite is 100-150°C. Lower temperatures prior to high-temperature annealing should be used to avoid rapid crystallization. During our experiment, we tested three different temperatures, namely 70°C, 80°C, and 90°C for a duration of 2 minutes. The short annealing process helped to mitigate the problem by enabling rapid, controlled spreading and drying of the solution, as shown in Figure V.2b. Additionally, this process facilitated a more

uniform deposition of the solution on the surface. However, we could not achieve complete surface coverage at 70°C. While at 80°C, we could not obtain a shiny surface as usual. Reducing the amount of light reflected from a surface improves light transmission, but neither completely shiny nor matte surfaces are ideal. In addition, small fluctuations related to antisolvent evaporation in the surface were observed at 90°C.

As a second option to improve the surface coverage can be UV-ozone (UV-O$_3$) treatment. It can alter the surface chemistry, promoting adhesion or enhancing film wettability, making the degree of change crucial on material properties. During the halide perovskite deposition onto STFO, the halide perovskite deposition was applied after treating the STFO thin films by UV-O$_3$ for 3 to 5 minutes. In this case, proper surface coverage was obtained for both cases (in Figure V.2c).

V.1.2. UV-Ozone Effects on Optical Properties of STFO Thin Films

Exposing a thin film to UV light in the presence of ozone (O$_3$) can lead to various effects on its properties, which are dependent on the material type and process conditions. Oxygen-containing functional groups like hydroxyl (-OH) and carbonyl (C=O) groups can be incorporated into the surface of the thin film of STFO. After treatment, the thin film can experience changes in its optical, structural, and electrical properties due to reduced oxygen vacancies, increasing its surface energy. Oxide-based materials such as TiO$_2$, SnO$_2$, and NiO$_x$ have been discovered to undergo changes in their work function and chemical composition after being subjected to UV-O$_3$[321].

In Figure V.3, the optical transparency of the STFO thin films is affected by the treatment duration despite having the same thicknesses (~50 nm). The thickness of the film remained almost constant after the treatment. After the 5-minute treatment, the transparency of the thin film decreased compared to the 3-minute treatment. As the treatment time increases, the level of transparency decreases. Similarly, after 5 minutes of treatment, the halide perovskite-coated sample appeared darker in color, as we observed previously (in Figure V.2c). UV-O$_3$ can cause surface oxidation, leading to a slight decrease in transparency due to changes in the refractive index[322]. In addition, it has been reported that UV-O$_3$ treatment can decrease the number of oxygen vacancies on the surface of oxide materials[191][323]. Also it has the function to remove contaminates from the surface as well. This can lead to an increase in conductivity, but may also result in decrease in transparency. Considering the observed trends, we therefore decided to use a 3-minute UV-O$_3$ process as it has a minimal impact on the optical properties of the material.
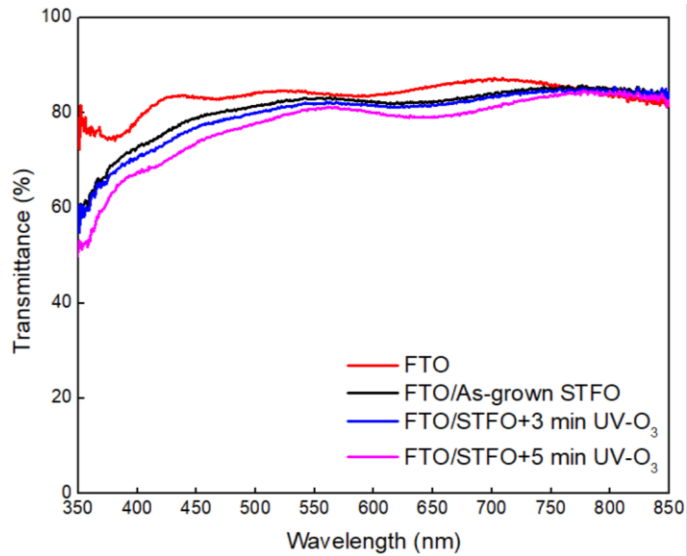
Figure V.3: The effect of UV-O$_3$ treatment on the optical transparency of as-grown STFO thin film

In Chapter 3, we discussed that STFO thin films undergo two additional thermal treatments, namely RTP and TA, which impart distinct characteristics to the films. We therefore now investigate the influence of a UV-O$_3$ treatment on the optical properties of these films. In Figure V.4, the effect of the UV-O$_3$ treatment is consistent and similar for each type of STFO (they are all 50 nm-thick). It is observed that the application time of 3 minutes has a negligible impact on the optical properties, as previously demonstrated which allow us to further validate a common procedure for each of these layers.
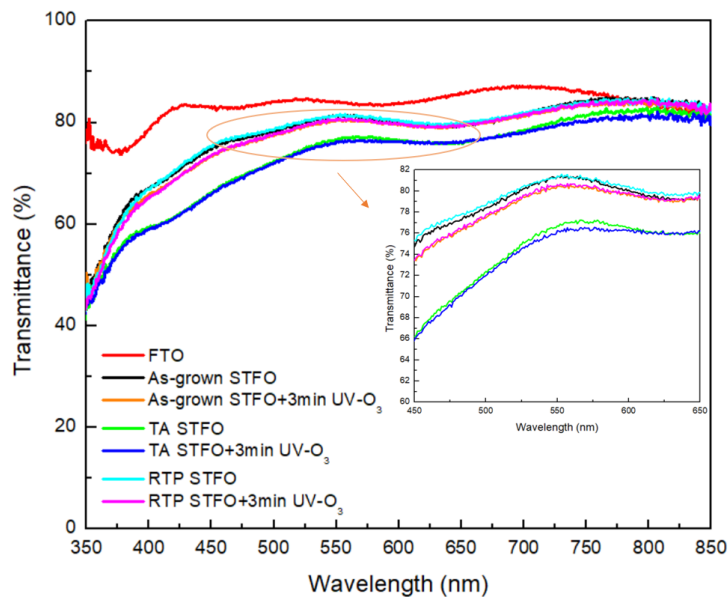
Figure V.4: The effect of UV-O$_3$ treatment (3 minutes) on the optical transparency of as-grown, RTP, and TA STFO thin films

V.1.3. UV-Ozone Effects on Structural Properties of STFO Thin Films

We also examine the impact of the UV-ozone treatment on the structural properties of the films, through XRD patterns presented in Figure V.5.
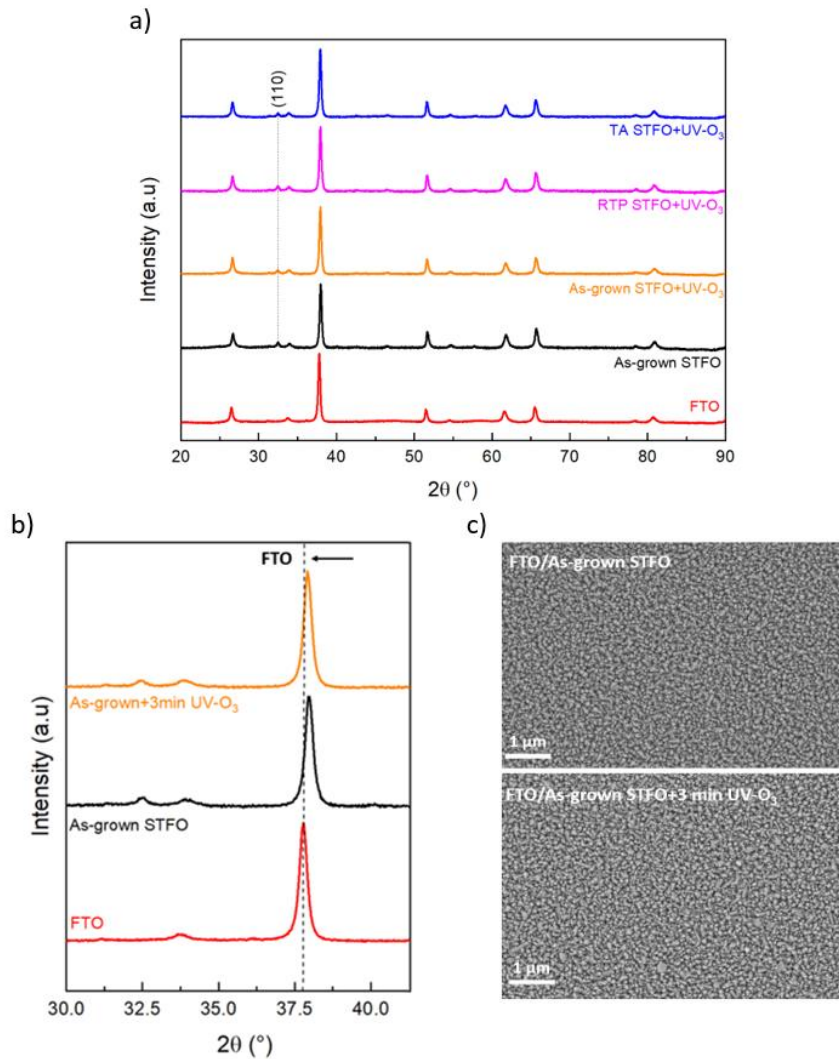
Figure V.5: a) XRD analysis of as-grown, RTP, and TA STFO thin films, b) FTO peak shift on as-grown STFO, and c) SEM images in-plane for as-grown STFO before and after UV-O₃

All STFO types have a thickness of approximately 100 nm in this analysis. There was no difference in the shift of the (110) plane of STFO at 32.3° before and after treatment. However, the peak at 37.7°, which belongs to the FTO, is shifted to 0.02° to the left at 2θ while maintaining its intensity (in Figure V.5b). Surface modification using UV-O₃ can alter the optical properties of a film by changing its surface character, which affects its response to light. This is coherent with the small change in optical properties, which is acceptable as well.

The XRD peak showed a slight shift, but the surface morphology of the film did not undergo significant alterations due to the UV-O₃ treatment, as can be seen in SEM images in Figure V.5c. After undergoing 3 minutes of UV-O₃ treatment, it can be concluded that it alters the surface's chemical properties (i.e. decontamination, oxygen vacancies, surface energy) without affecting the STFO's structural and optical properties.

V.1.4. Structural Properties of Halide Perovskite on STFO Thin Films

After successfully depositing halide perovskite onto STFO using UV-O₃ treatment, the structural properties of STFO/halide perovskite are critical for full device fabrication in the next section. In this part, we will explore the characterization of crystalline quality and grain, respectively.

a. Crystalline properties of halide perovskite on STFO thin films:

The XRD pattern of the CsFAPbIBr halide perovskite film is obtained on various layers, as illustrated in Figure V.6. PEDOT:PSS, STFO thin-film types, and CsFAPbIBr thicknesses are 50 nm, 50 nm, and 500 nm, respectively.
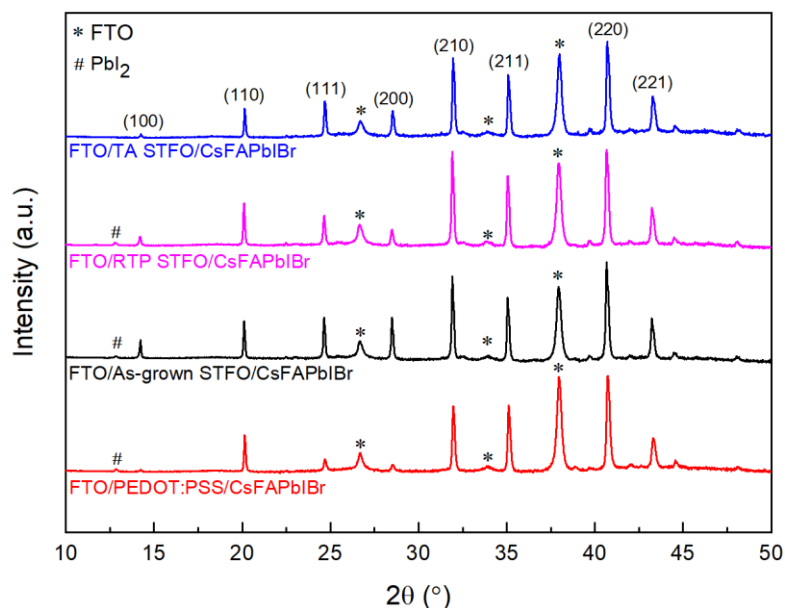
Figure V.6 : XRD pattern of CsFAPbIBr perovskite layer on PEDOT:PSS, as-grown STFO, RTP STFO, and TA STFO

The primary features of the black or α-phase of the CsFAPbIBr film belong to the (100) plane, with the peak positioned around 14.2° in 2θ[291]. The average crystallite diameter is calculated from the Scherrer equation as 7.8 nm, 80.2 nm, 42.2 nm, and 54.7 nm for PEDOT:PSS, as-grown STFO, RTP STFO, and TA STFO based on α-phase. The FWHM of the halide perovskite peak (2θ=14.2°) for as-grown STFO is 0.08°, which is smaller than the FWHM of 0.12° for PEDOT:PSS. Additionally, the values of FWHM for RTP STFO and TA STFO are 0.13° and 0.10°, respectively. The bigger crystalline size and smaller FWHM of XRD patterns indicate less intense crystallinity for STFO thin-film types. There is noticeable reduction in the size of halide perovskite crystals when it is deposited on RTP and TA STFO. As discussed in Chapter 3, the surface roughness of STFO increases slightly after RTP and TA, which can affect the interface growth kinetics between halide perovskite and STFO thin films. When the surface is rough, it can act as fixation points for crystal growth and limit the lateral expansion of grains[324]. This can result in smaller crystals unlike smoother surface of as-grown STFO.

The XRD pattern reveals also significant information about the conversion process of PbI$_2$ to halide perovskite. The PbI$_2$ peak is an identifier of the yellowish at 12.8° in the 2θ which indicate perovskite degradation. It generally observes with degradation mechanism under certain conditions, such as exposure to moisture, heat, or light. It is essential to understand this perovskite-iodide phase transformation for assessing stability. From the XRD patterns, no significant signatures of PbI$_2$ at 2θ=12.8° can be seen for both TA STFO and PEDOT:PSS - based perovskite films. At the opposite, a significant amount of PbI$_2$ is revealed for as-grown and RTP-treated films. TA STFO prevents degradation by suppressing both phase separation and defect formation more than other types can be related to have more cubic crystal expansion.

b. Grain size of halide perovskite on STFO thin films:

Preparing perovskite absorber layers with full coverage, uniformity, and no pinholes is crucial. Therefore, it is crucial to characterize the main physical features of $(FA_{0.85}Cs_{0.15}Pb(I_{0.85}Br_{0.15})_3$, CsFAPbIBr) halide perovskite layers deposited on STFO films, compared to reference layers deposited on classical PEDOT:PSS HTL. SEM images of the halide perovskite top surface are displayed in Figure V.7 as a function of substrate type (PEDOT:PSS or STFO-based FTO/HTL). The thickness of halide perovskite itself is 500 nm, and the HTL thickness is 50 nm in all cases.
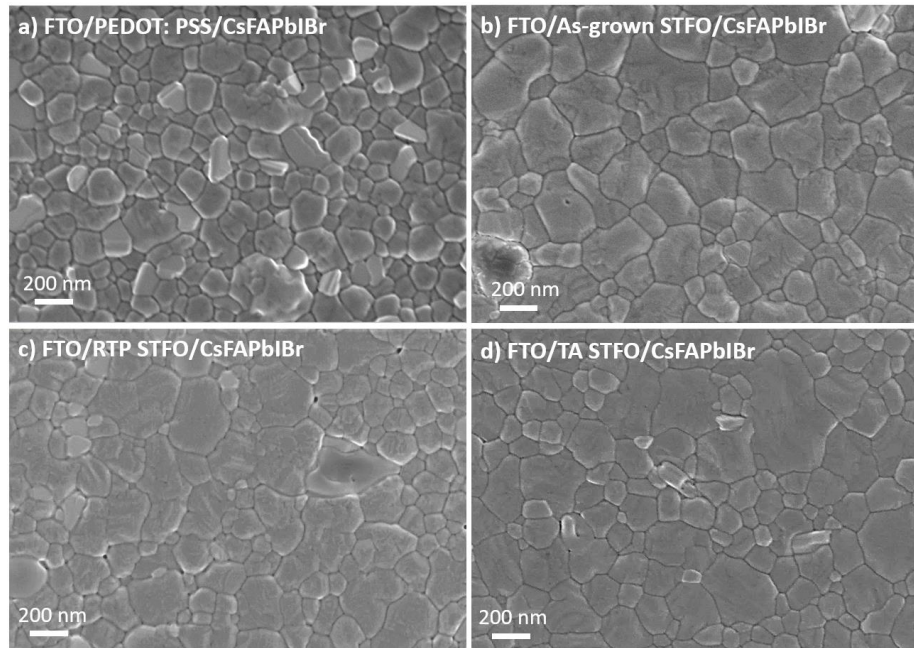
Figure V.7: Top-view SEM images of CsFAPbIBr halide perovskite deposited on a) PEDOT:PSS, b) As-grown STFO, c) RTP STFO, and d) TA STFO

The corresponding average grain sizes of halide perovskite deposited on PEDOT:PSS, as-grown STFO, RTP STFO, and TA STFO are 172 nm, 360 nm, 236 nm, and 333 nm, respectively. The light-absorbing layer in PSCs highly efficient and stable should have grain sizes ranging from 300 nm to 500 nm[325]. Average crystallite size based on (100) plane of halide perovskite aligns with grain sizes of SEM images. It is clearly noticeable that the STFO types (as-grown, RTP, and TA) are more qualitative for grain growth mechanisms and have a significant influence on nucleation, leading to the formation of highly crystalized and large polycrystalline grains in halide perovskite films, as compared to PEDOT:PSS. Furthermore, from SEM images and compared to other STFO types, RTP STFO seems to show few voids (or pin-holes) along halide perovskite grain boundaries. One possible explanation for this phenomenon occurring in only one type of thermally treated samples is the differences in the perovskite solvent evaporation process on STFO thin film surfaces with different surface qualities.

STFO thin films can make a significant difference when integrated into a device. The size of grains in a halide perovskite film is a crucial factor that affects the property of all layers and interfaces of a solar cell. Shortly, halide perovskite materials have the potential to achieve remarkable results, and the key to unlocking this potential lies in their electronic properties. By improving electronic properties by minimizing defects, reducing grain boundaries, less recombination and longer charge diffusion length, lateral charge transport can become more

efficient. These electronic properties, when combined with charge transport layers, directly impact interfacial properties which ultimately determine PV performance. In halide perovskite films with large grain size, photogenerated carriers can easily be collected in large quantities without encountering bulk defects and grain boundaries, where leakage current and charge recombination can be greatly reduced[326]. The grain size affects the fill factor more than the open circuit voltage and short circuit current. Moreover, minimizing the number of grain boundaries can decrease the device's series resistance and prevent charge trapping, resulting in improved photovoltaic performance[327]. To ensure comprehensive analysis, it is important to consider other features such as light transmission and charge transfer kinetics of interfacial in addition to their structural properties.

V.1.5. Optical Properties of Halide Perovskite on STFO Thin Films

The optical properties of halide perovskite (CsFAPbIBr) based on PEDOT:PSS and STFO-types thin films deposited on glass substrate are shown in Figure V.8.

a)　　　　　　　　　　　　　　　　　　　　b)
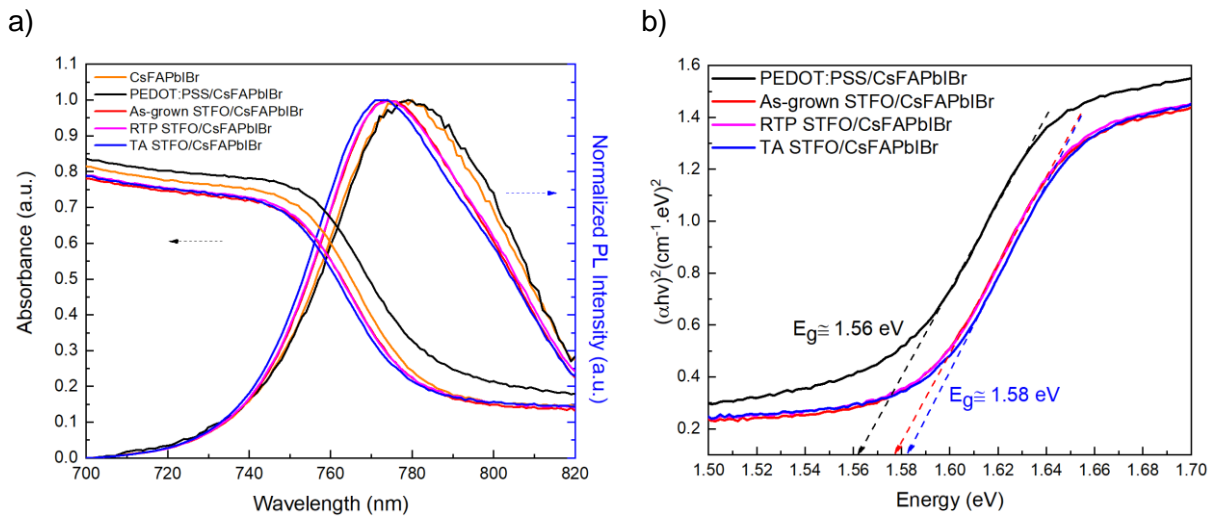
Figure V.8 : a) UV-Vis absorbance and normalized steady-state PL spectra and b) Tauc's plot of CsFAPbIBr perovskite layer on PEDOT:PSS, as-grown STFO, RTP STFO, and TA STFO

Glass/CsFAPbIBr shows a 5 nm red shift compared to glass/PEDOT:PSS/CsFAPbIBr and a 3 nm blue shift compared to glass/STFO/CsFAPbIBr types, although the absorbance curve shape is consistent with expected pattern of STFO thin films. CsFAPbIBr deposited on as-grown STFO has the highest grain size and crystallinity but exhibits lower absorbance. While the grain size of the thin film can impact its optical properties, it is not the only influential factor. Thin film grain boundaries can scatter and absorb light and affect the optical properties in complex ways. In some cases, larger grain sizes can result in reduced absorbance because fewer grain boundaries are present for light to interact with, leading to lower scattering and absorption[328].

According to the steady-state PL, CsFAPbIBr and CsFAPbIBr/PEDOT:PSS exhibit a peak at 780 nm, whereas STFO types exhibit one at 774 nm. There is almost no peak shift between CsFAPbIBr alone and onto PEDOT:PSS, while a small blue shift of 4 nm is observed between STFO types and PEDOT:PSS. The blueshift is due to the filling of the density of states by dynamic free carriers. The observed PL peak positions align with the absorbance onsets in the their absorbance spectra. The STFO types demonstrate sharper unlike non-uniform PL caused by defect formation. As-grown and RTP STFOs display similar behavior, while TA

STFO differ slightly from them. The grain size of halide perovskite film, its crystallinity, and the presence of non-defects can significantly positively impact PL characteristics without fluctuations (CsFAPbIBr and CsFAPbIBr/PEDOT:PSS here) and reduction in intensity. There is noticeable differences PL spectra based on the sublayer thin films and slight variations in absorbance related to the these structural properties of halide perovskite thin films.

It seems that CsFAPbIBr perovskite is able to maintain its phase stability thanks to the absence of photoinduced halide phase segregation with light on. If phase segregation were to occur, it could result in distinct PL emission characteristics in different areas of the material, causing a broadening and/or blue/red shifts in the PL spectrum depending on the composition of the separated phases[329].

As another assumption, research has shown that altering the size of a crystal can have a significant impact on its bandgap[330]. While lattice strain has been suggested as a possible factor affecting optoelectronic properties, the actual underlying cause remains uncertain. In the case of perovskite, smaller crystals within the perovskite layer exhibit a blue-shifted absorbance, indicating that smaller crystals have larger band gaps due to lattice strain. However, no changes in crystal size have been observed based on XRD pattern (Figure V.6). Our findings suggest that the bandgap actually decreases with larger nanocrystalline sizes due to structural effects induced by the surface, which may depend on the orientation of the perovskite PbI_6 octahedra[331].

We also performed time-resolved PL (TRPL) measurements as a tool to indirectly monitor charge transfer kinetics at the halide perovskite/HTL interface. The TRPL decay is influenced by various radiative and non-radiative recombination process in and around a system. The TRPL intensity measured after pulses is the sum of the TRPL intensity after each excitation pulse. The exponential component analysis of PL decay in perovskite thin films can be described by the following function[332]:

$$R(t) = \sum_{i=1}^{n} A_i . exp\left(-\frac{t}{\tau_i}\right)$$

Equation V.1

in which $R(t)$ is number of counted photon in the "t" time, A_i is amplitude of the ith exponential component, and τ_i is the time constant is the component. Multi-exponential decays can be used to fit PL decay.

The literature often reports that a bi-exponential model describes the PL decay of FAPI-based CsFAPbIBr[333][334]. However, it did not fit our measurements due to lower number of counted photon in residual separation part of fitting. To obtain the carrier lifetimes, we fit our calculated TRPL spectra with a tri-exponential decay function, which fits all the calculated spectrum results well. The lifetime of the material is represented by $\tau_{1,2,3}$, while $\alpha_{1,2,3}$ represents the relative amplitude of the lifetime values. One possibility to interpret the global decays is to evaluate the average PL lifetime (τ_{ave}), which can be calculated using Equation V.2 below:

$$\tau_{ave} = \frac{\alpha_1 . \tau_1^2 + \alpha_2 . \tau_2^2 + \alpha_3 . \tau_3^2}{\alpha_1 . \tau_1 + \alpha_2 . \tau_2 + \alpha_3 . \tau_3}$$

Equation V.2

Trap-mediated recombination corresponds to fast decay (τ_3), second-fast or intermaediate decay (τ_2), while radiative recombination corresponds to slow decay (τ_1) which

is dependent on each of the rate constant[332]. All samples except for the as-grown STFO show similar lifetimes for charge transport and interfacial recombination. Figure V.9 and shows the PL decays of layers with three exponential decay models that are used to fit the data and presents the data acquired from Equation V.2.
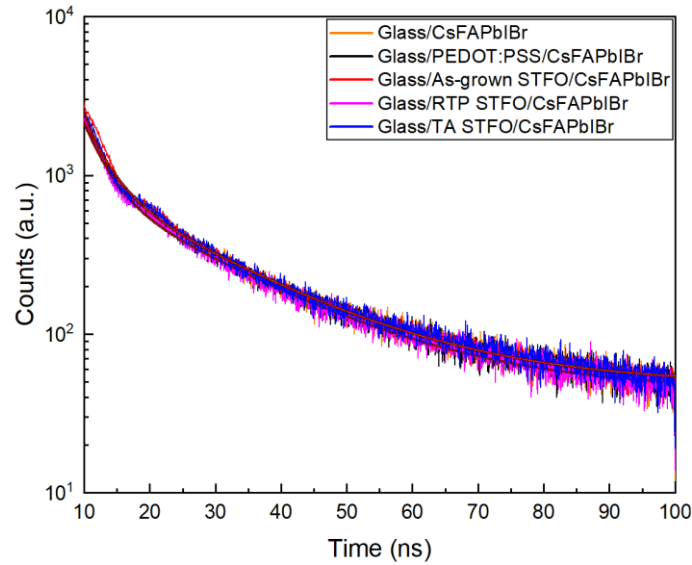
Figure V.9 : Time-resolved PL decay curves of CsFAPbIBr perovskite layer alone and on PEDOT:PSS, as-grown STFO, RTP STFO, and TA STFO thin films

Table V.I : Estimated PL lifetime values of CsFAPbIBr perovskite layer alone and on PEDOT:PSS, as-grown STFO, RTP STFO, and TA STFO thin films

	τ_1 (ns)	p_1 (%)	τ_2 (ns)	p_2 (%)	τ_3 (ns)	p_3 (%)	τ_{ave} (ns)
Glass/CsFAPbIBr	0.4	9.9	3.2	34.0	18.5	56.1	11.5
Glass/PEDOT:PSS/CsFAPbIBr	0.4	9.6	3.1	34.1	18.1	56.3	11.3
Glass/As-grown STFO/CsFAPbIBr	0.3	15.2	2.5	34.7	16.2	50.1	9.0
Glass/RTP STFO/CsFAPbIBr	0.4	10.8	3.2	33.8	18.4	55.4	11.3
Glass/TA STFO/CsFAPbIBr	0.4	8.3	3.0	32.2	17.8	59.4	11.6

Essentially, the as-grown STFO differs from the others by having the shortest average PL lifetime of 9.0 ns. The τ_2 value is reduced by almost 20% (from ~3 ns down to ~2.5 ns) for the as-grown STFO film compared to other layers, indicating slightly poorer film quality than for other samples. When recombination is slow for other thin films, more carriers exists and contribute to charge accumulation at the interface. The number of radiatively inactive channels increases with an increase in polycrystals, indicating that the perovskite kinetics are highly dependent on the morphology of the sample[335]. All samples, expect for as-grown STFO, showed longer charge carrier lifetime when compared to PEDOT:PSS. This indicates that their charge diffusion properties can be higher in device. In addition, the different band gap and XRD pattern characteristics identified earlier suggest that halide perovskite deposited on different properties interlayer may change slightly different compositions over time[336].

V.1.6. Photovoltaic Performance of PSC with STFO Thin Films

As already justified in a previous chapter, the use of STFO thin films as HTL in PSCs requires a specific inverted device architecture which is depicted in Figure V.10a. In this structure, the conventional PEDOT:PSS HTL will be replaced by STFO thin films processed by PLD. For the deposition of halide perovskite, spin-coating remains the preferred method in this work (see device optimization steps in Chapter 4). C_{60} and BCP n-type interfacial layers, as well as Ag top electrode, are deposited through thermal evaporation under vacuum, in a similar way than for the reference PSC (for more information, please refer to Chapters 3 and 4.) We previously discussed about the optical properties of STFO thin films with perovskite. However, it is crucial to also analyze the optical properties of STFO in the device (without metal electrode), as the overall absorption of the fully-assembled device is directly related to the maximum current that can be achieved. Figure V.10b displays the absorbance spectra of CsFaPbIBr, C_{60} and BCP respectively deposited on PEDOT:PSS and STFO thin films with equal thickness (~50 nm). STFO/CsFAPbIBr/C_{60}/BCP exhibits 10% higher absorbance than PEDOT:PSS with the same structure. The previously observed larger grain and higher crystallinity of CsFAPbIBr perovskite on STFO can provide a more continuous and efficient way for light absorption.

a)

b)
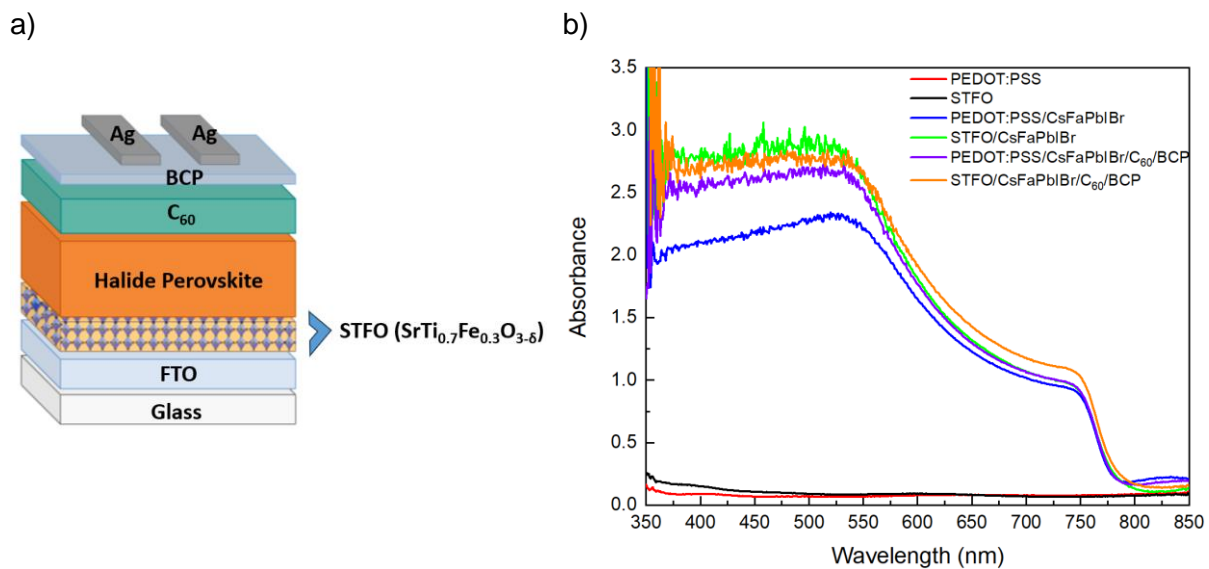
Figure V.10 : a) Inverted PSC architecture illustrating the integration of STFO thin film as HTL and b) absorbance spectra of PEDOT:PSS and STFO-based devices without Ag electrode

STFO thin films with 15 nm, 25 nm, 50 nm, and 75 nm thicknesses were initially tested, based on the classical knowledge of interlayer thickness used for such structures in the laboratory and in the literature. The current density-voltage (J-V) characteristic obtained in the dark (Figure V.11a) indicates that as-grown STFOs with different thicknesses have lower J_{sc} than PEDOT:PSS ($>10^2$ mA/cm^2). Among the different thickness types tested, the highest J_{sc} is obtained for the 25 nm thick STFO sample (~10^2 mA/cm^2), while the lowest is for the 15 nm thick STFO sample (10^0 mA/cm^2) even though it is thinnest layer. 50 nm STFO exhibits continuous leakage due to the absence of barrier reduction of charge potential[337] or it can be possible due to poor shunt resistance. The decrease in J_{sc} for the 75 nm sample could be due to its thickness, which may cause insufficient charge transport.
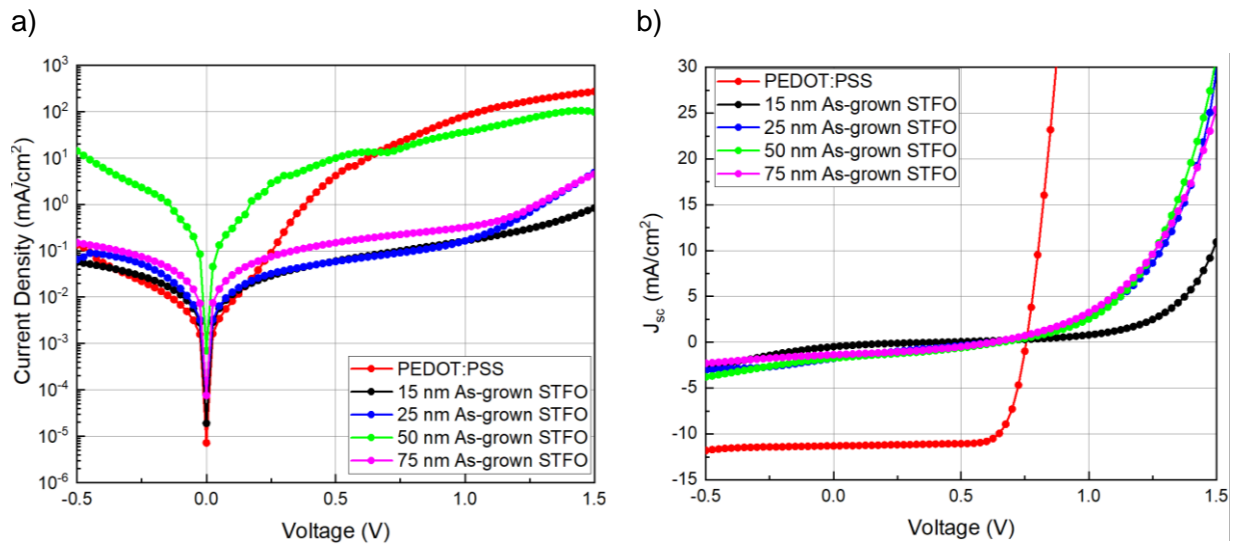
Figure V.11: J-V characteristics of the PSC with STFO thin films of different thicknesses (15 nm, 25 nm, 50 nm, and 75 nm) and by comparison of PEDOT:PSS a) dark condition and b) under 1 sun illumination

Photovoltaic characteristics are finally measured under 100 mW.cm^{-2} (AM 1.5G) of simulated solar illumination. The STFO-based devices display similar behavior, with no clear dependence on layer thickness (Figure V.11b). Despite diode-like behaviors, we observe very poor J_{sc} (< 4.13 mA/cm²), which suggest ineffective current collection in this case. The low current observed in the devices is primarily due to the presence of STFO layers. This is despite the fact that the halide perovskite active layer was similar across all devices. This conclusion is supported by the level of optical absorption shown in Figure V.10b over the visible spectrum. Several factors linked with the HTL can explain such performance, including poor interface quality (from the electronic point of view) with the perovskite layer or with FTO, presence of interfacial trap distributions, poor charge transport properties in relation with the layer thickness, and so on. Inadequate charge transport properties can usually be compensated by tuning the HTL thickness, and indeed we observe different short-circuit current for the different STFO thicknesses. In parallel, V_{oc} is found to be slightly lower for STFO layers compared to PEDOT:PSS, indicating for sure charge recombination or leakage in the corresponding devices. Giving more relevant conclusions remain difficult considering these poorly-performing devices, but these preliminary tests performed on as-grown STFO films indicate that some optimization is required. The thickness of 25 nm can be considered optimal under these circumstances.

In order to try to achieve decent device performance using STFO layers, and considering the previous observations made on as-grown devices, we now discuss the impact of annealed STFO layers on solar cell behavior and performance. To do so, we compare as-grown and TA STFO layers of thickness 15 or 25 nm, as shown in Figure V.12. Annealing the STFO layers was responsible of increasing the structural quality, as already discussed in the previous chapters. Therefore, annealing can also have a positive impact on device performance.

a) b)
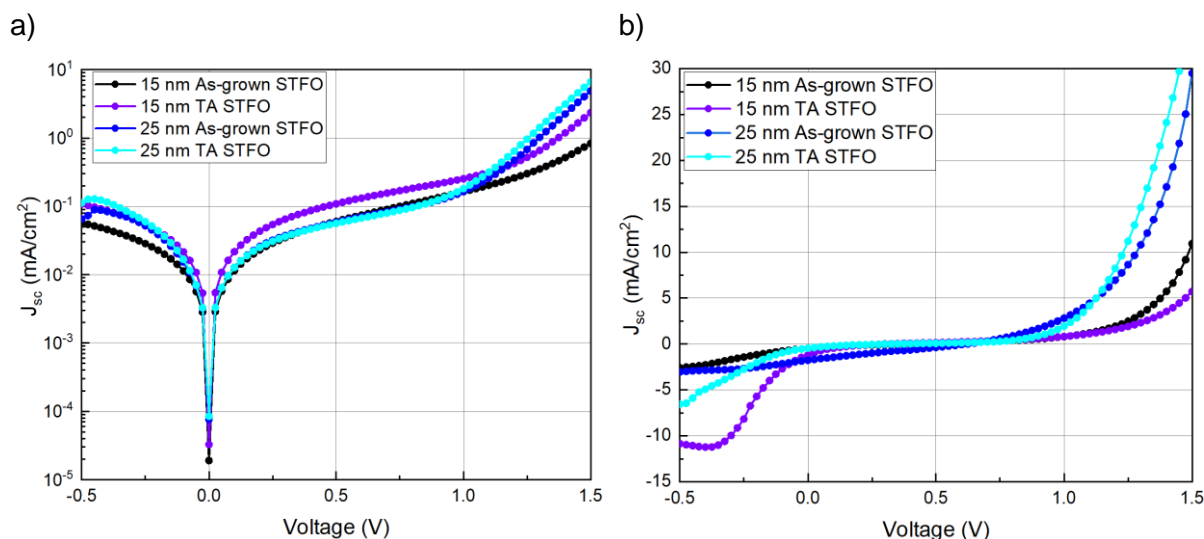
Figure V.12 : J-V characteristics of PSC with as-grown STFO and TA STFO thin films of different thicknesses (15 nm and 25 nm) a) in dark conditions and b) under 1 sun illumination

Thin films with the same thickness display similar rectifying properties and maintain low short current density, as seen in Figure V.12a. Similar to the previous set of devices, the 25 nm thick STFO types exhibit higher short-circuit current densities ($\sim 10^1$ mA.cm^{-2}) compared to 15 nm (in Figure V.12b). As previously discussed, the leakage current (>10^{-4} mA.cm^{-2}) trend of 15 nm STFO is also present in this set of devices as well. However, STFOs treated with TA contributed slightly to short current ($\sim 10^0$ mA.cm^{-2}) density and photocurrent (<10 mA.cm^{-2}) at both thicknesses. Moreover, it is common to exhibits high series resistance (>10^3 Ω) in TA-based devices and facing poor device performance (mainly due to low current levels). Unlike bigger grain size, the issue could be due to the material properties of the STFO or problems arising at the STFO/halide perovskite interface as well. It is also challenging to draw conclusive remarks about STFO-based devices due to the low photocurrent reference in PSC. But an hypothesis can be that the thicknesses chosen are still too high and lead to too high electrical resistance, increasing the resistance in series, and leading to the accumulation of charge carrier at the interface favoring recombination. Unfortunately, when depositing materials using plasma, the plasma plume that is generated initially expands very quickly and changes its properties over time. The exposure time of the substrate to the plasma cloud plays a crucial role. For example, in the case of 15 nm STFO, a shorter exposure time is preferable, but this may lead to lower crystal quality and current density in PLD. In future, the next stage of this work would therefore be to improve the crystallization of very thin layers.

As a conclusion, it was difficult to determine the actual performance of the as-grown and TA STFO thin films due to limited reference PSC performance. The most noticeable aspect of STFO-based devices is their low J_{sc} and it can be due to their low electrical conductivity (10^{-6} Ω.cm^{-1}), which as a first reason affects the charge transport properties of devices directly. The higher conductivity of electron transport material compared to STFO may disrupt charge transfer balance between ETL and HTL. Second reason can be the conductivity type. As mentioned in Chapter 2, STFO is mixed-ionic material and the deposition conditions can impact the conductivity. The oxygen partial pressure used in PLD (9×10^{-2} mbar), which is at the limit of the p-type conductivity and intrinsic properties of. The integration of STFO as HTL into planar structure (FTO/STFO/CsFAPbIBr/Spiro-OMeTAD/Au) has been accomplished and used to indirectly determine the conductivity type. However, non-functioning device has been observed

with this structure either. The characteristic suggest that more precise electrical analyzes are needed. Third one, the device performance can suffer the mismatching in the energy band diagram at STFO and halide perovskite interface. This mismatch increases the energy offset, leading to more charge recombination, which ultimately reduces the device's performance. Additionally to as-grown and TA STFO poor device performance, high resistivity is observed in RTP STFO thin films (see Chapter 3 for more information), making it unsuitable for device applications. Therefore, PeLED will be used for further characterizations and integration into the device as it provides better performance.

V.2. Oxide Perovskites as HTL in Perovskite Light-Emitting Diodes (PeLED)

In this section, we will be discussing the characteristic of quasi-2D perovskite light-emitting diodes based on a quasi-2D halide perovskite emissive layer ($(PEA)_2(MA)PbBr_4$, see experimental details in Chapter 4), for two types of hole injection layers: either the reference PEDOT:PSS or using STFO layers. A first step towards this goal is the achievement of homogenous quasi-2D halide perovskite films on top of STFO HTL. However, we did not face any particular wettability issues during film deposition using the conventional spin-coating process of the quasi-2D perovskite solution onto the STFO surface, thanks to a beneficial combination of factors related to the solution's properties and surface interactions with the STFO substrates. There are variations in terms of adhesive and cohesive forces balance between CsFAPbIBr (the absorber in PSC) and quasi-2D perovskite solutions on the same STFO surfaces. The short reminder of experimental process of fabrication of PeLED with STFO-based device is as follow: 50 nm-thick STFO thin films is first deposited using PLD. If preferred, additional thermal treatments can be applied after deposition. Next, a solution of quasi-2D perovskite precursor (PEA:MA with 1:2 ratio) with a molar concentration 0.5 M is spin coated onto STFO. Finally, TPBi, Ca, and Ag are coated onto the surface in sequence using a thermal evaporator.

V.2.1. Structural Properties of Quasi-2D Perovskite on STFO Thin Films

The larger crystals and grains of the STFO/quasi-2D perovskite's structure is crucial for device fabrication. In this section, we will examine the characterization of crystalline quality and grain.

a. Crystalline properties of quasi-2D perovskite on STFO thin films:

Concerning the structural properties of the samples, Figure V.13 shows the crystal orientation of quasi-2D perovskite films deposited on PEDOT or STFO thin films.
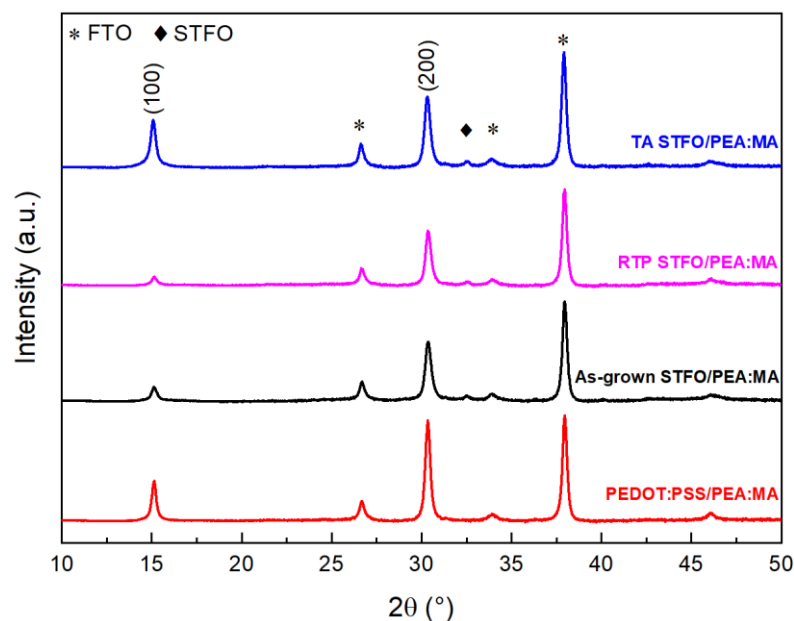
Figure V.13 : XRD analysis of quasi-2D perovskite (PEA:MA) on PEDOT:PSS and STFO thin films

The characteristics diffraction peaks of the (100) and (200) planes for the quasi-2D perovskite are observed at 2θ = 14.8° and 30.3°, respectively. The crystal intensity is higher for TA STFO at the (100) plane and for PEDOT:PSS at the (200) plane. This demonstrates that the quasi-2D perovskite grown on different sublayers shows different microstructures. It has been expected that thin films display varying lattice parameters depending on their orientation. Furthermore, the FWHM values (2θ = 30.3°) for PEDOT:PSS and TA STFO are different: 0.30 and 0.34, respectively. Additionally, PEDOT:PSS exhibits 1.5 times higher diffraction intensity on the (200) plane. This is a consequence of the increased FWHM resulting from the smaller TA STFO crystal. To summarize, PEDOT:PSS exhibits a greater crystal quality as compared to STFO types thin films.

b. Grain size of quasi-2D perovskite on STFO thin films:

The SEM images presented in Figure V.14 show the top view of quasi-2D perovskite thin film layers on different sublayers. The PEDOT:PSS and STFO films are both 50 nm thick, while the quasi-2D perovskite layer ranges from 100 to 120 nm for this characterization.
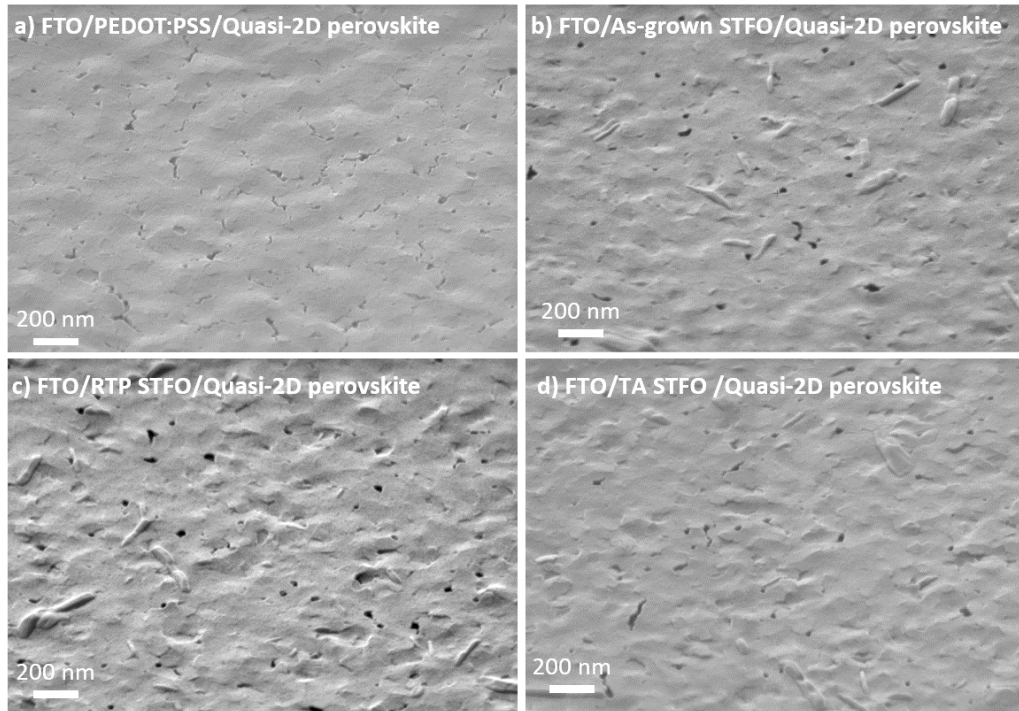
Figure V.14 : Top-view of SEM images of quasi-2D perovskite deposited on a) PEDOT:PSS, b) As-grown STFO, c) RTP STFO, and d) TA STFO

The grains in certain regions are elliptical in shape due to the presence of the large organic cation PEA$^+$, which is hydrophobic. It was established that this causes the precursor solution to have a larger contact angle on surfaces such as PEDOT:PSS and STFO thin films in the literature[338]. As a result, the density of nucleation sites at the beginning of the crystallization phase is lower, but the process itself is not affected[339]. It is evident that STFO thin films are leading to more defects and less uniformity in the quasi-2D layer compared to PEDOT:PSS. However, although pinholes are not visible for the PEDOT:PSS-based sample, the halide perovskite layer shows some cracks at its surface. The lower wettability that was determined earlier may have an impact on this crystallization process. A comparison between STFO films evidences that TA STFO is associated with fewer defects in the halide perovskite film, while RTP STFO has relatively large pinholes ranging from 20 nm to 50 nm in diameter. These pinholes can promote non-radiative charge recombination pathways or even current leakages, which might reduce the efficiency of electroluminescence of the final PeLED.

As a result of structural properties, the quasi-2D perovskite grown on different sublayers shows different microstructures in SEM and correlates with XRD patterns with variation of peaks and their intensity. PEDOT:PSS has a more homogenous surface than STFO types.

V.2.2. Optical Properties of Quasi-2D Perovskite on STFO Thin Films

The effects of different sublayer (PEDOT:PSS and STFO types) on the optical properties of quasi-2D perovskite thin films were studied, as illustrated in Figure V.15.
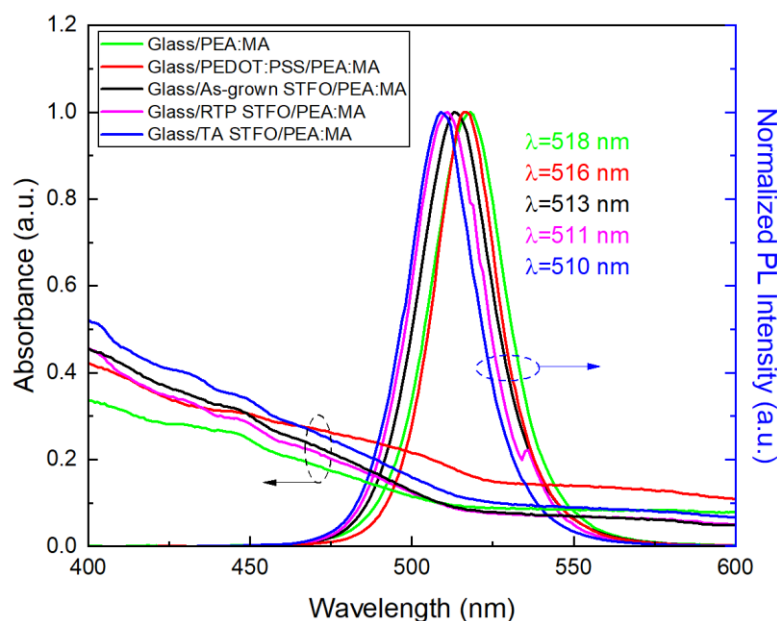
Figure V.15: UV-Vis absorbance and PL spectra of quasi-2D perovskite (PEA:MA) on PEDOT:PSS and STFO films

Regarding to UV-Vis region, a distinct difference in quasi-2D perovskite absorbance on different sublayers can be observed. At wavelength below 450 nm, quasi-2D perovskite on TA STFO exhibits higher absorbance, while at wavelengths above 450 nm, all types of STFO have lower absorbance than PEDOT:PSS. When compared within STFO categories, as-grown and RTP show similar spectra, while TA displays higher absorbance. This may lead to an increased number of charges for PEDOT:PSS and TA STFO-based devices, which may result in more effective radiative recombination.

There are various peaks found between the wavelengths of 400 nm and 520 nm, each defining a particular phase of "n" in the quasi-2D ($PEA_2MA_{n-1}Pb_nBr_{3n+1}$) perovskite structures. For example, the peak at 402 nm represents the n=1 phase, which is a pure 2D phase (only 1 layer of octahedra connected in 2 directions, and separated by the large organic cation PEA^+). Likewise, the peak at 435 nm represents n=2, and the peak at 455 nm represents n=3. In mixed-sized perovskites, such as quasi-2D perovskites, the energy band gaps become nearly identical if the n-phase is equal to or greater than 5[340]. As a result, absorption peaks often have energetic disorder in the measurement process, leading to a shift in the range of 5-10 nm at the absorption edge.

The steady-state PL spectra of all types of thin films exhibit peaks ranging from 510 nm to 518 nm. There is a noticeable blue shift observed from quasi-2D perovskite (PEA:MA) on glass to quasi-2D perovskite deposited on TA STFO. Furthermore, there is a 6 nm blue shift between the peaks of PEDOT:PSS and TA STFO. This shift can be attributed to variations in energy funnels towards the lowest or highest band gap areas due to the change of incorporation of long-chain ligands into the perovskite lattice. In addition, different defects density and crystallite properties (broadening, intensity etc.) can affect the energy cascade in materials (recombination density of excitons and their spatial distribution) and cause changes in the PL spectrum.

TRPL measurements used to monitor exciton injection kinetics at the quasi-2D perovskite/HTL interface, as shown in Figure V.16. It depicts the TRPL decays of the quasi-2D perovskite emission (probed at 51X nm) measured in quasi-2D perovskites deposited on

various HTL films. Additionally, Table V.II provides the average PL lifetime of the samples. Again, the PL decays are adjusted by tri-exponential functions.
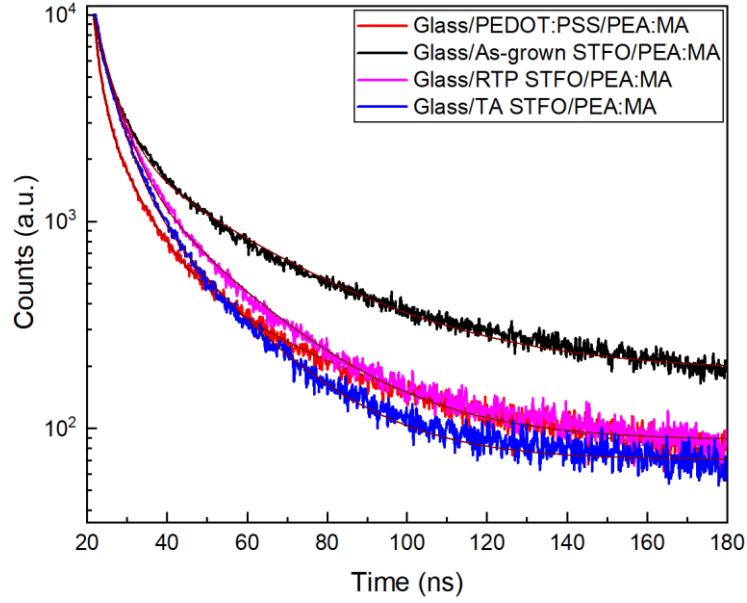
Figure V.16: Time-resolved PL decay curves of quasi-2D perovskite (PEA:MA) on PEDOT:PSS and STFO thin films

Table V.II: Estimated PL lifetime values of quasi-2D perovskite (PEA:MA) on PEDOT:PSS and STFO thin films

	τ_1 (ns)	p_1 (%)	τ_2 (ns)	p_2 (%)	τ_3 (ns)	p_3 (%)	τ_{ave} (ns)
Glass/PEDOT:PSS/PEA:MA	1.6	16.4	7.7	41.1	35.8	42.5	19
Glass/As-grown STFO/PEA:MA	2.7	14.3	11.5	36.9	48.8	48.9	28
Glass/RTP STFO/PEA:MA	2.6	16.2	9.7	50.1	34.8	33.7	17
Glass/TA STFO/PEA:MA	2.7	20.3	8.7	50.6	28.8	29.1	13

As a brief reminder about tri-exponential functions, τ_3 is the fastest decay and τ_2 is the second-fastest decay which are caused by trap-assisted recombination. τ_1 is the slowest decay and is related to radiative recombination. The outcome obtained from PEDOT:PSS is line with the findings of the literature[341]. Average PL lifetime based on PEDOT:PSS and RTP STFO have quite close values. While RTP STFO stands out with trap-mediated recombination, PEDOT:PSS is more efficient in radiative recombination property. In addition, the PL emission and decay are in agreement with each other. As shift move towards the blue part in the emission spectrum (from PEDOT:PSS to TA STFO-based quasi 2D perovskite), the average PL lifetime decreases. The blue shift of PL spectra can be due to faster excitons loading of the quasi-2D perovskite interface with TA STFO, resulting in a shorter excitation lifetime as it gets longer towards the TA STFO spectrum. This situation leads to non-radiative recombination[342]. Moreover, the τ_2 component of as-grown STFO decays faster than other thin films. The average PL lifetime of as-grown STFO is calculated to have τ_{ave}= 28 ns. This particular species of quasi-2D perovskite on as-grown STFO is considerably different from others in terms of its trend. The charge transport mechanism is slow and inefficient. This may be attributed to the

crystallinity and surface morphology of the quasi-2D perovskite with as-grown STFO, as well as the impact of contact between their interfaces. Consequently, additional thermal annealing is required for effective interface transfer by passivating trap states and enhancing radiative recombination.

To summarize the main findings from various physical characterizations of the STFO layers and the properties of the quasi-2D perovskite emitter layer, it can be concluded that TA STFO has different features from as-grown and RTP in terms of less defect, more homogenous surface and higher crystallization quality. It is important to note that the optical properties are different from the structural properties. Although quasi-2D perovskite on PEDOT:PSS and TA STFO have lowest defect density and close absorbance, a blue shift of 6 nm was detected in PL spectrum from PEDOT:PSS to TA STFO side. This can be due to TA treatment of STFO that resulted in an enlargement of the cubic grain shape related to less local deformations in the crystal structure associated with the bending of the Pb-X-Pb bond angles with high symmetrical cubic lattice[343]. The fact that TA STFO has the shortest average PL lifetime may be a consequence of this case. Moreover, quasi-2D perovskite on as-grown STFO showed the longest lifetime with out of trend related to non-radiative recombination. The average PL lifetime of quasi-2D perovskite deposited on as-grown STFO is 47% longer than that of PEDOT:PSS. In the upcoming part, STFOs will be integrated into PeLEDs, and their performance in the device will be investigated.

V.2.3. Electroluminescent Performance of PeLED with STFO Thin Films

Figure V.17 illustrates the PeLED architecture used in our work to assess the potentialities of STFO thin films as HTL. $(PEA)_2(MA)PbBr_4$ quasi-2D perovskite is used as the emissive layer and STFO oxide perovskites are used as HTL and compared to PEDOT:PSS-based reference devices (see Chapter 4).
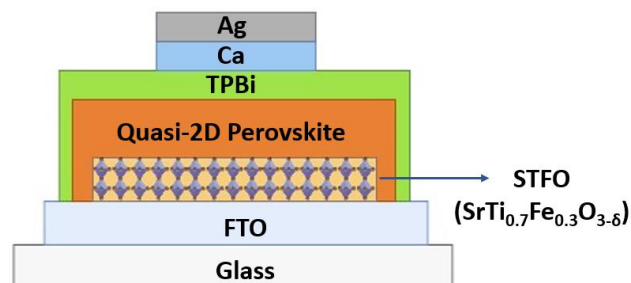
Figure V.17 : The integration of STFO thin film as HTL in PeLED structure

Initially, the integration of STFO into the PeLED device was made using three different film thicknesses, namely 25 nm, 50 nm, and 75 nm, based on our know-how on LED processing. Figure V.18 presents the corresponding electrical characteristics of the devices.

a)

b)
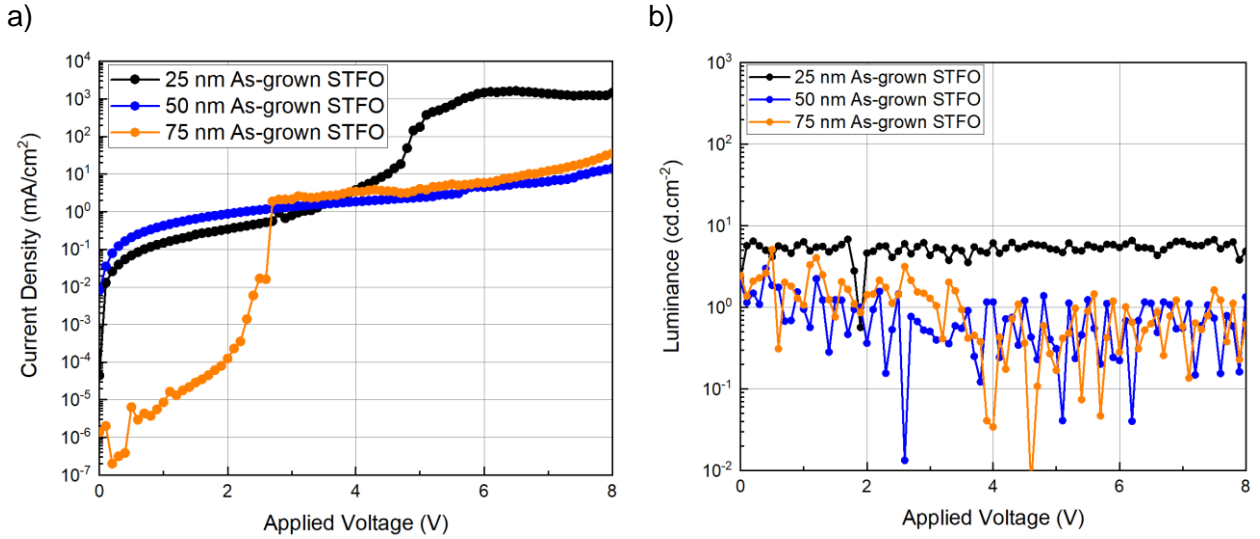
Figure V.18 : a) J-V and b) L-V characteristics of 25 nm, 50 nm, and 75 nm STFO-based PeLEDs

Regarding to J-V characteristics (in Figure V.18), only the devices that had a thickness of 25 nm of STFO demonstrated a high leakage current (>10^{-4} mA.cm^{-2}) and a high current density of 10^3 mA/cm^2 at turn on voltage (V_{ON}~4 V). The STFO with 50 nm thickness exhibited lower leakage current (~10^{-2} mA.cm^{-2}) and current density (10^1 mA/cm^2) compared to the 25 nm STFO. However, turn-on voltage increased from 4V to 6V, indicating a decrease in the radiative recombination. 75 nm STFO showed fluctuations even after multiple tests with different devices. This could be due to the increase in grain size caused by PLD process long deposition time compared to 25 and 50 nm thickness, resulting in a rough surface and interface problems within the device. Upon examining the L-V characteristic, it was observed that the luminescence (<10 cd.m^{-2}) was present even before any optimization with 25 nm STFO. This device represent the first PeLED working with STFO as HTL. Therefore, 25 nm thickness was chosen as reference thickness further device optimization.

In Figure V.19, the J-V and L-V characteristics of electroluminescent devices using PEDOT:PSS and 25 nm as-grown STFO as HTL are shown.
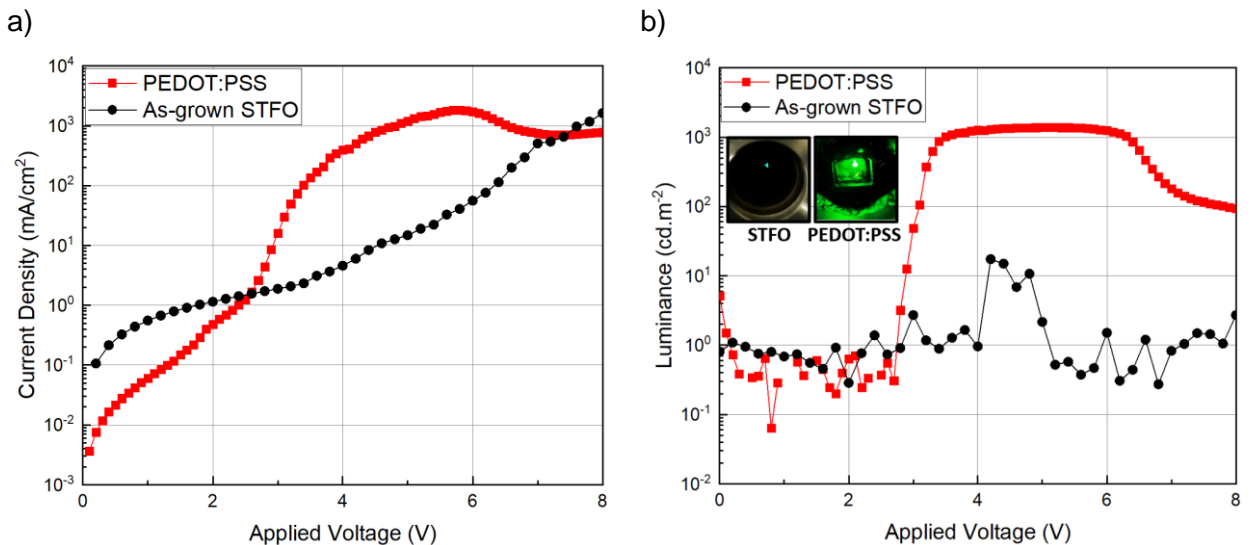
a)

b)

The PEDOT:PSS has a decent performance with 1000 cd.m^{-2} at 3V with a high homogenous and brightness surface. This performance is typical for this type of devices. STFO's device performance is limited luminance (<10 cd.m^{-2}) at V_{ON}= 4V. STFO-based devices require a higher voltage to be activated compared to PEDOT:PSS. These voltages are related to the emissive material properties, but also to the potential energy barriers for charge injection, including charge recombination losses.

Interestingly, STFO-based emission is not uniformly distributed over the active area of the device and is only observed at the edges of the device's active area, as shown in the inset image (left image). This demonstrates that ion migration is not efficient within the emissive perovskite layer or at the interfaces under the electrical field[344]. Moreover, variations in the electric field within the device can cause inconsistencies in charge injection. If the STFO thin film contains regions with different field strengths, it may exhibit diverse emission characteristics[345]. Micro-shunting paths and leakage current are the typical reasons for there cases. Pin-holes in the active area of the device or in the interfacial layers can be the root cause. As we mentioned previously, small sizes of pin-holes observed on quasi-2D surface morphology when it is deposited on STFO thin film, which is linked to leakage current. Energy barriers within the device and issues with STFO/quasi-2D perovskite interfaces may be contributing to factors.

Our objective now is to comprehend the reason behind the poor device performance. As previously establish, the quasi-2D perovskite that was deposited on TA STFO exhibited the less defects (i.e. pin-holes and cracks) and more homogenous among all the STFO types. To achieve this proper device performance, we have used TA STFO thin film as the HTL in device. Figure V.20 shows the electrical characteristics of PeLEDs with TA STFO based on 25, 50, and 75 nm thicknesses.

a) b)
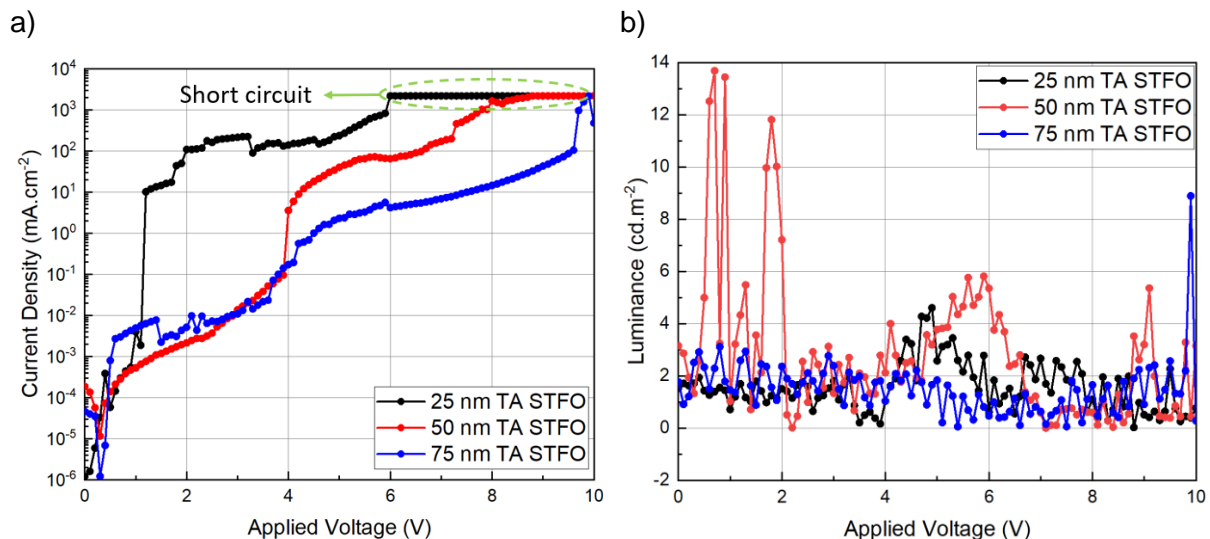
Figure V.20: a) J-V and b) L-V curves of PeLEDs with 25, 50, and 75 nm TA STFO as HTL

The characteristics of devices based on TA STFO can vary significantly over a wide range of values, both electrically and optically. The device's very low brightness and fluctuating current density can be attributed to easy decoupling, which can occur due to poor device

quality and problems with device interfaces. For instance, 25 nm TA STFO short-circuited within a very short period (after 6 V) while the PeLED was operating. TA STFO was determined to have the shortest PL lifetime unlike its surface homogeneity and higher crystallinity. The reason behind is that TA STFO/quasi-2D perovskite interface can have low quality (i.e. strain, bad contact) and degrade after a very short exciton transfer due to the heating effect caused by local charge accumulation[346].

Among the different hypotheses raised to understand the poor performance of the device based on our STFO layer, the electronic properties of the oxide perovskites can play a major role in the optoelectronic properties of the final LED. In particular, STFO commonly have oxygen vacancies or surface defects, which can hinder their performance. Indeed, when a voltage is applied, oxygen vacancies can move under the electric field, accumulating at the oxide perovskite/quasi-2D perovskite interface. This space-charge build-up effect can slow down charge injection and affect device functionality[347]. Surface modification techniques like coating with another layer[348] or using UV-ozone treatment[349] are generally used in literature to address the issue. The use of oxide-based charge injection layers, often in combination with other materials for surface enhancements or passivation is also a common method in the literature (for more details, please refer to Chapter 1). For instance, NiO_x deposited with sputtered often has uncontrollable defects and to improve its interface with perovskite, interlayer deposition is often used[350]. This techniques can help optimize the interface and reduce the defects of STFO associated with PLD. Additionally, it can help the possible mismatching issue of energy band-diagram due to missing information about VBM and CBM of STFO.

In our study, we aimed to better understand the limitation of our 25 nm-thick STFO by combining it with a 50 nm thick PEDOT:PSS layer , as presented in Figure V.21. All other steps are performed as in the reference device of PeLED.
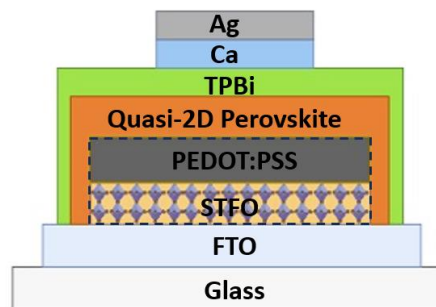
Figure V.21 : PeLED device structure using STFO/PEDOT:PSS as HTL

In Figure V.22, we compare the J-V and L-V characteristics of the as-grown STFO/PEDOT:PSS dual structure, used as the HTL, with those of the reference device based on the classical PEDOT:PSS HTL.
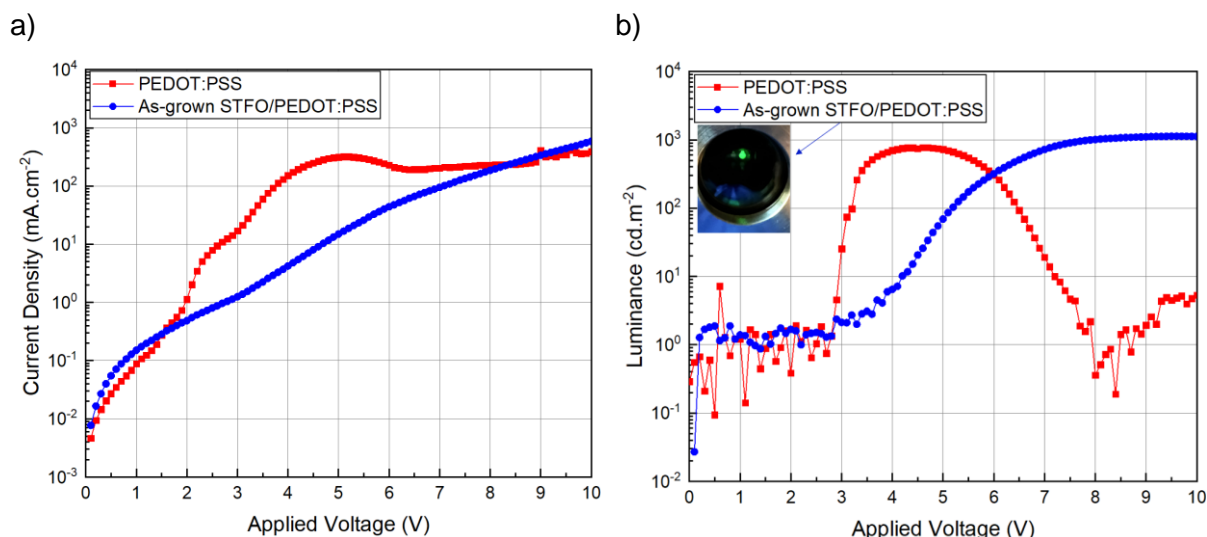
Figure V.22 : a) J-V and b) L-V curves of PeLEDs with reference PEDOT:PSS and as-grown STFO/PEDOT:PSS combination as HTL (Inset: Image of operational as-grown STFO/PEDOT:PSS combination with full emission)

The J-V curves of dual structure of the devices exhibit a weak diode characteristic with an exponential leakage current at low driving voltages (<2V). This implies that high current density is necessary to functionalize the device. The dual device exhibits additional current limitation, which may be attributed to the poor conductivity of the STFO. However, using STFO in dual structure does not have any negative impact on the performance of the device. The L-V graph shows that the noise in the device is significantly reduced compared to when PEDOT:PSS is used alone. Both device types produce similar luminance levels ($\sim 10^3$ cd.m^{-2}). Even devices of the same type can have the same differences. Nevertheless, the effect of STFO on the device is not yet clear.

Our primary goal is to improve the stability of devices using inorganic oxide perovskites, which are known for their robust structure and superior stability compared to organic HTL. Ensuring stability is quite important for long-term performance and durability of perovskite optoelectronic devices. On the other hand, on a longer timescale, various mechanisms contribute to the degradation of PeLEDs, including cation migration at area of grain boundaries, electrochemical reactions, interfacial reactions and electrode corrosion[332]. To prevent the interaction between the unbound surface oxygen in FTO and the ionized hydrogen atom (H$^+$) of the sulfonic acid in PEDOT:PSS, it is common to integrate interlayers such as SAM[351], MoO$_x$[163], and LiF[352] between the two. Therefore, STFO/PEDOT:PSS dual structure can also help overcome the limitation of PEDOT:PSS. After fabricating and characterizing the performance of PEDOT:PSS and STFO/PEDOT:PSS dual structure, the samples stored a shelf life during two months. They were kept in dark and nitrogen filled atmosphere inside the glove box. The change in performance of the PEDOT:PSS and STFO/PEDOT:PSS devices over a span of 2 months, as presented in Figure V.23.
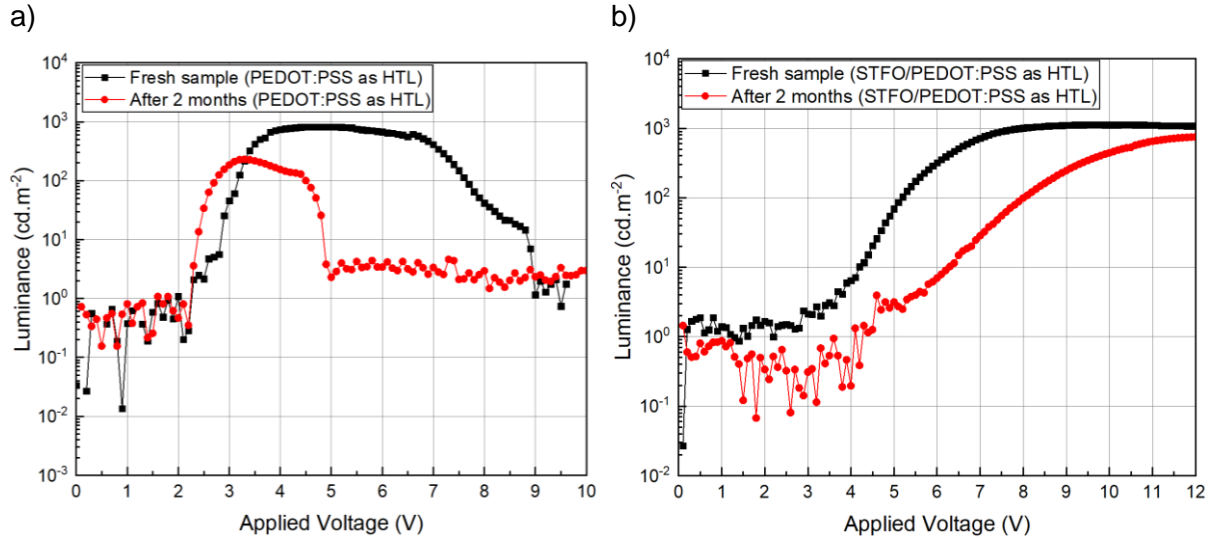
Figure V.23 : Time-dependent L-V curves of a) PEDOT:PSS and b) STFO/PEDOT:PSS dual structure as HTL for PeLED

The maximum luminance of PEDOT:PSS right after fabrication (fresh sample) was 818 cd.m^{-2}. However, after two months of shelf life, it decreased to 228 cd.m^{-2}, which means 72% performance losses. On the other hand, the STFO/PEDOT:PSS dual structure had 1117 cd.m^{-2} maximum luminance for fresh sample, which decreased to 737 cd.m^{-2} after two months. This means that dual structure only suffered a 34% performance loss. In addition, non-fresh PEDOT:PSS sample has a significantly shorter emission time and its emission starts decaying rapidly at almost ends of 5 V.

This technique not only protects the device from acidic damage of PEDOT:PSS but also improves the low charge transfer capacity due to the low WF of PEDOT:PSS. The energy-band balance is more harmoniously tuned, resulting in better device stability due to less charge accumulation at the interfaces. Not only did the WF balance have a positive impact on the charge transfer capacity, but the longer PL lifetime feature we determined previously in STFO also contributed to this improvement. Additional, halide perovskite can degrade over time and halide ions starts to migrate to other interlayers. STFO can help in reducing the density of halide ion migration to FTO thanks to its high chemical stability. Before drawing any definitive conclusions, a more comprehensive investigation such as XPS and SEM is required to identify presence of degradation states. Additionally, detailed stability analysis, such as time-dependent luminance under operation, is necessary to determine the degradation processes.

V.3. Conclusion

This chapter discussed the optical and structural characterization processes of STFO-type oxide perovskite and their assessment to be used as HTL in combination with $FA_{0.85}Cs_{0.15}Pb(I_{0.85}Br_{0.15})_3$ halide perovskite (in PSC) and $(PEA)_2(MA)PbBr_4$ quasi-2D perovskite (in PeLED). In addition, a comparison was made between the commercial PEDOT:PSS, which is one of the best-selling hole transport materials, to investigate its advantages and drawbacks. These processes were required before integrating the oxide perovskite into perovskite optoelectronic devices. Finally, the integration of STFO thin films was carried out.

Regarding to photovoltaic part, when CsFAPbIBr perovskite was deposited on STFO thin film types, it resulted in structures with high crystallinity and grain size compared to PEDOT:PSS. Among these, it was found that TA STFO strongly suppressed the yellowish phase (PbI_2) related to degradation mechanism. This could be attributed to the fact that TA additional thermal treatment on as-grown STFO increased the expansion of cubic grains, as previously determined. The symmetry and regularity of the cubic lattices facilitated the growth of high-quality crystals with fewer defects. CsFAPbIBr perovskite was delayed, suppressing both defect formation and phase separation. Furthermore, STFO types distinct optical properties following CsFAPbIBr perovskite deposition. The band gap values are nearly identical for as-grown and RTP STFO (1.57 eV), and slightly higher compared to TA STFO (1.58 eV). This is attributed to the varying orientation of perovskite PbI_6 octahedra across the STFO types and shorter crystal length in TA STFO. In summary, they have different crystal growth mechanism that can be related to difference of homogeneity of surface individually. Lastly, thin films of the CsFAPbIBr perovskite deposited on RTP and TA STFO, exhibit long-lasting radiative degradation properties due to their advanced structural and interface compared to PEDOT:PSS. Although the PSC integrated STFO showed solar cell behavior, its performance was limited particularly with respect to J_{sc}. In conclusion, STFO interface quality with halide perovskite or FTO, the presence of interfacial trap distributions, and the possibility of poor charge transport properties should be analyzed related to this issue.

Regarding to electroluminescent part, quasi-2D perovskite on TA STFO is distinct from other types due to the presence of nanograins, well-defined crystal structures, and lower defect density in terms of structural properties. It has also a higher absorbance after 450 nm, which can lead to an increased number of excitons and more radiative recombination. However, it was found to have the shortest PL lifetime. TA STFO can have interface problems with quasi-2D perovskite due to its higher roughness or slightly higher resistive characteristic which can be a limit. On the other hand, as-grown STFO has the longest exciton lifetime of 28 ns, which can help to prevent radiative recombination in device. For electroluminescent performance, emissive PeLEDs were produced with STFO, which exhibited inhomogeneous emission only at the edge of the active area. To solve this problem, PEDOT:PSS deposition on STFO was applied as a passivation layer, resulting in full emission. STFO had a positive impact on the device stability over time. PEDOT:PSS lost 72% of its performance after two months of shelf life, while STFO/PEDOT:PSS lost only 34%. This dual structure can offers some advantages such as energy band balance, improvement of exciton lifetime time of device thanks to STFO passivation or non-radiative recombination, and decreasing the density of halide ion migration from emissive layer to FTO due to the chemical stability of STFO.

These findings represent a promising initial effort in recognizing the strong potential of STFO thin films as HTL in perovskite optoelectronic devices.

Conclusion

Halide perovskite-based devices have a low chemical stability, resulting in rapid degradation during operation. The commonly used p-type interlayer poses significant challenges in this regards. It is essential to develop innovative p-type interlayer materials that offer high photochemical stability and tunable properties. This work focuses on the development of $SrTi_{0.7}Fe_{0.3}O_{3-\delta}$ (STFO) type oxide perovskite as p-type interlayer in halide perovskite optoelectronics, aiming to improve device stability.

A main challenge associated with optoelectronic application arises from the requirement to use transparent conductive oxide of poor thermal stability, which limit the range of processing temperatures below 450-500°C. While using inorganic interlayers such as perovskite oxides is particularly relevant to stabilize device operation in ambient conditions due to their excellent photochemical stability, it requires the development of efficient deposition techniques at low temperatures to achieve the desired optical and electrical properties. Pulsed laser deposition process has been used for the development of STFO perovskite oxide films under controlled oxygen partial pressures. This process corresponds to a physical vapor deposition method using laser irradiation on a target with the formation of a plasma plume composed of atoms and ions. Although high-temperature processing is usually required for the deposition of oxide material (>700°C), in this study, the crystallization of thin film has been achieved at low temperatures (~400°C) by our specific method with damage-free FTO. The ideal conditions for achieving high crystallinity, a pinhole-free, dense, and homogeneous surface with low roughness in STFO thin films are 400°C at 9×10^{-2} mbar of oxygen partial pressure.

STFO thin films exhibit a characteristic peak (110) plane in the body-centered cubic unit cell, which is one of the most common structures for perovskites due to its high symmetry. In addition, these films display high optical transparency (>75%) in the visible regime, even at high thickness (~100 nm). All STFO films demonstrate an indirect and wide band gap between ~3.1 to 3.6 eV material properties. Its work function was evaluated at 4.90±0.05 eV, which is quite close to that of the reference PEDOT:PSS interlayer, confirming the suitable electronic properties of STFO for the targeted applications.

Additional thermal treatments have been applied to the films to support grain growth and tune the optical-electrical properties via rapid thermal process (RTP) and conventional annealing (TA). The RTP annealing method can reach high temperatures with a very fast ramp based on flashes using a high-intensity infra-red lamp. After applying two different thermal treatments, RTP and TA, on as-grown STFO, the roughness of the thin films increased from 20 to 33%, respectively. Furthermore, it has been observed that the cubic grain size expands and thin film optical transparency decreases ~4% after conventional TA. Changing the transparency can be attributed to two different reasons. Firstly, there is an increase in absorbance due to cubic grain growth or expansion, and secondly, there is an increase in roughness, which causes isotropic light scattering, ultimately leading to a decrease in transparency. The current density-voltage characteristics can help in studying the properties of electron and hole transport, injection, and production of charge carriers. It was found that among the thin films that were studied using space charge limited current (SCLC) method to investigate their electrical properties. The as-grown STFO showed a trap-free transport regime, while RTP and TA STFO showed trap-limited SCLC characteristics. However, it is important to note that as-grown STFO did not exhibit linear or SCLC regime in the 2V-6V. It is

likely that SCLC regime would be observed at higher voltages, but the severe joule effect prevented us from reaching such as regime. Additionally, it was observed that RTP surprisingly decreased electrical conductivity, while TA slightly increased it among the thermal treatment.

Additional thermal treatments are anticipated to reduce the resistive characteristics of materials by enhancing their crystallinity, decreasing their defect density, and softening their grain boundaries. However, the distinction between RTP and TA lies in the annealing time. The process of filling oxygen vacancies in oxide perovskites is time consuming. In contrast, the very rapid temperature rise of RTP, coupled with short annealing time of just 100 seconds, is insufficient for oxygen diffusion into the thin film. During the annealing process, the RTP pressure drops to lower levels, leading to a deficiency of oxygen. This is attributed to the absence of inert gas (oxygen) in the process. Consequently, the oxygen deficiency can significantly impact electrical conductivity and it reduces after RTP.

Two reference devices were created before integrating STFO thin films into perovskite optoelectronic devices. The first reference device was an inverted solar cell which was developed using different materials for HTL, metal electrodes, and ETL. The second reference device was a green PeLED that achieved decent luminance using previously developed quasi-2D perovskites, resulting in reliable benchmark devices with high reproducibility.

Firstly, before focusing on the photovoltaic performance of devices based on STFO HTL, we initially explored the influence of STFO properties on the structural and optical properties of the $FA_{0.85}Cs_{0.15}Pb(I_{0.85}Br_{0.15})_3$ halide perovskite active layer itself. It shows larger grain sizes and better crystallization when deposited on STFO substrates, compared to PEDOT:PSS. Such an effect can be a direct consequence of the perovskite nature of the active and oxide interfacial layers. Additionally, TA STFO significantly reduces the formation of the yellowish PbI_2 phase, indicating a better conversion of the precursors into the expected halide perovskite phase. We attribute this effect to the fact that TA STFO induces fewer distortions of halide perovskite, leading to suppressing or limiting δ-phase separation and surface defect formation. Such observation was found to be highly promising for integration into the final devices. From the optical point of view, we observed a reduced absorbance of the halide perovskite active layer when deposited on top of all types of STFO substrates (as-grown, or non-annealed), compared to PEDOT:PSS-based substrates. This phenomenon is attributed to the presence of fewer grain boundaries in layers presenting larger grain sizes, leading to lower scattering and absorbance. Moreover, halide perovskite films deposited on TA and RTP STFO show a longer photoluminescence lifetime compared to PEDOT:PSS and as-grown STFO. Finally, and for the first time, we integrated STFO thin films grown on FTO substrate as a p-type interfacial layer in p-i-n inverted perovskite solar cells and compared device performance with regard to reference devices based on PEDOT:PSS. While poor photovoltaic effect is evidenced in all types of STFO-based devices, we discuss the main assumptions for performance limitations responsible for poor short-circuit current densities. Halide perovskite solar cells with STFO interlayer have shown poor solar cell characteristics, particularly in terms of current density. There can be multiple primary reasons for this. Despite numerous attempts to evaluate the material type properties of the STFO layer, consistent results have yet to be obtained. It is possible that the low current may be attributed to the weak p-type characteristic of the film. It can also be their low electrical conductivity due to the oxygen and low Fe (30%) stoichiometry of thin films.

Secondly, before the final integration into devices, we started by evaluating the influence of the STFO layers on the quasi-2D $(PEA)_2(MA)PbBr_4$ perovskite film, from the

morphologic, structural, and optical point of view. Although, quasi-2D perovskite onto PEDOT:PSS has a higher crystal quality than both as-grown and RTP STFO type thin films, it has similar structural features to TA in terms of high crystallinity and homogenous surface. It is surprising that the average PL lifetime of quasi-2D perovskite on as-grown STFO is 47% longer than PEDOT:PSS, which goes against the trend. This drawback implies that an HTL may offer inefficient longer charge transport, leading non-radiative recombination.

In the first green PeLED created with STFO as HTL, homogeneous emission was not observed. This could be due to non-radiative recombination losses occurring frequently on the radiative path due to energy barriers in device and the interface problems. To address inhomogeneous emission issue, a dual structure was created with PEDOT:PSS to solve any possible interface problems of STFO and provide surface passivation of oxides. Efficient green PeLED devices were demonstrated for the first time using a dual STFO/PEDOT:PSS HTL. Homogeneous light emission over the entire active area was observed, with luminance values above 1000 cd/m² indicating the possibility of effectively directing current toward the active layer using a perovskite oxide-based interface. The threshold voltage was found to be 3V and 4V for PEDOT:PSS and STFO/PEDOT:PSS, respectively, indicating a partial restriction of the flow of charge carriers. We have shown that using STFO in PeLEDs leads to devices that have better performance and longer lifetimes when subjected to electrical stress. When stored for two months under controlled conditions (dark, inert atmosphere), the efficiency roll-off observed in STFO-based devices was only around 34%. In comparison, the efficiency roll-off in PEDOT:PSS-based LEDs was much higher at approximately 72% during the same storage period. STFO is presumed to mitigate ion migration in halide perovskite, thus potentially retarding the degradation process caused by the acidic nature of PEDOT:PSS, attributed to its chemical stability. In conclusion, these results provide evidence for STFO's long-term stability improvement.

Based on the above discussion, it is evident that the investigation of oxide perovskites potential for halide perovskite stability is still in its early stages. There are several crucial questions that remain unresolved, particularly regarding the electrical characteristics, charge transport mechanism, and properties of these materials. Improving the long-term durability of optoelectronic devices based on halide perovskites can result in significant improvements in reliability, longevity, and overall performance.

General and Particular Works

Publications

1) Electrical and optical properties of $CaTi_{1-y}Fe_yO_{3-\delta}$ perovskite films as interlayers for optoelectronic applications

C. Yildirim, F. Devoize, P.M.Geffroy, F. Dumas-Bouchiat, J. Bouclé, S. Vedraine

Materials (2022)

2) Preparation of perovskite $CsPbI_2Br$ thin films under nitrogen flow and effect of a 2D inorganic halide material on the texture and solar cell performances

E. Breniaux, P. Dufour, S. Karthick, C. Yildirim, J. Bouclé, N. Ratel-Ramond, C. Tenailleau

European Journal of Organic Chemistry (2022)

3) D-π-A-Type Pyrazolo[1,5-a]pyrimidine-Based Hole-Transporting Materials for Perovskite Solar Cells: Effect of the Functionalization Position

F. Bouihi, B. Schmaltz, F. Mathevet, D. Kreher, J. Faure-Vincent, C. Yildirim, A. Elhakmaoui, J. Bouclé, M. Akssira, F. Tran-Van, M. Abarbri

Materials (2022)

Congress / Workshops

National Congress / Workshops:

1) Progress in $SrTi_{0.7}Fe_{0.3}O_{3-\delta}$ as Interlayer in Perovskite-based Optoelectronic Devices

Oral Presentation, European Materials Research Society (E-MRS), D-symposium, Advanced sustainable materials for energy applications, 29 May – 02 June 2023, Strasbourg

2) Electrical and Optical Properties of $SrTi_{0.7}Fe_{0.3}O_{3-\delta}$ Perovskite-Type Oxide

Poster Presentation, European Materials Research Society (E-MRS), A-symposium, Solid state ionics: bulk, interfaces, and integration in devices 29 May – 02 June 2023, Strasbourg

3) Using a Perovskite Oxide Interlayer in a Halide Perovskite Optoelectronic Device

Poster Presentation, Hybrid and Organic Photovoltaics (HOPV),12-14 June 2023, London

4) Perovskite Oxide Interface Layer in a Perovskite Solar Cell

Oral Presentation, JPH2022 Journées Perovskite Halogénées,16 – 18 March 2022, Lyon

5) A Perovskite Oxide Interface Layer in a Perovskite Active Layer Solar Cell

Poster Presentation, Peroquium: two-day workshop on perovskites, 31 March-01 April 2022, Palaiseau

Bibliography

[1]   E.A. Katz, *HCA* **2020**, *103*.

[2]   L. Ortega-San-Martin, in *Revolution of Perovskite* (Eds: N.S. Arul, V.D. Nithya), Springer Singapore, Singapore **2020**, C1.

[3]   M.A. Peña, J.L.G. Fierro, *Chem. Rev.* **2001**, *101*, 1981.

[4]   Q.A. Akkerman, L. Manna, *ACS Energy Lett.* **2020**, *5*, 604.

[5]   A. Pérez-Tomás, A. Mingorance, D. Tanenbaum, M. Lira-Cantú, in *The Future of Semiconductor Oxides in Next-Generation Solar Cells*, Elsevier**2018**, 267.

[6]   Q. Ji, L. Bi, J. Zhang, H. Cao, X.S. Zhao, *Energy Environ. Sci.* **2020**, *13*, 1408.

[7]   B. Yang, F. Zhang, J. Chen, S. Yang, X. Xia, T. Pullerits, W. Deng, K. Han, *Adv. Mater.* **2017**, *29*, 1703758.

[8]   Z. Fan, K. Sun, J. Wang, *J. Mater. Chem. A* **2015**, *3*, 18809.

[9]   Q. Shen, Y. Ogomi, J. Chang, T. Toyoda, K. Fujiwara, K. Yoshino, K. Sato, K. Yamazaki, M. Akimoto, Y. Kuga, K. Katayama, S. Hayase, *J. Mater. Chem. A* **2015**, *3*, 9308.

[10]   G. Volonakis, M.R. Filip, A.A. Haghighirad, N. Sakai, B. Wenger, H.J. Snaith, F. Giustino, *J. Phys. Chem. Lett.* **2016**, *7*, 1254.

[11]   L. Duan, A. Uddin, *Mater. Chem. Front.* **2022**, *6*, 400.

[12]   C.J. Bartel, C. Sutton, B.R. Goldsmith, R. Ouyang, C.B. Musgrave, L.M. Ghiringhelli, M. Scheffler, *Sci. Adv.* **2019**, *5*, eaav0693.

[13]   R.A. Kerner, L. Zhao, Z. Xiao, B.P. Rand, *J. Mater. Chem. A* **2016**, *4*, 8308.

[14]   D. Kumar, R. Sagar Yadav, Monika, A. Kumar Singh, S. Bahadur Rai, in *Perovskite Materials, Devices and Integration* (Ed: H. Tian), IntechOpen**2020**.

[15]   F. Mahmoudi, K. Saravanakumar, V. Maheskumar, L.K. Njaramba, Y. Yoon, C.M. Park, *Journal of Hazardous Materials* **2022**, *436*, 129074.

[16]   T. Jeon, S.J. Kim, J. Yoon, J. Byun, H.R. Hong, T.-W. Lee, J.-S. Kim, B. Shin, S.O. Kim, *Adv. Energy Mater.* **2017**, *7*, 1602596.

[17]   A. Kojima, K. Teshima, Y. Shirai, T. Miyasaka, *J. Am. Chem. Soc.* **2009**, *131*, 6050.

[18]   C.C. Stoumpos, D.H. Cao, D.J. Clark, J. Young, J.M. Rondinelli, J.I. Jang, J.T. Hupp, M.G. Kanatzidis, *Chem. Mater.* **2016**, *28*, 2852.

[19]   R. Gautier, M. Paris, F. Massuyeau, *J. Am. Chem. Soc.* **2019**, *141*, 12619.

[20]   I.C. Smith, E.T. Hoke, D. Solis-Ibarra, M.D. McGehee, H.I. Karunadasa, *Angew. Chem. Int. Ed.* **2014**, *53*, 11232.

[21]   Y. Jiang, J. Yuan, Y. Ni, J. Yang, Y. Wang, T. Jiu, M. Yuan, J. Chen, *Joule* **2018**, *2*, 1356.

[22]   W. Ke, L. Mao, C.C. Stoumpos, J. Hoffman, I. Spanopoulos, A.D. Mohite, M.G. Kanatzidis, *Adv. Energy Mater.* **2019**, *9*, 1803384.

[23]   A.A. Sutanto, N. Drigo, V.I.E. Queloz, I. Garcia-Benito, A.R. Kirmani, L.J. Richter, P.A. Schouwink, K.T. Cho, S. Paek, M.K. Nazeeruddin, G. Grancini, *J. Mater. Chem. A* **2020**, *8*, 2343.

[24]   J. Zhang, J. Qin, M. Wang, Y. Bai, H. Zou, J.K. Keum, R. Tao, H. Xu, H. Yu, S. Haacke, B. Hu, *Joule* **2019**, *3*, 3061.

[25]   Y. Hu, L.M. Spies, D. Alonso-Álvarez, P. Mocherla, H. Jones, J. Hanisch, T. Bein, P.R.F. Barnes, P. Docampo, *J. Mater. Chem. A* **2018**, *6*, 22215.

[26] P. Zhu, J. Zhu, *InfoMat* **2020**, *2*, 341.

[27] J. Jiang, Z. Chu, Z. Yin, J. Li, Y. Yang, J. Chen, J. Wu, J. You, X. Zhang, *Advanced Materials* **2022**, *34*, 2204460.

[28] I. Metcalf, S. Sidhik, H. Zhang, A. Agrawal, J. Persaud, J. Hou, J. Even, A.D. Mohite, *Chem. Rev.* **2023**, *123*, 9565.

[29] H.-S. Kim, C.-R. Lee, J.-H. Im, K.-B. Lee, T. Moehl, A. Marchioro, S.-J. Moon, R. Humphry-Baker, J.-H. Yum, J.E. Moser, M. Grätzel, N.-G. Park, *Sci Rep* **2012**, *2*, 591.

[30] B.R. Sutherland, E.H. Sargent, *Nature Photon* **2016**, *10*, 295.

[31] C. Katan, N. Mercier, J. Even, *Chem. Rev.* **2019**, *119*, 3140.

[32] Y.-H. Chang, J.-C. Lin, Y.-C. Chen, T.-R. Kuo, D.-Y. Wang, *Nanoscale Res Lett* **2018**, *13*, 247.

[33] Y. Jiang, J. Wei, M. Yuan, *J. Phys. Chem. Lett.* **2021**, *12*, 2593.

[34] Q. Wang, Y. Shao, Q. Dong, Z. Xiao, Y. Yuan, J. Huang, *Energy Environ. Sci.* **2014**, *7*, 2359.

[35] H. Zhou, Q. Chen, G. Li, S. Luo, T. Song, H.-S. Duan, Z. Hong, J. You, Y. Liu, Y. Yang, *Science* **2014**, *345*, 542.

[36] A.S.R. Bati, Y.L. Zhong, P.L. Burn, M.K. Nazeeruddin, P.E. Shaw, M. Batmunkh, *Commun Mater* **2023**, *4*, 2.

[37] J. Wu, H. Cha, T. Du, Y. Dong, W. Xu, C. Lin, J.R. Durrant, *Advanced Materials* **2022**, *34*, 2101833.

[38] X. Qiu, B. Cao, S. Yuan, X. Chen, Z. Qiu, Y. Jiang, Q. Ye, H. Wang, H. Zeng, J. Liu, M.G. Kanatzidis, *Solar Energy Materials and Solar Cells* **2017**, *159*, 227.

[39] Y. Zhao, F. Ma, Z. Qu, S. Yu, T. Shen, H.-X. Deng, X. Chu, X. Peng, Y. Yuan, X. Zhang, J. You, *Science* **2022**, *377*, 531.

[40] www.nrel.gov/pv/cell-efficiency.html

[41] X. Cui, Y. Li, Z. Chen, Y. Zou, Y. Liu, B. Sun, Z. Bo, *Journal of Alloys and Compounds* **2023**, *960*, 170823.

[42] D.B. Mitzi, in *Progress in Inorganic Chemistry* (Ed: K.D. Karlin), Wiley**1999**, 1.

[43] Z.-K. Tan, R.S. Moghaddam, M.L. Lai, P. Docampo, R. Higler, F. Deschler, M. Price, A. Sadhanala, L.M. Pazos, D. Credgington, F. Hanusch, T. Bein, H.J. Snaith, R.H. Friend, *Nature Nanotech* **2014**, *9*, 687.

[44] Z. Li, K. Cao, J. Li, Y. Tang, X. Ding, B. Yu, 1.National & Local Joint Engineering Research Center of Semiconductor Display and Optical Communication Devices, South China University ofTechnology, Guangdong 510640, China, 2.Foshan Nationstar Optoelectronics Company Ltd., Foshan 528000, China., *Opto-Electronic Advances* **2021**, *4*, 20001901.

[45] C.-H.A. Li, Z. Zhou, P. Vashishtha, J.E. Halpert, *Chem. Mater.* **2019**, *31*, 6003.

[46] W. Bai, T. Xuan, H. Zhao, H. Dong, X. Cheng, L. Wang, R. Xie, *Advanced Materials* **2023**, 2302283.

[47] Z. Guan, Y. Li, Z. Zhu, Z. Zeng, Z. Chen, Z. Ren, G. Li, S. Tsang, H. Yip, Y. Xiong, C. Lee, *Adv Funct Materials* **2022**, *32*, 2203962.

[48] Y. Jiang, C. Sun, J. Xu, S. Li, M. Cui, X. Fu, Y. Liu, Y. Liu, H. Wan, K. Wei, T. Zhou, W. Zhang, Y. Yang, J. Yang, C. Qin, S. Gao, J. Pan, Y. Liu, S. Hoogland, E.H. Sargent, J. Chen, M. Yuan, *Nature* **2022**, *612*, 679.

[49]   F.A. Lindholm, J.G. Fossum, E.L. Burgess, *IEEE Trans. Electron Devices* **1979**, *26*, 165.

[50]   P.W.M. Blom, V.D. Mihailetchi, L.J.A. Koster, D.E. Markov, *Adv. Mater.* **2007**, *19*, 1551.

[51]   www.pveducation.org

[52]   M. Liu, M.B. Johnston, H.J. Snaith, *Nature* **2013**, *501*, 395.

[53]   B. Qi, J. Wang, *Phys. Chem. Chem. Phys.* **2013**, *15*, 8972.

[54]   M. Diantoro, T. Suprayogi, A. Hidayat, A. Taufiq, A. Fuad, R. Suryana, *International Journal of Photoenergy* **2018**, *2018*, 1.

[55]   S. Colella, M. Mazzeo, A. Rizzo, G. Gigli, A. Listorti, *J. Phys. Chem. Lett.* **2016**, *7*, 4322.

[56]   A. Muthukumar, G. Rey, G. Giusti, V. Consonni, E. Appert, H. Roussel, A. Dakshnamoorthy, D. Bellet, Indian Institute of Technology, Bombay, Mumbai, India **2013**, 710.

[57]   T. Liu, K. Chen, Q. Hu, R. Zhu, Q. Gong, *Adv. Energy Mater.* **2016**, *6*, 1600457.

[58]   Y. Li, L. Meng, Y. Yang, G. Xu, Z. Hong, Q. Chen, J. You, G. Li, Y. Yang, Y. Li, *Nat Commun* **2016**, *7*, 10214.

[59]   J.H. Heo, H.J. Han, D. Kim, T.K. Ahn, S.H. Im, *Energy Environ. Sci.* **2015**, *8*, 1602.

[60]   B. Chen, M. Yang, S. Priya, K. Zhu, *J. Phys. Chem. Lett.* **2016**, *7*, 905.

[61]   V.M. Le Corre, M. Stolterfoht, L. Perdigón Toro, M. Feuerstein, C. Wolff, L. Gil-Escrig, H.J. Bolink, D. Neher, L.J.A. Koster, *ACS Appl. Energy Mater.* **2019**, *2*, 6280.

[62]   P. Kung, M. Li, P. Lin, Y. Chiang, C. Chan, T. Guo, P. Chen, *Adv. Mater. Interfaces* **2018**, *5*, 1800882.

[63]   G. Ren, W. Han, Y. Deng, W. Wu, Z. Li, J. Guo, H. Bao, C. Liu, W. Guo, *J. Mater. Chem. A* **2021**, *9*, 4589.

[64]   S. Zhang, M. Stolterfoht, A. Armin, Q. Lin, F. Zu, J. Sobus, H. Jin, N. Koch, P. Meredith, P.L. Burn, D. Neher, *ACS Appl. Mater. Interfaces* **2018**, *10*, 21681.

[65]   A. Gheno, S. Vedraine, B. Ratier, J. Bouclé, *Metals* **2016**, *6*, 21.

[66]   C. Redondo-Obispo, T.S. Ripolles, S. Cortijo-Campos, A.L. Álvarez, E. Climent-Pascual, A. De Andrés, C. Coya, *Materials & Design* **2020**, *191*, 108587.

[67]   H. Yan, T. Jo, H. Okuzaki, *Polym. J.* **2009**, *41*, 1028.

[68]   Q. Wei, M. Mukaida, Y. Naitoh, T. Ishida, *Adv. Mater.* **2013**, *25*, 2831.

[69]   W. Han, G. Ren, J. Liu, Z. Li, H. Bao, C. Liu, W. Guo, *ACS Appl. Mater. Interfaces* **2020**, *12*, 49297.

[70]   Y. Yao, C. Cheng, C. Zhang, H. Hu, K. Wang, S. De Wolf, *Advanced Materials* **2022**, *34*, 2203794.

[71]   T. Salim, S. Sun, Y. Abe, A. Krishna, A.C. Grimsdale, Y.M. Lam, *J. Mater. Chem. A* **2015**, *3*, 8943.

[72]   J.-Y. Jeng, Y.-F. Chiang, M.-H. Lee, S.-R. Peng, T.-F. Guo, P. Chen, T.-C. Wen, *Adv. Mater.* **2013**, *25*, 3727.

[73]   S. Bai, Z. Wu, X. Wu, Y. Jin, N. Zhao, Z. Chen, Q. Mei, X. Wang, Z. Ye, T. Song, R. Liu, S. Lee, B. Sun, *Nano Res.* **2014**, *7*, 1749.

[74]   Z.-K. Wang, M. Li, D.-X. Yuan, X.-B. Shi, H. Ma, L.-S. Liao, *ACS Appl. Mater. Interfaces* **2015**, *7*, 9645.

[75]   Q. Xue, G. Chen, M. Liu, J. Xiao, Z. Chen, Z. Hu, X.-F. Jiang, B. Zhang, F. Huang, W. Yang, H.-L. Yip, Y. Cao, *Adv. Energy Mater.* **2016**, *6*, 1502021.

[76] L. Hu, K. Sun, M. Wang, W. Chen, B. Yang, J. Fu, Z. Xiong, X. Li, X. Tang, Z. Zang, S. Zhang, L. Sun, M. Li, *ACS Appl. Mater. Interfaces* **2017**, *9*, 43902.

[77] C.-H. Chiang, C.-G. Wu, *ACS Nano* **2018**, *12*, 10355.

[78] K. Jiang, F. Wu, G. Zhang, P.C.Y. Chow, C. Ma, S. Li, K.S. Wong, L. Zhu, H. Yan, *J. Mater. Chem. A* **2019**, *7*, 21662.

[79] K.M. Reza, A. Gurung, B. Bahrami, S. Mabrouk, H. Elbohy, R. Pathak, K. Chen, A.H. Chowdhury, M.T. Rahman, S. Letourneau, H.-C. Yang, G. Saianand, J.W. Elam, S.B. Darling, Q. Qiao, *Journal of Energy Chemistry* **2020**, *44*, 41.

[80] W. Li, H. Wang, X. Hu, W. Cai, C. Zhang, M. Wang, Z. Zang, *Sol. RRL* **2021**, *5*, 2000573.

[81] Y. Qi, M. Almtiri, H. Giri, S. Jha, G. Ma, A.K. Shaik, Q. Zhang, N. Pradhan, X. Gu, N.I. Hammer, D. Patton, C. Scott, Q. Dai, *Advanced Energy Materials* **2022**, *12*, 2202713.

[82] X. Zheng, B. Chen, J. Dai, Y. Fang, Y. Bai, Y. Lin, H. Wei, X.C. Zeng, J. Huang, *Nat Energy* **2017**, *2*, 17102.

[83] H. Cho, S.-H. Jeong, M.-H. Park, Y.-H. Kim, C. Wolf, C.-L. Lee, J.H. Heo, A. Sadhanala, N. Myoung, S. Yoo, S.H. Im, R.H. Friend, T.-W. Lee, *Science* **2015**, *350*, 1222.

[84] P. Chen, Z. Xiong, X. Wu, M. Shao, Y. Meng, Z. Xiong, C. Gao, *J. Phys. Chem. Lett.* **2017**, *8*, 3961.

[85] S.-H. Jeong, H. Kim, M.-H. Park, Y. Lee, N. Li, H.-K. Seo, T.-H. Han, S. Ahn, J.-M. Heo, K.S. Kim, T.-W. Lee, *Nano Energy* **2019**, *60*, 324.

[86] X. Xiao, K. Wang, T. Ye, R. Cai, Z. Ren, D. Wu, X. Qu, J. Sun, S. Ding, X.W. Sun, W.C.H. Choy, *Commun Mater* **2020**, *1*, 81.

[87] K. Lin, J. Xing, L.N. Quan, F.P.G. De Arquer, X. Gong, J. Lu, L. Xie, W. Zhao, D. Zhang, C. Yan, W. Li, X. Liu, Y. Lu, J. Kirman, E.H. Sargent, Q. Xiong, Z. Wei, *Nature* **2018**, *562*, 245.

[88] N. Liu, L. Kong, W. Meng, M. Fan, L. Wang, C. Zhang, X. Yang, *IEEE Electron Device Lett.* **2022**, *43*, 1705.

[89] G. Tumen-Ulzii, T. Matsushima, C. Adachi, *Energy Fuels* **2021**, *35*, 18915.

[90] G. Zhu, L. Yang, C. Zhang, G. Du, N. Fan, Z. Luo, X. Zhang, J. Zhang, *ACS Appl. Energy Mater.* **2022**, *5*, 3595.

[91] H.J. Snaith, M. Grätzel, *Applied Physics Letters* **2006**, *89*, 262114.

[92] M.M. Lee, J. Teuscher, T. Miyasaka, T.N. Murakami, H.J. Snaith, *Science* **2012**, *338*, 643.

[93] J.J. Yoo, G. Seo, M.R. Chua, T.G. Park, Y. Lu, F. Rotermund, Y.-K. Kim, C.S. Moon, N.J. Jeon, J.-P. Correa-Baena, V. Bulović, S.S. Shin, M.G. Bawendi, J. Seo, *Nature* **2021**, *590*, 587.

[94] G. Kim, H. Min, K.S. Lee, D.Y. Lee, S.M. Yoon, S.I. Seok, *Science* **2020**, *370*, 108.

[95] C. Bi, Q. Wang, Y. Shao, Y. Yuan, Z. Xiao, J. Huang, *Nat Commun* **2015**, *6*, 7747.

[96] D.B. Khadka, Y. Shirai, M. Yanagida, J.W. Ryan, K. Miyano, *J. Mater. Chem. C* **2017**, *5*, 8819.

[97] S. Liu, X. Jiang, H. Ma, M.S. Liu, A.K.-Y. Jen, *Macromolecules* **2000**, *33*, 3514.

[98] J.H. Heo, S.H. Im, J.H. Noh, T.N. Mandal, C.-S. Lim, J.A. Chang, Y.H. Lee, H. Kim, A. Sarkar, Md.K. Nazeeruddin, M. Grätzel, S.I. Seok, *Nature Photon* **2013**, *7*, 486.

[99] Q. Wang, C. Bi, J. Huang, *Nano Energy* **2015**, *15*, 275.

[100] E. Gutierrez-Partida, H. Hempel, S. Caicedo-Dávila, M. Raoufi, F. Peña-Camargo, M. Grischek, R. Gunder, J. Diekmann, P. Caprioglio, K.O. Brinkmann, H. Köbler, S. Albrecht, T. Riedl, A. Abate, D. Abou-Ras, T. Unold, D. Neher, M. Stolterfoht, *ACS Energy Lett.* **2021**, *6*, 1045.

[101] A.Y. Alsalloum, B. Turedi, K. Almasabi, X. Zheng, R. Naphade, S.D. Stranks, O.F. Mohammed, O.M. Bakr, *Energy Environ. Sci.* **2021**, *14*, 2263.

[102] S. Chen, X. Dai, S. Xu, H. Jiao, L. Zhao, J. Huang, *Science* **2021**, *373*, 902.

[103] Z. Li, B. Li, X. Wu, S.A. Sheppard, S. Zhang, D. Gao, N.J. Long, Z. Zhu, *Science* **2022**, *376*, 416.

[104] D. Zhao, M. Sexton, H.-Y. Park, G. Baure, J.C. Nino, F. So, *Adv. Energy Mater.* **2015**, *5*, 1401855.

[105] S. Sun, T. Salim, N. Mathews, M. Duchamp, C. Boothroyd, G. Xing, T.C. Sum, Y.M. Lam, *Energy Environ. Sci.* **2014**, *7*, 399.

[106] O. Malinkiewicz, C. Roldán-Carmona, A. Soriano, E. Bandiello, L. Camacho, M.K. Nazeeruddin, H.J. Bolink, *Adv. Energy Mater.* **2014**, *4*, 1400345.

[107] X. Xu, C. Ma, Y. Cheng, Y.-M. Xie, X. Yi, B. Gautam, S. Chen, H.-W. Li, C.-S. Lee, F. So, S.-W. Tsang, *Journal of Power Sources* **2017**, *360*, 157.

[108] F. Zhang, Y. Hou, S. Wang, H. Zhang, F. Zhou, Y. Hao, S. Ye, H. Cai, J. Song, J. Qu, *Solar RRL* **2021**, *5*, 2100190.

[109] X. Zhao, Z.-K. Tan, *Nat. Photonics* **2020**, *14*, 215.

[110] C. Chen, T. Xuan, Y. Yang, F. Huang, T. Zhou, L. Wang, R.-J. Xie, *ACS Appl. Mater. Interfaces* **2022**, *14*, 16404.

[111] Y. Sun, L. Ge, L. Dai, C. Cho, J. Ferrer Orri, K. Ji, S.J. Zelewski, Y. Liu, A.J. Mirabelli, Y. Zhang, J.-Y. Huang, Y. Wang, K. Gong, M.C. Lai, L. Zhang, D. Yang, J. Lin, E.M. Tennyson, C. Ducati, S.D. Stranks, L.-S. Cui, N.C. Greenham, *Nature* **2023**, *615*, 830.

[112] S. Wang, H. Guo, Y. Wu, *Mater. Futures* **2023**, *2*, 012105.

[113] H. Cheng, Y. Li, Y. Zhong, *Mater. Chem. Front.* **2023**, *7*, 3958.

[114] L. Liu, Y. Yang, M. Du, Y. Cao, X. Ren, L. Zhang, H. Wang, S. Zhao, K. Wang, S. (Frank) Liu, *Advanced Energy Materials* **2023**, *13*, 2202802.

[115] F. Ali, C. Roldán-Carmona, M. Sohail, M.K. Nazeeruddin, *Adv. Energy Mater.* **2020**, *10*, 2002989.

[116] A. Magomedov, A. Al-Ashouri, E. Kasparavičius, S. Strazdaite, G. Niaura, M. Jošt, T. Malinauskas, S. Albrecht, V. Getautis, *Adv. Energy Mater.* **2018**, *8*, 1801892.

[117] A. Al-Ashouri, A. Magomedov, M. Roß, M. Jošt, M. Talaikis, G. Chistiakova, T. Bertram, J.A. Márquez, E. Köhnen, E. Kasparavičius, S. Levcenco, L. Gil-Escrig, C.J. Hages, R. Schlatmann, B. Rech, T. Malinauskas, T. Unold, C.A. Kaufmann, L. Korte, G. Niaura, V. Getautis, S. Albrecht, *Energy Environ. Sci.* **2019**, *12*, 3356.

[118] R. Azmi, E. Ugur, A. Seitkhan, F. Aljamaan, A.S. Subbiah, J. Liu, G.T. Harrison, M.I. Nugraha, M.K. Eswaran, M. Babics, Y. Chen, F. Xu, T.G. Allen, A.U. Rehman, C.-L. Wang, T.D. Anthopoulos, U. Schwingenschlögl, M. De Bastiani, E. Aydin, S. De Wolf, *Science* **2022**, *376*, 73.

[119] X. Deng, F. Qi, F. Li, S. Wu, F.R. Lin, Z. Zhang, Z. Guan, Z. Yang, C. Lee, A.K. -Y. Jen, *Angewandte Chemie* **2022**, *134*.

[120] Q. Jiang, J. Tong, Y. Xian, R.A. Kerner, S.P. Dunfield, C. Xiao, R.A. Scheidt, D. Kuciauskas, X. Wang, M.P. Hautzinger, R. Tirawat, M.C. Beard, D.P. Fenning, J.J. Berry, B.W. Larson, Y. Yan, K. Zhu, *Nature* **2022**, *611*, 278.

[121] M.-C. Hsiao, P.-C. Chien, L.-S. Jhuang, F.-C. Chen, *Phys. Chem. Chem. Phys.* **2019**, *21*, 7867.

[122] M. Gedda, D. Gkeka, M.I. Nugraha, A.D. Scaccabarozzi, E. Yengel, J.I. Khan, I. Hamilton, Y. Lin, M. Deconinck, Y. Vaynzof, F. Laquai, D.D.C. Bradley, T.D. Anthopoulos, *Advanced Energy Materials* **2022**, 2201396.

[123] S.Y. Kim, H. Kang, K. Chang, H.J. Yoon, *ACS Appl. Mater. Interfaces* **2021**, *13*, 31236.

[124] W. Li, T. Li, Y. Tong, H. Qi, Y. Zhang, Y. Guo, H. Wang, H. Wang, K. Wang, H. Wang, *ACS Appl. Mater. Interfaces* **2023**, *15*, 36602.

[125] M. Shahinuzzaman, S. Afroz, H. Mohafez, M. Jamal, M. Khandaker, A. Sulieman, N. Tamam, M. Islam, *Nanomaterials* **2022**, *12*, 3003.

[126] X. Li, H. Yu, Z. Liu, J. Huang, X. Ma, Y. Liu, Q. Sun, L. Dai, S. Ahmad, Y. Shen, M. Wang, *Nano-Micro Lett.* **2023**, *15*, 206.

[127] Q. Wang, Z. Lin, J. Su, Z. Hu, J. Chang, Y. Hao, *Nano Select* **2021**, *2*, 1055.

[128] S. Ko, T. Yong, S.-K. Kim, J.Y. Park, G. Lee, H.R. You, S. Han, D.H. Lee, S. Choi, Y.C. Choi, Y. Kim, N.-S. Lee, S. Song, J. Choi, *Solar RRL* **2023**, *7*, 2300049.

[129] A. Corani, M.-H. Li, P.-S. Shen, P. Chen, T.-F. Guo, A. El Nahhas, K. Zheng, A. Yartsev, V. Sundström, C.S. Ponseca, *J. Phys. Chem. Lett.* **2016**, *7*, 1096.

[130] K.-C. Wang, J.-Y. Jeng, P.-S. Shen, Y.-C. Chang, E.W.-G. Diau, C.-H. Tsai, T.-Y. Chao, H.-C. Hsu, P.-Y. Lin, P. Chen, T.-F. Guo, T.-C. Wen, *Sci Rep* **2014**, *4*, 4756.

[131] W. Chen, Y. Wu, J. Liu, C. Qin, X. Yang, A. Islam, Y.-B. Cheng, L. Han, *Energy Environ. Sci.* **2015**, *8*, 629.

[132] J.H. Park, J. Seo, S. Park, S.S. Shin, Y.C. Kim, N.J. Jeon, H.-W. Shin, T.K. Ahn, J.H. Noh, S.C. Yoon, C.S. Hwang, S.I. Seok, *Adv. Mater.* **2015**, *27*, 4013.

[133] S.R. Pae, S. Byun, J. Kim, M. Kim, I. Gereige, B. Shin, *ACS Appl. Mater. Interfaces* **2018**, *10*, 534.

[134] K.-C. Wang, P.-S. Shen, M.-H. Li, S. Chen, M.-W. Lin, P. Chen, T.-F. Guo, *ACS Appl. Mater. Interfaces* **2014**, *6*, 11851.

[135] S. Yue, K. Liu, R. Xu, M. Li, M. Azam, K. Ren, J. Liu, Y. Sun, Z. Wang, D. Cao, X. Yan, S. Qu, Y. Lei, Z. Wang, *Energy Environ. Sci.* **2017**, *10*, 2570.

[136] W. Chen, F.-Z. Liu, X.-Y. Feng, A.B. Djurišić, W.K. Chan, Z.-B. He, *Adv. Energy Mater.* **2017**, *7*, 1700722.

[137] W. Chen, Y. Zhou, L. Wang, Y. Wu, B. Tu, B. Yu, F. Liu, H.-W. Tam, G. Wang, A.B. Djurišić, L. Huang, Z. He, *Adv. Mater.* **2018**, *30*, 1800515.

[138] W. Chen, Y. Zhou, G. Chen, Y. Wu, B. Tu, F. Liu, L. Huang, A.M.C. Ng, A.B. Djurišić, Z. He, *Adv. Energy Mater.* **2019**, *9*, 1803872.

[139] H. Chen, S. Teale, B. Chen, Y. Hou, L. Grater, T. Zhu, K. Bertens, S.M. Park, H.R. Atapattu, Y. Gao, M. Wei, A.K. Johnston, Q. Zhou, K. Xu, D. Yu, C. Han, T. Cui, E.H. Jung, C. Zhou, W. Zhou, A.H. Proppe, S. Hoogland, F. Laquai, T. Filleter, K.R. Graham, Z. Ning, E.H. Sargent, *Nat. Photon.* **2022**, *16*, 352.

[140] C.C. Boyd, R.C. Shallcross, T. Moot, R. Kerner, L. Bertoluzzi, A. Onno, S. Kavadiya, C. Chosy, E.J. Wolf, J. Werner, J.A. Raiford, C. De Paula, A.F. Palmstrom, Z.J. Yu, J.J. Berry,

S.F. Bent, Z.C. Holman, J.M. Luther, E.L. Ratcliff, N.R. Armstrong, M.D. McGehee, *Joule* **2020**, *4*, 1759.

[141] Y. Liu, J. Cui, K. Du, H. Tian, Z. He, Q. Zhou, Z. Yang, Y. Deng, D. Chen, X. Zuo, Y. Ren, L. Wang, H. Zhu, B. Zhao, D. Di, J. Wang, R.H. Friend, Y. Jin, *Nat. Photonics* **2019**, *13*, 760.

[142] J. Xing, Y. Zhao, M. Askerka, L.N. Quan, X. Gong, W. Zhao, J. Zhao, H. Tan, G. Long, L. Gao, Z. Yang, O. Voznyy, J. Tang, Z.-H. Lu, Q. Xiong, E.H. Sargent, *Nat Commun* **2018**, *9*, 3541.

[143] Z. Ren, X. Xiao, R. Ma, H. Lin, K. Wang, X.W. Sun, W.C.H. Choy, *Adv. Funct. Mater.* **2019**, *29*, 1905339.

[144] M. Karlsson, Z. Yi, S. Reichert, X. Luo, W. Lin, Z. Zhang, C. Bao, R. Zhang, S. Bai, G. Zheng, P. Teng, L. Duan, Y. Lu, K. Zheng, T. Pullerits, C. Deibel, W. Xu, R. Friend, F. Gao, *Nat Commun* **2021**, *12*, 361.

[145] P. Pattanasattayavong, G.O.N. Ndjawa, K. Zhao, K.W. Chou, N. Yaacobi-Gross, B.C. O'Regan, A. Amassian, T.D. Anthopoulos, *Chem. Commun.* **2013**, *49*, 4154.

[146] S. Ye, W. Sun, Y. Li, W. Yan, H. Peng, Z. Bian, Z. Liu, C. Huang, *Nano Lett.* **2015**, *15*, 3723.

[147] M. Jung, Y.C. Kim, N.J. Jeon, W.S. Yang, J. Seo, J.H. Noh, S. Il Seok, *ChemSusChem* **2016**, *9*, 2592.

[148] N. Wijeyasinghe, A. Regoutz, F. Eisner, T. Du, L. Tsetseris, Y.-H. Lin, H. Faber, P. Pattanasattayavong, J. Li, F. Yan, M.A. McLachlan, D.J. Payne, M. Heeney, T.D. Anthopoulos, *Adv. Funct. Mater.* **2017**, *27*, 1701818.

[149] J.-W. Liang, Y. Firdaus, R. Azmi, H. Faber, D. Kaltsas, C.H. Kang, M.I. Nugraha, E. Yengel, T.K. Ng, S. De Wolf, L. Tsetseris, B.S. Ooi, T.D. Anthopoulos, *ACS Energy Lett.* **2022**, *7*, 3139.

[150] J. Wang, S. Gong, Z. Chen, S. Yang, *ACS Appl. Mater. Interfaces* **2021**, *13*, 22684.

[151] J. Liu, S.K. Pathak, N. Sakai, R. Sheng, S. Bai, Z. Wang, H.J. Snaith, *Adv. Mater. Interfaces* **2016**, *3*, 1600571.

[152] V. Manjunath, S. Bimli, P.A. Shaikh, S.B. Ogale, R.S. Devan, *J. Mater. Chem. C* **2022**, *10*, 15725.

[153] J.A. Christians, R.C.M. Fung, P.V. Kamat, *J. Am. Chem. Soc.* **2014**, *136*, 758.

[154] W.-Y. Chen, L.-L. Deng, S.-M. Dai, X. Wang, C.-B. Tian, X.-X. Zhan, S.-Y. Xie, R.-B. Huang, L.-S. Zheng, *J. Mater. Chem. A* **2015**, *3*, 19353.

[155] H. Wang, Z. Yu, J. Lai, X. Song, X. Yang, A. Hagfeldt, L. Sun, *J. Mater. Chem. A* **2018**, *6*, 21435.

[156] J. Cao, B. Wu, J. Peng, X. Feng, C. Li, Y. Tang, *Sci. China Chem.* **2019**, *62*, 363.

[157] C. Yang, D. Souchay, M. Kneiß, M. Bogner, H.M. Wei, M. Lorenz, O. Oeckler, G. Benstetter, Y.Q. Fu, M. Grundmann, *Nat Commun* **2017**, *8*, 16076.

[158] K. Zhu, Z. Cheng, S. Rangan, M. Cotlet, J. Du, L. Kasaei, S.J. Teat, W. Liu, Y. Chen, L.C. Feldman, D.M. O'Carroll, J. Li, *ACS Energy Lett.* **2021**, *6*, 2565.

[159] C. Zuo, L. Ding, *Small* **2015**, *11*, 5528.

[160] T. Ye, X. Sun, X. Zhang, S. Hao, *Journal of Energy Chemistry* **2021**, *62*, 459.

[161] J. Liu, S. Li, A. Mei, H. Han, *Small Science* **2023**, 2300020.

[162] B.-S. Kim, T.-M. Kim, M.-S. Choi, H.-S. Shim, J.-J. Kim, *Organic Electronics* **2015**, *17*, 102.

[163] F. Hou, Z. Su, F. Jin, X. Yan, L. Wang, H. Zhao, J. Zhu, B. Chu, W. Li, *Nanoscale* **2015**, *7*, 9427.

[164] D.M. Torres-Herrera, P.M. Moreno-Romero, D. Cabrera-German, H.J. Cortina-Marrero, M. Sotelo-Lerma, H. Hu, *Solar Energy* **2020**, *206*, 136.

[165] Q. Guo, C. Wang, J. Li, Y. Bai, F. Wang, L. Liu, B. Zhang, T. Hayat, A. Alsaedi, Z. Tan, *Phys. Chem. Chem. Phys.* **2018**, *20*, 21746.

[166] M. Xiao, M. Gao, F. Huang, A.R. Pascoe, T. Qin, Y. Cheng, U. Bach, L. Spiccia, *ChemNanoMat* **2016**, *2*, 182.

[167] P. Docampo, J.M. Ball, M. Darwich, G.E. Eperon, H.J. Snaith, *Nat Commun* **2013**, *4*, 2761.

[168] S. Chu, R. Zhao, R. Liu, Y. Gao, X. Wang, C. Liu, J. Chen, H. Zhou, *Semicond. Sci. Technol.* **2018**, *33*, 115016.

[169] H. Sun, X. Hou, Q. Wei, H. Liu, K. Yang, W. Wang, Q. An, Y. Rong, *Chem. Commun.* **2016**, *52*, 8099.

[170] L. Xu, M. Qian, Q. Lu, H. Zhang, W. Huang, *Materials Letters* **2019**, *236*, 16.

[171] L. Xu, H. Wang, X. Feng, Y. Zhou, Y. Chen, R. Chen, W. Huang, *Adv Photo Res* **2021**, *2*, 2000132.

[172] P. Qin, G. Fang, N. Sun, X. Fan, Q. Zheng, F. Chen, J. Wan, X. Zhao, *Thin Solid Films* **2011**, *519*, 4334.

[173] M. Kaltenbrunner, G. Adam, E.D. Głowacki, M. Drack, R. Schwödiauer, L. Leonat, D.H. Apaydin, H. Groiss, M.C. Scharber, M.S. White, N.S. Sariciftci, S. Bauer, *Nature Mater* **2015**, *14*, 1032.

[174] P.-L. Qin, H.-W. Lei, X.-L. Zheng, Q. Liu, H. Tao, G. Yang, W.-J. Ke, L.-B. Xiong, M.-C. Qin, X.-Z. Zhao, G.-J. Fang, *Adv. Mater. Interfaces* **2016**, *3*, 1500799.

[175] P. Qin, Q. He, G. Yang, X. Yu, L. Xiong, G. Fang, *Surfaces and Interfaces* **2018**, *10*, 93.

[176] S. Thampy, W. Xu, J.W.P. Hsu, *J. Phys. Chem. Lett.* **2021**, *12*, 8495.

[177] F. Farjadian, S. Abbaspour, M.A.A. Sadatlu, S. Mirkiani, A. Ghasemi, M. Hoseini-Ghahfarokhi, N. Mozaffari, M. Karimi, M.R. Hamblin, *ChemistrySelect* **2020**, *5*, 10200.

[178] A.N. Ghulam, O.A.L. Dos Santos, L. Hazeem, B. Pizzorno Backx, M. Bououdina, S. Bellucci, *JFB* **2022**, *13*, 77.

[179] Y. Wang, A. Hu, *J. Mater. Chem. C* **2014**, *2*, 6921.

[180] T. Dürkop, S.A. Getty, E. Cobas, M.S. Fuhrer, *Nano Lett.* **2004**, *4*, 35.

[181] E. Jokar, Z.Y. Huang, S. Narra, C.-Y. Wang, V. Kattoor, C.-C. Chung, E.W.-G. Diau, *Adv. Energy Mater.* **2018**, *8*, 1701640.

[182] T.H. Chowdhury, Md. Akhtaruzzaman, Md.E. Kayesh, R. Kaneko, T. Noda, J.-J. Lee, A. Islam, *Solar Energy* **2018**, *171*, 652.

[183] Q. Lou, G. Lou, R. Peng, Z. Liu, W. Wang, M. Ji, C. Chen, X. Zhang, C. Liu, Z. Ge, *ACS Appl. Energy Mater.* **2021**, *4*, 3928.

[184] J. Niu, D. Yang, X. Ren, Z. Yang, Y. Liu, X. Zhu, W. Zhao, S. (Frank) Liu, *Organic Electronics* **2017**, *48*, 165.

[185] Y. Wen, G. Zhu, Y. Shao, *J Mater Sci* **2020**, *55*, 2937.

[186] J. Ryu, S. Yoon, J. Park, S.M. Jeong, D.-W. Kang, *Applied Surface Science* **2020**, *516*, 146116.

[187] V.T. Tiong, N.D. Pham, T. Wang, T. Zhu, X. Zhao, Y. Zhang, Q. Shen, J. Bell, L. Hu, S. Dai, H. Wang, *Adv. Funct. Mater.* **2018**, *28*, 1705545.

[188] T.-B. Song, Q. Chen, H. Zhou, C. Jiang, H.-H. Wang, Y. (Michael) Yang, Y. Liu, J. You, Y. Yang, *J. Mater. Chem. A* **2015**, *3*, 9032.

[189] Y. Han, S. Meyer, Y. Dkhissi, K. Weber, J.M. Pringle, U. Bach, L. Spiccia, Y.-B. Cheng, *J. Mater. Chem. A* **2015**, *3*, 8139.

[190] T.A. Berhe, W.-N. Su, C.-H. Chen, C.-J. Pan, J.-H. Cheng, H.-M. Chen, M.-C. Tsai, L.-Y. Chen, A.A. Dubale, B.-J. Hwang, *Energy Environ. Sci.* **2016**, *9*, 323.

[191] P.-M. Geffroy, S. Vedraine, F. Dumas-Bouchiat, Sudip.K. Saha, A. Gheno, F. Rossignol, P. Marchet, R. Antony, J. Bouclé, B. Ratier, *J. Phys. Chem. C* **2016**, *120*, 28583.

[192] W.-J. Yin, B. Weng, J. Ge, Q. Sun, Z. Li, Y. Yan, *Energy Environ. Sci.* **2019**, *12*, 442.

[193] B.E. Hayden, F.K. Rogers, *Journal of Electroanalytical Chemistry* **2018**, *819*, 275.

[194] P.I. Cowin, R. Lan, C.T.G. Petit, S. Tao, *Solid State Sciences* **2015**, *46*, 62.

[195] R. Waser, T. Bieger, J. Maier, *Solid State Communications* **1990**, *76*, 1077.

[196] N.H. Perry, N. Kim, E. Ertekin, H.L. Tuller, *Chem. Mater.* **2019**, *31*, 1030.

[197] R. Merkle, J. Maier, *Angew. Chem. Int. Ed.* **2008**, *47*, 3874.

[198] M. Vračar, A. Kuzmin, R. Merkle, J. Purans, E.A. Kotomin, J. Maier, O. Mathon, *Phys. Rev. B* **2007**, *76*, 174107.

[199] S. Steinsvik, R. Bugge, J. Gjønnes, J. Taftø, T. Norby, *Journal of Physics and Chemistry of Solids* **1997**, *58*, 969.

[200] C. Lenser, A. Kalinko, A. Kuzmin, D. Berzins, J. Purans, K. Szot, R. Waser, R. Dittmann, *Phys. Chem. Chem. Phys.* **2011**, *13*, 20779.

[201] A.D. Prasetiyo, D.R. Novianti, H. Maulidianingtiyas, A. Prasetyo, Surabaya, Indonesia **2020**.

[202] A. Rothschild, W. Menesklou, H.L. Tuller, E. Ivers-Tiffée, *Chem. Mater.* **2006**, *18*, 3651.

[203] E. Sediva, *Mechanistic and Defect Chemical Study of SrTiO3 and Sr(Ti,Fe)O3-y Resistive Switches*, ETH Zurich, **2019**.

[204] T.-H. Xie, X. Sun, J. Lin, *J. Phys. Chem. C* **2008**, *112*, 9753.

[205] F.J. Morin, J.R. Oliver, *Phys. Rev. B* **1973**, *8*, 5847.

[206] Z. Li, M. Yang, J.-S. Park, S.-H. Wei, J.J. Berry, K. Zhu, *Chem. Mater.* **2016**, *28*, 284.

[207] J. Mizusaki, M. Okayasu, S. Yamauchi, K. Fueki, *Journal of Solid State Chemistry* **1992**, *99*, 166.

[208] V. Damljanovic, *Raman Scattering, Magnetization and Magnetotransport Study of SrFeO3-Delta, Sr3Fe2O7-Delta and CaFeO3*, University of Stuttgart, **2008**.

[209] K. Iben Nassar, M. Slimi, N. Rammeh, S. Soreto Teixeira, M.P.F. Graça, *Appl. Phys. A* **2021**, *127*, 940.

[210] R.I. Walton, *Chemistry A European J* **2020**, *26*, 9041.

[211] P.H.T. Ngamou, N. Bahlawane, *Journal of Solid State Chemistry* **2009**, *182*, 849.

[212] M.D. McDaniel, T.Q. Ngo, S. Hu, A. Posadas, A.A. Demkov, J.G. Ekerdt, *Applied Physics Reviews* **2015**, *2*, 041301.

[213] S.A. Chambers, *Adv. Mater.* **2010**, *22*, 219.

[214] M. Ohring, *The Materials Science of Thin Films*, Academic Press **2002**.

[215] L. Sun, G. Yuan, L. Gao, J. Yang, M. Chhowalla, M.H. Gharahcheshmeh, K.K. Gleason, Y.S. Choi, B.H. Hong, Z. Liu, *Nat Rev Methods Primers* **2021**, *1*, 5.

[216] S. Hashmi, G. Ferreira Batalha, C.J. Van Tyne, B. Yilbas, *Comprehensive Materials Processing*, Elsevier**2014**.

[217] B. Demaurex, S. De Wolf, A. Descoeudres, Z. Charles Holman, C. Ballif, *Applied Physics Letters* **2012**, *101*, 171604.

[218] M. Henini, *Molecular Beam Epitaxy*, Elsevier Science**2013**.

[219] P. Bhattacharya, R. Fornar, H. Kamimura, *Comprehensive Semiconductor Science and Technology*, Elsevier Science**2011**.

[220] H.N.-R. Khan, M. Mehmood, F.C.C. Ling, A.F. Khan, S.M. Ali, *Semiconductors* **2020**, *54*, 999.

[221] J. Chen, M. Döbeli, D. Stender, K. Conder, A. Wokaun, C.W. Schneider, T. Lippert, *Appl. Phys. Lett.* **2014**, *105*, 114104.

[222] C. Yu, A.S. Sokolov, P. Kulik, V.G. Harris, *Journal of Alloys and Compounds* **2020**, *814*, 152301.

[223] J. Lapano, M. Brahlek, L. Zhang, J. Roth, A. Pogrebnyakov, R. Engel-Herbert, *Nat Commun* **2019**, *10*, 2464.

[224] J. Schou, M. Gansukh, R.B. Ettlinger, A. Cazzaniga, M. Grossberg, M. Kauk-Kuusik, S. Canulescu, *Appl. Phys. A* **2018**, *124*, 78.

[225] J. Schou, *Applied Surface Science* **2009**, *255*, 5191.

[226] P.E. Rodríguez-Hernández, J.G. Quiñones-Galván, M. Meléndez-Lira, J. Santos-Cruz, G. Contreras-Puente, F. De Moure-Flores, *Mater. Res. Express* **2020**, *7*, 015908.

[227] T. Maiti, M. Saxena, P. Roy, *J. Mater. Res.* **2019**, *34*, 107.

[228] L.W. Martin, Y.-H. Chu, R. Ramesh, *Materials Science and Engineering: R: Reports* **2010**, *68*, 89.

[229] S. Naseem, I.A. Rauf, K. Hussain, N.A. Malik, *Thin Solid Films* **1988**, *156*, 161.

[230] N. Blumenschein, T. Paskova, J.F. Muth, *Physica Status Solidi (a)* **2019**, *216*, 1900098.

[231] J.A. Padilla, E. Xuriguera, L. Rodríguez, A. Vannozzi, M. Segarra, G. Celentano, M. Varela, *Nanoscale Res Lett* **2017**, *12*, 226.

[232] V. Stanev, V.V. Vesselinov, A.G. Kusne, G. Antoszewski, I. Takeuchi, B.S. Alexandrov, *Npj Comput Mater* **2018**, *4*, 43.

[233] A.L. Patterson, *Phys. Rev.* **1939**, *56*, 978.

[234] W. Haron, A. Wisitsoraat, S. Wongnawa, *IJCEA* **2014**, *5*, 123.

[235] Y. Sharma, B.L. Musico, X. Gao, C. Hua, A.F. May, A. Herklotz, A. Rastogi, D. Mandrus, J. Yan, H.N. Lee, M.F. Chisholm, V. Keppens, T.Z. Ward, *Phys. Rev. Materials* **2018**, *2*, 060404.

[236] J.I. Goldstein, D.E. Newbury, P. Echlin, D.C. Joy, A.D. Romig, C.E. Lyman, C. Fiori, E. Lifshin, in *Scanning Electron Microscopy and X-Ray Microanalysis*, Springer US, Boston, MA **1992**, 671.

[237] T. Walther, *Nanomaterials* **2022**, *12*, 2220.

[238] T. Katayama, A. Chikamatsu, Y. Hirose, R. Takagi, H. Kamisaka, T. Fukumura, T. Hasegawa, *J. Mater. Chem. C* **2014**, *2*, 5350.

[239] R.C. Rai, *Journal of Applied Physics* **2013**, *113*, 153508.

[240] Y. Pan, M. Rahaman, L. He, I. Milekhin, G. Manoharan, M.A. Aslam, T. Blaudeck, A. Willert, A. Matković, T.I. Madeira, D.R.T. Zahn, *Nanoscale Adv.* **2022**, *4*, 5102.

[241] M. Lanza, *Conductive Atomic Force Microscopy: Applications in Nanomaterials*, Wiley-VCH Verlag GmbH & Co. KGaA**2017**.

[242] B. Xu, S.-A. Gopalan, A.-I. Gopalan, N. Muthuchamy, K.-P. Lee, J.-S. Lee, Y. Jiang, S.-W. Lee, S.-W. Kim, J.-S. Kim, H.-M. Jeong, J.-B. Kwon, J.-H. Bae, S.-W. Kang, *Sci Rep* **2017**, *7*, 45079.

[243] A. Ihalage, Y. Hao, *Npj Comput Mater* **2021**, *7*, 75.

[244] N. Maccaferri, Y. Zhao, T. Isoniemi, M. Iarossi, A. Parracino, G. Strangi, F. De Angelis, *Nano Lett.* **2019**, *19*, 1851.

[245] G.J. Pridham, *Electron. Power UK* **1970**, *16*, 34.

[246] B.S. Simpkins, M.A. Mastro, C.R. Eddy, J.K. Hite, P.E. Pehrsson, *Journal of Applied Physics* **2011**, *110*, 044303.

[247] P. López Varo, J.A. Jiménez Tejada, J.A. López Villanueva, J.E. Carceller, M.J. Deen, *Organic Electronics* **2012**, *13*, 1700.

[248] H. Wang, M. Bruna, P. Olivero, S. Borini, F. Picollo, O. Budnyk, F. Bosia, Ž. Pastuovic, N. Skukan, M. Jakšič, E. Vittone, *IOP Conf. Ser.: Mater. Sci. Eng.* **2010**, *16*, 012004.

[249] A. Moliton, *Optoelectronics of Molecules and Polymers*, Springer New York, NY, New York **2006**.

[250] M.B. Heaney, *Electrical Conductivity and Resistivity*, CRC Press**2003**.

[251] E.A. Duijnstee, J.M. Ball, V.M. Le Corre, L.J.A. Koster, H.J. Snaith, J. Lim, *ACS Energy Lett.* **2020**, *5*, 376.

[252] M. Dressel, M. Scheffler, *Annalen Der Physik* **2006**, *518*, 535.

[253] L.H. Lalasari, T. Arini, L. Andriyah, F. Firdiyono, A.H. Yuwono, Jakarta, Indonesia **2018**, 020001.

[254] S. Choi, S. Choi, B.K. Min, W.Y. Lee, J.S. Park, I. Kim, *Macro Materials & Eng* **2013**, *298*, 521.

[255] Q. Zhang, X. He, J. Shi, N. Lu, H. Li, Q. Yu, Z. Zhang, L.-Q. Chen, B. Morris, Q. Xu, P. Yu, L. Gu, K. Jin, C.-W. Nan, *Nat Commun* **2017**, *8*, 104.

[256] K. Chan-Joong, K. Ki-Baik, W. Dong-Yeon, *Materials Letters* **1992**, *14*, 268.

[257] V.M. Le Corre, E.A. Duijnstee, O. El Tambouli, J.M. Ball, H.J. Snaith, J. Lim, L.J.A. Koster, *ACS Energy Lett.* **2021**, *6*, 1087.

[258] H.-S. Kim, L. Bi, G.F. Dionne, C.A. Ross, *Applied Physics Letters* **2008**, *93*, 092506.

[259] P.C. Bowes, J.N. Baker, D.L. Irving, *J Am Ceram Soc* **2020**, *103*, 1156.

[260] Y.B. Zhu, K. Geng, Z.S. Cheng, R.H. Yao, *IEEE Trans. Plasma Sci.* **2021**, *49*, 2107.

[261] G. Zuo, Z. Li, O. Andersson, H. Abdalla, E. Wang, M. Kemerink, *J. Phys. Chem. C* **2017**, *121*, 7767.

[262] I. Chakraborty, N. Panwar, A. Khanna, U. Ganguly, **2016**.

[263] J.A. Schwenzer, T. Hellmann, B.A. Nejand, H. Hu, T. Abzieher, F. Schackmar, I.M. Hossain, P. Fassl, T. Mayer, W. Jaegermann, U. Lemmer, U.W. Paetzold, *ACS Appl. Mater. Interfaces* **2021**, *13*, 15292.

[264] K.A. Bush, A.F. Palmstrom, Z.J. Yu, M. Boccard, R. Cheacharoen, J.P. Mailoa, D.P. McMeekin, R.L.Z. Hoye, C.D. Bailie, T. Leijtens, I.M. Peters, M.C. Minichetti, N. Rolston,

R. Prasanna, S. Sofia, D. Harwood, W. Ma, F. Moghadam, H.J. Snaith, T. Buonassisi, Z.C. Holman, S.F. Bent, M.D. McGehee, *Nat Energy* **2017**, *2*, 17009.

[265] D.P. McMeekin, G. Sadoughi, W. Rehman, G.E. Eperon, M. Saliba, M.T. Hörantner, A. Haghighirad, N. Sakai, L. Korte, B. Rech, M.B. Johnston, L.M. Herz, H.J. Snaith, *Science* **2016**, *351*, 151.

[266] M. Saliba, T. Matsui, J.-Y. Seo, K. Domanski, J.-P. Correa-Baena, M.K. Nazeeruddin, S.M. Zakeeruddin, W. Tress, A. Abate, A. Hagfeldt, M. Grätzel, *Energy Environ. Sci.* **2016**, *9*, 1989.

[267] S. Karthick, H. Hawashin, N. Parou, S. Vedraine, S. Velumani, J. Bouclé, *Solar Energy* **2021**, *218*, 226.

[268] S. Karthick, S. Velumani, J. Bouclé, *Solar Energy* **2020**, *205*, 349.

[269] A. Gheno, Y. Huang, J. Bouclé, B. Ratier, A. Rolland, J. Even, S. Vedraine, *Solar RRL* **2018**, *2*, 1800191.

[270] A.A. Eliwi, M. Malekshahi Byranvand, P. Fassl, M.R. Khan, I.M. Hossain, M. Frericks, S. Ternes, T. Abzieher, J.A. Schwenzer, T. Mayer, J.P. Hofmann, B.S. Richards, U. Lemmer, M. Saliba, U.W. Paetzold, *Mater. Adv.* **2022**, *3*, 456.

[271] F. Yang, P. Zhang, M.A. Kamarudin, G. Kapil, T. Ma, S. Hayase, *Adv Funct Materials* **2018**, *28*, 1804856.

[272] K. Wang, T. Ye, X. Huang, Y. Hou, J. Yoon, D. Yang, X. Hu, X. Jiang, C. Wu, G. Zhou, S. Priya, *Matter* **2021**, *4*, 2522.

[273] B.R. Krishna, G. Veerappan, P. Bhyrappa, C. Sudakar, E. Ramasamy, *Mater. Adv.* **2022**, *3*, 2000.

[274] K. Zhao, R. Munir, B. Yan, Y. Yang, T. Kim, A. Amassian, *J. Mater. Chem. A* **2015**, *3*, 20554.

[275] Y. Yang, M.T. Hoang, D. Yao, N.D. Pham, V.T. Tiong, X. Wang, H. Wang, *J. Mater. Chem. A* **2020**, *8*, 12723.

[276] F.H. Isikgor, A.S. Subbiah, M.K. Eswaran, C.T. Howells, A. Babayigit, M. De Bastiani, E. Yengel, J. Liu, F. Furlan, G.T. Harrison, S. Zhumagali, J.I. Khan, F. Laquai, T.D. Anthopoulos, I. McCulloch, U. Schwingenschlögl, S. De Wolf, *Nano Energy* **2021**, *81*, 105633.

[277] N. Arora, M.I. Dar, A. Hinderhofer, N. Pellet, F. Schreiber, S.M. Zakeeruddin, M. Grätzel, *Science* **2017**, *358*, 768.

[278] P. Xu, J. Liu, J. Huang, F. Yu, C.-H. Li, Y.-X. Zheng, *New J. Chem.* **2021**, *45*, 13168.

[279] Y. Rong, S. Venkatesan, R. Guo, Y. Wang, J. Bao, W. Li, Z. Fan, Y. Yao, *Nanoscale* **2016**, *8*, 12892.

[280] T. Li, Q. Li, X. Tang, Z. Chen, Y. Li, H. Zhao, S. Wang, X. Ding, Y. Zhang, J. Yao, *J. Phys. Chem. C* **2021**, *125*, 2850.

[281] B.R. Patil, M. Ahmadpour, G. Sherafatipour, T. Qamar, A.F. Fernández, K. Zojer, H.-G. Rubahn, M. Madsen, *Sci Rep* **2018**, *8*, 12608.

[282] C. Chen, S. Zhang, S. Wu, W. Zhang, H. Zhu, Z. Xiong, Y. Zhang, W. Chen, *RSC Adv.* **2017**, *7*, 35819.

[283] C.-Y. Chang, W.-K. Huang, Y.-C. Chang, K.-T. Lee, C.-T. Chen, *J. Mater. Chem. A* **2016**, *4*, 640.

[284] J. Jiang, Z. Jin, F. Gao, J. Sun, Q. Wang, S. (Frank) Liu, *Advanced Science* **2018**, *5*, 1800474.

[285] T.S. Sherkar, C. Momblona, L. Gil-Escrig, J. Ávila, M. Sessolo, H.J. Bolink, L.J.A. Koster, *ACS Energy Lett.* **2017**, *2*, 1214.

[286] Y.-C. Chin, M. Daboczi, C. Henderson, J. Luke, J.-S. Kim, *ACS Energy Lett.* **2022**, *7*, 560.

[287] A. Gheno, *Printable and Printed Perovskites Photovoltaic Solar Cells for Autonomous Sensors Network*, Ph.D., University of Limoges, **2017**.

[288] C. Otero-Martínez, N. Fiuza-Maneiro, L. Polavarapu, *ACS Appl. Mater. Interfaces* **2022**, *14*, 34291.

[289] Y. Lin, Y. Firdaus, F.H. Isikgor, M.I. Nugraha, E. Yengel, G.T. Harrison, R. Hallani, A. El-Labban, H. Faber, C. Ma, X. Zheng, A. Subbiah, C.T. Howells, O.M. Bakr, I. McCulloch, S.D. Wolf, L. Tsetseris, T.D. Anthopoulos, *ACS Energy Lett.* **2020**, *5*, 2935.

[290] M. Pitaro, J.S. Alonso, L. Di Mario, D. Garcia Romero, K. Tran, T. Zaharia, M.B. Johansson, E.M.J. Johansson, M.A. Loi, *J. Mater. Chem. A* **2023**, *11*, 11755.

[291] S. Prathapani, P. Bhargava, S. Mallick, *Applied Physics Letters* **2018**, *112*, 092104.

[292] T. Wahl, J. Hanisch, E. Ahlswede, *J. Phys. D: Appl. Phys.* **2018**, *51*, 135502.

[293] H. Back, G. Kim, J. Kim, J. Kong, T.K. Kim, H. Kang, H. Kim, J. Lee, S. Lee, K. Lee, *Energy Environ. Sci.* **2016**, *9*, 1258.

[294] K.M.M. Salim, S. Masi, A.F. Gualdrón-Reyes, R.S. Sánchez, E.M. Barea, M. Krečmarová, J.F. Sánchez-Royo, I. Mora-Seró, *ACS Energy Lett.* **2021**, *6*, 3511.

[295] S.N. Pugliese, J.K. Gallaher, M.A. Uddin, H.S. Ryu, H.Y. Woo, J.M. Hodgkiss, *J. Mater. Chem. C* **2022**, *10*, 908.

[296] C.-H. Chiang, C.-G. Wu, *Nature Photon* **2016**, *10*, 196.

[297] R. Li, X. Liu, J. Chen, *Exploration* **2023**, *3*, 20220027.

[298] O. Almora, C. Aranda, I. Zarazua, A. Guerrero, G. Garcia-Belmonte, *ACS Energy Lett.* **2016**, *1*, 209.

[299] C.-H. Tsai, C.-M. Lin, C.-H. Kuei, *Coatings* **2020**, *10*, 237.

[300] Y. Wu, M. Yang, T.W. Ueltschi, M.A. Mosquera, Z. Chen, G.C. Schatz, R.P. Van Duyne, *J. Phys. Chem. C* **2019**, *123*, 29908.

[301] G. Bernardo, M. Melle-Franco, A.L. Washington, R.M. Dalgliesh, F. Li, A. Mendes, S.R. Parnell, *RSC Adv.* **2020**, *10*, 4512.

[302] M. Socol, N. Preda, C. Breazu, G. Petre, A. Stanculescu, I. Stavarache, G. Popescu-Pelin, A. Stochioiu, G. Socol, S. Iftimie, C. Thanner, O. Rasoga, *Materials* **2022**, *16*, 144.

[303] N. Wu, Y. Wu, D. Walter, H. Shen, T. Duong, D. Grant, C. Barugkin, X. Fu, J. Peng, T. White, K. Catchpole, K. Weber, *Energy Tech* **2017**, *5*, 1827.

[304] M.A. Aegerter, M.M. Mennig, *Sol-Gel Technologies for Glass Producers and Users*, Springer New York, NY, New York **2004**.

[305] S. Thomas, A. Thankappan, *Perovskite Photovoltaics: Basic to Advanced Concepts and Implementation*, Academic Press**2018**.

[306] D.M. Mattox, *The Foundations of Vacuum Coating Technology*, William Andrew**2003**.

[307] X. Yang, Z. Chu, J. Meng, Z. Yin, X. Zhang, J. Deng, J. You, *J. Phys. Chem. Lett.* **2019**, *10*, 2892.

[308] T.-H. Han, K.Y. Jang, Y. Dong, R.H. Friend, E.H. Sargent, T.-W. Lee, *Nat Rev Mater* **2022**, *7*, 757.

[309] K. Ji, M. Anaya, A. Abfalterer, S.D. Stranks, *Advanced Optical Materials* **2021**, *9*, 2002128.

[310] J. Byun, H. Cho, C. Wolf, M. Jang, A. Sadhanala, R.H. Friend, H. Yang, T. Lee, *Advanced Materials* **2016**, *28*, 7515.

[311] N. Liu, S. Mei, D. Sun, W. Shi, J. Feng, Y. Zhou, F. Mei, J. Xu, Y. Jiang, X. Cao, *Micromachines* **2019**, *10*, 344.

[312] Y. Zou, T. Wu, F. Fu, S. Bai, L. Cai, Z. Yuan, Y. Li, R. Li, W. Xu, T. Song, Y. Yang, X. Gao, F. Gao, B. Sun, *J. Mater. Chem. C* **2020**, *8*, 15079.

[313] D.G. Zheng, D.H. Kim, *Nanophotonics* **2023**, *12*, 451.

[314] A. Vyšniauskas, S. Keegan, K. Rakstys, T. Seewald, V. Getautis, L. Schmidt-Mende, A. Fakharuddin, *Organic Electronics* **2022**, *111*, 106655.

[315] H. Kim, L. Zhao, J.S. Price, A.J. Grede, K. Roh, A.N. Brigeman, M. Lopez, B.P. Rand, N.C. Giebink, *Nat Commun* **2018**, *9*, 4893.

[316] J.H. Park, A.K. Harit, C.H. Jang, J.-E. Jeong, H.Y. Woo, M.H. Song, *Materials Today Energy* **2021**, *21*, 100755.

[317] https://www.rsc.org/periodic-table/element/20/calcium

[318] http://www.surface-tension.de

[319] M. Petrosino, A. Rubino, *Synthetic Metals* **2012**, *161*, 2714.

[320] D.P. Birnie, *Langmuir* **2013**, *29*, 9072.

[321] K. Jung, D.H. Kim, J. Kim, S. Ko, J.W. Choi, K.C. Kim, S.-G. Lee, M.-J. Lee, *Journal of Materials Science & Technology* **2020**, *59*, 195.

[322] J.R. Vig, *Journal of Vacuum Science & Technology A: Vacuum, Surfaces, and Films* **1985**, *3*, 1027.

[323] A. Klasen, P. Baumli, Q. Sheng, E. Johannes, S.A. Bretschneider, I.M. Hermes, V.W. Bergmann, C. Gort, A. Axt, S.A.L. Weber, H. Kim, H.-J. Butt, W. Tremel, R. Berger, *J. Phys. Chem. C* **2019**, *123*, 13458.

[324] Y. Cho, H.R. Jung, W. Jo, *Nanoscale* **2022**, *14*, 9248.

[325] A. Chandel, Q.B. Ke, S.-E. Chiang, H.-M. Cheng, S.H. Chang, *Nanoscale Adv.* **2023**, *5*, 2190.

[326] Z. Liang, S. Zhang, X. Xu, N. Wang, J. Wang, X. Wang, Z. Bi, G. Xu, N. Yuan, J. Ding, *RSC Adv.* **2015**, *5*, 60562.

[327] C. Chiang, C. Wu, *ChemSusChem* **2016**, *9*, 2666.

[328] Z. Chu, M. Yang, P. Schulz, D. Wu, X. Ma, E. Seifert, L. Sun, X. Li, K. Zhu, K. Lai, *Nat Commun* **2017**, *8*, 2230.

[329] S. Wang, A. Wang, F. Hao, *iScience* **2022**, *25*, 103599.

[330] D.J. Vogel, A. Kryjevski, T. Inerbaev, D.S. Kilin, *J. Phys. Chem. Lett.* **2017**, *8*, 3032.

[331] A. Ummadisingu, S. Meloni, A. Mattoni, W. Tress, M. Grätzel, *Angew Chem Int Ed* **2021**, *60*, 21368.

[332] E.V. Péan, S. Dimitrov, C.S. De Castro, M.L. Davies, *Phys. Chem. Chem. Phys.* **2020**, *22*, 28345.

[333] T. Liu, Y. Zhou, Z. Li, L. Zhang, M. Ju, D. Luo, Y. Yang, M. Yang, D.H. Kim, W. Yang, N.P. Padture, M.C. Beard, X.C. Zeng, K. Zhu, Q. Gong, R. Zhu, *Advanced Energy Materials* **2018**, *8*, 1800232.

[334] H. Tan, F. Che, M. Wei, Y. Zhao, M.I. Saidaminov, P. Todorović, D. Broberg, G. Walters, F. Tan, T. Zhuang, B. Sun, Z. Liang, H. Yuan, E. Fron, J. Kim, Z. Yang, O. Voznyy, M. Asta, E.H. Sargent, *Nat Commun* **2018**, *9*, 3100.

[335] C. Qiu, L. Wagner, J. Liu, W. Zhang, J. Du, Q. Wang, Y. Hu, H. Han, *EcoMat* **2023**, *5*, e12268.

[336] M. Zhang, H. Yu, M. Lyu, Q. Wang, J.-H. Yun, L. Wang, *Chem. Commun.* **2014**, *50*, 11727.

[337] V. Rodov, A.L. Ankoudinov, Taufik, *IEEE Trans. on Ind. Applicat.* **2008**, *44*, 234.

[338] L. Zhu, D. Liu, J. Wang, N. Wang, *J. Phys. Chem. Lett.* **2020**, *11*, 8502.

[339] A. Caiazzo, R.A.J. Janssen, *Advanced Energy Materials* **2022**, *12*, 2202830.

[340] H. Lee, D. Ko, C. Lee, *ACS Appl. Mater. Interfaces* **2019**, *11*, 11667.

[341] L. Zhang, C. Sun, T. He, Y. Jiang, J. Wei, Y. Huang, M. Yuan, *Light Sci Appl* **2021**, *10*, 61.

[342] A.D. Golinskaya, A.M. Smirnov, M.V. Kozlova, E.V. Zharkova, R.B. Vasiliev, V.N. Mantsevich, V.S. Dneprovskii, *Results in Physics* **2021**, *27*, 104488.

[343] M. Coduri, T.B. Shiell, T.A. Strobel, A. Mahata, F. Cova, E. Mosconi, F. De Angelis, L. Malavasi, *Mater. Adv.* **2020**, *1*, 2840.

[344] X. Yang, X. Zhang, J. Deng, Z. Chu, Q. Jiang, J. Meng, P. Wang, L. Zhang, Z. Yin, J. You, *Nat Commun* **2018**, *9*, 1169.

[345] Y.C. Kim, S.-D. Baek, J.-M. Myoung, *Journal of Alloys and Compounds* **2019**, *786*, 11.

[346] Q. Dong, L. Lei, J. Mendes, F. So, *J. Phys. Mater.* **2020**, *3*, 012002.

[347] S.S. Shin, S.J. Lee, S.I. Seok, *APL Materials* **2019**, *7*, 022401.

[348] C. Duan, Z. Liu, L. Yuan, H. Zhu, H. Luo, K. Yan, *Advanced Optical Materials* **2020**, *8*, 2000216.

[349] K. Wang, Y. Tian, H. Jiang, M. Chen, S. Xu, *International Journal of Photoenergy* **2019**, *2019*, 1.

[350] A.R.M. Alghamdi, M. Yanagida, Y. Shirai, G.G. Andersson, K. Miyano, *ACS Omega* **2022**, *7*, 12147.

[351] D. Akın Kara, K. Kara, G. Oylumluoglu, M.Z. Yigit, M. Can, J.J. Kim, E.K. Burnett, D.L. Gonzalez Arellano, S. Buyukcelebi, F. Ozel, O. Usluer, A.L. Briseno, M. Kus, *ACS Appl. Mater. Interfaces* **2018**, *10*, 30000.

[352] J. Wang, F. Zhang, L. Li, Q. An, J. Zhang, W. Tang, F. Teng, *Solar Energy Materials and Solar Cells* **2014**, *130*, 15.

[353] M. Kim, *Analysis of Ion Migration and Ageing Characteristics for Triple-Cation and CH3NH3PbI3-xClx Perovskite Based Thin-Film Solar Cells*, Ph.D., l'Institut Polytechnique de Paris, **2021**.

[354] www.nanoscience.com/techniques/scanning-electron-microscopy/

[355] www.maxiv.lu.se/beamlines-accelerators

[356] https://jascoinc.com/learning-center/theory/spectroscopy/uv-visspectroscopy

[357] www.picoquant.com/applications/category/materials-science/time-resolved photoluminescence

[358] A.Ch. Lazanas, M.I. Prodromidis, *ACS Meas. Sci. Au* **2023**, *3*, 162.

[359] V. Ezhilmaran, R. Damodaram, *Lasers Manuf. Mater. Process.* **2021**, *8*, 15.

Appendices

Appendix 1. Solid-State Synthesis and PLD Processing

Appendix 1.1. XRD Pattern of STFO Powder After Calcination Process

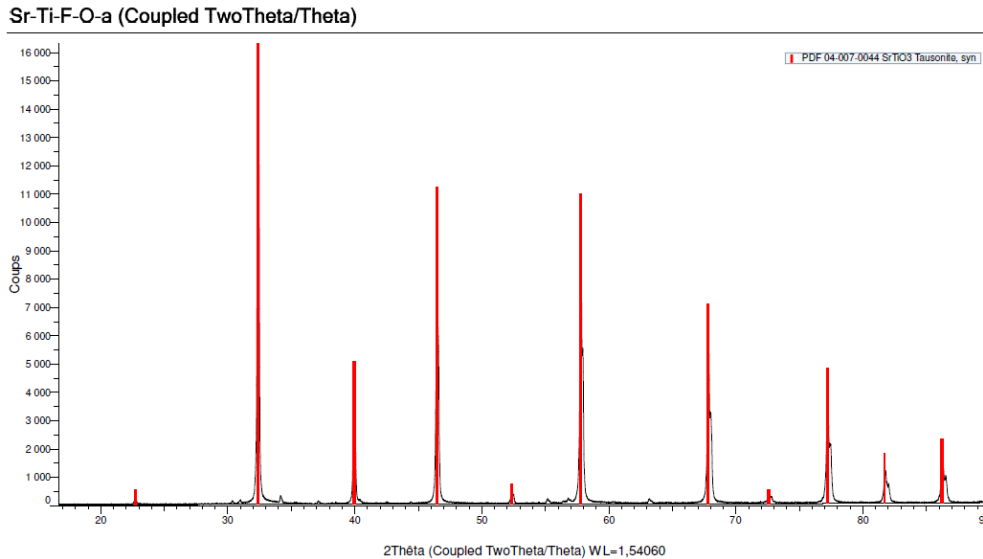The phase purity of STFO powders obtained by solid-state synthesis was confirmed by XRD (Siemens D5000, Cu-Kα).

Figure A. 1: XRD pattern (2θ-θ [degree]) of STFO powder after calcination process

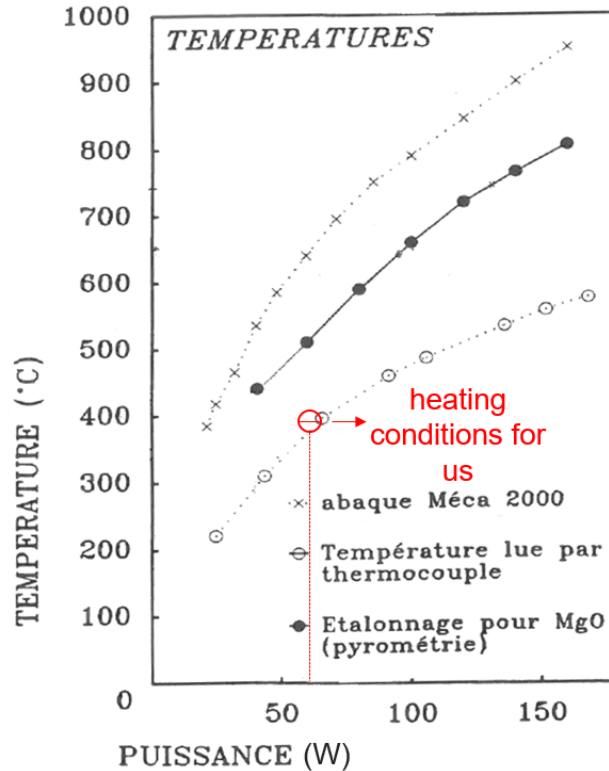### Appendix 1.2. Voltage-Temperature Profile of PLD Process

Figure A. 2: Temperature-power relation in PLD process

Appendix 2. Experimental Details

a. Additional Thermal Annealing

- Conventional Thermal Annealing (TA): The TA is carried out by Caderal©, Compact muffle furnace model.

- Rapid Thermal Processing: The RTP is carried out by Annealsys©, AS-One model. The operation recipe that has been applied is as follows:

Operation Type	Operation Details
Pumping	Starting primary pumping chamber
Condition	Waiting for strain is < 1 mbar
Condition	Waiting for duration is 60s
Pressure	Pressure control: Setpoint 5 mbar
Condition	Waiting for duration is 120s
RTP Temp	Power control to 10% and waiting for Pyro 1 is >150°C
RTP Temp	Pyro 1 control to 550°C with ramp at 10°C/s
Condition	Waiting for duration is =100 s
RTP Temp	Pyro control to 20°C with ramp at 10°C/s
Condition	Waiting for duration is =150 s
Pumping	Stop
Purge	Purging until ATM

Figure A. 3: The operation recipe of RTP

b. Structural Characterizations

- X-ray Diffraction: Crystallinity of thin films is characterized by Bruker©, D8 Advance Model with Cu Kα X-ray source (λ=0.154 nm), equipped with LynxEye type detector (A17-B60 model) and Kα1 mono filter.
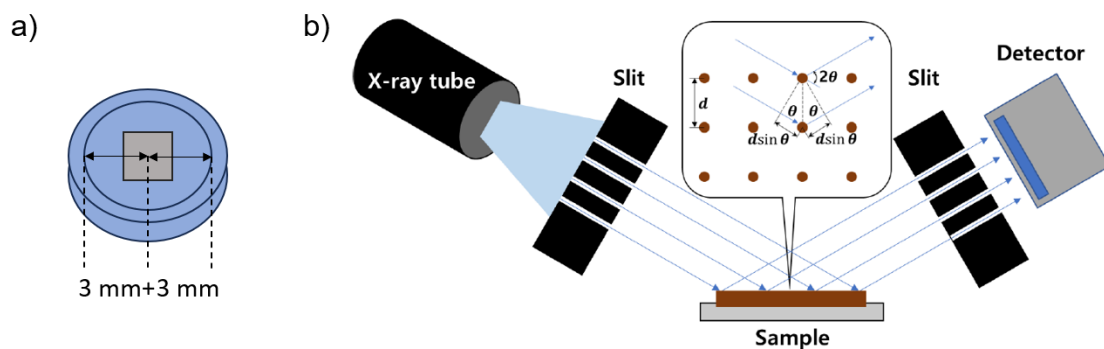

Figure A. 4: XRD analysis of a) the sample preparation on a holder b) 2θ-θ scan[353]

First, the sample is precisely placed in the holder with the help of a gum, centered and leveled between the holder and sample heights. In general, XRD measurements are performed without rotation in the 2θ-θ range between 10°-90° with a step size of 0.0194° and an acquisition time of 318.7 seconds per step. The "DIFFRAC.EVA" program is also used for XRD data processing.

- SEM and SEM-FIB: SEM FEI© (Model Quanta FEG 450) and ZEISS© (Model Crossbeam 550) are used for morphology and microstructure characteristics of thin films.
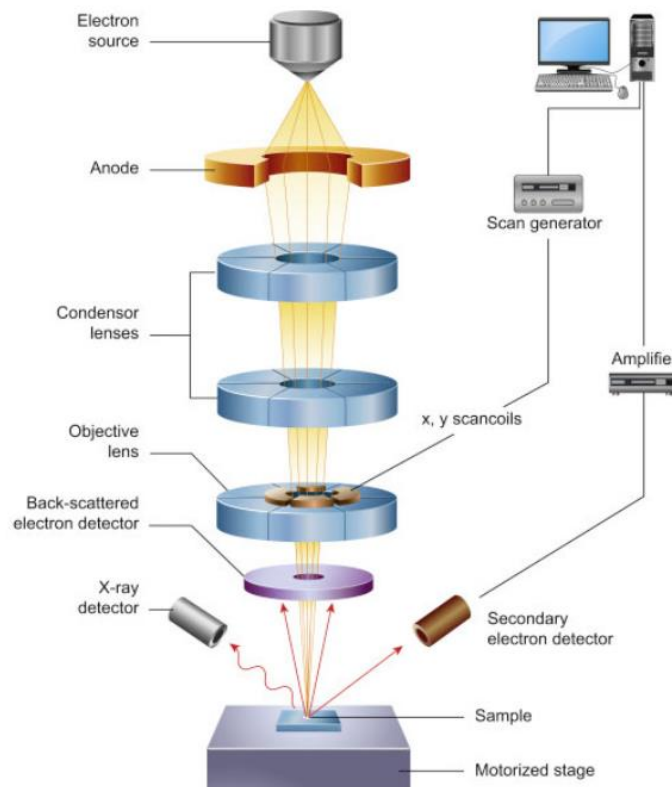

Figure A. 5: Principle of the scanning electron microscopy[354]

In order to use conventional imaging in SEM, samples need to be electrically conductive at least on the surface and electrically grounded to prevent electrostatic charge built-up. To achieve this, samples are first coated with a 10-15 nm thick layer of platinum or carbon using low-vacuum sputter coating (Bruker©, High Resolution Sputter Coating 208HR). Afterwards, the samples are integrated into the SEM setup by being securely mounted onto the sample holder, generally using a conductive adhesive. In general, SEM measurements are performed in secondary electron imaging mode at a working distance of 5 mm. Probe current and voltage are 500 pA and 2-3 kV, respectively.

- EDS or EDX: Oxford Instruments© (Model Advanced) is used for elemental composition analysis of thin films.

Chemical investigations of EDS has been conducted using the SEM setup's integrated system.

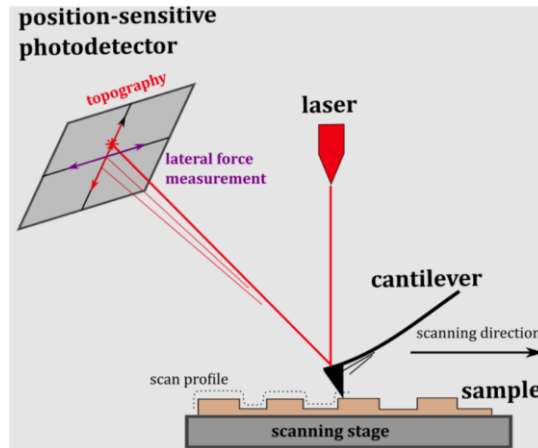- Atomic Force Microscopy: Bruker© (Model IconXR) is used for surface topography analysis of thin films.

Figure A. 6: Principle of the atomic force microscopy[355]

This equipment includes a motorized platform which can be programmed for analyzing several sites at once. Measurement are performed automatically with the help of a pre-existing program by using non-contact mode and data processing is done using "Pico Image" surface imaging and analysis software.

c. Optical Characterizations

- UV-Vis Spectrometer: The measurement is carried out by Agilent Technologies© Cary 300 Spectrometer over 200-800 nm range.
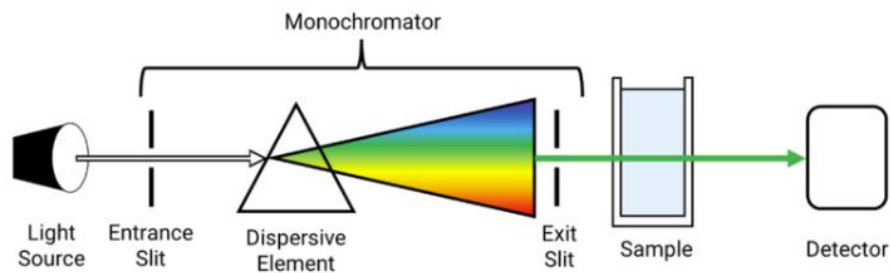

Figure A. 7: Principle of the UV-Vis spectrometer[356]

- Photoluminescence Spectrometer: Edinburgh Instrument© FLS980 Spectrometer is used for steady-state and time-resolved photoluminescence characteristics. The PL decay kinetics is performed using the built-in Fluorescence Analysis Software Technology (FAST) software.
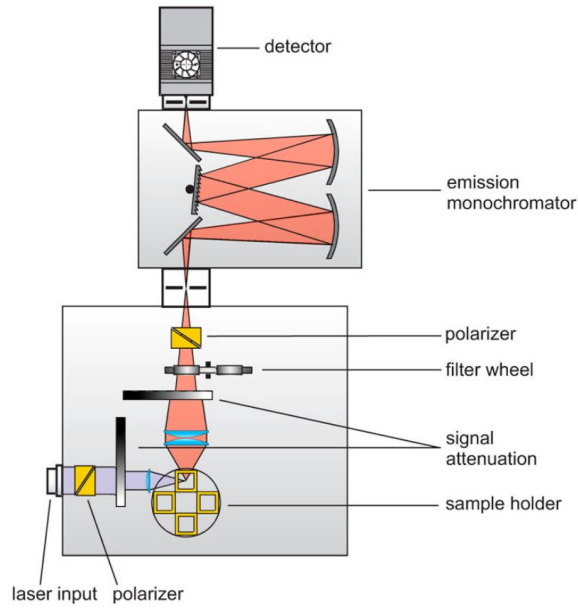
Figure A. 8: Principle of the photoluminance spectrometer[357]

d. Electrical Properties

- <u>Impedance Spectroscopy:</u> Resistance of STFO types is controlled by Hewlett Packard© LCR meter, 4284A model.
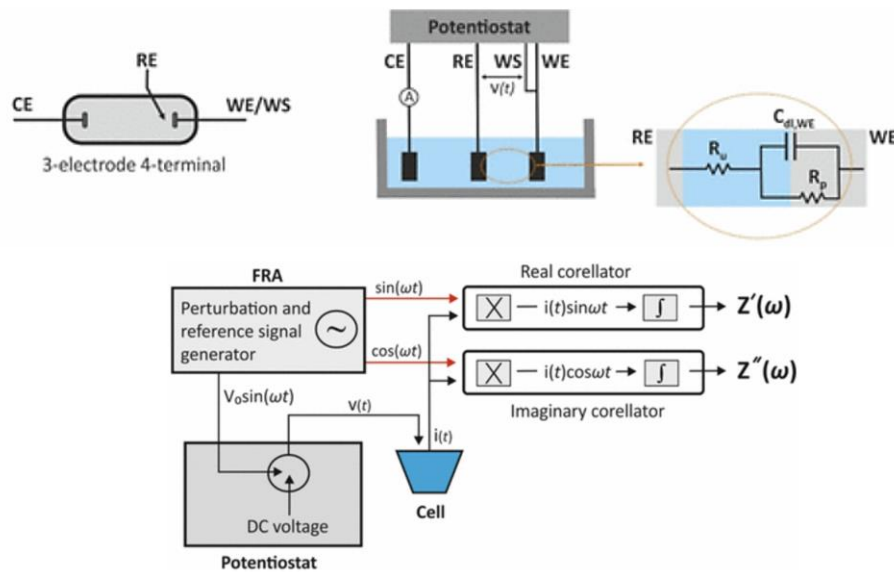

Figure A. 9: Principle of the electrochemical impedance spectrometer[358]

e. Rheological Properties

- <u>Tensiometer:</u> Contact angel measurement of thin films is carried out with Dataphysics© tensiometer, LDU 25 model.
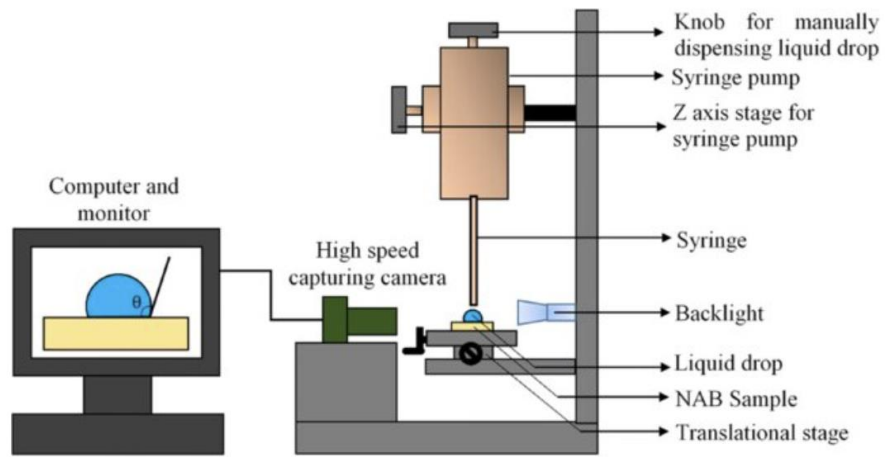
Figure A. 10: Principle of the contact angle measurement[359]

Using a Perovskite Oxide as Interfacial Layer for Halide Perovskite Optoelectronics

Les cellules photovoltaïques et les diodes électroluminescentes pérovskites requièrent des couches d'injection/extraction de charges, qui sont cruciales pour plusieurs processus importants régissant les performances et la durée de vie. Bien que des études intensives aient été consacrées au développement de couches interfaciales innovantes de type p, des matériaux présentant des propriétés hautement ajustables et une stabilité photochimique élevée restent très recherchés. Cette thèse explore l'utilisation d'oxydes pérovskites comme couches d'interface pour des applications optoélectroniques en raison de leurs propriétés ajustables et de leur stabilité en conditions ambiantes. Des couches minces d'oxydes de pérovskites de type $SrTi_{0.7}Fe_{0.3}O_{3-\delta}$ (STFO) sont utilisées comme couches d'extraction ou d'injection de charge pour les cellules solaires et les diodes électroluminescentes à base de pérovskites halogénées. En utilisant la technique de dépôt par laser pulsé (PLD), des couches minces STFO hautement cristallines ont été déposées sur des substrats en verre/FTO à des températures relativement modérées (<400 °C) par rapport aux techniques de dépôt traditionnelles. Des post-traitements thermiques, soit par traitement thermique rapide (RTP), soit par recuit thermique conventionnel (TA), ont été utilisés dans le but d'améliorer la plus grand cristalline des films polycristallins et pour ajuster leurs propriétés optiques et électroniques.

Lorsqu'ils sont déposés sur la pérovskite d'oxyde, les couches d'halogénure de pérovskite de type $FA_{0.85}Cs_{0.15}Pb(I_{0.85}Br_{0.15})_3$ (adaptées à la conversion d'énergie photovoltaïque PV) présentent des tailles de grains plus grandes et un meilleur ordre cristallin par rapport à des films similaires déposés sur une couche interfaciale de type p de référence telle que le PEDOT:PSS commercial. De plus, la présence de l'oxyde a entraîné une nette réduction de la phase de pérovskite halogénée optiquement inactive, illustrant l'impact positif de la couche d'oxyde pérovskite sous-jacente. Les couche de STFO recuites (RTP et le TA) induisent par ailleurs une plus grande durée de vie de l'exciton dans la couche active par rapport au PEDOT :PSS. De façon similaire, la cristallisation d'une pérovskite halogénée quasi-2D de type $(PEA)_2(MA)PbBr_4$ (adaptée à la fabrication de LED) sur des couches de STFO a été réalisée avec succès, conduisant à des propriétés similaires que pour des couches références déposées sur du PEDOT:PSS. Dans ce cas, la pérovskite quasi-2D déposée sur STFO a montré une durée de vie de l'exciton relativement longue. Bien que l'intégration de couches minces de STFO dans les deux types de dispositifs ait donné lieu à des performances limitées, ce travail démontre le fort potentiel de la classe des oxydes de pérovskites pour la création de dispositifs tout-pérovskite efficaces et stables.

Using a Perovskite Oxide as Interfacial Layer for Halide Perovskite Optoelectronics

Halide organic-inorganic photovoltaics and light-emitting diodes require suitable charge injection/extraction layers, which are crucial for several important processes governing performance and lifetime. While intensive research has been devoted to developing innovative p-type interfacial layers, materials with highly tunable properties and high photochemical stability remain in demand. This thesis explores oxide perovskites as interlayers for optoelectronic applications due to their stable physical properties under ambient conditions. $SrTi_{0.7}Fe_{0.3}O_{3-\delta}$ (STFO) oxide perovskite thin film is utilized as charge extraction/injection layers for planar halide perovskite solar cells and light-emitting diodes. Using pulsed laser deposition (PLD), highly crystalline STFO thin layers on glass/FTO substrates have been successfully processed at relatively moderate temperatures (<400 °C) as compared to traditional deposition techniques. Additional thermal treatments, either by rapid thermal processing (RTP) or conventional thermal annealing, have been applied to the oxide thin films to further improve the larger crystal of the polycrystalline layers, and to tune their optical and electronic properties.

When deposited on top of the oxide perovskite, $FA_{0.85}Cs_{0.15}Pb(I_{0.85}Br_{0.15})_3$ halide perovskite layer (suitable for photovoltaic PV energy conversion) show larger grain sizes and better crystalline order than compared to similar films deposited on top of reference p-type interlayer such as commercial PEDOT:PSS. Furthermore, the presence of the oxide resulted in a clear reduction of the fraction of optically inactive halide perovskite phase. This observation suggests that the perovskite interlayer positively impacts the growth mechanism of the halide perovskite active layer. Finally, annealed STFO layers induce longer exciton lifetime in the halide perovskite active layer, compared PEDOT:PSS. Similarly, the crystallization of the $(PEA)_2(MA)PbBr_4$ quasi-2D perovskite (suitable for light-emitting LED applications) on STFO layers was found to be of high quality, leading to comparable properties of layers deposited on top of classical PEDOT:PSS. Moreover, quasi-2D perovskite on STFO showed quite a long exciton lifetime. Although STFO thin films integrated into both halide perovskite PV and LED devices have conducted to limited performance, this work demonstrates the high potential of oxide perovskites towards efficient and stable all-perovskite devices.